

**ADVANCED OXIDATION AND REDUCTION PROCESSES FOR THE REMOVAL
OF RECALCITRANT POLLUTANTS IN WATER**

A Dissertation

By

YINGHAO WEN

Submitted to the Graduate and Professional School of Texas A&M University
in partial fulfillment of the requirement for the degree of
DOCTOR OF PHILOSOPHY

Chair of Committee,	Xingmao Ma
Committee Members,	Virender K. Sharma
	Garrett McKay
	Ying Li
Head of Department,	Zachary Grasley

May 2022

Major: Civil Engineering

Copyright 2022 Yinghao Wen

ABSTRACT

Due to the rapidly growing population, industrial manufacturers and agricultural producers are seeking every opportunity to meet the booming demands, which have inevitably led to the aggravated water contamination by a variety of recalcitrant pollutants. Among the various water treatment technologies, advanced oxidation processes (AOPs) and advanced reduction processes (ARPs) possess significant potentials owing to their capability of degrading recalcitrant pollutants via highly reactive species. This dissertation aims to further explore the potentials of homogeneous AOPs induced by persulfates and ARPs mediated by heterogeneous photocatalysts in the removal of persistent legacy and emerging pollutants.

Chapter I of this dissertation provides an overview of the urgent situation of water contamination and the basics of AOPs and ARPs.

Chapter II describes the first catalyst-free activation of peroxydisulfate (PDS) by visible light. Importantly, the formation of reactive species is distinctively different in the PDS visible light system with and without pollutant (e.g., atrazine (ATZ)). In addition to the sulfate radical ($\text{SO}_4^{\bullet-}$) generated via $\text{S}_2\text{O}_8^{2-}$ dissociation under visible light, $\text{O}_2^{\bullet-}$ and $^1\text{O}_2$ are also produced in both systems. In the absence of ATZ, H_2O_2 and $\text{O}_2^{\bullet-}$ are key intermediates and precursors for $^1\text{O}_2$, whereas in the presence of ATZ, oxidation of ATZ by $\text{SO}_4^{\bullet-}$ under oxic condition is critical for the formation of $^1\text{O}_2$. Overall, both radical and nonradical processes contribute to the degradation of ATZ.

Chapter III discusses the direct activation of peroxymonosulfate (PMS) by co-existing phosphate and carbonate to produce $\text{SO}_4^{\bullet-}$. Overall, $\text{SO}_4^{\bullet-}$ -induced degradation was the major

pathway for the degradation of atrazine, whereas direct oxidation by PMS served as a supporting pathway. Without any catalysts, PMS also displayed appreciable effectiveness in real lake and river waters.

In chapter IV, a zinc ferrite/zero-valent iron (ZFO/nZVI) nanocomposite with a unique core-shell-skin tertiary structure consisting of an nZVI core surrounded by ZnFe₂O₄ shell and further wrapped by wrinkled ZnFe₂O₄ skin layer is reported. The nanocomposite displayed an impressive 100% and 99.7% simultaneous removal for nitrate and arsenate at pH 7.0 under visible light. Reduction by photogenerated electrons was the dominant mechanism for nitrate removal, while adsorption is the primary process for arsenate removal.

Chapter V demonstrates the efficient photocatalytic degradation of perfluorooctanoic acid (PFOA) by a titanium-based metal-organic framework (MOF) MIL-125-NH₂ with glucose as the sacrificial reductant. A 100% removal rate of PFOA and a 66.7% of total defluorination rate were achieved within 24 hours. Based on the untargeted analysis for degradation metabolites, H/F exchange and chain-shortening initiated by hydrated electron (e_{aq}^-) were proposed as the dominant degradation pathways for PFOA. In addition, the MOF almost completely removed PFOA after three cycles and maintained a high degree of structural integrity, illustrating excellent recyclability and stability.

In the last chapter, chapter VI, a summary of the dissertation is described along with my recommendations for future research.

DEDICATION

To my family and friends, especially my Mom, my Dad and my Wife

Thank you for all your love and support

ACKNOWLEDGEMENTS

First, I would like to thank my Ph.D. advisor and committee chair, Dr. Xingmao (Samuel) Ma, without whom none of these would have been possible. Thank you for guiding me throughout my Ph.D. program and always motivating me to be an outstanding researcher. Thank you for being encouraging whenever I need it and being strict with science. I have benefited so much from you in every aspect. I am also grateful to Dr. Virender K. Sharma, who has offered me tremendous help during my study at TAMU. I would also like to express my appreciation to my other committee members, Dr. Garrett McKay and Dr. Ying Li for supporting me in completing my dissertation.

I am thankful for all the people I have worked with, who have offered me generous helps. I would like to thank Jieming Yuan, Xiaoxuan Wang and Binglin Guo as my fellow Ph.D. students for their friendship over these years. I would like to express my gratitude to Dr. Hong-Cai (Joe) Zhou for teaching me about MOFs and guiding me on the MOF/PFAS studies. I would like to thank Mallory Smith and Hannah Drake for helping me characterize MOFs and teaching me about EPR. I would also like to thank Dr. Gregory S. Day, Carlos Ybanez, Anne Boehme, and Ray Ozdemir at the Framergy Inc. for their help with my MOF/PFAS studies. I am also grateful to Dr. Weilan Zhang and Dr. Mingbao Feng for their advices on research.

Finally, I want to thank my family and friends, especially my mother (Ying Huang), father (Youping Wen), wife (Lu Yang), aunt (Ming Yang), uncle (Houquan Dai), and best friends (Mojun Li and Yanhao Feng) for their love, support, and understanding. Without any of them, my journey to a Ph.D. would have been impossible. Thank you for always believing me and encouraging me to be the best person I could be.

CONTRIBUTORS AND FUNDING SOURCES

Contributors

This work was supported by a dissertation committee consisting of Dr. Xingmao Ma and Dr. Garrett McKay of the Department of Civil and Environmental Engineering, Dr. Virender K. Sharma of the School of Public Health, and Dr. Ying Li of the Department of Mechanical Engineering. The material characterizations in chapter IV were performed by Dr. Jiechao Jiang from the University of Texas at Arlington. The LC-MS data was collected by Smriti Shankar and Dr. Cory Klemashevich from the Integrated Metabolomics Analysis Core. The material characterizations in chapter V were performed by Dr. Gregory S. Day from Framergy Inc. and Mallory Smith from the Department of Chemistry. All other work conducted in this dissertation was completed by the student.

Funding Sources

This work was supported by the Development of Water Programs of Excellence by Texas Water Resources Institute and the State of Texas as part of the program of the Texas Hazardous Waste Research Center.

ABBREVIATIONS

AFFF	Aqueous fire-fighting foam
ANOVA	Analysis of variance
AOP	Advanced oxidation process
ARP	Advanced reduction process
ATR-FTIR	Attenuated total reflection-fourier transform infrared spectroscopy
ATZ	Atrazine
BDE	Bond dissociation energy
BE	Binding energy
BJH	Barrett-Joyner-Halenda
CB	Conduction band
CCC	Critical coagulation concentration
CMZ	Carbamazepine
DEA	2-chloro-4-amino-6-isopropylamino-1,3,5-triazine
DFT	Density functional theory
DIA	2-chloro-4-ethylamino-6-amino-1,3,5-triazine
DLS	Dynamic light scattering
DO	Dissolved oxygen
DOC	Dissolved organic carbon
DMPO	5,5-dimethyl-1-pyrroline N-oxide
EDS	X-ray energy dispersive spectroscopy

EPA	Environmental protection agency
EPR	Electron paramagnetic resonance
FA	Formic acid
FE-SEM	Field-emission scanning electron microscopy
FFA	Furfuryl alcohol
HPLC	High-performance liquid chromatograph
HR-TEM	High-resolution transmission electron microscopy
IBP	Ibuprofen
IC	Ion chromatography
ICDD	International Centre for Diffraction Data
ICP-MS	Inductively coupled plasma-mass spectrometry
IFE	Inner filter effect
IHSS	International Humic Substances Society
IPA	Iso-propanol
IS	Ionic strength
LC-HRAM	Liquid chromatography high resolution accurate mass spectrometry
LC-MS	Liquid chromatography mass spectrometry
L-his	L-histidine
LOQ	Limit of quantification
MCL	Maximum contaminant level
MeOH	Methanol
MIL	Materials from Institut Lavoisier

MOF	Metal-organic framework
NBD	Nano-beam electron diffraction
NHANES	National Health and Nutrition Examination Survey
NOM	Natural organic matter
PAA	Peracetic acid
PBQ	P-benzoquinone
PDS	Peroxydisulfate
PFAS	Per- and polyfluorinated substances
PFBA	Perfluorobutanoic acid
PFCA	Perfluorinated carboxylic acids
PFHpA	Perfluoroheptanoic acid
PFHxA	Perfluorohexanoic acid
PFHxS	Perfluorohexane sulfonate
PFNA	Perfluorononanoic acid
PFOA	Perfluorooctanoic acid
PFOS	Perfluorooctanoic sulfonate
PFPeA	Perfluoropentanoic acid
PFPrA	Perfluoropropanoic acid
PL	Photoluminescence
PMS	Peroxymonosulfate
PPCP	Pharmaceuticals and personal care product
RCS	Reactive chlorine species

ROS	Reactive oxygen species
RSE	Reaction stoichiometric efficiency
SAC	Single-atom catalyst
SAED	Selected-area electron diffraction
SDM	Sulfadimethoxine
SMX	Sulfamethoxazole
SOD	Superoxide dismutase
SPE	Solid-phase-extraction
SRNOM	Suwannee river natural organic matter
STP	Standard temperature and pressure
TBA	Tert-butanol
TEMP	2,2,6,6-tetramethyl-4-piperidine
TEMPO	2,2,6,6-tetramethyl-1-piperidinyloxy
TGA	Thermogravimetric analysis
TMP	Trimethoprim
UV	Ultraviolet
UV-Vis	Ultraviolet-visible
UV-Vis DRS	Ultraviolet-visible diffuse reflectance spectra
VB	Valence band
XPS	X-ray photoelectron spectroscopy
XRD	X-ray diffraction
ZFO/ZVI	Zinc ferrite/zero-valent iron

TABLE OF CONTENTS

ABSTRACT.....	ii
DEDICATION	iv
ACKNOWLEDGEMENTS.....	v
CONTRIBUTORS AND FUNDING SOURCES	vi
ABBREVIATIONS.....	vii
TABLE OF CONTENTS.....	xi
LIST OF FIGURES	xiii
LIST OF TABLES	xviii
CHAPTER I INTRODUCTION.....	1
The prevalence and threat of recalcitrant pollutants in water	1
Advanced oxidation and reduction processes in water decontamination	3
CHAPTER II CATALYST-FREE ACTIVATION OF PEROXYDISULFATE BY VISIBLE LIGHT: POLLUTANT-DEPENDENT PRODUCTION OF REACTIVE SPECIES.....	9
Introduction.....	9
Experimental Section	12
Results and Discussion	17
Conclusions.....	34
CHAPTER III ACTIVATION OF PEROXYMONOSULFATE BY PHOSPHATE AND CARBONATE FOR THE ABATEMENT OF ATRAZINE: ROLES OF RADICAL AND NON-RADICAL SPECIES	36

Introduction.....	36
Experimental Section	38
Results and Discussion	43
Conclusions.....	55
CHAPTER IV SIMULTANEOUS REMOVAL OF NITRATE AND ARSENATE BY VISIBLE LIGHT ACTIVE ZINC FERRITE/ZERO-VALENT IRON NANOCOMPOSITE	57
Introduction.....	57
Experimental Section	61
Results and Discussion	67
Conclusions.....	91
CHAPTER V PHOTOCATALYTIC DEGRADATION OF PERFLUOROOCCTANOIC ACID BY TITANIUM-BASED METAL-ORGANIC FRAMEWORK MIL-125-NH ₂	93
Introduction.....	93
Experimental Section	96
Results and Discussion	101
Conclusions.....	110
CHAPTER VI CONCLUSIONS AND RECOMMENDATIONS	112
SUPPORTING INFORMATION.....	114
Supporting Figures.....	114
Supporting Tables	148
REFERENCES	161

LIST OF FIGURES

Figures	Page
Figure 1. The redox potentials of common reactive species in ARPs and AOPs	6
Figure 2. The basic mechanism for the production of reactive species in heterogeneous photocatalysis.....	7
Figure 3. The overall structure and main objectives of this dissertation.....	8
Figure 4. Degradation of (a) ATZ, (b) SMX, (c) TMP, (d) SDM, (e) IBP, and (f) CMZ by PDS in dark and under light.....	18
Figure 5. The effect of (a) phosphate buffer and (b) ATZ on the decay of PDS in dark and under light.....	20
Figure 6. EPR spectra of (a) $\bullet\text{OH}$ and $\text{SO}_4^{\bullet-}$, (b) $\text{O}_2^{\bullet-}$, and (c) $^1\text{O}_2$ of PDS Dark and PDS Light in the absence of ATZ.....	22
Figure 7. Potential reaction pathways for the formation of reactive species by PDS Light in the absence of ATZ.....	24
Figure 8. Effects of different scavengers on the degradation of ATZ by PDS Light under (a) oxic and (b) anoxic condition.....	28
Figure 9. EPR spectra of (a) $\bullet\text{OH}$ and $\text{SO}_4^{\bullet-}$, (b) $\text{O}_2^{\bullet-}$, and (c) $^1\text{O}_2$ of PDS Dark and PDS Light with presence of ATZ.....	30
Figure 10. Potential reaction pathways for the formation of reactive species by PDS Light in presence of ATZ.....	32
Figure 11. Degradation of ATZ (a) with and without phosphate and (b) under different temperatures.....	44
Figure 12. Degradation of ATZ by PMS in the presence of scavengers under (a) oxic and (b) anoxic conditions, and (c) in H_2O and D_2O	46
Figure 13. EPR spectra of (a) $\text{DMPO-SO}_4^{\bullet-}$, (b) $\text{DMPO-O}_2^{\bullet-}$, and (c) $\text{TEMP-}^1\text{O}_2$ for PMS with and without phosphate buffer.....	48
Figure 14. The decay of PMS and ATZ with and without the presence of each other..	50
Figure 15. Two proposed degradation pathways of ATZ by PMS with and without phosphate.....	52

Figure 16. (a) Degradation of ATZ by PMS and (b) decay of PMS in presence of HCO_3^- ; (c) effects of various quenchers on the degradation of ATZ by PMS in presence of 10 mM HCO_3^- , and (d) EPR spectra of $\text{SO}_4^{\bullet-}$ for PMS in presence of HCO_3^-	53
Figure 17. Degradation of ATZ by PMS in water samples of Lake Bryan and Brazos River.....	55
Figure 18. XRD spectra of as-received ZnO nanoparticles and synthesized $\text{ZnFe}_2\text{O}_4/\text{nZVI}$ nanocomposite.....	68
Figure 19. SEM images of (a) as-received ZnO nanoparticles and (b-c) the synthesized $\text{ZnFe}_2\text{O}_4/\text{nZVI}$ nanocomposite.....	69
Figure 20. TEM image, EDS and SAED patterns of (a-c) the as-received ZnO nanoparticles, (d-f) the $\text{ZnFe}_2\text{O}_4/\text{nZVI}$ chain-and-bead structures, and (g-i) the ZnFe_2O_4 skin layer structures.....	71
Figure 21. (a) HRTEM of a ZnO particle; (b-g) TEM results for sample of nZVI; (b) TEM image of core-shelled chain structures of $\text{ZnFe}_2\text{O}_4/\text{nZVI}$ composite; (c) zoomed-in TEM image of core-shell particle in a chain structure; (d) NBD pattern taken from particle i in (c); (e) TEM image of an area with core, shell and skins; (f) HR-TEM image a core-shell structure; (g) HR-TEM image of core-shell-skins.....	73
Figure 22. (a) XPS survey spectra of ZnO nanoparticle and $\text{ZnFe}_2\text{O}_4/\text{nZVI}$ nanocomposite and (b) high-resolution spectra of Zn 2p, (c) O 1s peak for ZnO and $\text{ZnFe}_2\text{O}_4/\text{nZVI}$, (d) Fe 2p and (e) N 1s for $\text{ZnFe}_2\text{O}_4/\text{nZVI}$	75
Figure 23. (a) The removal of NO_3^- over time by ZnO and $\text{ZnFe}_2\text{O}_4/\text{nZVI}$ nanocomposite under visible light and (b) the removal rate of NO_3^- at $t = 120$ min; (c) the removal of As(V) over time in dark and (d) the removal rate of As(V) at $t = 720$ min in dark and under visible light.....	77
Figure 24. Effects of various scavengers on the removal rate of (a) NO_3^- by $\text{ZnFe}_2\text{O}_4/\text{nZVI}$ by 120 min and (b) As(V) by ZnO and $\text{ZnFe}_2\text{O}_4/\text{nZVI}$ by 720 min...	79
Figure 25. (a) The UV-Vis DRS spectra, (b) Tauc plots and (c) photoluminescence spectra of ZnO and $\text{ZnFe}_2\text{O}_4/\text{nZVI}$	82
Figure 26. The effect of pH on the removal of (a) NO_3^- by $\text{ZnFe}_2\text{O}_4/\text{nZVI}$ and (b) As(V) by ZnO and $\text{ZnFe}_2\text{O}_4/\text{nZVI}$; the effect of IS on the removal of (c) NO_3^- by $\text{ZnFe}_2\text{O}_4/\text{nZVI}$ and (d) As(V) by ZnO and $\text{ZnFe}_2\text{O}_4/\text{nZVI}$	87
Figure 27. The effect of phosphate on the removal of (a) NO_3^- by $\text{ZnFe}_2\text{O}_4/\text{nZVI}$ and (b) As(V) by ZnO and $\text{ZnFe}_2\text{O}_4/\text{nZVI}$; the effect of NOM on the removal of (c) NO_3^- by $\text{ZnFe}_2\text{O}_4/\text{nZVI}$ and (d) As(V) by ZnO and $\text{ZnFe}_2\text{O}_4/\text{nZVI}$	89

Figure 28. (a) Effect of glucose concentration on the removal efficiency of PFOA by MIL-125-NH ₂ under light; (b) the decay of PFOA and corresponding overall deF% under light.....	103
Figure 29. Plausible degradation metabolites and proposed degradation pathways of PFOA by MIL-125-NH ₂ /glucose under light.....	105
Figure 30. Changes in concentrations of PFOA, PFHpA, PFHxA, PFPeA, and PFBA over time.....	106
Figure 31. (a) Effects of quenchers on the removal of PFOA. The EPR spectra in presence of (b) AgNO ₃ , (c) glucose, and (d) glucose and SOD.....	108
Figure 32. The (a) PXRD patterns, (b) N ₂ adsorption isotherms, and (c) density functional theory (DFT) and (d) Barrett-Joyner-Halenda (BJH) pore size distribution curves of MIL-125-NH ₂ before and after three cycles of photodegradation experiments.....	110
Figure S1. The pseudo-first-order rate constants of ATZ degradation by PDS Light with and without the UV filter.....	114
Figure S2. Decay of PDS and ATZ in the absence and presence of each other in dark	115
Figure S3. Detection of H ₂ O ₂ based on the UV-Vis absorbance spectra of PDS Dark and PDS Light in the absence of ATZ.....	116
Figure S4. Decay of PDS with the presence of scavengers under (a) oxic and (b) anoxic condition under light.....	117
Figure S5. Pseudo-first-order rate constants of ATZ degradation by PDS in water and D ₂ O.....	118
Figure S6. MS1 and MS2 spectra of identified degradation metabolites of ATZ in PDS Dark and PDS Light systems.....	119
Figure S7. Proposed degradation pathways of ATZ by PDS Dark and PDS Light.....	120
Figure S8. Possible degradation pathway of ATZ by ¹ O ₂ in the PDS light system.....	121
Figure S9. Detection of H ₂ O ₂ based on the UV-Vis absorbance spectra of samples of PDS Dark and PDS Light in the presence of ATZ.....	122
Figure S10. Decay of PMS with and without phosphate.....	123
Figure S11. Relationship between rate constants of ATZ degradation and temperature	124
Figure S12. Decay of PMS in the presence and absence of L-his.....	125

Figure S13. Detection of H ₂ O ₂ based on the UV-Vis absorbance spectra of PMS with and without phosphate buffer.....	126
Figure S14. MS1 and MS2 spectra of identified oxidation products of ATZ by PMS	128
Figure S15. Linear relationship between the pseudo-first-order rate constant of ATZ degradation and HCO ₃ ⁻ concentration.....	129
Figure S16. Degradation of ATZ by PMS in H ₂ O and D ₂ O in presence of 10 mM HCO ₃ ⁻	130
Figure S17. EPR spectra of (a) O ₂ ^{•-} and (b) ¹ O ₂ for PMS with and without 10 mM HCO ₃ ⁻	131
Figure S18. (a) Zeta potentials and (b) hydrodynamic sizes of ZnO and ZnFe ₂ O ₄ /nZVI at pH 2.0-11.5.....	132
Figure S19. N ₂ adsorption-desorption isotherm of ZnFe ₂ O ₄ /nZVI nanocomposite....	133
Figure S20. Total leaching of Fe from ZnFe ₂ O ₄ /nZVI in dark and under light at pH 3.0-11.0.....	134
Figure S21. Linear fits of As adsorption with (b) pseudo-first-order and (c) pseudo-second-order kinetic models.....	135
Figure S22. Linearized plots of As adsorption on ZnO and ZnFe ₂ O ₄ /nZVI with (a) Langmuir and (b) Freundlich model; (c) the experimental data of adsorption isotherm in comparison with <i>q_e</i> predicted by Langmuir and Freundlich model.....	136
Figure S23. ATR-FITR spectra of the ZnFe ₂ O ₄ /nZVI nanocomposite before and after As adsorption.....	137
Figure S24. The decay of PFOA under different conditions.....	138
Figure S25. Fitted linear regression of PFOA decay by MIL-125-NH ₂ in presence of different glucose concentrations.....	139
Figure S26. MS1 and MS2 spectra of possible degradation metabolites (part 1).....	140
Figure S27. MS1 and MS2 spectra of possible degradation metabolites (part 2).....	141
Figure S28. MS1 and MS2 spectra of possible degradation metabolites (part 3).....	142
Figure S29. Removal efficiency of PFBA by direct photolysis and MIL-125-NH ₂ /glucose (in dark and under light irradiation).....	143
Figure S30. Changes in peak areas of PFCAs, FTCAs from PFOA, and FTCAs from	144

PFHpA over time.....

Figure S31. Decay of PFOA by MIL-125-NH₂ under light over three cycles..... **145**

Figure S32. The TGA curves of MIL-125-NH₂ before and after three cycles of PFOA removal experiments under light..... **146**

Figure S33. The SEM images of MIL-125-NH₂ (a) before and (b) after three cycles of PFOA removal experiments under light..... **147**

LIST OF TABLES

Tables	Page
Table S1. Light fluxes received by the PDS reaction solutions with and without UV filter.....	148
Table S2. Information about the identified degradation intermediates of ATZ by PDS in dark and under light.....	149
Table S3. Pseudo-first-order rate constants of ATZ degradation by PMS at different temperatures.....	150
Table S4. Tentative oxidation products of ATZ in the PMS system.....	151
Table S5. Pseudo-first-order rate constants of ATZ degradation by PMS in presence of HCO_3^-	152
Table S6. Pseudo-first-order rate constants of ATZ degradation by PMS in lake water and river water.....	153
Table S7. Light fluxes received by the $\text{ZnFe}_2\text{O}_4/\text{nZVI}$ nanocomposite.....	154
Table S8. Kinetic parameters for As adsorption on ZnO and $\text{ZnFe}_2\text{O}_4/\text{nZVI}$	155
Table S9. Isotherm parameters for As adsorption on ZnO and $\text{ZnFe}_2\text{O}_4/\text{nZVI}$	156
Table S10. Light fluxes emitted by the medium pressure Hg-lamp.....	157
Table S11. Pseudo-first-order rate constants of PFOA removal by MIL-125-NH ₂ in presence of different glucose concentrations.....	158
Table S12. Pseudo-first-order rate constants of PFOA removal by MIL-125-NH ₂ in presence of different quenchers.....	159
Table S13. Pseudo-first-order rate constants of PFOA removal by MIL-125-NH ₂ and recovery rate of dry mass over three cycles.....	160

CHAPTER I

INTRODUCTION

The prevalence and threat of recalcitrant pollutants in water

In the past few decades, the synthesis and usage of chemicals have grown exponentially owing to the increasing demand from the society.¹⁻⁴ Currently, more than 85,000 types of chemicals are being produced over the world, many of which enter the natural water systems through anthropogenic disposing, leaching, and natural runoff from land.^{1,5,6} The release of these chemicals into the environment gives rise to a variety of recalcitrant pollutants that pose serious risks to natural ecosystems as well as public health, including pesticides, antibiotics, toxic oxyanions, and per- and polyfluorinated substances (PFAS).⁷⁻¹⁴

Pesticides contain a variety of chemicals such as herbicides, insecticides, and fungicides, and are commonly applied in agriculture.^{15,16} An estimated 3 million tons of pesticides are applied to croplands worldwide every year, which is about 15 to 20 times higher than that used 30 years ago.^{17,18} More strikingly, half of the pesticide residues detected in the groundwater in industrialized countries are originated from pesticides that were phased out many years ago.¹⁹ Herbicides account for about 62% of pesticide usage in agriculture in the United States, and the five most used herbicides during the past two decades were glyphosate, atrazine, metolachlor-(*S*), 2,4-D, and acetochlor.²⁰ As one of the most frequently detected pesticides, the concentration of atrazine in surface water in the Midwest and South of the US reached 53 µg/L in 2018.²¹ Very few pesticides are completely mineralized after biotic or abiotic degradation. Some of their degradation intermediates, which possess even higher toxicity, have been

detected at higher concentrations in drinking water and surface water compared to their parent forms.¹⁶ Pesticides have also been reported to induce harmful physiological responses in many wildlife such as honey bees^{22,23}, butterflies²⁴ and humans.²⁵⁻²⁷ Health impacts of pesticides include irritation, damages to nervous and endocrine systems, and carcinogenic effects.^{27,28}

Veterinary antibiotics have been extensively used worldwide to treat and prevent bacterial infection, promote growth, and improve feed efficiency for livestock.²⁹⁻³¹ The U.S. alone consumed approximately 22,700 tons of antibiotics, and the global consumption of antibiotics reached almost 200,000 tons in 2002.³² Owing to its potential for inducing antibiotic resistance, the presence of antibiotics in natural waters has drawn intensive attention. Around 30-90% of consumed antibiotics are not absorbed by animals and are excreted in urines and manures in their parent or metabolized forms. Many of these metabolites are still bioactive and can be converted back to their parent forms.³¹ During the agricultural process, antibiotics enter the environment mainly through disposal of leftovers and spread of contaminated feces.^{31,33} Since antibiotics have a wide range of solubility, absorptivity, volatility, biodegradability, polarity, and stability, traditional wastewater treatment processes are incapable of effectively degrading these pollutants.³⁴⁻³⁶ For many antibiotics such as sulfamethoxazole and diclofenac, the removal rates by traditional wastewater treatment plants are less than 20%.^{32,34}

Inorganic oxyanions such as arsenate/arsenite ($\text{AsO}_4^{3-}/\text{AsO}_3^{3-}$), selenate (SeO_4^{2-}), chromate (CrO_4^{2-}), and nitrate (NO_3^-), are common byproducts released from industrial manufacturing and agricultural practices.^{37,38} Elevated levels of these oxyanions in water have become a pressing concern due to their high mobility in water as well as high toxicity to humans.^{37,39} In particular, acute exposure to arsenic can lead to vomiting, blood vessel damage, impaired nerve

function, whereas chronic exposure has been associated with several types of cancer.³⁹ Long-term exposure to nitrate may lead to adverse pregnancy outcomes, ovarian and bladder cancer, and methemoglobinemia, or “blue baby syndrome”. The maximum contaminant levels (MCL) of arsenic and nitrate in drinking water were set at 10 µg/L and 10 mg/L, respectively, by the U.S. environmental protection agency (EPA).

Applications of per- and polyfluoroalkyl substances (PFAS) in water-repellent fabrics, non-stick products, food packaging, textiles, and aqueous fire-fighting foams (AFFF) worldwide since the 1940s have led to their rapid accumulation in soils, sediments and different water bodies (e.g., surface water, groundwater, landfill leachate).^{40–45} As one of the most widespread PFAS representatives, perfluorooctanoic acid (PFOA) has been associated with multiple adverse health effects such as endocrine disruption, and carcinogenicity.^{46–49} The concentrations of perfluorooctanoic acid (PFOA), one of the most extensively used PFAS, in contaminated groundwater near U.S. military bases can reach up to 6,570 ppb, which is almost five orders of magnitude higher than the EPA health advisory level of PFOA in drinking water (70 ppt).⁵⁰ PFAS are highly stable owing to the abundance of C-F bonds, which is the strongest bond in organic chemistry with a bond dissociation energy (BDE) up to 544 kJ·mol⁻¹, and are notorious for being largely immune to conventional water treatment processes.^{51–53}

Advanced oxidation and reduction processes in water decontamination

Over the past two decades, the field of water remediation has aroused considerable attentions worldwide due to the advancement in the detection technologies for the vast diversity of pollutants. Considering the ubiquitous occurrence, high persistence, and potential toxicity of these pollutants, a diversity of treatment technologies have been developed, including

adsorption, coagulation, ion exchange, membrane filtration, microbial degradation, advanced oxidation processes (AOPs), and advanced reduction processes (ARPs).^{34,54-60} Non-destructive technologies such as adsorption and membrane filtration have been widely applied in real practices, yet they tend to suffer from high costs for material regeneration, need for post-treatment of concentrated pollutants, and potential release of pollutants back to the environment.^{61,62} Furthermore, the recyclability and stability of materials in extended exposure to the treatment processes are also a concern. To overcome these limitations, destructive technologies such as AOPs and ARPs that are capable of breaking down recalcitrant pollutants into less toxic or innocuous byproducts have attracted considerable attention both in research and practical applications.^{63,64}

AOPs can degrade pollutants via various oxidative reactive species such as ozone (O_3), hydroxyl radical ($\bullet OH$), sulfate radical ($SO_4^{\bullet -}$), and reactive chlorine species (RCS).⁶⁵⁻⁶⁸ The $\bullet OH$ is one of the strongest oxidants ($E^0 = +1.90$ to $+2.70 V_{NHE}$) that non-selectively attacks a variety of organic pollutants.^{67,69} As an alternative to $\bullet OH$, $SO_4^{\bullet -}$ possesses an equivalent redox potential ($E^0 = +2.60$ to $+3.10 V_{NHE}$) and several important advantages over $\bullet OH$ including longer life time in water, higher selectivity, and less dependence on pH.⁶⁷ The number of publications on $SO_4^{\bullet -}$ -based AOPs has been surging rapidly in recent years, and thanks to these efforts, substantial progresses have been made in the activation methods and the underlying chemistry of $SO_4^{\bullet -}$ -based AOPs.⁷⁰⁻⁷³ However, a closer look at the recent literatures reveals that the overwhelming majority of them are focused on the activation of persulfates via electron-transfer by designing novel heterogenous catalysts, whereas activation methods that do not rely on heterogeneous catalysts have been largely overlooked.⁷⁰⁻⁷² Although excellent

performance can be achieved by using heterogeneous catalysts, higher difficulties and costs in actual operations are inevitable. In this regard, catalyst-free activation of persulfates is still not well-understood and deserves more attention. In particular, peroxydisulfate (PDS) has been considered as UV-active only, while calculation for the BDE suggests that the O-O bond can be broken by visible light ($\lambda < 854$ nm). Although the enhanced performance of PDS under visible light has been shown as the control groups in several previous studies that use heterogeneous catalysts to activate PDS, its importance was ignored.⁷⁰⁻⁷² Furthermore, the interaction between PMS and innocuous inorganic oxyanions and the chemistry of peroxymonosulfate (PMS) itself have not been well-studied. Hence, the first two objectives of this dissertation are to discover the novel activation methods for persulfates without using heterogeneous catalysts.

On the other hand, the term “ARP” was established in the late 1990s when highly oxidized organic pollutants were degraded unintentionally by reducing reactive species such as hydrated electron (e_{aq}^-), hydrogen radical (H^\bullet), sulfite radical anion ($SO_3^{\bullet-}$), and sulfur dioxide radical anion ($SO_2^{\bullet-}$).^{74,75} ARPs offer a novel solution to the degradation of pollutants that are not readily oxidizable, including high-valent oxyanions (e.g., NO_3^- , ClO_3^- , BrO_3^- , CrO_4^{2-}), vinyl chloride, 2,4,6-trichlorophenol, and PFAS. As the strongest reducing species known to date with a redox potential of -2.87 V vs. NHE, e_{aq}^- has a half-life of ~ 300 μs and tend to undergo a one-electron transfer mechanism with an activation energy ranging from 6 to 30 kJ/mol.⁵¹⁻⁵³ As a reference, the redox potentials of common reactive species involved in AOPs and ARPs are summarized in [Figure 1](#).⁷⁶

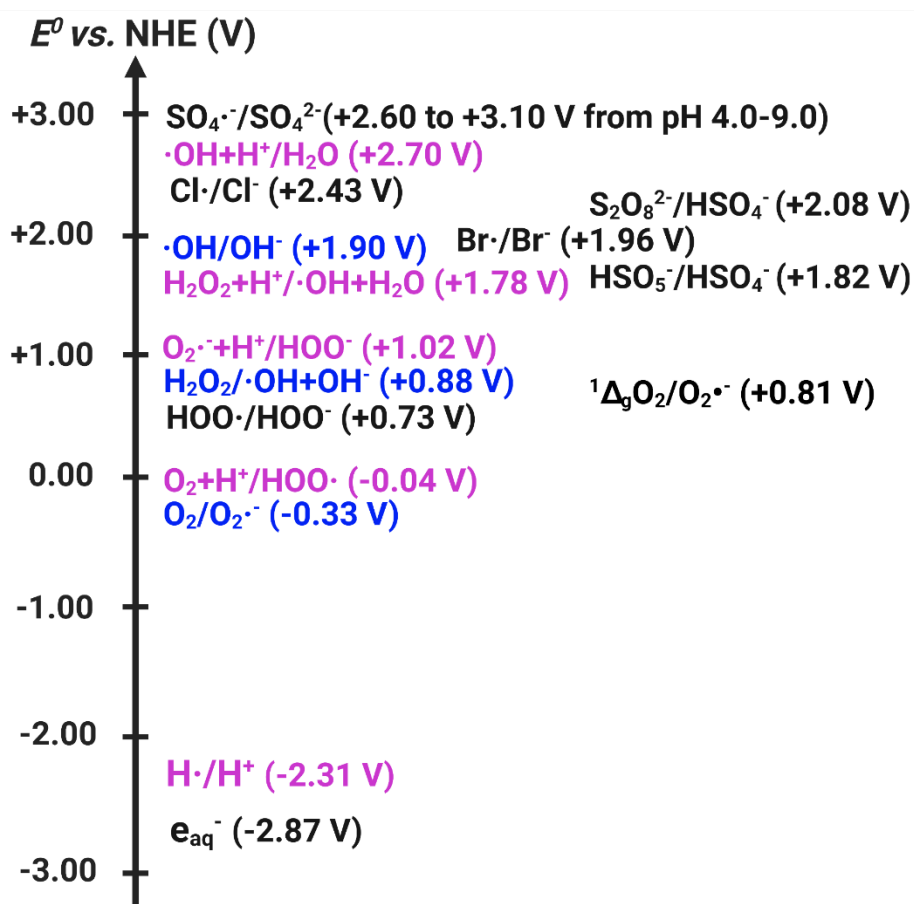


Figure 1. The redox potentials of common reactive species in ARPs and AOPs. Reactions occurred under acidic and alkaline condition are highlighted in pink and blue, respectively. Reactions denoted in black are either under neutral condition or relatively less pH-dependent (created with BioRender.com).

Heterogeneous photocatalysis has attracted intense interests in recent decades owing to its low operational cost and utilization of light as a green and sustainable energy source.^{54–56,77–82}

When the energy of light irradiation is equal to or greater than the bandgap energy (E_g), an electron in the valence band (VB) of the photocatalyst absorbs a photon and then gets promoted to the conduction band (CB), creating a free electron (e_{CB}^-) in the CB and leaving a positive hole (h_{VB}^+) in the VB. The produced e_{CB}^- could migrate to the surface of the photocatalyst and then participate in reactions with water constituents.^{83,84} Adjacent water molecules can be polarized by the excited electron and bind to it to form a meta-stable species called e_{aq}^- .⁷⁴ The

e_{aq}^- can be oxidized by dissolved oxygen to form superoxide radical ($O_2^{\bullet-}$), and the h_{VB}^+ can react with water or hydroxide to produce $\bullet OH$.⁸⁵ The basic mechanism for the production of reactive species in heterogeneous photocatalysis is shown in **Figure 2**.

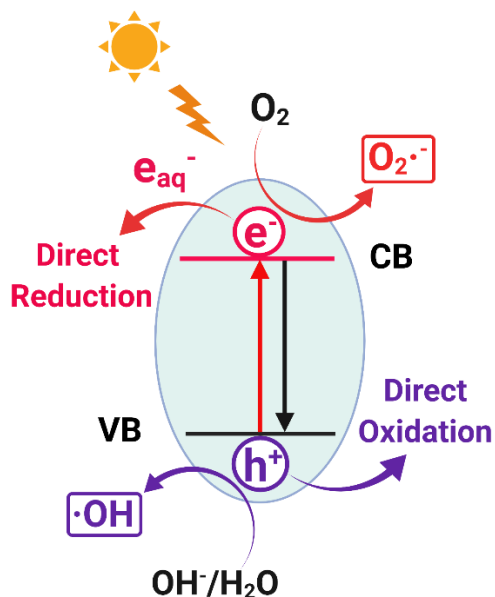


Figure 2. The basic mechanism for the production of reactive species in heterogeneous photocatalysis (created with BioRender.com).

Owing to the utilization of green and sustainable energy, heterogeneous photocatalysis is deemed as a promising technology to generate e_{aq}^- in ARPs.⁷⁴ However, despite of the worldwide prevalence of highly oxidized pollutants, especially PFAS, investigations on ARPs are still in the infant stage compared to AOPs. The last two objectives of this dissertation are to explore the potentials of ARPs mediated by heterogeneous photocatalysts in the degradation of persistent pollutants. The overall structure and four main objectives in this dissertation are summarized in **Figure 3**.

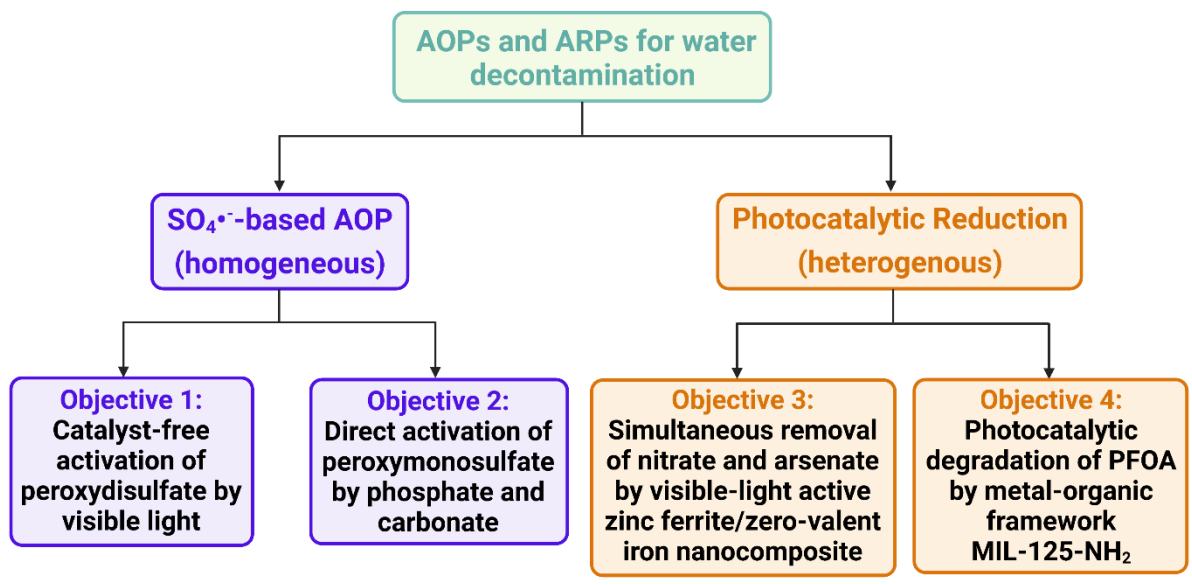


Figure 3. The overall structure and main objectives of this dissertation

CHAPTER II

CATALYST-FREE ACTIVATION OF PEROXYDISULFATE BY VISIBLE LIGHT: POLLUTANT-DEPENDENT PRODUCTION OF REACTIVE SPECIES*

Introduction¹

A 40% global water deficit is projected by 2030, and the reuse of wastewater is a promising alternative to decrease water stress in different parts of the world. Among various technologies to treat wastewater, advanced oxidation processes (AOPs) using highly reactive species (*e.g.*, hydroxyl radicals ($\bullet\text{OH}$) and sulfate radicals ($\text{SO}_4\bullet^-$) with redox potentials in the ranges of $+1.8\text{-}2.7 V_{\text{NHE}}$ and $+2.5\text{-}3.1 V_{\text{NHE}}$, respectively)^{69,76,86} have been used in treatments.^{67,87}

The $\bullet\text{OH}$ produced from Fenton-based processes has a life time of $< 1 \mu\text{s}$ while $\text{SO}_4\bullet^-$ generated from peroxymonosulfate (PMS, HSO_5^-) and peroxydisulfate (PDS, $\text{S}_2\text{O}_8^{2-}$) has a much longer life time (30–40 μs) and is applicable to a wide range of pH.^{88–90} In addition, $\text{SO}_4\bullet^-$ is more selective and has lower reactivity than $\bullet\text{OH}$ toward natural organic matter, and thus $\text{SO}_4\bullet^-$ -based AOPs have recently received great attention for their potentials in water treatment, especially for recalcitrant organic pollutants.^{67,91–93} A vast amount of research has been conducted to activate PMS and PDS via different approaches, including electron-transfer-based (*e.g.* reduced transition metals, electron-donating functional groups) methods in both homogeneous and heterogeneous systems and energy-transfer-based (*e.g.* heat, photons)

*Reprinted with permission from: Visible light-induced catalyst-free activation of peroxydisulfate: pollutant-dependent production of reactive species. Wen, Y., Huang, CH., Ashely, D., Meyerstein, D., Dionysious, D.D., Sharma, V.K., Ma, X., 2022. *Environmental Science & Technology*, 56, 2626-2636. Copyright 2022 American Chemical Society.

methods.^{67,94-102}

The peroxide bonds (O-O) in PMS and PDS can be dissociated to generate $\bullet\text{OH}$ and $\text{SO}_4^{\bullet-}$ after activation ($^-\text{O}_3\text{SO-OH} \rightarrow \text{SO}_4^{\bullet-} + \bullet\text{OH}$ and $^-\text{O}_3\text{SO-OSO}_3^- \rightarrow 2\text{SO}_4^{\bullet-}$). The O-O bond in PMS is more polar and could be more effectively cleaved by electron transfer from nucleophiles.¹⁰³ Comparatively, the O-O bond in PDS is relatively non-polar and less vulnerable to nucleophilic attack.⁶⁷ However, the O-O bond in PDS is markedly weaker than that in PMS due to its longer bond length (1.497 Å vs. 1.453 Å) and lower bond dissociation energy (BDE). The BDE of the O-O in PDS is estimated to be $<140 \text{ kJ}\cdot\text{mol}^{-1}$,¹⁰⁴⁻¹⁰⁶ whereas the reported BDE of O-O in PMS is up to $377 \text{ kJ}\cdot\text{mol}^{-1}$.^{67,103,107} Based on the Planck's equation, the O-O bond in PDS could be potentially broken by irradiation with wavelength shorter than 854 nm without any chemical catalyst, which covers the entire visible light spectrum. However, PMS requires irradiation with wavelength shorter than 317 nm to break the peroxide bond at the reported higher BDE. Compared with PMS, PDS is also more cost effective (\$0.18/mol versus \$1.36/mol).¹⁰³ Moreover, PDS showed higher reaction stoichiometric efficiency (RSE), defined as the number of moles of pollutant degraded over the number of moles of PDS consumed, than PMS.^{108,109} Therefore, the use of visible light for PDS activation offers a unique opportunity for a greener and more efficient technology to break down hazardous organic chemicals.

Surprisingly, very little attention has been paid to the potential activation of PDS by visible light in a catalyst-free condition. In contrast, extensive studies have been conducted to activate PDS by ultraviolet light (UV), and PDS activation by visible light often relies on the assistance of homo- and hetero-catalysts (including dye-photosensitizers).⁷⁰⁻⁷³ However, a

closer examination of the literature suggests that visible light activation of PDS without additional catalyst is possible. A recent study on the inactivation of *Escherichia coli*, *Staphylococcus aureus*, and *Pseudomonas aeruginosa* implied the activation of PDS by visible light to generate reactive species such as $\text{SO}_4^{\bullet-}$, OH^{\bullet} , and $\text{O}_2^{\bullet-}$.¹¹⁰ Unfortunately, PDS alone with visible light was often treated as a control in these studies, and thus, the possible activation of PDS by visible light was ignored.⁷⁰⁻⁷² Our study demonstrates conclusively for the first time the activation of PDS by visible light in a catalyst-free system and formation of various reactive species through an in-depth mechanistic investigation.

Importantly, although some recent literature started proposing $^1\text{O}_2$ as a dominant nonradical species in the PDS system, convincing evidence is still missing.^{67,111} For example, $^1\text{O}_2$ was considered as a major reactive species if the addition of scavengers reduces the degradation efficiency of target compounds. However, common scavengers for $^1\text{O}_2$ such as L-histidine (L-his), azide (N_3^-), and furfuryl alcohol (FFA) do not quench $^1\text{O}_2$ selectively. They can quench $\text{SO}_4^{\bullet-}$ and OH^{\bullet} even more rapidly than $^1\text{O}_2$, which was often ignored.¹¹²⁻¹¹⁷ For example, the second-order rate constants between N_3^- and $\text{SO}_4^{\bullet-}$ and OH^{\bullet} are around 1 to 2 orders of magnitude higher than that with $^1\text{O}_2$ ($k(\text{N}_3^-/\text{SO}_4^{\bullet-}) = 3.0 \times 10^9 \text{ M}^{-1} \cdot \text{s}^{-1}$;¹¹⁷ $k(\text{N}_3^-/\text{OH}^{\bullet}) = 1.4 \times 10^{10} \text{ M}^{-1} \cdot \text{s}^{-1}$;¹¹³ $k(\text{N}_3^-/^1\text{O}_2) = 4.5 \times 10^8 \text{ M}^{-1} \cdot \text{s}^{-1}$).¹¹² Hence, the results of quenching study alone are not convincing and sometimes can be misleading, especially in heterogeneous medium in which the quencher can occupy active sites on the catalyst and alter the kinetics. Confirmation of the participation of $^1\text{O}_2$ requires more conclusive evidence. In addition, the reported generation of $^1\text{O}_2$ by PDS was mostly achieved through the activation of heterogeneous catalysts such as carbon-based materials and metal oxides.¹¹⁸⁻¹²² To the best of

our knowledge, production of $^1\text{O}_2$ via direct energy input to a PDS system without any catalyst has not been reported.

In the present study, we aimed to demonstrate the feasibility of visible light activation of PDS, and subsequently elucidate the roles of reactive species ($\text{SO}_4^{\bullet-}$, $\bullet\text{OH}$, $\text{O}_2^{\bullet-}$, and $^1\text{O}_2$) in degrading organic pollutants in the PDS-visible light system via electron paramagnetic resonance (EPR) spectroscopy measurements. We also demonstrated unequivocally the generation of $^1\text{O}_2$ by taking advantage of its solvent-specific quenching capacity. Importantly, distinctively different mechanisms were noticed for the generation of reactive species by PDS under visible light in the absence and presence of pollutants. The selected pollutants were herbicides and pharmaceuticals, which are prevalent in the environment and are of great concern because of their hazardous effects on human health and ecological systems.

Experimental Section

Chemicals and Materials

Potassium peroxydisulfate (PDS, $\geq 99.0\%$) and tert-butanol (TBA) anhydrous ($\geq 99.5\%$) were purchased from Sigma-Aldrich (St. Louis, USA). Atrazine (ATZ, $\geq 97.0\%$), sulfamethoxazole (SMX, $\geq 98.0\%$), trimethoprim (TMP, $\geq 98.0\%$), sulfadimethoxine (SDM, $\geq 98.0\%$), and carbamazepine (CMZ, $\geq 97.0\%$) were purchased from TCI America (Portland, USA). Sodium phosphate dibasic anhydrous ($\geq 98.0\%$), sodium thiosulfate (99.0%), sodium hydroxide ($\geq 97.0\%$), sulfuric acid (98.0%), 5,5-dimethyl-1-pyrroline N-oxide (DMPO, $\geq 98.0\%$) and superoxide dismutase (SOD, 3500 U/mg) were obtained from Thermo Fisher Scientific (Waltham, USA). Ibuprofen (IBP, 99%), 2,2,6,6-tetramethyl-4-piperidine (TEMP,

99%), and ammonium metavanadate (99.5%) were purchased from ACROS Organics (Waltham, USA). L-histidine (L-his, $\geq 98.0\%$) and deuterium oxide (D_2O , 99.8%) were purchased from Alfa Aesar (Haverhill, USA). Methanol (MeOH, reagent grade) was purchased from VWR Chemicals (Radnor, USA). Waters Oasis HLB cartridges (WAT106202, 6 cc/200 mg) were purchased from Waters (Milford, USA). All chemicals were used as received. Thin wall quartz sample tubes (4 mm and 2 mm) were purchased from Wilmad Labglass (Vineland, USA). A simulated sunlight lamp (GLBULBM1000 metal halide bulb, 1000 W, 92,000 lm) was purchased from iPower and used as the light source. A UV filter film was purchased from Edmund Optics (Barrington, USA).

Catalyst-Free Activation of PDS

The reactions were carried out in 40 mL glass tubes with constant stirring at 300 rpm at 25 ± 0.5 °C. The temperature of solutions was monitored using a thermometer throughout the experiments. The initial concentration of atrazine (ATZ) was 10.0 μM , and the initial concentration of PDS was 5.0 mM. The irradiation fluxes emitted from the lamp and received by the solutions were measured with a LS125 UV light meter (Linshang Technology, Shenzhen, China) and a Solar Light PMA2100 radiometer (Solar Light Company, Philadelphia, USA) 10 cm away from the lamp. The tubes in the dark treatments were covered with aluminum foil. To further confirm the PDS activation by visible light, experiments were also conducted with a UV filter film covering the simulated sunlight lamp to eliminate the effect of UV light. 1.0 mL of sample was withdrawn from each tube at different elapsed times ($t=0, 1, 2, 3, 4, 5, 10, 20, 30, 60, 90, 120,$ and 240 min) and immediately quenched by 20 μL of 5.0 M sodium thiosulfate.

The concentrations of all pollutants in collected samples were measured with a Dionex UltiMate 3000 high-performance liquid chromatograph (HPLC) (Sunnyvale, USA) with a Restek C18 column (4.6 × 250 mm, 5 μm). The mobile phase was composed of methanol and water (60/40, v/v) at a flow rate of 1.0 mL/min. The column temperature was set at 30 °C. The change in the concentration of PDS under different conditions was determined spectrophotometrically via an oxidation decolorization method and a modified iodometric titration method, respectively.^{123,124} The initial and final pH in each tube were measured with an Accumet AE150 pH meter (Westford, USA).

Electron Paramagnetic Resonance (EPR) Spectroscopy

EPR was used to probe possible reactive species in the reaction systems. The measurement was performed using a Bruker Elexsys E500 EPR equipped with both a standard resonator and a CoolEdge cryo system (Billerica, USA). The instrument settings are: 20.0 mW microwave power, 9.8 GHz microwave frequency, 100 kHz modulation frequency, 1.00 G modulation amplitude, 3515 G center field, 150 G sweep width, and 40.0 s sweep time. 50.0 mM of 5,5-dimethyl-1-pyrroline N-oxide (DMPO) was used as the spin trapping agent for •OH, SO₄•⁻, and O₂•⁻, while 50.0 mM of 2,2,6,6-tetramethyl-4-piperidine (TEMP) was used to probe ¹O₂. The EPR measurements for •OH and SO₄•⁻ were carried out in 1:1 mixture of 10.0 mM phosphate buffer and acetonitrile, and the measurement for O₂•⁻ was performed in pure methanol (MeOH) to quench •OH and SO₄•⁻. The reaction solution was injected into a 2 mm quartz EPR tube using a syringe needle, which was then placed into a 4 mm quartz EPR tube. The EPR tubes containing the reaction solution were irradiated under the simulated sunlight

lamp for 1 min and then measured by EPR. The EPR measurement was repeated with D₂O as the solvent for phosphate buffer with the same experimental setup to investigate the role of ¹O₂. In the PDS light system with and without ATZ, The EPR measurements for O₂^{•-} and ¹O₂ were also conducted under anoxic condition after 10 min of N₂ purging. The dissolved oxygen (DO) after N₂ purging was 0.12 ± 0.02 mg/L, measured by an Orion Star A123 Dissolved Oxygen Meter, which falls in the DO range of anoxic condition (0 - 0.2 mg/L).

Quenching of Reactive Species

In order to identify the main reactive species involved in the degradation of ATZ by PDS under light and in dark, four quenchers were added in the beginning of the reactions to scavenge possible reactive species. The concentration of MeOH, tert-butanol (TBA), and L-histidine (L-his) was 0.5 M, and the concentration of superoxide dismutase (SOD) was 50 U·ml⁻¹. To study the impact of oxygen, purified N₂ gas was used to purge the system for 10 min before the quenching experiments. All tubes were capped and then sealed with parafilm to maintain an anoxic environment throughout the reaction. The ATZ concentrations in the samples taken at various time points (t=0, 5, 10, 30, 60, 120, and 240 min) were measured using HPLC. The degradation of ATZ was also repeated with D₂O as the solvent for phosphate buffer with the same experimental setups.

Quantification of Hydrogen Peroxide (H₂O₂)

The presence of H₂O₂ in PDS Dark and PDS Light was determined with a previously reported spectrophotometric method based on the reaction between H₂O₂ and metavanadate

under acidic medium to produce peroxovanadate with a main absorption peak at around 450 nm using a UV-Vis-NIR spectrophotometer (Hitachi U-4100).^{125,126}

Identification of Degradation Metabolites

To identify the degradation pathways of ATZ by PDS, samples were collected at 120 min and 10 min for PDS Dark and PDS Light, respectively, followed by solid-phase-extraction (SPE) to extract remaining ATZ and degradation metabolites. The Waters Oasis HLB cartridges (WAT106202, 6 cc/200 mg) cartridges were sequentially pre-conditioned with 5.0 ml of methanol and 5.0 ml of ultrapure water, loaded with 50.0 ml of samples, and dried with purified N₂ gas for 30 minutes. The final extracted products were eluted with 2.0 ml of methanol. Untargeted liquid chromatography high resolution accurate mass spectrometry (LC-HRAM) analysis was performed on a Q Exactive Plus orbitrap mass spectrometer (Thermo Fisher Scientific, Waltham, USA) coupled to a binary pump UltiMate 3000 HPLC to detect the degradation metabolites of ATZ.

Data Analysis

One-way analysis of variance (ANOVA) was used to determine the statistical differences among the pseudo-first-order rate constants of ATZ degradation with and without UV filter film, and in water and D₂O. Different letters in the figures indicate significant differences between the rate constants ($p \leq 0.05$) according to one-way ANOVA followed by Tukey's test.

Results and Discussion

Catalyst-free Activation of PDS

A simulated sunlight lamp was used as the light source in this study. The light fluxes that reaction solutions received in glass vials contained $39.8 \pm 0.5 \times 10^{-3}$ W/cm² of visible light in the wavelength (λ) range of 400-700 nm. The fluxes in the UV ranges contained $8.1 \pm 0.2 \times 10^{-6}$ W/cm² of UV-A ($\lambda=315-400$ nm) and $2.5 \pm 0.4 \times 10^{-6}$ W/cm² of UV-B ($\lambda=280-315$ nm), respectively. The UV-C flux ($\lambda=230-280$ nm) was negligible. Based on the flux measurement, UV light only accounted for < 0.03% of the total light flux, and thus the light source used in our study represents almost exclusively the visible light. The chemistry of PDS with visible light irradiation (PDS Light) and without (PDS Dark) was explored using six common herbicides and pharmaceuticals, namely atrazine (ATZ), sulfamethoxazole (SMX), trimethoprim (TMP), sulfadimethoxine (SDM), ibuprofen (IBP), and carbamazepine (CMZ) (**Figure 4**). Interestingly, the degradation efficiencies of all six pollutants by PDS were significantly improved by visible light irradiation. Using ATZ as an example, complete degradation of ATZ was achieved by PDS Light in 30 min ($k_{obs} = 11 \pm 3.0 \times 10^{-2}$ min⁻¹), however, only 37% of ATZ was degraded by PDS Dark within 30 min ($k_{obs} = 0.72 \pm 0.09 \times 10^{-2}$ min⁻¹) (**Figure 4a**). To further confirm that PDS was activated by visible light, the degradation experiments of ATZ by PDS were repeated with a UV filter film placed between the sunlight lamp and glass vials to block the UV light, which completely blocked UV-B and UV-C, and only allowed $2.0 \pm 0.2 \times 10^{-6}$ W/cm² of UV-A (**Table S1**). The obtained pseudo-first-order rate constants of ATZ degradation by PDS were not statistically different from the one obtained without a UV filter (**Figure S1**). The results demonstrated that PDS activation was due to

visible light, consistent with the postulation that the energy from visible light is sufficient to break the O-O bond in PDS.

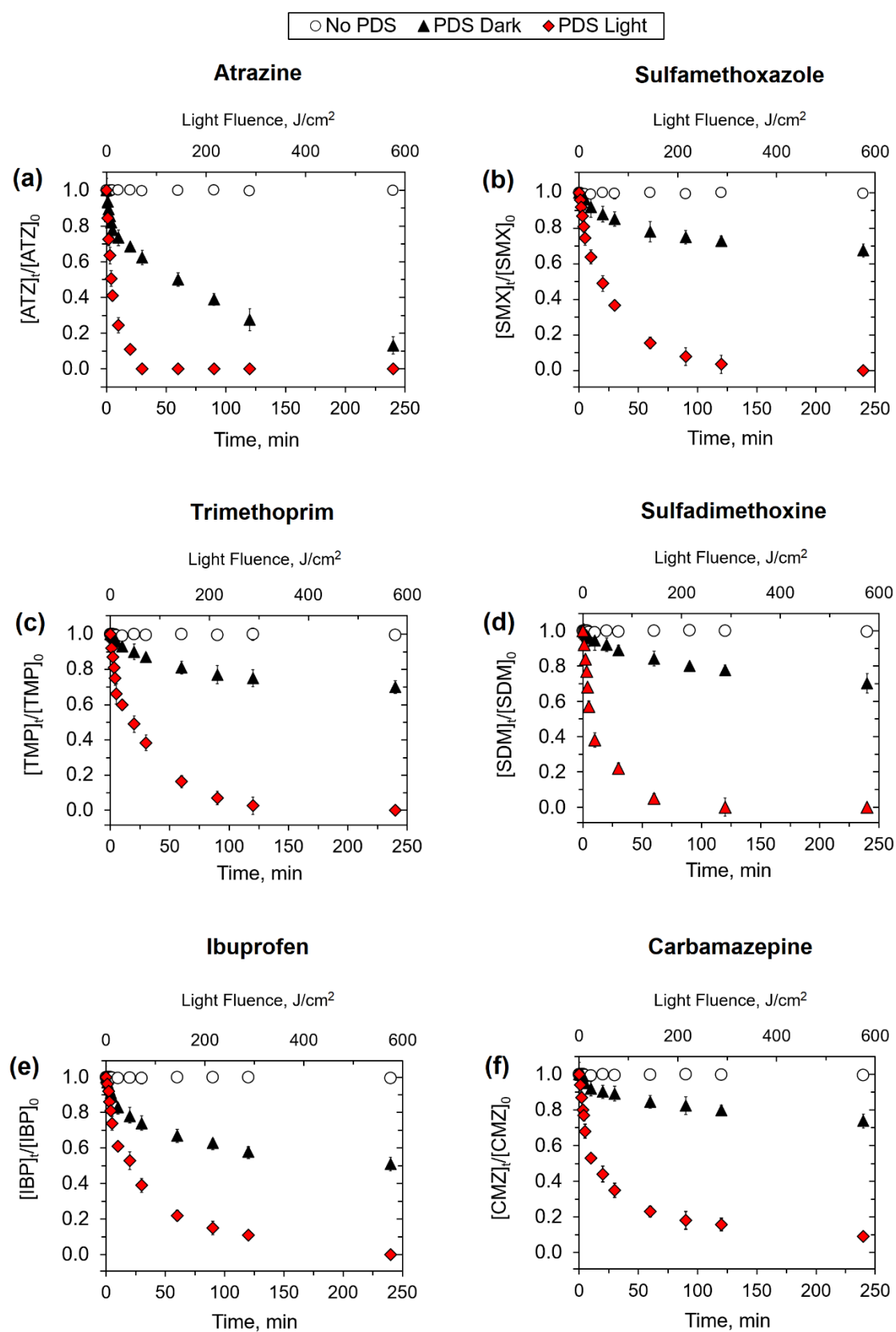


Figure 4. Degradation of (a) ATZ, (b) SMX, (c) TMP, (d) SDM, (e) IBP, and (f) CMZ by PDS in dark and under light; the fluence of visible light received by the reaction solution is shown in the secondary x-axis ($[\text{pollutant}]_0 = 10.0 \mu\text{M}$, $[\text{PDS}]_0 = 5.0 \text{ mM}$, $[\text{Na}_2\text{HPO}_4] = 10.0 \text{ mM}$, $\text{pH}_0 = 7.0$, $T = 25 \text{ }^\circ\text{C}$).

In order to verify whether PDS was directly activated by visible light, the impacts of solution constituents were examined. Because 10 mM phosphate buffer was added to control the initial pH to 7.0 to take into account of the typical pH of natural waters, the impact of phosphate buffer on the decay of PDS was investigated. Apparently, phosphate displayed negligible impact on PDS decay both in dark and under visible light (**Figure 5a**). Approximately 20% and 90% of PDS decayed within 240 min in dark and under visible light, respectively, regardless of the phosphate. Next, the effect of ATZ was also determined. According to **Figure 5b**, the presence of ATZ showed negligible effect on the decay of PDS in dark because the initial concentration of ATZ was only 0.2% of the initial concentration of PDS. The comparable rate constants of PDS decay in dark with and without ATZ supported the negligible role of ATZ in PDS decay in the experimental setup when $[\text{ATZ}]_0/[\text{PDS}]_0$ ratio was low. However, the notable degradation of ATZ by PDS in dark suggests that direct ATZ and PDS redox reaction could occur. To confirm this hypothesis, a separate experiment with the initial concentrations of PDS and ATZ both controlled at 5.0 mM in dark was performed. The decay of PDS and ATZ in dark were both enhanced in the presence of each other, indicating direct oxidation of ATZ by PDS (**Figure S2**). The relative concentration differences of ATZ and PDS explains the notable degradation of ATZ by PDS in dark (**Figure 4**) but minimal effect of ATZ on PDS decay (**Figure 5b**), even though direct reaction between ATZ and PDS took place in both experiments discussed above.

The above results showed unambiguously that PDS can be directly activated by visible

light without the assistance of catalysts. To gain further understanding on the different behaviors of PDS in the presence and absence of ATZ, the underlying chemistry of PDS under visible light in two different systems were examined separately. The first system is relatively “clean”, which only contains PDS, and the second system contains ATZ in addition of PDS.

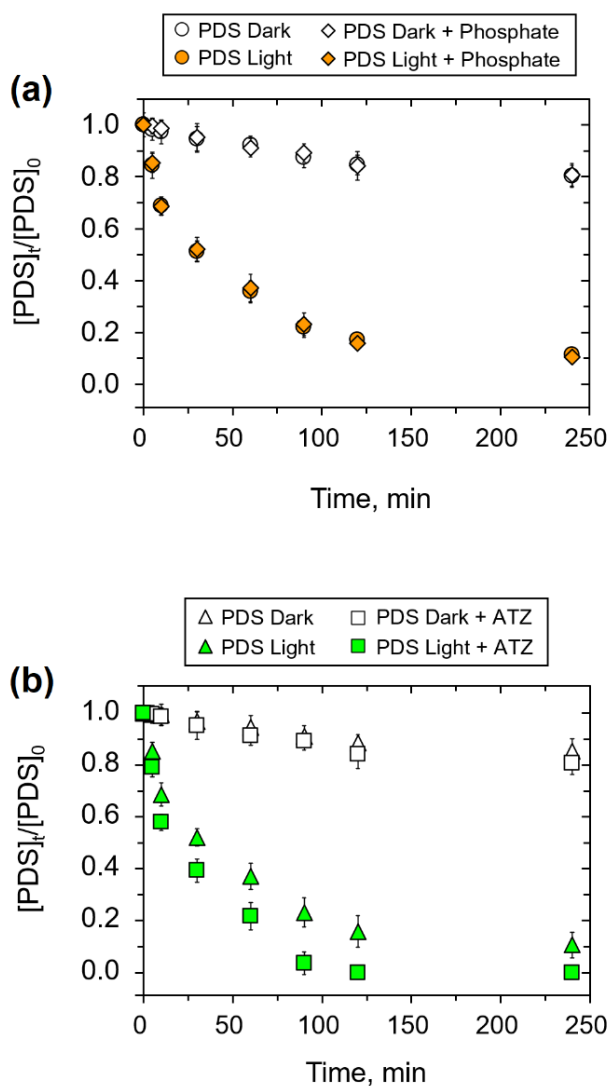


Figure 5. The effect of (a) phosphate buffer ($[PDS]_0 = 5.0$ mM, $[Na_2HPO_4] = 0$ or 10.0 mM, $T = 25$ °C) and (b) ATZ ($[PDS]_0 = 5.0$ mM, $[Na_2HPO_4] = 10.0$ mM, $[ATZ]_0 = 0$ or 10.0 μ M, $pH_0 = 7.0$, $T = 25$ °C) on the decay of PDS in dark and under light.

PDS Light (without ATZ)

Four reactive species that are commonly present in persulfate-based systems were

probed in order to reveal the undergoing reactions of PDS Light, namely $\text{SO}_4^{\bullet-}$, $\bullet\text{OH}$, superoxide radical ($\text{O}_2^{\bullet-}$), and singlet oxygen ($^1\text{O}_2$). EPR spectroscopy was employed to directly detect the reactive species, with 5,5-dimethyl-1-pyrrolineN-oxide (DMPO) as the spin trapping agent for $\bullet\text{OH}$, $\text{SO}_4^{\bullet-}$ and $\text{O}_2^{\bullet-}$, and 2,2,6,6-tetramethyl-4-piperidine (TEMP) for $^1\text{O}_2$ (Figure 6). The EPR detection for $\text{O}_2^{\bullet-}$ was performed in pure methanol to quench $\bullet\text{OH}$ and $\text{SO}_4^{\bullet-}$. Clear signals of DMPO- OH^{\bullet} , DMPO- $\text{SO}_4^{\bullet-}$, and DMPO- $\text{O}_2^{\bullet-}$ adducts in PDS Light confirmed the formation of $\bullet\text{OH}$, $\text{SO}_4^{\bullet-}$, and $\text{O}_2^{\bullet-}$,^{119,127–129} while the corresponding signals in PDS Dark were negligible (Figure 6a-b). The characteristic 1:1:1 peak for 2,2,6,6-tetramethyl-1-piperidinyloxy (TEMPO), the TEMP- $^1\text{O}_2$ adduct, was also observed for PDS Light in water (Figure 6c). Although the signal of TEMPO was observed, it could originate either from direct oxidation of TEMP by $^1\text{O}_2$ or one-electron abstraction from TEMP as a heterocyclic amine.¹³⁰ Consequently, EPR signal alone still cannot conclusively confirm the role of $^1\text{O}_2$.⁶⁷ The solvent-dependent lifetime of $^1\text{O}_2$ is a crucial but often overlooked characteristic. $^1\text{O}_2$ is quenched more slowly by deuterium oxide ($k(\text{D}_2\text{O}) = 1.5 \times 10^4 \text{ s}^{-1}$) than by water ($k(\text{H}_2\text{O}) = 2.5 \times 10^5 \text{ s}^{-1}$).^{67,131} To take advantage of that, EPR detections were also conducted with D_2O as the solvent. The peak intensity of TEMPO for PDS Light in D_2O was nearly 1.5 times higher than that in water, confirming the formation of TEMPO via direct oxidation by $^1\text{O}_2$ (Figure 6c). Because the dissolved oxygen (O_2) could be an important precursor for $\text{O}_2^{\bullet-}$ and $^1\text{O}_2$,^{132–134} EPR detections for $\text{O}_2^{\bullet-}$ and $^1\text{O}_2$ were also performed under anoxic conditions to examine the role of O_2 in PDS Light. Interestingly, the absence of O_2 had little influence on the signal intensities of DMPO- $\text{O}_2^{\bullet-}$ and TEMPO in PDS Light, indicating that O_2 was not involved in the generation of $\text{O}_2^{\bullet-}$ and $^1\text{O}_2$.

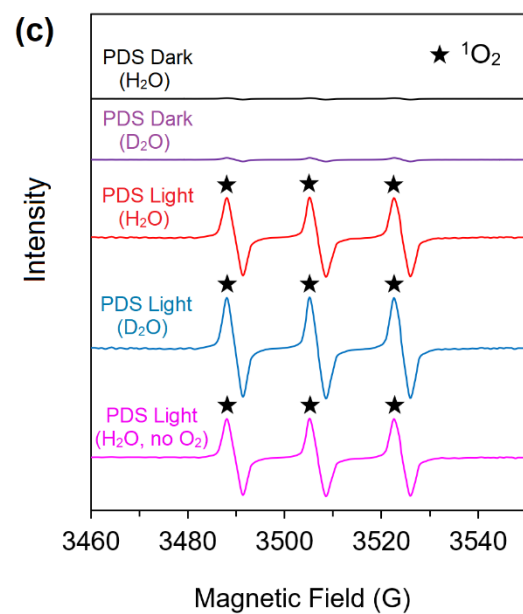
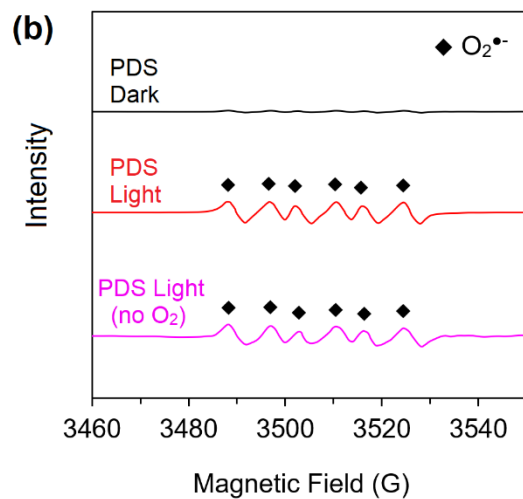
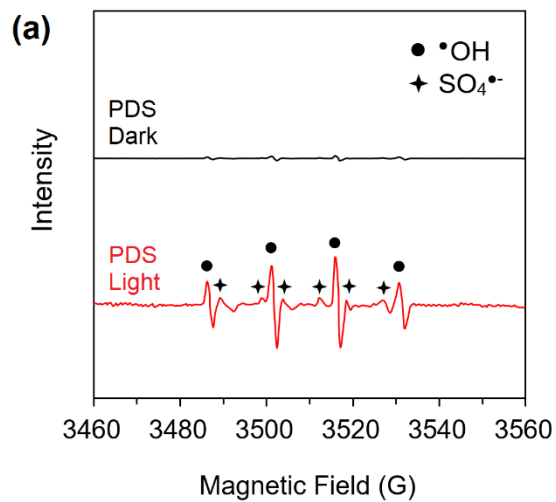
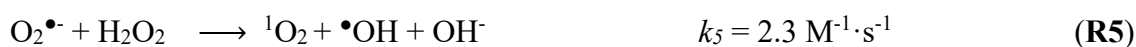
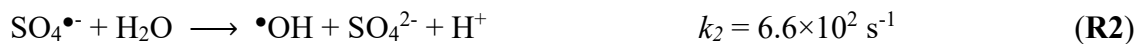


Figure 6. EPR spectra of (a) $\bullet\text{OH}$ and $\text{SO}_4^{\bullet-}$, (b) $\text{O}_2^{\bullet-}$, and (c) $^1\text{O}_2$ of PDS Dark and PDS Light in the absence of ATZ ($[\text{PDS}]_0 = 5.0 \text{ mM}$, $[\text{DMPO}] = [\text{TEMP}] = 50.0 \text{ mM}$, $[\text{Na}_2\text{HPO}_4] = 10.0 \text{ mM}$).

Based on the formation of reactive species in both oxic and anoxic conditions, the potential reactions involved in PDS Light clean system are presented in **Figure 7**. The photolysis of PDS by light can generate two $\text{SO}_4^{\bullet-}$ (**R1**).¹³⁵ Based on the rate constant of PDS decay in dark and under light, the rate constant for **R1** was estimated at around $8.8 \pm 1.1 \times 10^{-3} \text{ min}^{-1}$ in this study. The $\text{SO}_4^{\bullet-}$ can transform to $\bullet\text{OH}$ by snatching an electron from water molecule (**R2**).¹³⁶ Importantly, even though the dominant species in phosphate buffer at pH 7.0 can quench $\text{SO}_4^{\bullet-}$ ($k(\text{SO}_4^{\bullet-}/\text{H}_2\text{PO}_4^-) < 7.0 \times 10^4 \text{ M}^{-1} \cdot \text{s}^{-1}$, $k(\text{SO}_4^{\bullet-}/\text{HPO}_4^{2-}) = 1.2 \times 10^6 \text{ M}^{-1} \cdot \text{s}^{-1}$),¹¹⁷ a portion of $\text{SO}_4^{\bullet-}$ can still undergo **R2** to produce $\bullet\text{OH}$ based on competitive kinetics. Subsequently, a series of reactions may take place to produce $\text{O}_2^{\bullet-}$, a key precursor for $^1\text{O}_2$ (**R3-R10**).^{117,137-151}



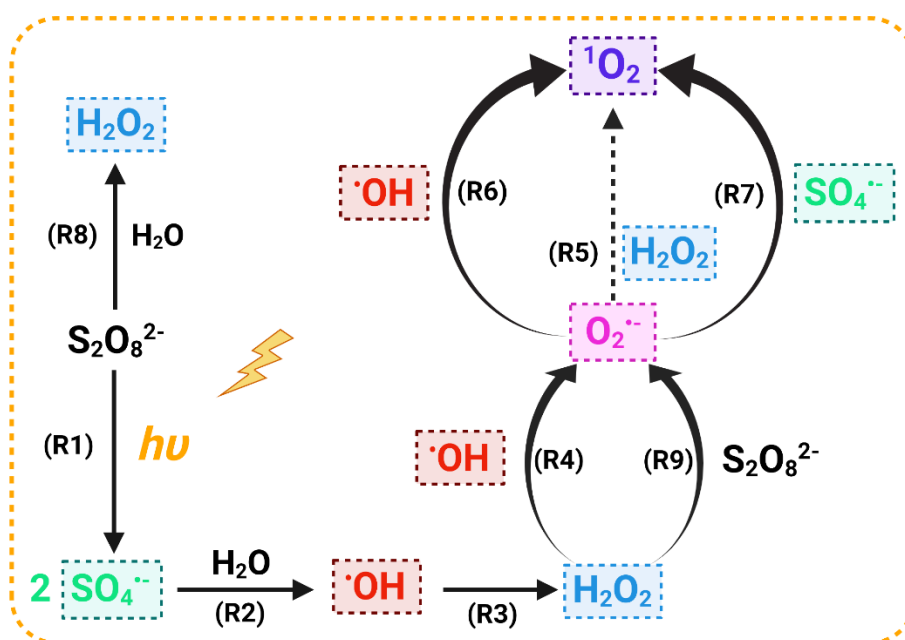


Figure 7. Potential reaction pathways for the formation of reactive species by PDS Light in the absence of ATZ (created with BioRender.com).

Based on these reactions, H_2O_2 is a key intermediate in generating $\text{O}_2^{\bullet-}$ and $^1\text{O}_2$. Specifically, the formation of H_2O_2 via the recombination of $\bullet\text{OH}$ can readily occur as a near-diffusion-controlled reaction with a low activation energy of $7.65 \text{ kJ}\cdot\text{mol}^{-1}$ (**R3**).^{137,144,145} The direct overlap between the $(p_u)^1$ orbitals of two $\bullet\text{OH}$ results in possible formation of H_2O_2 .¹⁴⁶ The produced H_2O_2 can react with $\bullet\text{OH}$ to produce $\text{O}_2^{\bullet-}$ (**R4**).^{144,147} Then $\bullet\text{OH}$ can react with $\text{O}_2^{\bullet-}$ to generate $^1\text{O}_2$ (**R5**).^{144,152} The calculated changes in the Gibb's free energy (ΔG°) for **R4** and **R5** are -83.0 and $-14.5 \text{ kJ}\cdot\text{mol}^{-1}$ respectively, based on ΔE° ($\Delta E^\circ(\bullet\text{OH}/\text{H}_2\text{O}) = +1.8 \text{ V}$; $\Delta E^\circ(\text{O}_2^{\bullet-}/\text{H}_2\text{O}_2 = +0.94 \text{ V}$; $\Delta E^\circ(\text{H}_2\text{O}_2/\bullet\text{OH}, \text{H}_2\text{O}) = +0.8 \text{ V}$; $\Delta E^\circ(^1\text{O}_2/\text{O}_2^{\bullet-} = +0.65 \text{ V})$), indicating thermodynamic feasibility of the reactions.¹³⁹ Despite its relatively low rate constant, **R4** may be accelerated by external energy sources (i.e., visible light).¹⁴⁶ It was reported that the reaction between $\text{O}_2^{\bullet-}$ and H_2O_2 (**R5**) requires direct overlap between the empty σ_u^* orbital of H_2O_2 and the filled or half-filled π_g^* orbital of $\text{O}_2^{\bullet-}$, which is hindered by the filled π_g^* orbital

of H₂O₂.¹⁴⁹ Hence, **R5** might not be a major reaction contributing to the production of ¹O₂.

Alternatively, •OH can directly oxidize O₂•⁻ to produce ¹O₂ (**R6**),¹⁵⁰ and formation of both singlet states of O₂ (¹Σ_g⁺O₂ and ¹Δ_gO₂) were proven to be thermodynamically favorable.¹³⁹ In addition, direct overlap between the π_g^{*} orbital in O₂•⁻ and the p_u orbital in •OH is also possible to produce ¹Δ_gO₂.¹⁴⁶ Similarly, SO₄•⁻ can also directly oxidize O₂•⁻ to produce O₂ (**R7**).¹³⁸ However, whether the produced O₂ is predominantly in the singlet or triplet state is unclear. It has also been proposed that PDS can be hydrolyzed to generate H₂O₂ (**R8**).¹⁵³ Given the relatively low redox potential of H₂O₂ (1.78 V) compared to PDS (2.08 V), H₂O₂ could reduce PDS to generate O₂•⁻ (**R9**) as proposed by a previous study.¹¹⁷ Furthermore, the formation of ¹O₂ by spontaneous disproportionation of O₂•⁻ has long been proposed (**R10a-b**).¹⁴¹ Quantitative determination in literature revealed that less than 10% of the O₂ produced was in singlet state, suggesting that this might be an inefficient pathway for ¹O₂ evolution.^{142,143} In order to confirm the critical role of H₂O₂ in PDS system, the presence of H₂O₂ in PDS Dark and PDS Light was determined following a spectrophotometric method developed based on the formation of red-orange peroxovanadate cation from the reaction between H₂O₂ and vanadate under acidic medium.^{125,126} No color change was observed for PDS Dark (**Figure S3**). By contrast, a red-orange color was observed when the PDS Light sample was added to the light-yellow vanadate solution, with a main absorption band at 453 nm, providing strong evidence for the formation of H₂O₂ and the proposed reaction **R3**.

PDS Light (with ATZ)

With the presence of ATZ, the mechanisms for the generation of reactive species are drastically different. First of all, ATZ has been reported to react rapidly with SO₄•⁻ (*k*(SO₄•⁻

$/ATZ) = 2.6-4.2 \times 10^9 \text{ M}^{-1} \cdot \text{s}^{-1}$),¹⁵⁴⁻¹⁵⁶ which could significantly inhibit **R2** based on competitive kinetics. Consequently, the subsequent **R3-R7** are very unlikely to occur, and it is reasonable to assume that $\text{SO}_4^{\bullet-}$ might be the dominant reactive species that contributed to the degradation of ATZ in PDS Light. To confirm this, four scavengers were introduced to selectively quench reactive species to probe their roles (**Figure 8a**).¹⁵⁷ Methanol (MeOH) was used to quench both $\text{SO}_4^{\bullet-}$ ($k = 1.0 \times 10^7 \text{ M}^{-1} \cdot \text{s}^{-1}$)¹⁵⁸ and $\bullet\text{OH}$ ($k = 9.7 \times 10^8 \text{ M}^{-1} \cdot \text{s}^{-1}$).¹⁵⁹ Tert-butyl alcohol (TBA), which has a higher rate constant with OH^{\bullet} ($k = 4.8 \times 10^8 \text{ M}^{-1} \cdot \text{s}^{-1}$)¹¹³ than with $\text{SO}_4^{\bullet-}$ ($k = 8.4 \times 10^5 \text{ M}^{-1} \cdot \text{s}^{-1}$),¹⁵⁸ was used to specifically quench $\bullet\text{OH}$. Superoxide dismutase (SOD) as an enzyme that catalyzes the disproportionation of $\text{O}_2^{\bullet-}$ was added to selectively quench $\text{O}_2^{\bullet-}$ ($k = 2.8 \times 10^9 \text{ M}^{-1} \cdot \text{s}^{-1}$),^{160,161} and L-histidine (L-his) was used to quench $^1\text{O}_2$ ($k = 9.0 \times 10^7 \text{ M}^{-1} \cdot \text{s}^{-1}$).¹¹² The concentration of each quencher was 100 times higher than that of PDS to ensure efficient quenching of reactive species. It should be noted that *p*-benzoquinone as a common quencher for $\text{O}_2^{\bullet-}$ was not used due to its potential to activate PDS via electron transfer.¹⁶² Furthermore, an often overlooked fact is that the second-order rate constants between L-his and $\text{SO}_4^{\bullet-}$ ($k = 2.5 \times 10^9 \text{ M}^{-1} \cdot \text{s}^{-1}$)¹⁶³ and $\bullet\text{OH}$ ($k = 4.8 \times 10^9 \text{ M}^{-1} \cdot \text{s}^{-1}$)¹¹³ are more than one order of magnitude higher than that between L-his and $^1\text{O}_2$. Other scavengers for $^1\text{O}_2$ such as N_3^- and FFA also suffer from the same limitations. Thus, quenching experiments can only provide preliminary information on the involvement of $^1\text{O}_2$. Overall, the ATZ degradation by PDS Light was significantly hindered by all four scavengers, with L-his almost completely inhibited the degradation.

The inhibitory effect of MeOH was stronger than that of TBA, consistent with our assumption that $\text{SO}_4^{\bullet-}$ might be the main radical species. Surprisingly, the presence of SOD

also reduced the degradation efficiency dramatically, suggesting the involvement of $O_2^{\bullet-}$, likely through different reactions from **R4**. The quenching experiments were also conducted under anoxic condition to investigate the role of O_2 in the generation of reactive species in the presence of ATZ (**Figure 8b**). Without scavengers, the degradation efficiency of ATZ was markedly retarded under anoxic condition, according to the corresponding pseudo-first-order rate constant ($k_{obs(anoxic)} = 7.3 \pm 0.9 \times 10^{-2} \text{ min}^{-1}$ vs. $k_{obs(oxic)} = 11 \pm 3.0 \times 10^{-2} \text{ min}^{-1}$), suggesting an important role of dissolved O_2 in the PDS Light system with ATZ. The appreciable removal of ATZ under anoxic condition was attributed to the degradation of ATZ by $SO_4^{\bullet-}$ as the main reactive species, and the higher rate constant under oxic condition suggested the formation of additional reactive species. The very similar effects of scavengers on the degradation of ATZ in both oxic and anoxic conditions, except for the much minor inhibitory effect of SOD under anoxic condition, further supports the role of O_2 in the PDS light system with ATZ.

To solidify the results, the impacts of scavengers themselves on the decay of PDS under light were examined under both oxic and anoxic conditions (**Figure S4**). No impact was observed for MeOH, TBA, and SOD on the decay of PDS. However, accelerated decay of PDS in the presence of L-his was noticed, suggesting that PDS can be directly consumed by L-his.^{164,165} Therefore, the hindered degradation of ATZ by PDS in the presence of L-his could be attributed to lower PDS concentration and/or simultaneous quenching of $SO_4^{\bullet-}$, $\bullet OH$ and 1O_2 .

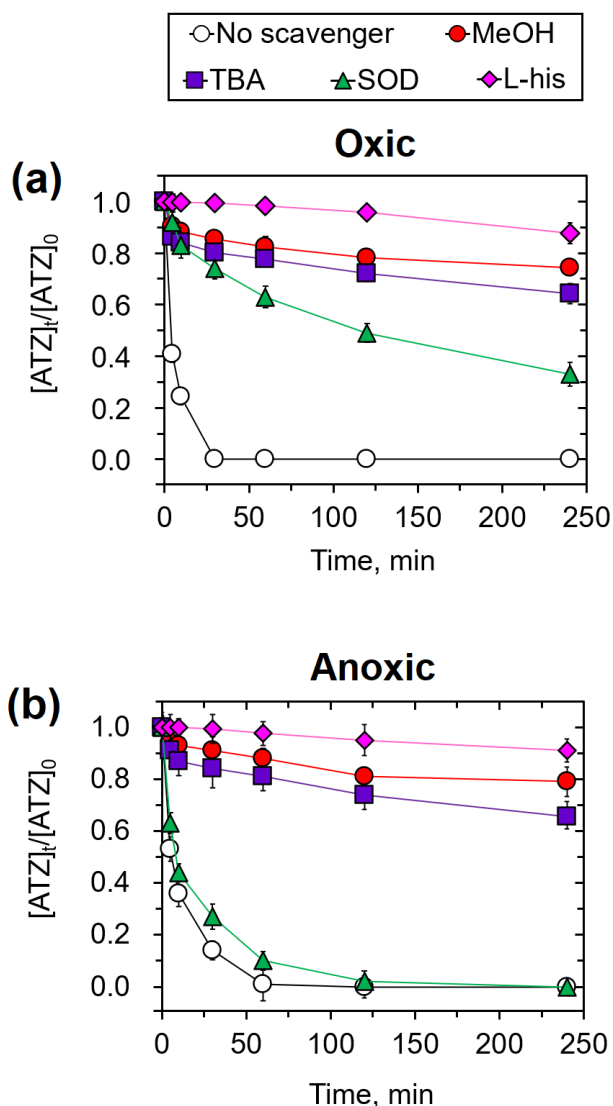


Figure 8. Effects of different scavengers on the degradation of ATZ by PDS Light under **(a)** oxic and **(b)** anoxic condition ($[ATZ]_0 = 10.0 \mu\text{M}$, $[PDS]_0 = 5.0 \text{ mM}$, $[\text{Na}_2\text{HPO}_4] = 10.0 \text{ mM}$, $[\text{scavenger}]_0 = 0.5 \text{ M}$, $\text{pH}_0 = 7.0$, $T = 25 \text{ }^\circ\text{C}$).

Overall, the quenching experiments inferred substantial roles of $\text{SO}_4^{\bullet-}$ and $\text{O}_2^{\bullet-}$, whereas the role of $^1\text{O}_2$ remains questionable. The importance of nonradical $^1\text{O}_2$ has been suggested in a few recent studies,^{118,166} however, this postulation was often not well-substantiated, making the role of $^1\text{O}_2$ a contentious issue in PDS-based AOPs. More direct evidence is needed to determine the role of $^1\text{O}_2$ in the PDS Light system in the presence of ATZ.

EPR spectroscopy was used to detect the four reactive species in the PDS system with

ATZ. It is clear that signals of both DMPO-SO₄^{•-} and DMPO-OH[•] adducts were observed in PDS Light with ATZ (**Figure 9a**). It should be noted that in addition to the reaction between [•]OH and DMPO, DMPO-OH[•] adduct can also be formed via a nucleophilic substitution between DMPO-SO₄^{•-} and hydroxide ion (OH⁻).^{167,168} The fast transformation from DMPO-SO₄^{•-} to DMPO-OH[•] is the reason why DMPO-SO₄^{•-} is rarely detected alone. The quenching study and EPR measurements together strongly suggest the dominant role of SO₄^{•-} in the degradation of ATZ in the PDS Light system. Consistent with the quenching study, clear signals of DMPO-O₂^{•-} and TEMPO were observed under oxic condition, but both of them disappeared under anoxic condition (**Figure 9b-c**), indicating that the production of O₂^{•-} and ¹O₂ in PDS Light strongly relied on O₂. In order to further confirm the role of ¹O₂, the degradation of ATZ was repeated with D₂O as the solvent. The pseudo-first-order rate constant for ATZ degradation by PDS Light in D₂O was more than 2.5 times higher than that in water, whereas the effect of D₂O was negligible for PDS Dark (**Figure S5**). Together, our study provides deterministic evidence for the participation of ¹O₂ in the degradation of ATZ by PDS Light, and dissolved O₂ is a critical factor in the formation of ¹O₂. The non-detection of EPR signals in PDS Dark (**Figure 9**) further confirms the direct oxidation of ATZ by PDS in dark (**Figure S2**).

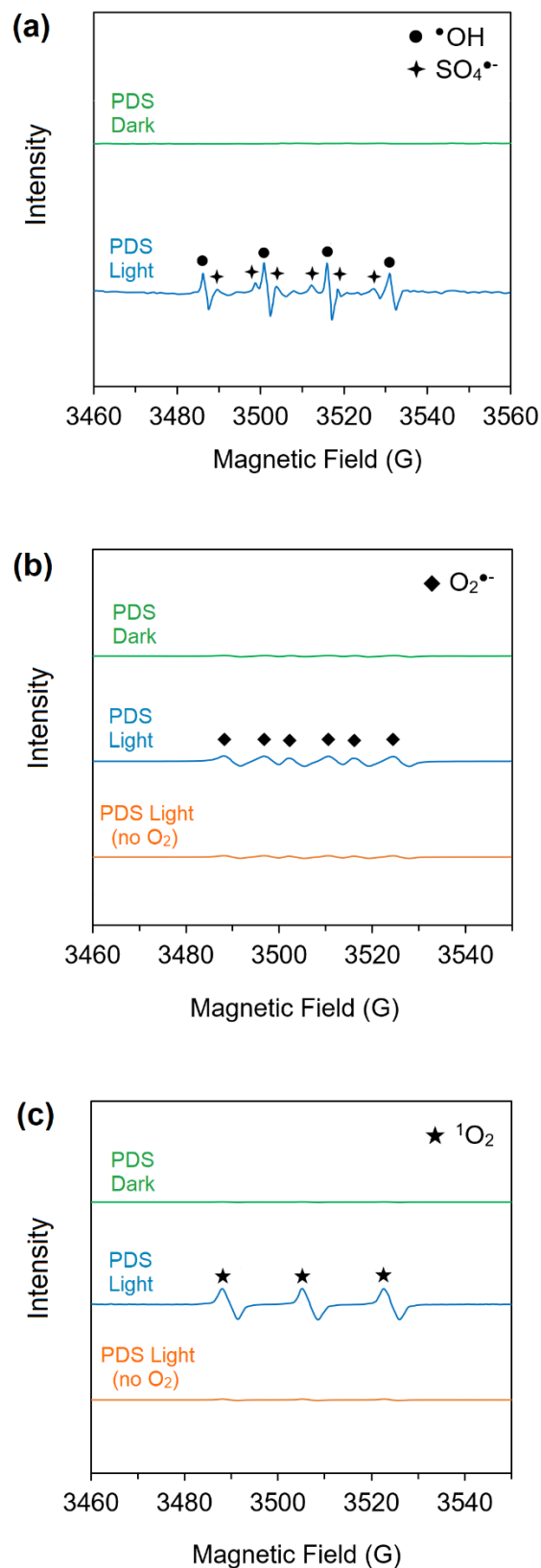
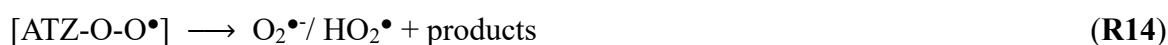


Figure 9. EPR spectra of (a) •OH and SO₄•⁻, (b) O₂•⁻, and (c) ¹O₂ of PDS Dark and PDS Light with presence of ATZ ([PDS]₀ = 5.0 mM, [ATZ]₀ = 10 μM, [DMPO]₀ = [TEMP]₀ = 50.0 mM, [Na₂HPO₄] = 10.0 mM).

To further understand the mechanisms of ATZ breakdown in the PDS Light system, the degradation intermediates of ATZ by PDS in dark and under light in oxic condition were identified (**Table S2, Figure S6**), and possible degradation pathways were illustrated (**Figure S7**). It has been suggested that electron transfer is the primary reaction pathway between $\text{SO}_4^{\bullet-}$ and electron-rich aromatic compounds,^{156,169,170} and in the case of ATZ, de-alkylation of the N-ethyl group on the side chain is widely accepted as the prevalent degradation pathway.^{169,171,172} Based on this, a reaction mechanism between $\text{SO}_4^{\bullet-}$ and ATZ has been proposed,¹⁶⁹ which reasonably justified the dominance of de-ethylation, accompanied by the release of $\text{O}_2^{\bullet-}$ (**R11-R14**). The slightly enhanced decay of PDS with the presence of ATZ under light (**Figure 5b**) may also be attributed to this mechanism. Overall, $\text{SO}_4^{\bullet-}$ was the dominant reactive species for ATZ degradation under the anoxic condition, whereas both $\text{SO}_4^{\bullet-}$ and $^1\text{O}_2$ contributed to ATZ degradation under the oxic condition (**Figure 10**).



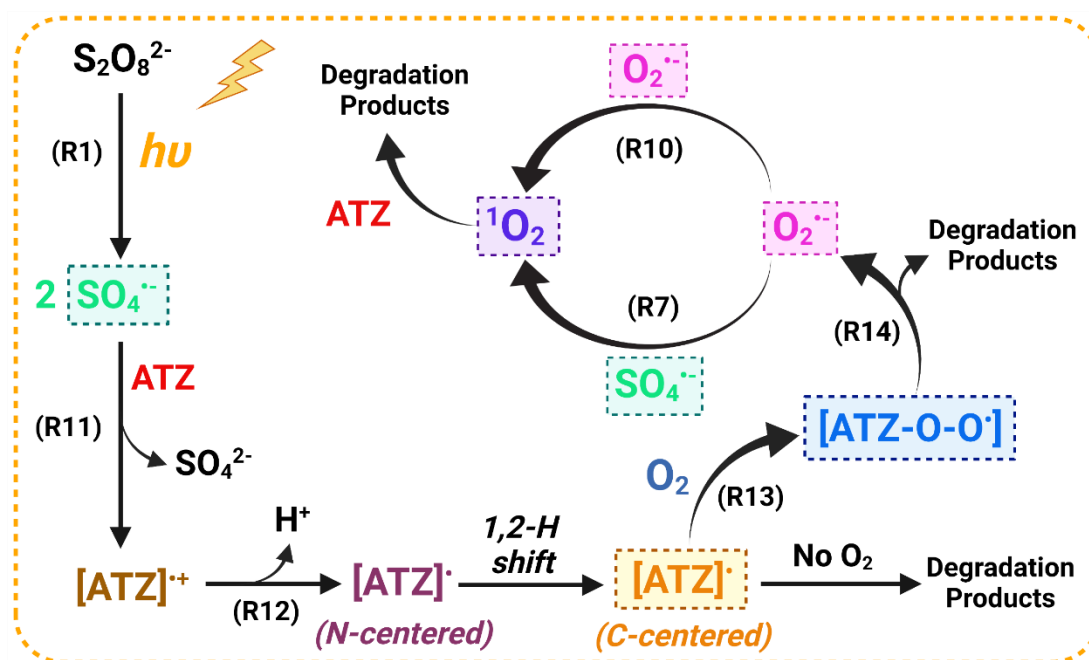


Figure 10. Potential reaction pathways for the formation of reactive species by PDS Light in presence of ATZ (created with BioRender.com).

The initial step involves the one-electron oxidation of ATZ by $\text{SO}_4^{\bullet-}$ to yield an ATZ radical cation ($[\text{ATZ}]^{\bullet+}$) (R11). After losing a proton either from the ethyl N-atom or the isopropyl N-atom on the side chain, the $[\text{ATZ}]^{\bullet+}$ is expected to transform to two N-centered radical forms ($[\text{ATZ}]^{\bullet}$) that are at equilibrium with each other (R12). The unpaired electron either sits on the N-atom of the N-ethyl or the N-isopropyl group. Under the catalysis of water molecule, a 1,2-H shift can occur on the N-centered radicals, similarly to the 1,2-H shift of alkoxy radicals, to produce C-centered radicals, with the unpaired electron shifting onto the nearest aliphatic C-atoms followed by the addition of a H-atom to the N-atom. Following that, the C-centered radicals can readily react with O_2 to form peroxy adduct ($k = 3 \times 10^9 \text{ M}^{-1} \cdot \text{s}^{-1}$) (R13)¹⁷³ and then release $\text{O}_2^{\bullet-}$ or hydroperoxyl radical (HO_2^{\bullet}) (R14). Consequently, a double bond can be formed between the N- and C- atom, which can be broken via hydrolysis to produce 2-chloro-4-amino-6-isopropylamino-1,3,5-triazine (DEA) or 2-chloro-4-ethylamino-

6-amino-1,3,5-triazine (DIA) (**Table S2**). the H-atom on the N-ethyl group is more likely to deprotonate due to the higher acidity of the H-atom on the N-ethyl group than that on the N-isopropyl group, which favors the formation of C-centered radicals and subsequent reactions.^[62] Therefore, formation of DEA might be more favorable than DIA. According to the oxidized products, the signal intensities of DEA and DIA were almost 10 times higher than the other products (**Figure S6**), consistent with the proposed mechanisms. In addition to $\text{SO}_4^{\bullet-}$, DEA and DIA can also be produced via the reaction between $^1\text{O}_2$ and ATZ. An Alder-ene reaction could be initiated by $^1\text{O}_2$, followed by hydrogen-abstraction, hemi-aminal ring opening, and imine hydrolysis, to degrade ATZ to DEA (**Figure S8**).¹⁷⁴ Similar pathway could also occur on the other side chain to form DIA. Overall, the reaction mechanisms mentioned above agreed well with the results of our quenching experiments and EPR spectra. It can be concluded that when ATZ is present, the $\text{SO}_4^{\bullet-}$ produced by PDS Light reacts rapidly with ATZ and might be the most dominant reactive species that contributes to the degradation of ATZ. The formation of $\bullet\text{OH}$ is expected to be limited. Generation of $[\text{ATZ}]^{\bullet+}$ as a result of ATZ oxidation by $\text{SO}_4^{\bullet-}$ led to the production of $\text{O}_2^{\bullet-}$ in the presence of O_2 (**R11-R14**). The slightly enhanced decay of PDS with the presence of ATZ under light (**Figure 5b**) may also be attributed to this mechanism. Overall, $\text{SO}_4^{\bullet-}$ was the dominant reactive species for ATZ degradation under anoxic condition, whereas both $\text{SO}_4^{\bullet-}$ and $^1\text{O}_2$ contributed to ATZ degradation under oxic condition.

To verify the mechanisms discussed above, presence of H_2O_2 in PDS Light under oxic and anoxic condition was determined (**Figure S9**). Under oxic condition, slight absorption at ~ 453 nm suggested that only a small amount of H_2O_2 was produced, possibly as a byproduct of **R10a-b** in addition to $^1\text{O}_2$. Moreover, the negligible absorption between 400 and 500 nm

under anoxic condition is expected, because formation of H_2O_2 in presence of ATZ is very unlikely when **R2** and **R13** are hindered.

To gain more understanding on the PDS utilization efficiency under visible light, corresponding RSE was calculated. Overall, the average RSE for PDS Light was less than 1.0%, which was lower than reported values in literature.^{175,176} This could be ascribed to the relatively high initial concentration of PDS (5 mM) and low initial concentration of ATZ (10 μM), which are unfavorable for a high RSE.¹⁷⁶ Scavenging of $\text{SO}_4^{\bullet-}$ by co-present inorganic anions (e.g. phosphate) could be another reason of low RSE which requires additional investigation.

Conclusions

Our study confirmed the activation of PDS by visible light to generate reactive radical and nonradical species that accelerate the degradation of organic pollutants. Significantly, the underlying mechanisms that contribute to the formation of reactive species were found to be highly pollutant-dependent. As shown in our study in the absence of ATZ, EPR spectra indicated that all four reactive species ($\text{SO}_4^{\bullet-}$, $\bullet\text{OH}$, $\text{O}_2^{\bullet-}$ and $^1\text{O}_2$) can be produced, with H_2O_2 and $\text{O}_2^{\bullet-}$ serving as key intermediates and precursors for $^1\text{O}_2$. In the presence of ATZ, $\text{SO}_4^{\bullet-}$ was rapidly consumed, and generation of $\bullet\text{OH}$ was largely inhibited. Quenching study and EPR spectra revealed the formation of $\text{O}_2^{\bullet-}$ and $^1\text{O}_2$ in the PDS Light system with ATZ, but only in the presence of O_2 . This is in contrast to the PDS Light system without ATZ, in which the dissolved oxygen plays a minor role in the formation of $\text{O}_2^{\bullet-}$ and $^1\text{O}_2$. In addition to $\text{SO}_4^{\bullet-}$ as the dominant reactive species, the crucial role of $^1\text{O}_2$ in the degradation of ATZ could be inferred by the higher degradation rate of ATZ and the stronger EPR signal in D_2O . Therefore,

in the PDS Light system with ATZ, a combined radical and nonradical pathway together contribute to the removal of ATZ. This study is noteworthy because it highlights for the first time the direct PDS activation by visible light without any catalyst, and conclusively demonstrates the significant roles of both radical and non-radical mechanisms in the PDS Light system with ATZ. In this system, the presence of O₂ is critical for the nonradical pathway. In natural water, many water constituents such as inorganic anions could further complicate the system because many of them are radical quenchers or can be activated to generate new radicals. Their roles in the breakdown of ATZ and other environmental pollutants in the PDS Light system will be investigated in future studies. Importantly, the removal efficiency of different pollutants varied appreciably, which could be due to their unique molecular structures. Further studies are needed to unveil the underlying reaction mechanisms between these pollutants and PDS under different environmental conditions.

CHAPTER III

ACTIVATION OF PEROXYMONOSULFATE BY PHOSPHATE AND CARBONATE FOR THE ABATEMENT OF ATRAZINE: ROLES OF RADICAL AND NON- RADICAL SPECIES*

Introduction

Owing to the increasing usage of synthetic chemicals in society, there has been a growing demand for effective technologies to remove released chemicals in natural waters.^{10,36} Sulfate radical ($\text{SO}_4^{\bullet-}$)-based advanced oxidation processes (AOPs) have attracted tremendous interests because of the strong oxidizing capability of $\text{SO}_4^{\bullet-}$ ($E^0 = +2.5\text{-}3.1 \text{ V}_{\text{NHE}}$).⁶⁹ Peroxymonosulfate (HSO_5^- , PMS) is a common precursor for $\text{SO}_4^{\bullet-}$ which can be activated via either energy-transfer or electron-transfer processes.⁶⁷ Since the peroxide bond in PMS is asymmetrical and polar, it is more effectively cleaved via electron-transfer.⁶⁷ As a result, a considerable amount of studies have been performed on the activation of PMS by heterogeneous catalysts such as metal oxides with reduced transition metals and carbonaceous materials containing electron-donating groups.¹⁷⁷⁻¹⁷⁹ Roles of different reactive species such as $\text{SO}_4^{\bullet-}$, hydroxyl radical ($\bullet\text{OH}$), superoxide ($\text{O}_2^{\bullet-}$), and singlet oxygen ($^1\text{O}_2$) in pollutant removal have also been investigated. Comparatively, the roles of the reactive species in a homogeneous system (i.e., without catalysts) are not fully comprehended.

PMS is often added as a pre-treatment chemical or “shock oxidizer” in swimming pools to remove pharmaceuticals and personal care products (PPCPs) and other organic matters so that

*Reprinted with permission from: Activation of peroxymonosulfate by phosphate and carbonate for the abatement of atrazine: Roles of radical and non-radical species. Wen, Y., Sharma, V.K., Ma, X., 2022. *ACS ES&T Water*. 2, 635-643. Copyright 2022 American Chemical Society.

free chlorine can effectively disinfect the water.^{164,180} Surprisingly, the chemistry of PMS itself and its interaction with common background water constituents such as oxyanions have been largely ignored. This is noteworthy because some of these water constituents are known to scavenge various radicals. Phosphate and carbonate are ubiquitous in natural waters and are commonly used as buffers. Therefore, in-depth studies on the effect of these two oxyanions on PMS-based systems are critically needed. The enhance effect of phosphate on the performance of PMS was observed in a previous study,¹⁸¹ but the underlying mechanisms have not been reported. Studies on the effect of HCO_3^- were mainly conducted in the presence of catalysts or focused on how HCO_3^- scavenges $\text{SO}_4^{\bullet-}$ and $\bullet\text{OH}$ to form secondary reactive species.^{182,183} Potential interactions between HCO_3^- and PMS in a homogeneous system were not studied.

Singlet oxygen ($^1\text{O}_2$) can be produced via the spontaneous decomposition of PMS and has been concluded as a primary reactive species in several recent PMS-based studies.^{184,185} However, substantiating the role of $^1\text{O}_2$ requires more solid evidence than results from quenching studies because many quenchers (e.g., L-histidine and azide) and probe molecules (e.g., furfuryl alcohol) can deplete PMS without producing any reactive species.^{131,164} Some of these compounds also react much faster with $\text{SO}_4^{\bullet-}$ than with $^1\text{O}_2$.^{114,116} Furthermore, the detection of $^1\text{O}_2$ using spin trapping agent in electron paramagnetic resonance (EPR) technique could also be inconclusive.⁶⁷ Therefore, the role of $^1\text{O}_2$ in a PMS system needs further clarification. Finally, PMS itself is a strong oxidant and direct reaction between PMS and various environmental pollutants has been reported.^{164,186} Consequently, the contribution of direct PMS contaminant reactions in contaminant removal needs greater attention.

This study had the following objectives: (i) investigate the interactions between two common anions (phosphate and carbonate) and PMS and their impacts on the degradation of atrazine (ATZ) by PMS, (ii) unveil the main reactive species involved in the degradation of ATZ and determine the contributions of radical and non-radical pathways, (iii) evaluate the influence of temperature on the degradation of ATZ by PMS in water, and (iv) demonstrate the removal of ATZ in river and lake water by PMS.

Experimental Section

Chemicals and Materials

Potassium peroxymonosulfate (Oxone, $\text{KHSO}_5 \cdot 0.5 \text{KHSO}_4 \cdot 0.5 \text{K}_2\text{SO}_4$, $\geq 99.0\%$) and tert-butanol (TBA) anhydrous ($\geq 99.5\%$) were obtained from Sigma-Aldrich (St. Louis, USA). Sodium phosphate dibasic anhydrous ($\geq 98.0\%$), sodium bicarbonate ($\geq 99.0\%$), potassium iodide (99.0%), sodium hydroxide ($\geq 97.0\%$), sulfuric acid (98.0%), sodium thiosulfate (99.0%), 5,5-dimethyl-1-pyrroline N-oxide (DMPO, $\geq 98.0\%$), superoxide dismutase (SOD, 3500 U/mg) were obtained from Thermo Fisher Scientific (Waltham, USA). Atrazine (ATZ, $\geq 97.0\%$) was purchased from TCI America (Portland, USA). Methanol (MeOH, reagent grade) was obtained from VWR Chemicals (Radnor, USA). Ammonium metavanadate (99.5%) and 2,2,6,6-tetramethyl-4-piperidine (TEMP, 99%) were obtained from ACROS Organics (Waltham, USA). Deuterium oxide (D_2O , 99.8%) and L-histidine (L-his, $\geq 98.0\%$) were obtained from Alfa Aesar (Haverhill, USA). Ultrapure deionized water ($>18.2 \text{ M}\Omega \cdot \text{cm}$) produced by a Millipore Milli-Q Direct 8 system (Millipore Sigma, Burlington, USA) was used as a solvent in all solutions unless specified otherwise. Oasis HLB cartridges (WAT106202, 6

cc/200 mg) were obtained from Waters (Milford, USA). Quartz EPR tubes (2 mm and 4 mm) were obtained from Wilmad Labglass (Vineland, USA). Natural surface water samples were collected from Lake Bryan (N 30°33'30", E 96°25'25", Bryan, Texas) and Brazos River (N 30°42'33", E 96°28'5", College Station, Texas). Neither ATZ nor PMS were detected in these water samples.

Degradation of atrazine by PMS in presence of phosphate

The experiments were performed in 40 mL glass vessels. The reaction solutions were constantly stirred at 300 rpm, and the temperature was maintained at 25 ± 0.5 °C. The initial concentrations of ATZ and PMS were 10.0 μ M and 5.0 mM, respectively. 10.0 mM phosphate was used to control the initial pH at 7.0 ± 0.2 . 1.0 mL of sample was collected at various time points ($t=0, 1, 2, 3, 4, 5, 10, 20, 30, 60, 90, 120,$ and 240 min). 20 μ L of 5.0 M sodium thiosulfate was added immediately to quench oxidative reactions after sample withdrawal. The ATZ concentration in each sample was measured with a Dionex UltiMate 3000 high-performance liquid chromatograph (HPLC) (Sunnyvale, USA) with a Restek C18 column (4.6×250 mm, 5 μ m). The mobile phase was composed of methanol and water (60/40, v/v) at a flow rate of 1.0 mL/min. The column temperature was set at 30 °C. The degradation of ATZ was also repeated in deuterium oxide (D₂O) under the same experimental conditions. The concentration of PMS was determined spectrophotometrically via a modified iodometric titration method.¹⁸⁷ The initial and final pH in each tube were measured using an Accumet AE150 pH meter (Westford, USA). The effect of temperature on the degradation of ATZ in presence of 10.0 mM phosphate buffer was performed at 10, 25, 40, and 55 °C, with the initial pH at 7.0.

Identifying reactive species in the degradation of ATZ by PMS/phosphate solution

The main reactive species involved in the degradation of ATZ by PMS were identified through quenching. Methanol (MeOH) was used to quench both $\text{SO}_4^{\bullet-}$ ($k = 1.0 \times 10^7 \text{ M}^{-1} \cdot \text{s}^{-1}$)¹⁵⁸ and $\bullet\text{OH}$ ($k = 9.7 \times 10^8 \text{ M}^{-1} \cdot \text{s}^{-1}$),¹⁵⁹ whereas tert-butyl alcohol (TBA) was used to selectively quench $\bullet\text{OH}$ ($k(\bullet\text{OH}) = 4.8 \times 10^8 \text{ M}^{-1} \cdot \text{s}^{-1}$ vs. $k(\text{SO}_4^{\bullet-}) = 8.4 \times 10^5 \text{ M}^{-1} \cdot \text{s}^{-1}$).^{113,158} Superoxide dismutase (SOD) was added to quench $\text{O}_2^{\bullet-}$ ($k = 2.8 \times 10^9 \text{ M}^{-1} \cdot \text{s}^{-1}$),¹⁶¹ and L-histidine (L-his) $^1\text{O}_2$ ($k = 9.0 \times 10^7 \text{ M}^{-1} \cdot \text{s}^{-1}$).¹¹² The concentration of MeOH, TBA, and L-his was 0.5 M, and the concentration of SOD was $50 \text{ U} \cdot \text{ml}^{-1}$. To investigate the impact of oxygen, purified N_2 gas was used to purge the system for 10 min before the quenching experiments, which lowered the dissolved oxygen levels to about 0.12 mg/L. The tubes were immediately capped and then sealed with parafilm to maintain an anoxic environment throughout the reaction. ATZ concentrations in samples taken at $t=0, 5, 10, 30, 60, 120,$ and 240 min were measured using HPLC. The degradation of ATZ by PMS and the corresponding decay of PMS were monitored with and without 10.0 mM phosphate buffer to investigate the effect of phosphate buffer. The initial pH was controlled at 7.0 ± 0.2 in vials without phosphate buffer. To investigate the direct reaction between PMS and ATZ, the initial concentration of ATZ was increased to 5.0 mM (same as PMS).

Electron paramagnetic resonance (EPR) spectroscopy measurements

A Bruker Elexsys E500 EPR, equipped with both a standard resonator and a CoolEdge cryo system (Billerica, USA) was used to identify different reactive species. The EPR

measurements were performed under the following instrument settings: 20.0 mW microwave power, 9.8 GHz microwave frequency, 1.00 G modulation amplitude, 100 kHz modulation frequency, 150 G sweep width, 3515 G center field, and 40.0 s sweep time. The concentration of 5,5-dimethyl-1-pyrroline N-oxide (DMPO) as the spin trapper for $\text{SO}_4^{\bullet-}$ and $\text{O}_2^{\bullet-}$ was 50.0 mM. For $^1\text{O}_2$, 50.0 mM of 2,2,6,6-tetramethyl-4-piperidine (TEMP) was used. The EPR measurements for $\text{SO}_4^{\bullet-}$, $\text{O}_2^{\bullet-}$, and $^1\text{O}_2$ were all conducted in 1:1 mixture of 10.0 mM phosphate buffer in ultrapure water and acetonitrile. In order to detect the signal of DMPO- $\text{O}_2^{\bullet-}$, 0.2 M MeOH was added to quench the formation of DMPO- $\bullet\text{OH}$ and DMPO- $\text{SO}_4^{\bullet-}$. A syringe needle was used to load the reaction solution into a 2 mm quartz EPR tube and then placed into a 4 mm quartz EPR tube and measured by EPR.

Detection of Hydrogen Peroxide (H_2O_2)

H_2O_2 was determined with a previously reported spectrophotometric method based on the reaction between H_2O_2 and metavanadate under acidic medium.¹²⁵ The red-orange peroxovanadate formed from the reaction was detected with an ultraviolet-visible-near infrared (UV-Vis-NIR) spectrophotometer (Hitachi U-4100) at 450 nm.

Effect of carbonate

Similar experiments as described in section 2.2. to 2.5 were also performed to determine the effect of carbonate in PMS solution. The initial concentration of carbonate in the form of HCO_3^- was fixed at 1.0, 5.0 and 10.0 mM.

Determining degradation metabolites of atrazine

To analyze the oxidation products of ATZ by PMS, 50.0 mL of sample was collected after 30 min of reaction from PMS with and without phosphate buffer, followed by solid-phase-extraction (SPE). Briefly, the Waters Oasis HLB cartridges (WAT106202, 6 cc/200 mg) were first conditioned with 5.0 ml of methanol and 5.0 ml of ultrapure water, respectively. After conditioning, the cartridges were loaded with 50.0 ml of samples containing ATZ and its degradation metabolites. They were then dried under medium vacuum (10-20 mmHg) for 10 minutes. The final products adsorbed on the cartridges were eluted with 2.0 ml of methanol. Untargeted liquid chromatography high resolution accurate mass spectrometry (LC-HRAM) analysis was performed on a Q Exactive Plus orbitrap mass spectrometer (Thermo Fisher Scientific, Waltham, USA), coupled to a binary pump UltiMate 3000 HPLC to identify the oxidation products of ATZ.

Applicability of PMS to surface water

The feasibility of PMS to degrade ATZ was tested with surface water samples collected from Brazos River and Lake Bryan near College Station, TX. 10.0 μM ATZ and 5.0 mM PMS were added to the water, but no buffer was added. Neither PMS nor ATZ was detected in the surface water samples.

Data Analysis

The degradation kinetics was fitted with pseudo-first-order model. One-way analysis of variance (ANOVA) was used to determine the statistical differences among the pseudo-first-

order rate constants of ATZ degradation in H₂O and D₂O. Different letters in the figures represent significant differences ($p \leq 0.05$) according to one-way ANOVA, followed by Tukey's test.

Results and Discussion

Degradation of ATZ by PMS in presence of phosphate

Phosphate significantly enhanced the degradation efficiency of ATZ by PMS (**Figure 11a**). Complete removal of ATZ was achieved within 90 min in the presence of 10.0 mM phosphate. Without phosphate, the removal of ATZ was incomplete (i.e., ~80%) even after 240 minutes. The observed pseudo-first-order reaction rate constant (k_{obs}) ($4.4 \pm 0.3 \times 10^{-2} \text{ min}^{-1}$) with phosphate was over four times of that without phosphate ($k_{obs} = 0.97 \pm 0.05 \times 10^{-2} \text{ min}^{-1}$). The results suggested that higher amounts of reactive species were generated when phosphate was present. Phosphate-catalyzed PMS activation was likely the reason because the decay of PMS was significantly higher in presence of phosphate (**Figure S10**). The results agreed with a previous study that showed the formation of SO₄^{•-} in a PMS/phosphate system based on density functional theory (DFT) calculation.¹⁸⁸

Owing to the wide fluctuation of temperature in natural waters, the effect of temperature on the degradation of ATZ by PMS in phosphate buffer was investigated. The degradation efficiency of ATZ substantially accelerated at higher temperatures (**Figure 11b**). The corresponding pseudo-first-order rate constants at different temperatures are listed in **Table S3**. The calculated activation energy (E_a) for the degradation of ATZ by PMS was $136.2 \pm 7.8 \text{ kJ}\cdot\text{mol}^{-1}$ (**Figure S11**), which is markedly higher than PMS systems with a heterogeneous

catalyst ($\sim 20\text{-}60 \text{ kJ}\cdot\text{mol}^{-1}$).^{178,189}

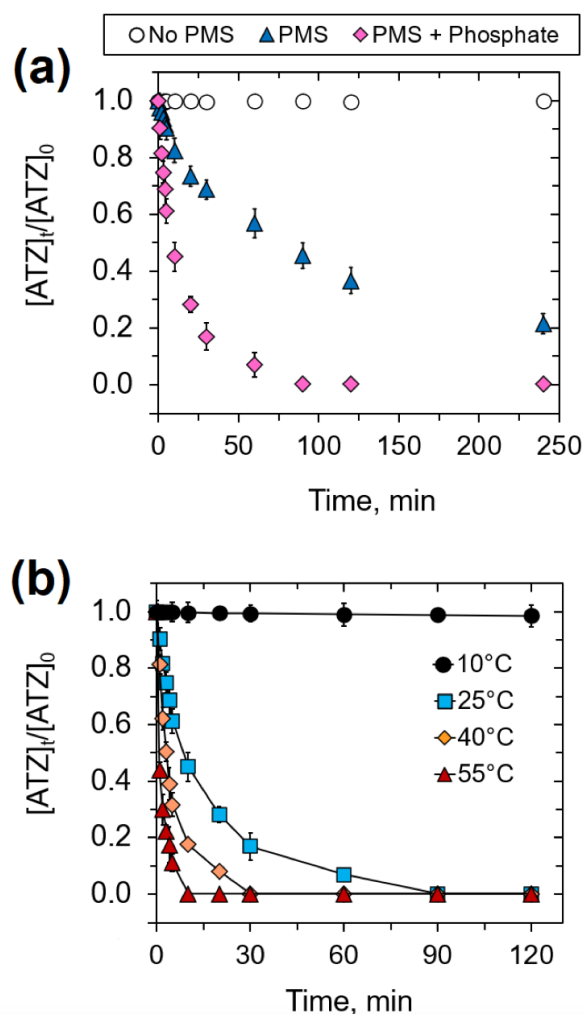


Figure 11. Degradation of ATZ (a) with and without phosphate ($[\text{ATZ}]_0 = 10.0 \mu\text{M}$; $[\text{PMS}]_0 = 5.0 \text{ mM}$; $[\text{Na}_2\text{HPO}_4] = 0$ or 10.0 mM ; $\text{pH}_0 = 7.0$; $T = 25 \text{ }^\circ\text{C}$) and (b) under different temperatures ($[\text{ATZ}]_0 = 10.0 \mu\text{M}$; $[\text{PMS}]_0 = 5.0 \text{ mM}$; $[\text{Na}_2\text{HPO}_4] = 10.0 \text{ mM}$; $\text{pH}_0 = 7.0$; $T = 10, 25, 40, 55 \text{ }^\circ\text{C}$).

Radical species in presence of phosphate - quenching study

Quenching experiments were performed to determine the roles of four possible reactive species. The insignificant effect of SOD suggested that $\text{O}_2^{\bullet-}$ was not involved in the degradation of ATZ (Figure 12a). Dissolved oxygen (O_2) can serve as a key precursor for $\text{O}_2^{\bullet-}$, and results shown in Figure 12b suggested no role of $\text{O}_2^{\bullet-}$ in degrading ATZ in presence of phosphate. The degradation of ATZ was significantly impeded by MeOH, while TBA displayed very little

impact (**Figure 12a**), suggesting that $\text{SO}_4^{\bullet-}$ was formed from the interaction between phosphate and PMS and was likely the primary radical for the degradation of ATZ. The transformation from $\text{SO}_4^{\bullet-}$ to $\bullet\text{OH}$ ($k(\text{SO}_4^{\bullet-}, \text{OH}) = 1.4 \times 10^7 \text{ M}^{-1} \cdot \text{s}^{-1}$) is unlikely due to the significantly faster reaction between $\text{SO}_4^{\bullet-}$ and ATZ ($k(\text{SO}_4^{\bullet-}, \text{ATZ}) = 2.8\text{-}4.2 \times 10^9 \text{ M}^{-1} \cdot \text{s}^{-1}$).^{136,154}

L-his showed the strongest inhibitory effect on ATZ degradation (**Figure 12a-b**). However, while L-his is often considered as a $^1\text{O}_2$ quencher, it can also react rapidly with $\text{SO}_4^{\bullet-}$ ($k(\text{L-his}/\text{SO}_4^{\bullet-}) = 2.5 \times 10^9 \text{ M}^{-1} \cdot \text{s}^{-1}$).¹¹⁴ In fact, the rate constant is two-orders of magnitude higher than that between MeOH and $\text{SO}_4^{\bullet-}$. Furthermore, L-his can rapidly consumes PMS without forming any reactive species (**Figure S12**).¹⁶⁴ Therefore, the quenching study with L-his was inconclusive. To further unravel the role of $^1\text{O}_2$, degradation experiments were conducted using deuterium oxide (D_2O) as a solvent. $^1\text{O}_2$ has a longer life time in D_2O than in water due to its slower decaying rate.⁶⁷ Therefore, ATZ degradation would be more efficient in D_2O if $^1\text{O}_2$ was involved. Interestingly, the decay of ATZ in D_2O was similar to that in H_2O (**Figure 12c**), suggesting that $^1\text{O}_2$ had almost no role in the degradation of ATZ in the PMS system.

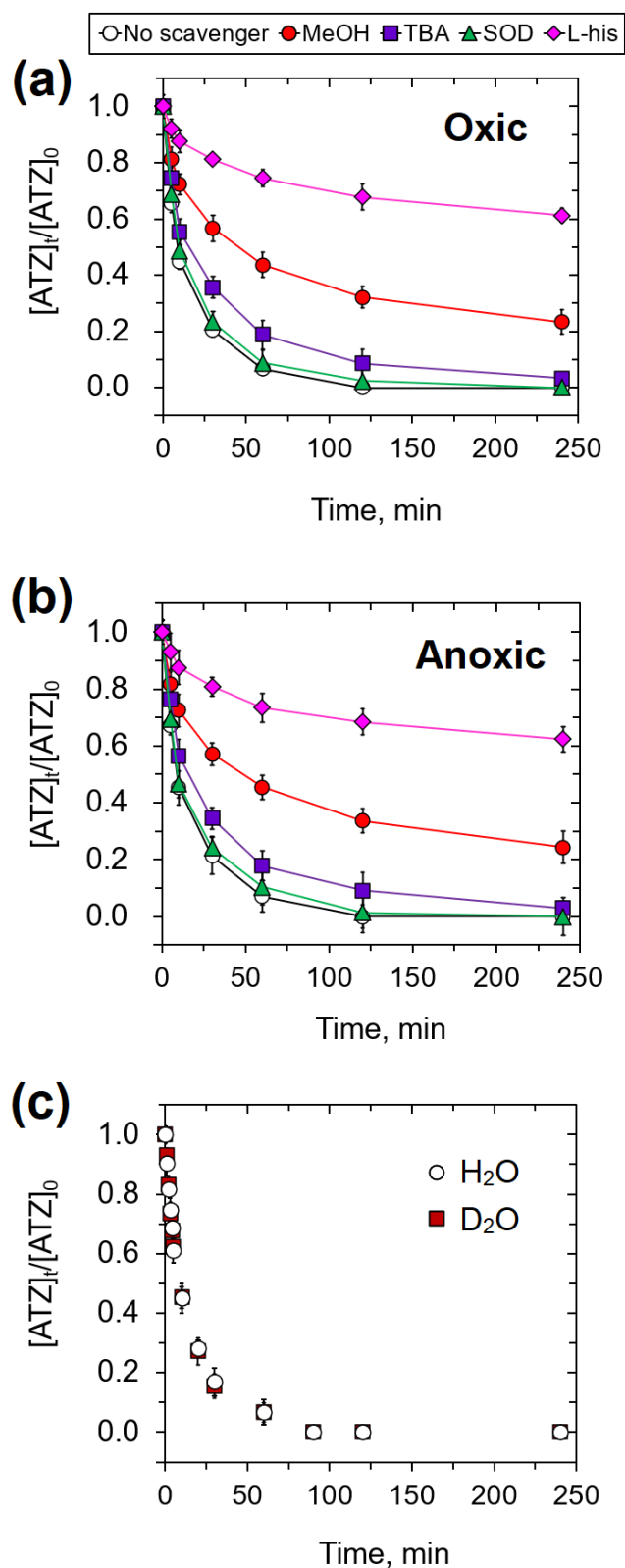


Figure 12. Degradation of ATZ by PMS in the presence of scavengers under (a) oxic and (b) anoxic conditions, and (c) in H_2O and D_2O ($[ATZ]_0 = 10.0 \mu M$; $[PMS]_0 = 5.0 mM$; $[scavengers]_0 = 0.5 M$; $[Na_2HPO_4] = 10.0 mM$; $pH_0 = 7.0$; $T = 25 \text{ }^\circ C$).

Direct measurement of reactive species

EPR spectroscopy was employed to provide further evidence on the formation of reactive species in the degradation of ATZ by PMS. No signal was detected in the PMS system without phosphate (**Figure 13a-c**). However, in the presence of phosphate, the formation of $\text{SO}_4^{\bullet-}$ was confirmed by the signals of DMPO- $\text{SO}_4^{\bullet-}$ adduct, (**Figure 13a**). The 1:2:2:1 peak signal of DMPO- $\bullet\text{OH}$ was also observed but did not explicitly suggest the presence of $\bullet\text{OH}$ because DMPO- $\text{SO}_4^{\bullet-}$ could undergo rapid nucleophilic substitution with H_2O or OH^- to form DMPO- $\bullet\text{OH}$.¹⁶⁸ The signal of DMPO- $\text{SO}_4^{\bullet-}$ confirmed our suggestion that phosphate can catalyze the activation of PMS to produce $\text{SO}_4^{\bullet-}$.

Surprisingly, the signal of DMPO- $\text{O}_2^{\bullet-}$ was also observed (**Figure 13b**), which was unexpected based on the quenching experiments (**Figure 12a-b**). The formation of $\text{O}_2^{\bullet-}$ could be attributed to the reaction between ATZ and $\text{SO}_4^{\bullet-}$. This reaction could generate an ATZ radical cation ($[\text{ATZ}]^{\bullet+}$), which can undergo a series of transformation to form a carbon-centered ATZ radical ($[\text{ATZ}]^{\bullet}$) and be converted to a peroxy adduct ($[\text{ATZ-O-O}^{\bullet}]$) in presence of dissolved O_2 .¹⁵⁴ Subsequently, the $[\text{ATZ-O-O}^{\bullet}]$ adduct can release a $\text{O}_2^{\bullet-}$ or hydroperoxyl radical (HO_2^{\bullet}) and produce 2-chloro-4-amino-6-isopropylamino-1,3,5-triazine (DEA) as a major degradation metabolite via de-ethylation.

The formation of $^1\text{O}_2$ was also explored by the characteristic peak signal of 2,2,6,6-tetramethyl-1-piperidinyloxy (TEMPO), or TEMP- $^1\text{O}_2$ adduct, in the presence of phosphate (**Figure 13c**). The higher signal intensity in D_2O suggested the formation of $^1\text{O}_2$, which could be ascribed to the oxidation of $\text{O}_2^{\bullet-}$ by $\text{SO}_4^{\bullet-}$ (**R7**) and spontaneous disproportionation of $\text{O}_2^{\bullet-}$ (**R10a-b**).^{138,141}

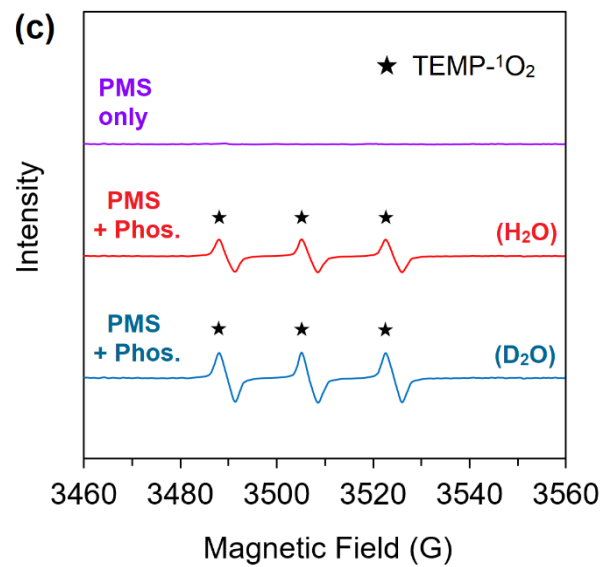
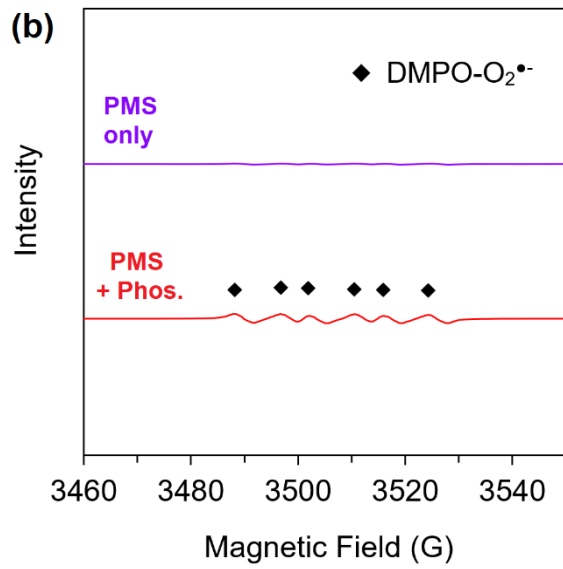
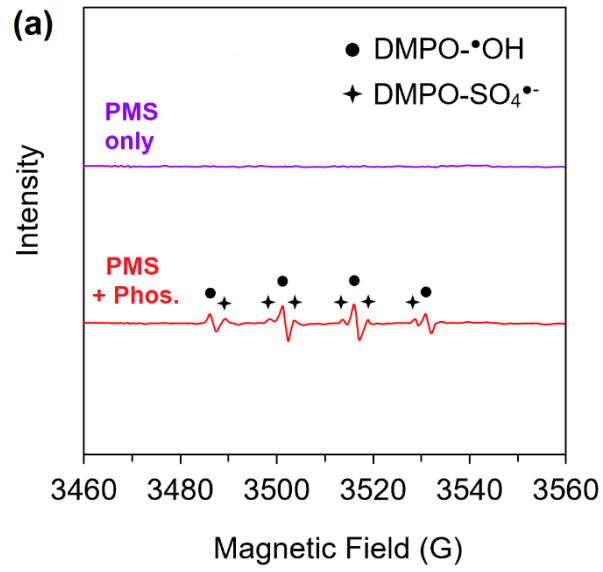


Figure 13. EPR spectra of (a) DMPO-SO₄^{•-}, (b) DMPO-O₂^{•-}, and (c) TEMP-¹O₂ for PMS with and without phosphate buffer (abbreviated as Phos.) ([PMS]₀ = 5.0 mM; [DMPO] = [TEMP] = 50.0 mM; [Na₂HPO₄] = 0 or 10.0 mM; pH₀ = 7.0; T = 25 °C).

No H₂O₂ was detected in the PMS system without phosphate. However, a small peak at 451 nm was observed in presence of phosphate (**Figure S13**), which confirmed the detection of H₂O₂ and the occurrence of Eqs.2a-b.¹²⁵ The self-decay of PMS may also produce ¹O₂. However, this reaction requires complete deprotonation of PMS and is inefficient at neutral pH. Overall, EPR measurements confirmed that PMS was activated to form SO₄^{•-} in the presence of phosphate, and SO₄^{•-} can subsequently generate O₂^{•-} and ¹O₂ via the reaction with ATZ under oxic condition. However, O₂^{•-} and ¹O₂ did not contribute to ATZ degradation in the PMS system, according to the quenching experiments and the rate constants of ATZ degradation in D₂O.

Degradation of ATZ by PMS in absence of phosphate

The degradation of ATZ by PMS in the absence of phosphate is shown in **Figure 14**. Both chemicals decayed faster in the presence of each other, suggesting that ATZ could be directly oxidized by PMS. The result agrees with the literature that PMS can directly oxidize various aromatic compounds without the involvement of reactive species.^{164,186} Putting together, our results showed that the degradation of ATZ by PMS in presence of phosphate was caused by both SO₄^{•-} and direct reaction with PMS. The rate constants of ATZ degradation with and without phosphate buffer (i.e., $4.4 \pm 0.3 \times 10^{-2} \text{ min}^{-1}$ versus $0.97 \pm 0.05 \times 10^{-2} \text{ min}^{-1}$) were applied to **R15-16** to estimate the relative importance of these pathways. The results suggested that SO₄^{•-} and direct PMS oxidation accounted for approximately 78 % and 22% of ATZ

degradation, respectively. This estimate could be further supported by the quenching study (Figure 12a). The $\text{SO}_4^{\bullet-}$ was effectively quenched by MeOH because the reaction rate ($k(\text{MeOH}, \text{SO}_4^{\bullet-}) \cdot [\text{MeOH}] \cdot [\text{SO}_4^{\bullet-}]$) was more than 200 times higher than the reaction rate between $\text{SO}_4^{\bullet-}$ and ATZ ($k(\text{ATZ}, \text{SO}_4^{\bullet-}) \cdot [\text{ATZ}] \cdot [\text{SO}_4^{\bullet-}]$). In the absence of phosphate, the degradation of ATZ is solely through the direction reaction between ATZ and PMS. Based on the rate constants of ATZ degradation with and without MeOH ($1.1 \pm 0.2 \times 10^{-2} \text{ min}^{-1}$ versus $4.4 \pm 0.3 \times 10^{-2} \text{ min}^{-1}$) (Figure 12a), $\text{SO}_4^{\bullet-}$ and direct PMS oxidation accounted for ~75% and ~25% of ATZ degradation, respectively, similar to the earlier estimate.

$$\ln \frac{[\text{ATZ}]}{[\text{ATZ}]_0} = -(k_{\text{SO}_4^{\bullet-}, \text{ATZ}} + k_{\text{PMS}, \text{ATZ}}) \cdot t \quad (\text{R15})$$

$$\frac{k_{\text{SO}_4^{\bullet-}, \text{ATZ}}}{k_{\text{PMS}, \text{ATZ}}} = \frac{\text{Fraction of ATZ degraded by } \text{SO}_4^{\bullet-}}{\text{Fraction of ATZ degraded by PMS}} \quad (\text{R16})$$

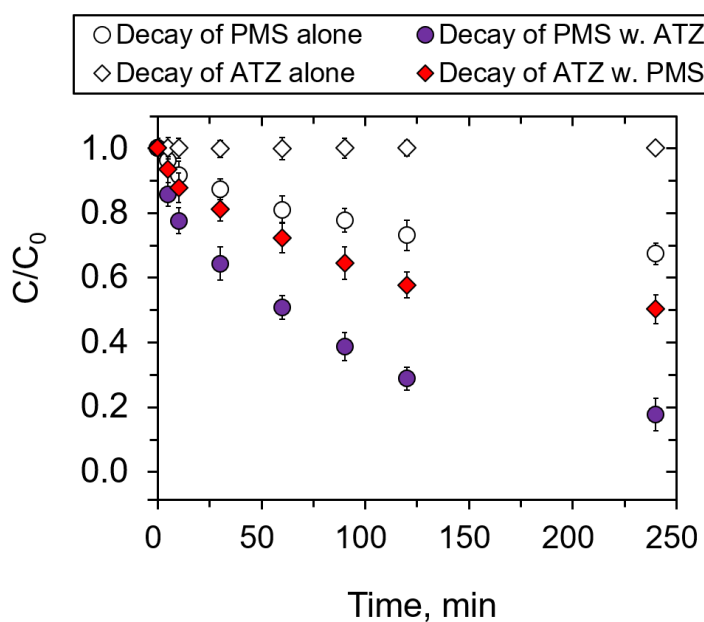


Figure 14. The decay of PMS and ATZ with and without the presence of each other ($[\text{ATZ}]_0 = [\text{PMS}]_0 = 5.0 \text{ mM}$; no phosphate buffer; $\text{pH}_0 = 7.0$; $T = 25 \text{ }^\circ\text{C}$).

Degradation metabolites of ATZ by PMS

To determine the degradation pathways of ATZ by PMS with and without phosphate, the

possible OPs were identified (**Table S4, Figure S14**). Two pathways are proposed based on the OPs. Pathway 1 was likely the only pathway for ATZ degradation in absence of phosphate, while both pathway 1 and 2 were possible in presence of phosphate. In pathway 1, hydroxylation can be initiated by PMS, in which the H-atom in the amino-ethyl side chain can be substituted by an -OH group to form CNIT (m/z 232), consistent with literatures (**Figure 15**).^{186,190} CNIT can be directly oxidized by PMS to produce CDIT (m/z 230) via alkylic-oxidation, and then de-isopropylation can occur on the electron-rich amino-isopropyl group in CDIT to form CDAT (m/z 188). In presence of phosphate, the same three OPs were also detected, but four additional OPs suggested an alternative degradation pathway was triggered by $\text{SO}_4^{\bullet-}$ (**Figure 15**). In pathway 2, H-abstraction as a favorable reaction for $\text{SO}_4^{\bullet-}$ can occur in the amino-ethyl side chain to produce CVIT (m/z 214) and then DEA (m/z 188) via de-ethylation. The highest signal intensity of DEA (**Figure S14**) as a major degradation OP also supported the release of $\text{O}_2^{\bullet-}$ from [ATZ-O-O \bullet] that we proposed. Subsequently, DEA can undergo de-isopropylation and dichlorination-hydroxylation to form DEIA (m/z 146) and DEHA (m/z 170), respectively. Overall, the distinctive OPs and corresponding degradation pathways in the PMS system with and without phosphate agreed well with our conclusion that $\text{SO}_4^{\bullet-}$ and direct PMS oxidation contributed jointly to the degradation of ATZ.

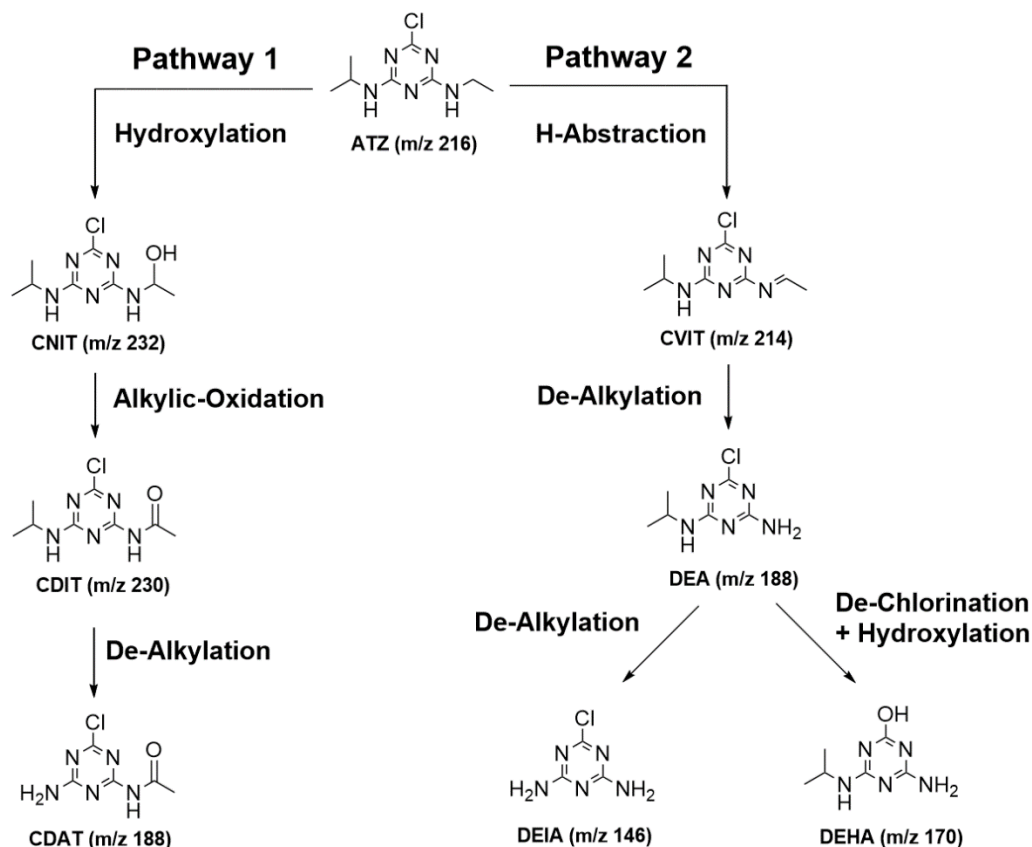


Figure 15. Two proposed degradation pathways of ATZ by PMS with and without phosphate.

Degradation of ATZ by PMS in presence of carbonate

HCO_3^- is the predominant carbonate species at pH 7.0. Similar to phosphate, HCO_3^- markedly promoted the degradation of ATZ by PMS (Figure 16a, Table S5). The values of k_{obs} for the degradation of ATZ increased from $k_{obs} = 0.97 \pm 0.05 \times 10^{-2} \text{ min}^{-1}$ without HCO_3^- to $1.1 \pm 0.2 \times 10^{-2} \text{ min}^{-1}$, $2.2 \pm 0.2 \times 10^{-2} \text{ min}^{-1}$, and $3.2 \pm 0.3 \times 10^{-2} \text{ min}^{-1}$ in presence of 1.0, 5.0, and 10.0 mM of HCO_3^- , respectively (Figure 16a). The final pH of the reaction solutions with 1.0, 5.0, and 10.0 mM HCO_3^- was changed to 7.2, 7.5, and 7.8, respectively, in 240 min. The values of k_{obs} had a nearly linear relationship with HCO_3^- concentration ($r^2 = 0.99$) (Figure S15), suggesting that HCO_3^- was largely responsible for enhancing ATZ degradation. To further examine the role of HCO_3^- , the decay of PMS in presence of 10 mM HCO_3^- was monitored

(Figure 16b). The decay of PMS increased with the increasing concentration of HCO_3^- , indicating that HCO_3^- promoted the degradation of PMS (Figure 16b). However, the decay of PMS in presence of 10 mM phosphate was slightly faster than in presence of 10 mM HCO_3^- (Figure 11b versus Figure 16b). A possible explanation is that HCO_3^- is a weaker nucleophile than phosphate due to the higher electronegativity of C (~2.55) than P (~2.19).

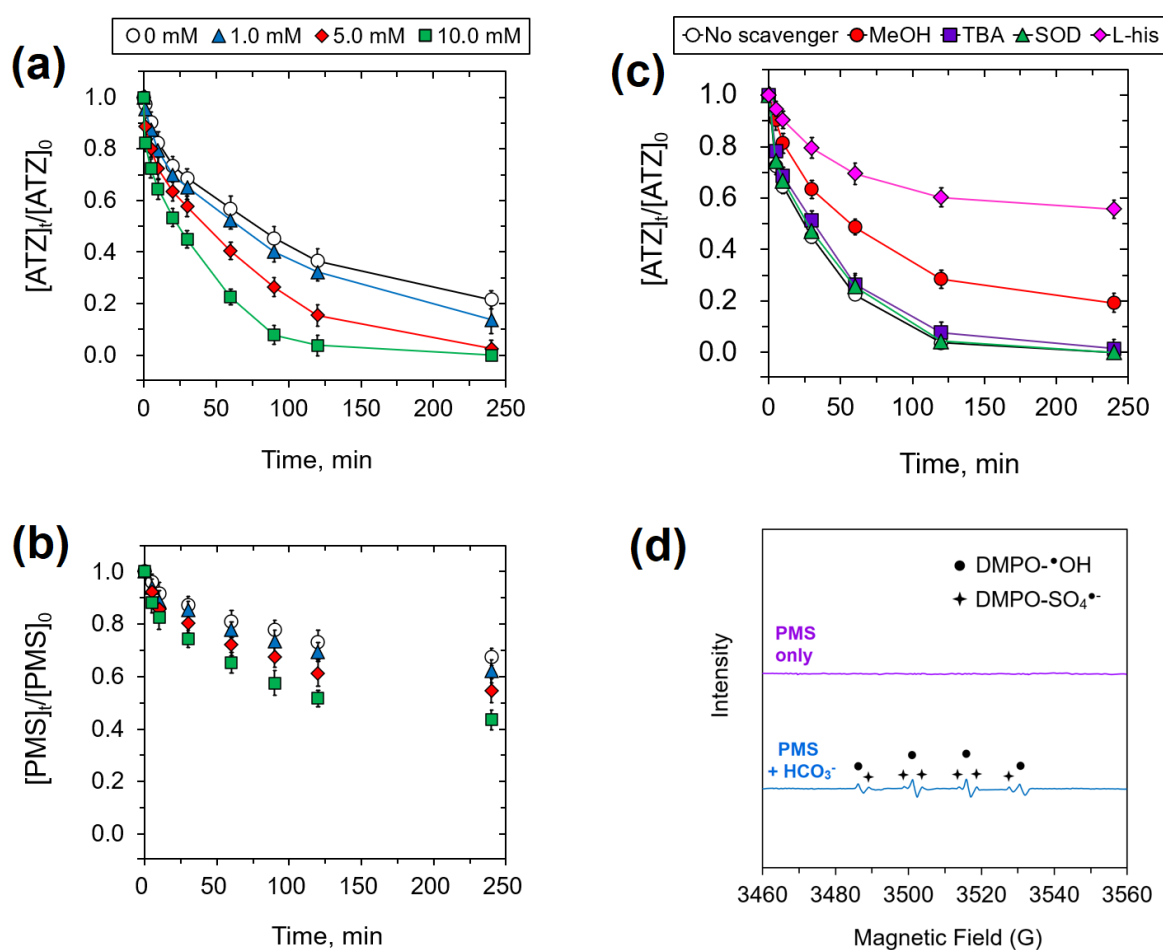


Figure 16. (a) Degradation of ATZ by PMS and (b) decay of PMS in presence of HCO_3^- ($[\text{ATZ}]_0 = 10.0 \mu\text{M}$; $[\text{PMS}]_0 = 5.0 \text{ mM}$; $[\text{HCO}_3^-]_0 = 0, 1.0, 5.0, 10.0 \text{ mM}$; $\text{pH}_0 = 7.0$; $T = 25 \text{ }^\circ\text{C}$); (c) effects of various quenchers on the degradation of ATZ by PMS in presence of 10 mM HCO_3^- ($[\text{ATZ}]_0 = 10.0 \mu\text{M}$; $[\text{PMS}]_0 = 5.0 \text{ mM}$; $[\text{HCO}_3^-]_0 = 10.0 \text{ mM}$; $[\text{quencher}]_0 = 0.5 \text{ M}$; $\text{pH}_0 = 7.0$; $T = 25 \text{ }^\circ\text{C}$), and (d) EPR spectra of $\text{SO}_4^{\bullet-}$ for PMS in presence of HCO_3^- ($[\text{PMS}]_0 = 5.0 \text{ mM}$; $[\text{DMPO}] = 50.0 \text{ mM}$; no phosphate buffer; $[\text{HCO}_3^-]_0 = 10.0 \text{ mM}$; $\text{pH}_0 = 7.0$; $T = 25 \text{ }^\circ\text{C}$).

Quenching experiments were performed in presence of 10 mM HCO_3^- to determine the main reactive species involved. The effect of MeOH and negligible effect of TBA on the

degradation of ATZ suggested the primary role of $\text{SO}_4^{\bullet-}$ (Figure 16c). L-his exhibited the strongest hindering effect (Figure 16c). However, lack of solvent isotope effect in D_2O suggested minimal involvement of $^1\text{O}_2$ in ATZ degradation. (Figure S16).

The results of quenching experiments were confirmed by EPR. No EPR signal was observed in PMS alone (Figure 16d). However, clear signals of $\text{DMPO-SO}_4^{\bullet-}$, $\text{DMPO-}\bullet\text{OH}$, $\text{DMPO-O}_2^{\bullet-}$ and $\text{TEMP-}^1\text{O}_2$ were detected in presence of 10 mM HCO_3^- , indicating similar pathways to produce reactive species as in presence of phosphate (Figure 16d, Figure S17).

Finally, the contribution of direct reaction of PMS with ATZ in the degradation of ATZ in presence of carbonate ion was calculated. The rate constants of ATZ degradation with and without 10 mM HCO_3^- are $2.6 \pm 0.3 \times 10^{-2} \text{ min}^{-1}$ and $0.97 \pm 0.05 \times 10^{-2} \text{ min}^{-1}$, respectively. Based on Eqs.3-4, $\text{SO}_4^{\bullet-}$ and direct PMS oxidation accounted for 63.0% and 37.0% of ATZ degradation in Figure 16a, respectively. Based on the rate constants of ATZ degradation with and without MeOH ($0.79 \pm 0.04 \times 10^{-2} \text{ min}^{-1}$ versus $2.6 \pm 0.3 \times 10^{-2} \text{ min}^{-1}$), $\text{SO}_4^{\bullet-}$ and direct PMS oxidation accounted for 69.8% and 30.2% of ATZ degradation, respectively in degradation of ATZ (Figure 16b), The two estimations agreed reasonably well with each other.

Applicability of PMS to remove ATZ in surface water

To investigate the effectiveness of PMS system in treating actual water, the degradation of ATZ was performed with water collected from Lake Bryan and Brazos River near College Station, TX. The initial pH of the lake water and river water after adding ATZ was 9.22 and 8.44, respectively. The dissolved organic carbon (DOC) in the lake and river water were $15.64 \pm 0.27 \text{ mg/L}$ and $12.95 \pm 0.16 \text{ mg/L}$, respectively.¹⁹¹ Appreciable degradation of ATZ was

observed by PMS in both water (Figure 17, Table S6). The k_{obs} of ATZ degradation was estimated to be $6.3 \pm 0.4 \times 10^{-3} \text{ min}^{-1}$ in lake water and $7.3 \pm 0.5 \times 10^{-3} \text{ min}^{-1}$ in river water. The efficient degradation of ATZ in tested natural waters by PMS suggested the applicability of PMS-enabled degradation of ATZ in actual waters.

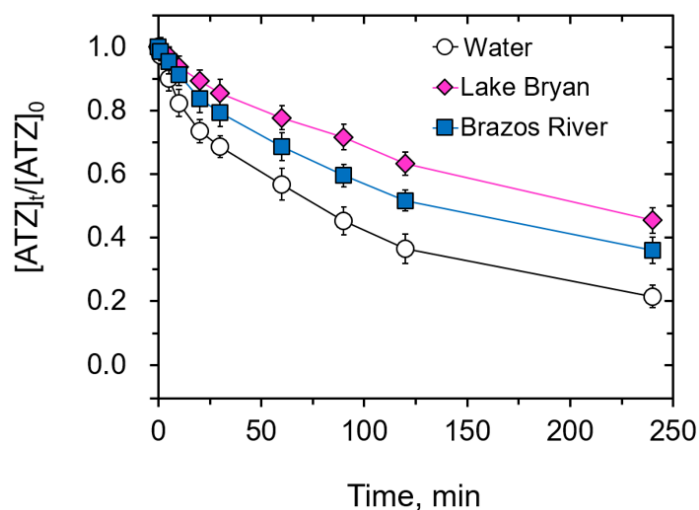


Figure 17. Degradation of ATZ by PMS in water samples of Lake Bryan and Brazos River ($[\text{ATZ}]_0 = 10.0 \mu\text{M}$; $[\text{PMS}]_0 = 5.0 \text{ mM}$; no phosphate buffer; $\text{pH}_0 = 9.22$ and 8.44 for lake water and river water, respectively; $T = 25 \text{ }^\circ\text{C}$).

Conclusions

In conclusion, we demonstrated that both phosphate and carbonate enhanced the degradation of ATZ at pH 7.0 by activating PMS to produce $\text{SO}_4^{\bullet-}$. The reaction between $\text{SO}_4^{\bullet-}$ and ATZ was a dominant pathway for ATZ degradation, whereas the direct oxidation of ATZ by PMS also contributed. In presence of dissolved oxygen, $\text{O}_2^{\bullet-}$ and $^1\text{O}_2$ were also produced via the reaction between $\text{SO}_4^{\bullet-}$ and ATZ, but they had no role in ATZ degradation. Increase in temperature remarkably promoted the degradation of ATZ by PMS. PMS also effectively removed ATZ in lake and river water, exhibiting high potential of PMS in water treatment. We believe that a deeper understanding on the chemistry of PMS itself and its interaction with

oxyanions in natural waters can provide crucial insights for a highly effective PMS system in real application.

CHAPTER IV

SIMULTANEOUS REMOVAL OF NITRATE AND ARSENATE BY VISIBLE LIGHT

ACTIVE ZINC FERRITE/ZERO-VALENT IRON NANOCOMPOSITE

Introduction

Oxyanions such as arsenate, nitrate, chromate, and selenite are among the most toxic contaminants and are serious threats to freshwater supply due to their high mobility.^{192,193} Arsenic (As) is one of the most prevalent toxic elements in drinking water sources. According to WHO, at least 140 million people in 50 countries have been drinking water containing elevated As. Both geogenic (*e.g.* rock weathering) and anthropogenic activities (*e.g.* mining) contributed to the elevated As. Arsenic in the environment exists as a mixture of organic (primarily methylated) and inorganic species, with the dominant species depending on the environmental pH, Eh and other co-present chemical species.¹⁹⁴ Among the As species, inorganic arsenite (As (III)) and arsenate (As (V)) are the most concerned As species because chronic exposure to these species even at trace levels could lead to serious diseases.¹⁹⁵ The maximum contaminant level (MCL) of As in drinking water in the U.S. is currently at 10 µg/L, and discussions are underway to lower it to 5 µg/L to better protect human health. Nitrate (NO₃⁻) is another steadily increasing oxyanion in drinking water sources due to the widespread application of nitrogen-containing fertilizers. Long-term exposure to nitrate may lead to adverse pregnancy outcomes, ovarian and bladder cancer, and methemoglobinemia, or “blue baby syndrome”.¹⁹⁶ The MCL of nitrate in drinking water is 10 mg/L at present. More than 18 states in the U.S. suffer from severe co-contamination of As and nitrate.^{197,198} Co-existence of

these two oxyanions in groundwater was also reported in many Asian countries, raising global health concerns.¹⁹⁹

Even though technologies are available to simultaneously remove As(V) and NO₃⁻ from water, they suffer from a variety of shortcomings. For example, reverse osmosis can effectively remove both oxyanions, but is costly and requires extensive pretreatment. Titanium oxide-based ion exchange resin was also reported to simultaneously remove As(V) and NO₃⁻ from groundwater.²⁰⁰ However, this technology relies on the adsorption of both oxyanions, which is a common but less effective strategy. Anaerobic reactors containing iron and/or sulfate reducing bacteria were shown to simultaneously catalyze the NO₃⁻ reduction and As precipitation through the formation of insoluble As sulfide minerals such as orpiment (As₂S₃).²⁰¹ However, the cost for the anaerobic reactor is high due to the need for external carbon source. Therefore, the need to develop an energy-efficient and cost-effective technology to simultaneously remove both oxyanions remains high.

Photocatalysis is an appealing treatment technology because of its low cost, easy operation, and absence of hazardous byproducts.²⁰²⁻²⁰⁴ Upon irradiation, an electron in the valence band (VB) absorbs light and is promoted to the conduction band (CB), creating a free electron (e_{CB}^-) and a positive hole (h_{VB}^+). The electron-hole pair could migrate to the surface of the photocatalyst and produce free radicals.^{83,84} Titanium and zinc oxide (TiO₂ and ZnO) nanoparticles are two widely explored photocatalysts.²⁰⁵ However, both semiconductors suffer from several key drawbacks including: (1) low quantum efficiency due to the fast recombination of electron-hole pairs, and (2) narrow absorption region due to relatively wide bandgaps ($E_g = 3.2-3.37\text{eV}$).^{83,84,204}

Spinel ferrites with the general molecular formula of MFe_2O_4 is a group of n-type semiconductors with a narrow bandgap ($E_g = 1.8\text{-}2.1\text{ eV}$), where M is a divalent transition metal (e.g. Co, Mn, Ni, Cu, Zn etc.) substituted into the Fe_2O_3 lattice.^{206,207} Among the common ferrites, zinc ferrite displays one of the narrowest bandgaps ($\sim 1.92\text{ eV}$) and high stability.^{208,209} Zinc ferrite ($ZnFe_2O_4$ or $ZnO \cdot Fe_2O_3$) can be considered as a cubic close-packed (or face-centered cubic) lattice formed by O, with octahedral sites occupied by Fe and tetrahedral sites substituted by Zn.²¹⁰ Zinc ferrite is stable in weak acidic and alkaline conditions.²¹¹ In addition to its well-known magnetic property,²¹² previous studies on $ZnFe_2O_4$ also showed its high removal efficiency for As and many organic compounds.^{210,213,214} Zinc ferrite exhibited higher adsorption capacity towards As(V) (7.68 mg/g) than other iron oxides because of the increased surface hydroxyl groups caused by Zn^{2+} doping.²¹⁰ Porous zinc ferrite nanorod could effectively produce H_2 through photocatalytic reduction and remain photostable with methanol as a hole scavenger.²¹⁵ The large adsorption capacity and high activity of photocatalytic reduction suggest that $ZnFe_2O_4$ can be a strong candidate for the simultaneous removal of As and NO_3^- .

Introduction of dopants and construction of heterojunction photocatalysts are common approaches to enhance photocatalytic activity. Dopant introduction can further reduce the bandgap of ferrites and enhances their light harvesting, whereas heterojunction photocatalysis can strengthen charge separation.^{216,217} Materials commonly used to construct a heterojunction with ferrites are either semiconductors that allow a p-n type charge transfer or supporting materials with abundant π -conjugations that facilitate fast migration of photo-generated electrons from ferrites.^{211,218,219} The photocurrent generated by a composite electrode of Fe_2O_3

cores and ZnFe₂O₄ thin films was significantly higher than that by α-Fe₂O₃ alone.²¹¹ By combining ZnFe₂O₄ and α-Fe₂O₃ as a composite material, a more effective separation of photogenerated electron-hole pairs at the α-Fe₂O₃/ZnFe₂O₄ interface was achieved via a p-n type heterojunction charge transfer.^{211,220} In another study, a ZnFe₂O₄:Fe₂O₃ nanocomposite photoelectrode showed a six-fold increase of the photocurrent compared to pure ZnFe₂O₄ and Fe₂O₃, and a donor density ($N_d \sim 10^{17} \text{ cm}^{-3}$) that was an order of magnitude higher than ZnFe₂O₄, possibly due to the improved charge transfer.²²¹ Despite of the outstanding photocatalytic properties of ferrites, their potential applications in water remediation have not been explored until recently.^{219,222} Simultaneous removal of oxyanions by ferrite-based materials is very scarce.

Zero-valent Iron (nZVI) has been a popular material for the removal of nitrate and arsenic.^{223,224} Since both ZnFe₂O₄ and nZVI offer attractive advantages in water treatment and nZVI may function as a steady electron source, a nanocomposite synergistically integrating the advantages of both materials could result in more effective treatment technologies. In addition, the magnetic properties of ZnFe₂O₄ and nZVI could allow easy separation and regeneration of the nanocomposite after use.

Hereby, we report a novel zinc ferrite/nano-sized zero-valent iron (ZnFe₂O₄/nZVI) nanocomposite with superior performance for the simultaneous removal of NO₃⁻ and As(V). The primary objectives of this study were to (1) synthesize and fully characterize the ZnFe₂O₄/nZVI nanocomposite and unveil the underlying mechanisms for its enhanced removal of NO₃⁻ and As(V) from water in comparison to ZnO; and (2) determine the impact of various environmental parameters on the performance of ZnFe₂O₄/nZVI.

Experimental Section

Chemicals and Materials

Zinc oxide ($\geq 99.0\%$), sodium arsenate dibasic heptahydrate ($\geq 98.0\%$), sodium nitrate ($\geq 99.0\%$), potassium phosphate dibasic ($\geq 99.0\%$) and silver nitrate ($\geq 99.0\%$) were purchased from Sigma-Aldrich (St. Louis, USA). Ferric chloride tetrahydrate (99%), sulfuric acid (95.0-98.0 w/w%), formic acid ($\geq 99.0\%$), iso-propanol (HPLC grade) and p-benzoquinone ($\geq 98\%$) were purchased from Thermo Fisher Scientific (Waltham, USA). Sodium borohydride ($> 95.0\%$) and sodium chloride ($\geq 99.5\%$) were purchased from TCI America (Portland, USA). Calcium chloride anhydrous (96% extra pure) was purchased from ACROS Organics (Waltham, USA). Suwannee River NOM (2R101N) was purchased from International Humic Substances Society (IHSS). Hach Nitrate TNTplus test vials were purchased from Hach (Loveland, USA). Purified nitrogen gas (industrial grade) was purchased from AirGas (Radnor, USA). All chemicals were used as received. All aqueous solutions were prepared using ultrapure water (Barnstead Nanopure II system). A simulated sunlight lamp (GLBULBM1000 metal halide bulb, 1000 W, 92,000 lm) was purchased from iPower and used as the light source.

Synthesis of $\text{ZnFe}_2\text{O}_4/\text{nZVI}$ Nanocomposite

ZnO powder was dispersed in ultrapure water and sonicated for 30 min at 20k Hz to achieve a homogeneous dispersion. To synthesize the $\text{ZnFe}_2\text{O}_4/\text{nZVI}$ nanocomposite, sonicated ZnO dispersion was well-mixed with FeCl_3 solution, followed by a liquid-phase reduction method with NaBH_4 as the reductant as previously reported.²²⁵ The entire reaction was conducted under an anoxic condition with nitrogen gas constant purging. Since optimal loading

for metallic doping onto nZVI was found to be <10 w/w%,²²⁶ the weight ratio of Zn:Fe for the synthesis of ZnFe₂O₄/nZVI nanocomposite used in this study was around 7% (molar ratio 1:10). The produced ZnFe₂O₄/nZVI nanoparticles were collected by centrifuging the reaction mixture at 10,000 rpm for 10 min. The collected nanoparticles were washed by de-oxygenated ultrapure water and ethanol, dried in an oven at 60 °C for 10 min, and then stored in sealed glass vials.

Characterization of ZnFe₂O₄/nZVI Nanocomposite

The size and shape of ZnO and ZnFe₂O₄/nZVI nano-structures were examined using a Hitachi S-4800 field-emission scanning electron microscopy (FE-SEM) equipped with an X-ray energy dispersive spectroscopy (EDS). The as-received ZnO powder and the synthesized ZnFe₂O₄/nZVI materials were examined by X-ray diffraction (XRD) θ -2 θ scans in a Bruker D8 Advance diffractometer using Cu K α radiation operating at 40 kV and 40 mA. The detailed microstructural analysis was conducted using a Hitachi H-9500 high-resolution transmission electron microscope (HR-TEM) operated at 300 kV with a point resolution of 0.18 nm and lattice resolution of 0.1 nm. For the ZnFe₂O₄/nZVI nanocomposite, the crystal structure was determined using selected-area electron diffraction (SAED) and nano-beam electron diffraction (NBD), and the unique core-shell structure was studied using HR-TEM. The elemental composition of the nanocomposite was determined by EDS. The chemical compositions of the ZnO powder and the synthesized ZnFe₂O₄/nZVI materials were investigated by X-ray photoelectron spectroscopy (XPS) conducted in a Perkin-Elmer Phi 560 ESCA/SAM system using an Al K α excitation source (1484.6 eV). Survey scans were conducted in the 0 - 1200 eV range using an increment of 0.5 eV and a pass energy of 100 eV and high-resolution scans were

conducted using an increment of 0.2 eV and a pass energy of 50 eV. The UV-Vis diffuse reflectance spectra (DRS) of ZnO and ZnFe₂O₄/nZVI nanocomposite were obtained using a UV-Vis-NIR spectrophotometer (Hitachi U-4100). The photoluminescence (PL) spectra were obtained using a spectrofluorometer (Horiba FluoroMax-4). The Brunauer-Emmett-Teller (BET) surface area of the nanocomposite was determined by N₂ adsorption-desorption isotherm measurements at 77 K on a Micromeritics ASAP 2020 high-performance adsorption analyzer (Norcross, USA). The zeta potential and hydrodynamic size of ZnO and ZnFe₂O₄/nZVI composite at 100 mg/L and between pH 2.0-11.5 were measured using a dynamic light scattering (DLS) instrument (Malvern Zetasizer Nano-ZS90) (Figure S18). Zeta potential of ZnO at pH<4.0 was not measured due to its rapid dissolution. The zero-point-charge (pH_{ZPC}) for ZnO and ZnFe₂O₄/nZVI were around 8.5 and 6.3, respectively (Figure S18a). The hydrodynamic size of ZnFe₂O₄/nZVI ranged from 1000 to 2500 nm over the pH range of 2.0 - 11.5 (Figure S18b).

Simultaneous Removal of NO₃⁻ and As(V)

The experiment was conducted in 50 ml transparent glass vials with caps. Nitrate and arsenate were introduced as NaNO₃ and Na₂HAsO₄·7H₂O. The initial concentrations for NO₃⁻ and As(V) were 50 mg/L and 100 µg/L respectively, and the catalyst loading was 0.2 g/L. Each vessel was purged with N₂ and then sealed to maintain an anoxic condition. Initial pH in each vessel was controlled at pH 7.0. Comparative experiments were performed both under visible light and in dark for ZnO and ZnFe₂O₄/nZVI. A UV filter film was purchased from Edmund Optics (Barrington, USA) to block the UV light emitted from the sunlight lamp. Formic acid

(3.5 mM) was added as a h^+ scavenger to inhibit the rapid recombination of e^-/h^+ pairs (Details on next section). All vessels were shaken in an incubator shaker (New Brunswick Excella E24, Eppendorf) at 300 rpm for 12 hours at 25°C. At termination, the mixture in each vessel was centrifuged at 10,000 rpm for 10 min. To measure the concentrations of NO_3^- in the supernatant, 2.0 mL of samples were collected at various time ($t = 0, 5, 10, 30, 60, 90, 120$ min) and measured using Hach Nitrate TNTplus test vials in a UV/Vis spectrophotometer (Lambda 35, PerkinElmer). To measure the concentrations of total As, 1.0 mL of sample was extracted at various time ($t = 0, 30, 60, 120, 240, 360, 480, 720$ min) and centrifuged at 10,000 rpm to separate adsorbents from the solution and to collect the supernatants at each sampling point. The total As concentration in the supernatants was measured using an inductively coupled plasma-mass spectrometry (ICP-MS) (NexIon 300D, PerkinElmer). The mechanism of As adsorption on the nanocomposite was probed using an attenuated total reflection-Fourier transform infrared (ATR-FTIR) spectroscopy (PerkinElmer Spectrum 100).

Identifying the Main Reactive Species

In order to identify the main reactive species in the simultaneous removal of NO_3^- and As(V), formic acid (FA), silver nitrate ($AgNO_3$), iso-propanol (IPA), and p-benzoquinone (PBQ) were used to scavenge the holes (h^+), electrons (e^-), hydroxyl radical ($\bullet OH$), and superoxide radical ($O_2^{\bullet -}$), respectively. FA was added as a h^+ scavenger in all groups except for the control group. The remaining concentrations of NO_3^- and As(V) were measured at $t = 120$ min and 720 min, respectively.

Adsorption Kinetics and Isotherms of As(V)

The results of As(V) removal by ZnO and ZnFe₂O₄/nZVI were fitted into both pseudo-first and -second order adsorption kinetic models. The pseudo-first-order kinetics model was expressed in **R17**:

$$q_t = q_e \cdot [1 - \exp(-k_{ads} \cdot t)] \quad (\text{R17})$$

where q_t is the amount of adsorbate adsorbed on the adsorbent at time t ($\text{mg} \cdot \text{g}^{-1}$); q_e is the equilibrium adsorption capacity ($\text{mg} \cdot \text{g}^{-1}$); k_{ads} is the adsorption rate constant (min^{-1}). The equation for pseudo-second-order kinetics and the initial adsorption rate h ($\text{mg} \cdot \text{g}^{-1} \cdot \text{min}^{-1}$) was given in **R18-19**:

$$\frac{t}{q_t} = \frac{1}{k_{ads} \cdot q_e^2} + \frac{1}{q_e} \cdot t \quad (\text{R18})$$

$$h = k_{ads} \cdot q_e^2 \quad (\text{R19})$$

Adsorption isotherms of As on ZnO and ZnFe₂O₄/nZVI were conducted at a similar condition. The initial concentrations of As(V) varied from 20, 50, 200, 500, 1000 and 2000 $\mu\text{g/L}$. All vials were stirred at 360 rpm for 24 hours to reach equilibrium. The same method was used to measure As concentrations in the supernatants. The results were fitted into the Langmuir and Freundlich isotherm models. Both isotherms are commonly used to describe adsorption²²⁷⁻²³⁰ and are shown in **R20-21**, respectively.

$$q_e = \frac{q_{max} \cdot C_e \cdot K_L}{C_e \cdot K_L + 1} \quad (\text{R20})$$

$$q_e = C_e^n \cdot K_F \quad (\text{R21})$$

where q_{max} is the maximum adsorption capacity ($\text{mg} \cdot \text{g}^{-1}$); C_e is the equilibrium concentration of As ($\text{mg} \cdot \text{L}^{-1}$); K_L is the Langmuir constant ($\text{L} \cdot \text{mg}^{-1}$); n and K_F are the Freundlich constants ($\text{mg} \cdot \text{L}^{-1} \cdot (\text{L} \cdot \text{mg}^{-1})^n$); and C_0 is the initial As concentration ($\text{mg} \cdot \text{L}^{-1}$). In

addition, a dimensionless separation factor R_L was calculated for the Langmuir isotherm using **R22**. For an adsorption that agrees with the fundamental assumptions of Langmuir isotherm, R_L normally falls between 0 and 1.

$$R_L = \frac{1}{1+K_L \cdot C_0} \quad (\mathbf{R22})$$

Effect of pH

The effect of pH on the removal of the two oxyanions was investigated by titrating the solution with H_2SO_4 (0.005M) or $NaOH$ (0.01M) to an initial pH of 3.0, 5.0, 7.0, 9.0, and 11.0. Removal by ZnO was not measured at pH 3.0 due to the rapid dissolution of ZnO at this pH. The stability of $ZnFe_2O_4/nZVI$ was determined by measuring the concentrations of Zn^{2+} and the summation of Fe^{3+} and Fe^{2+} in the supernatant using an ICP-MS (NexIon 300D, PerkinElmer).

Effects of Ionic Strength (IS), Phosphate (PO_4^{3-}) and Natural Organic Matters (NOMs)

The impact of IS on the removal of NO_3^- at pH 7.0 was investigated. IS was controlled at 0, 50, 100, 150, and 200 mM, respectively, by adding $NaCl$ or $CaCl_2$. These values were selected to mimic water bodies from fresh water to inland brackish water. The initial IS in the solution was < 0.5 mM before adding $NaCl$ and $CaCl_2$ and thus neglected. The effect of phosphate was assessed by adding K_2HPO_4 at the level of 0, 1.0 and 10.0 mg/L. The initial pH of the solutions was controlled at 7.0. Suwannee River NOM (SRNOM) was used to investigate the effect of NOMs on the performance of $ZnFe_2O_4/nZVI$ nanocomposite. The weight percentages of C and O in SRNOM are 50.7% and 41.5% respectively. Most of the carbon

derives from the carboxyl groups, aromatic rings, and aliphatic chains, along with small fractions of phenolic, carbonyl, and acetal groups. The $pK_{a,s}$ of carboxyl and phenolic group in SRNOM are 4.16 and 9.99, respectively (<http://humic-substances.org/#products>). Concentration of SRNOM in each vessel was controlled at 10.0 and 35.5 mg/L, or 5.0 and 18.0 mg/L as C respectively.

Data Analysis

One-way analysis of variance (ANOVA) was used to determine the statistical differences among the NO_3^- and As(V) removal by ZnO and $\text{ZnFe}_2\text{O}_4/\text{nZVI}$ in presence of different scavengers. Different letters in the figures indicate significant differences between the rate constants ($p \leq 0.05$) according to one-way ANOVA followed by Tukey's test.

Results and Discussion

Characterizations of $\text{ZnFe}_2\text{O}_4/\text{nZVI}$ Nanocomposite

The as-received ZnO and synthesized $\text{ZnFe}_2\text{O}_4/\text{nZVI}$ were then examined using θ -2 θ XRD analysis (**Figure 18**). The spectra of as-received ZnO powders exhibit sharp and strong peaks perfectly matching the diffractions of zincite in the powder diffraction file (PDF#36-1451, hexagonal, $a = 3.25 \text{ \AA}$, $c = 5.207 \text{ \AA}$, $P6_3mc$) (International Centre for Diffraction Data (ICDD), PDF-4 Database Sets, Pennsylvania, USA 2020). In contrast, the XRD spectra of synthesized $\text{ZnFe}_2\text{O}_4/\text{nZVI}$ present only a few faint peaks corresponding to the residue trace of ZnO. No other visible peaks were detected indicating that the synthesized $\text{ZnFe}_2\text{O}_4/\text{nZVI}$ materials possess a rather amorphous structure or very small nanocrystalline structures that were not

detectable by XRD.

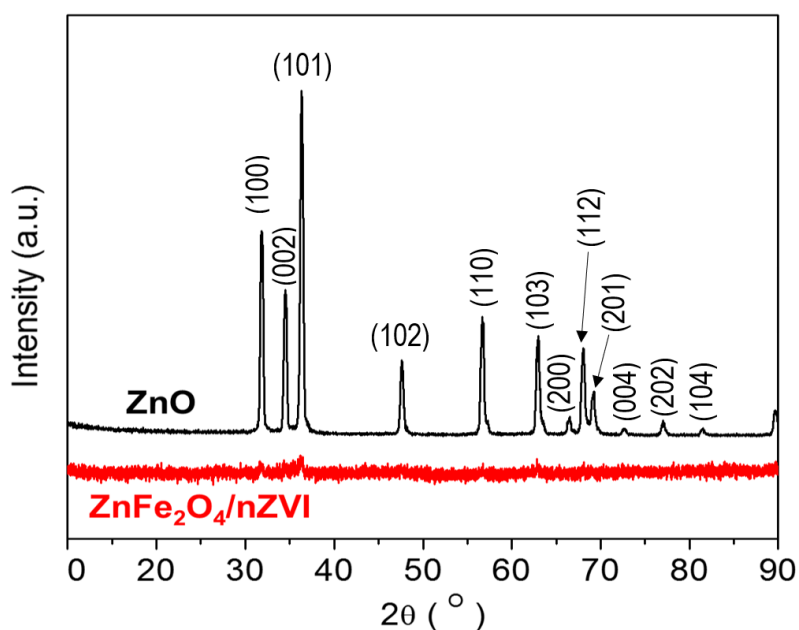


Figure 18. XRD spectra of as-received ZnO nanoparticles (black) and synthesized ZnFe₂O₄/nZVI nanocomposite (red).

Figure 19a presents a SEM image of the as-received ZnO nanoparticles exhibiting typical well-formed polyhedral single crystal structures with smooth surfaces jointed via sharp edges. The ZnO particles fell in the size range of ~60 to 290 nm. **Figure 19b** shows a SEM image of the synthesized ZnFe₂O₄/nZVI nanocomposite presenting a totally different morphology: beaded chain structures are formed by interlinked spherical nanoparticles (**area X**), and the chain structures are wrapped with heavily crumpled skin layers (**area Y**). **Figure 19c** is a high magnification SEM image that clearly presents this unique morphology. The nanoparticles size in the beaded chain structures is about 80 nm. The total diameter of beaded chains plus surrounding skin layers is about 200 nm.

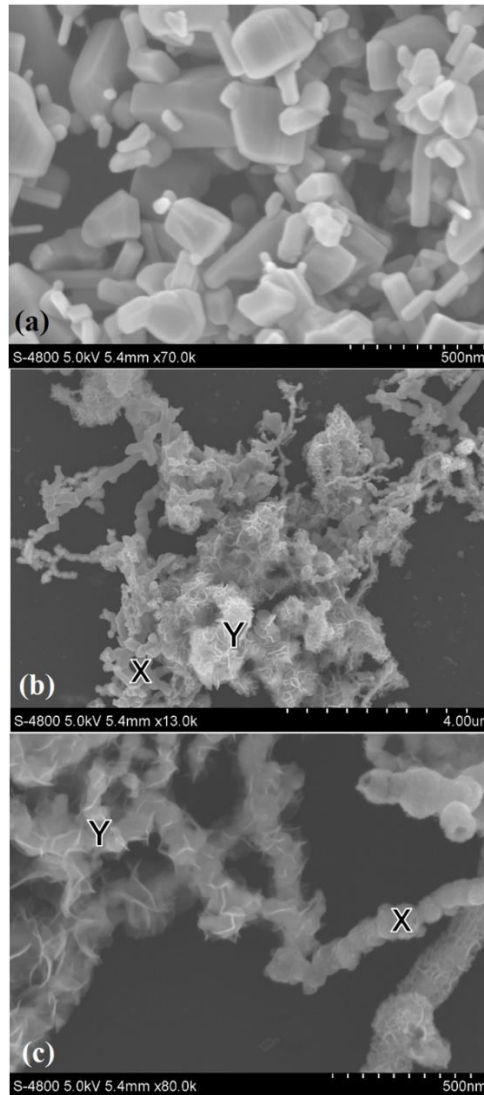


Figure 19. SEM images of as-received ZnO nanoparticles (a) and synthesized ZnFe₂O₄/nZVI nanocomposite (b-c).

Figure 20a is a TEM image of the as-received ZnO powder, confirming the particle size of ZnO from several tens to a couple of hundreds nm. EDS spectrum consisting of Zn and O only (C and Cu are from TEM grid) confirms its purity (**Figure 20b**). **Figure 20c** is a SAED pattern taken from the ZnO powder presenting a typical polycrystalline pattern of ZnO nanoparticles. The inner diffraction rings/spots 1, 2, 3, 4, 5, 6 and 7 have a lattice spacing of 2.8 Å, 2.6 Å, 2.5 Å, 1.9 Å, 1.6 Å, 1.5 Å and 1.4 Å corresponding to the (100), (002), (101), (102), (110), (103) and (200) of ZnO (PDF#65-3411, $a = 3.25 \text{ \AA}$, $c = 5.207 \text{ \AA}$, P6₃/mc) (ICDD

2020), respectively. **Figure 20d** is a TEM image of the synthesized $\text{ZnFe}_2\text{O}_4/\text{nZVI}$ nanocomposite presenting totally different microstructural characteristics. Spherical nanoparticles with a diameter of about 70 nm were interlinked together to form beaded chain structures. Some chain structures were encapsulated with light skin layers. The skin layers have a thickness of ~ 80 nm. EDS analysis revealed that the nanoparticle cores in **Figure 20d** are pure Fe, as shown in **Figure 20e** (C and Cu are scattered from the TEM grid). **Figure 20f** is a SAED pattern taken from the beaded chain structures, some of which were covered by skin structures presenting diffraction ring 1, 2, 3 and 4 with a lattice spacing of 2.48 Å, 2.04 Å, 1.43 Å and 1.16 Å, respectively. The diffraction ring 2, 3 and 4 corresponds to the (110), (200) and (211) of body-centered cubic (bcc) Fe (PDF#06-0696, $a = 2.866$ Å, $\text{Im}\bar{3}\text{m}$) (ICDD 2020). The diffraction ring 1 can be identified as the (311) of ZnFe_2O_4 (PDF#65-3111, $a = 8.433$ Å, $\text{Fd}\bar{m}\bar{3}\text{m}$) (ICDD 2020). **Figure 20g** is a TEM image of a segment of beaded chains covered by multiple skin layers. **Figure 20h** is an EDS spectrum taken from the skin layer in **Figure 20g**, confirming the presence of Fe, Zn and O and the formation of Fe-Zn-O compound. SAED pattern (**Figure 20i**) taken from the skin layers presenting diffused diffraction ring 1, 2 and 3 with a lattice spacing of 2.5 Å, 2.1 Å and 1.5 Å, which can be identified as (311), (400) and (440) of ZnFe_2O_4 , respectively.

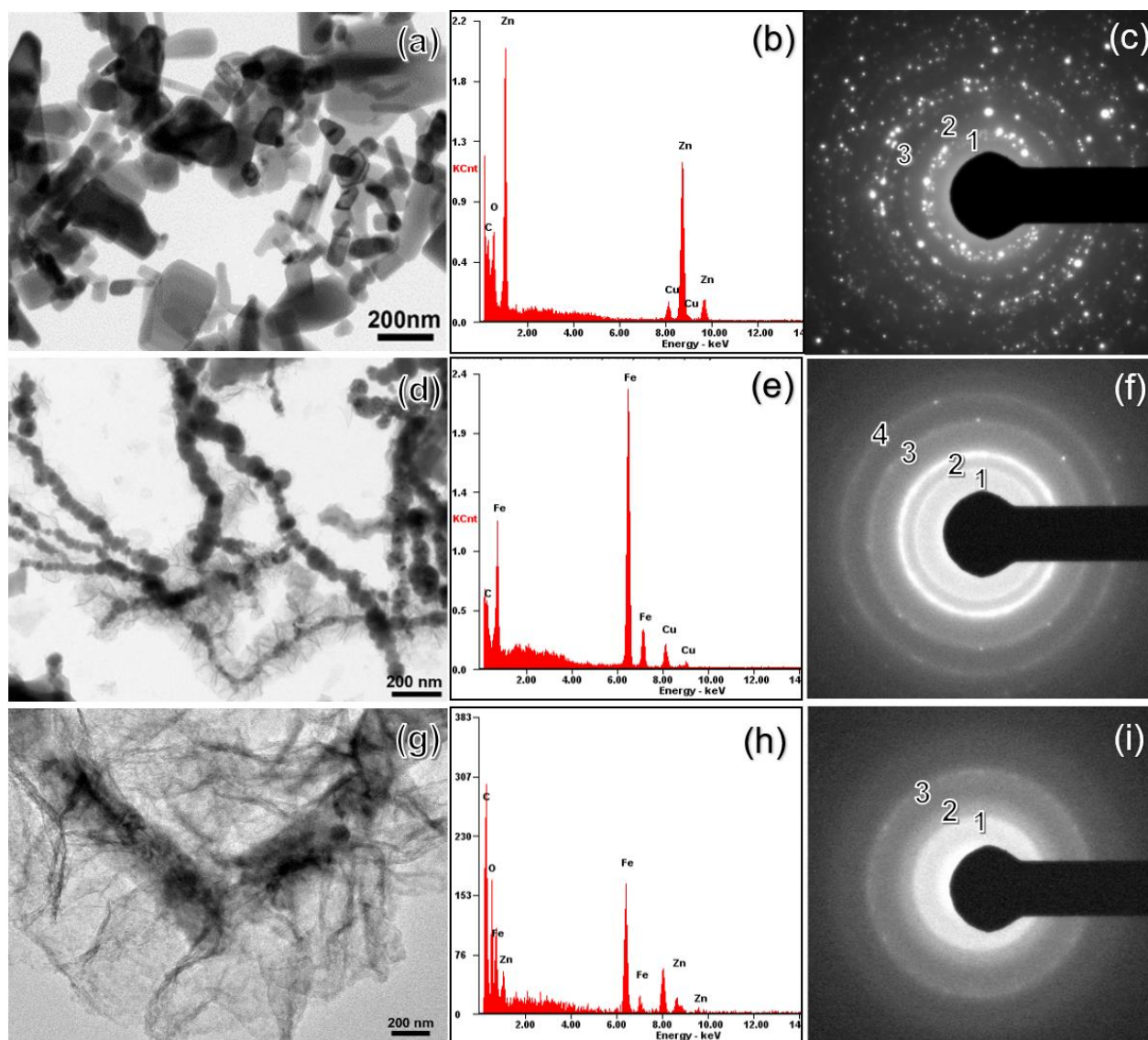


Figure 20. TEM image, EDS and SAED patterns of the as-received ZnO nanoparticles (a-c), (d-f) ZnFe₂O₄/nZVI chain-and-bead structures, and ZnFe₂O₄ skin layer structures (g-i).

Figure 21a shows a HRTEM image of a ZnO nanoparticle exhibit atomically clean surface structure with atomic planes and steps. **Figure 21b** is an amplified TEM image of the ZnFe₂O₄/nZVI materials displaying beaded chain structures that are attached by thin skin layers. The beads on the chains are pure metallic iron as determined by EDS and SAED. The chain structures were covered by a thin shell with a typical thickness of ~3 nm. **Figure 21c** is a zoomed-in TEM image of particles with core-shell structure in a chain, and **Figure 21d** is a

nanobeam diffraction pattern taken from the particle “i” in **Figure 21c**, presenting $[1\bar{1}0]$ zone diffraction pattern of bcc Fe, which further confirms the crystal structure of the Fe cores. **Figure 21e** shows a TEM image of core-shelled structure wrapped by thin skin layers. The shell and the thin skin layers are both ZnFe_2O_4 compound as determined by EDS and SAED. **Figure 21f** presents a HRTEM image of the core-shell particle “i” in **Figure 21c**, in which the lattices fringe in the core region correspond to the (110) of Fe and the shell presents a near amorphous or semi-crystalline structure. **Figure 21g** shows a HRTEM image presenting atomic structure of a core-shell-skins. The lattice fringes in the skin have a spacing of ~ 2.6 Å, closely corresponds to the (311) of ZnFe_2O_4 . The thin skin layers attached to the shell presents a layered structure with a lattice spacing of 2.93 Å, which closely corresponds to the (220) of ZnFe_2O_4 .

The above TEM studies show that the synthesized $\text{ZnFe}_2\text{O}_4/\text{nZVI}$ nanocomposite possesses a unique core-shell-skin structure, in which the metallic Fe^0 nanoparticles with a size of ~ 70 nm interlink with each other to form beaded long chains, which are coated by ZnFe_2O_4 shells with a thickness of ~ 3 nm and further wrapped by heavily crumpled ZnFe_2O_4 thin skin layers with a thickness of $\sim 1-2$ nm.

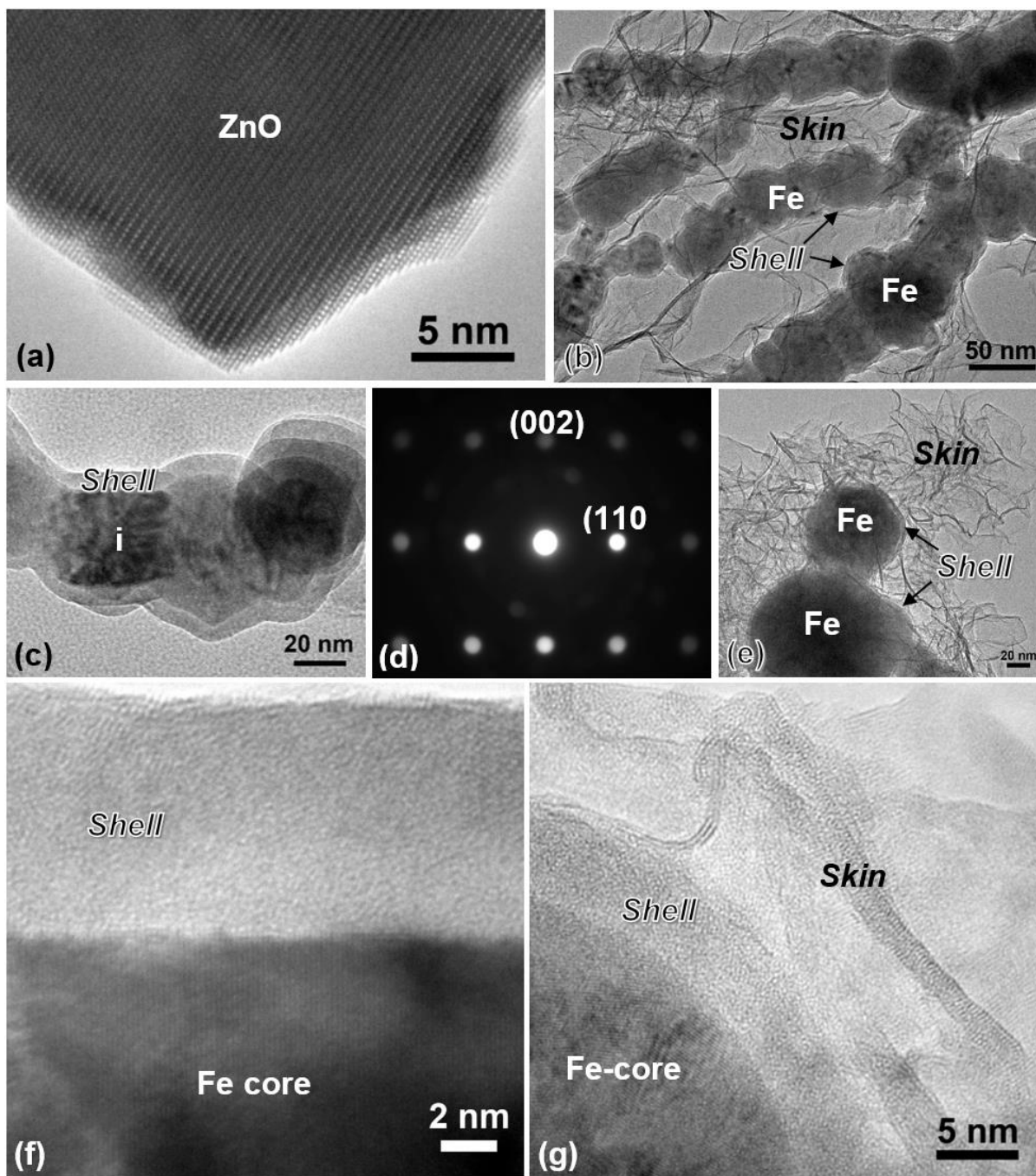


Figure 21. (a) HRTEM of a ZnO particle; (b-g) TEM results for sample of nZVI; (b) TEM image of core-shelled chain structures of ZnFe₂O₄/nZVI composite; (c) zoomed-in TEM image of core-shell particle in a chain structure; (d) NBD pattern taken from particle i in (c); (e) TEM image of an area with core, shell and skins; (f) HR-TEM image a core-shell structure; (g) HR-TEM image of core-shell-skins.

Figure 22a presents XPS survey spectra of as-received ZnO powder and the synthesized ZnFe₂O₄/nZVI nanocomposite before (ZFO/nZVI bt) and after (ZFO/nZVI at) treatment of

contaminants. The spectrum of the ZnO powder shows the presence of Zn and O. The C 1s peak was likely from the carbon absorption on the sample surface from the ambient atmosphere. The spectra of ZFO/nZVI bt revealed the presence of Fe, Zn, O and C. The intensity of Zn peaks on the spectra was significantly reduced compared with the spectrum of ZnO, clearly indicating that the synthesized ZnFe₂O₄/nZVI possesses a quite different chemical composition from ZnO.

Figure 22b-c show high-resolution spectra of the Zn 2p and O 1s peaks collected from the tested materials. The charge shifts of the binding energies (BEs) of the peaks were calibrated using C 1s BE of 284 eV. The Zn 2p_{3/2} and 2p_{1/2} peaks of ZnO powder show binding energies at 1020.8 and 1043.8 eV, respectively, that are very close to those reported in the literature.²³¹ The Zn 2p_{3/2} and 2p_{1/2} peaks for ZnFe₂O₄/nZVI bt shifted to high BE direction compared to those for ZnO, with BEs at 1022.8 and 1045.8 eV respectively, which are close to the BE of Zn 2p in ZnFe₂O₄ nanotubes.²³² The O1s for ZnO powder has a BE of 529.6 eV for ZnO, the same as reported for ZnO²³¹, 531.0 eV for ZnFe₂O₄/nZVI bt, close to the value reported for ZnFe₂O₄ nanotubes.²³² **Figure 22d** show high-resolution spectra of the Fe 2p peak exhibiting a BE of 712.0 eV for Fe 2p_{3/2} and 725.4 eV for 2p_{1/2} peak of ZnFe₂O₄/nZVI bt, also close to the value reported for ZnFe₂O₄ nanotubes.²³² In summary, XPS results showed that the synthesized ZnFe₂O₄/nZVI could possibly possess a similar microstructure of ZnFe₂O₄ nanotube, in agreement with the results from TEM and HRTEM measurements.

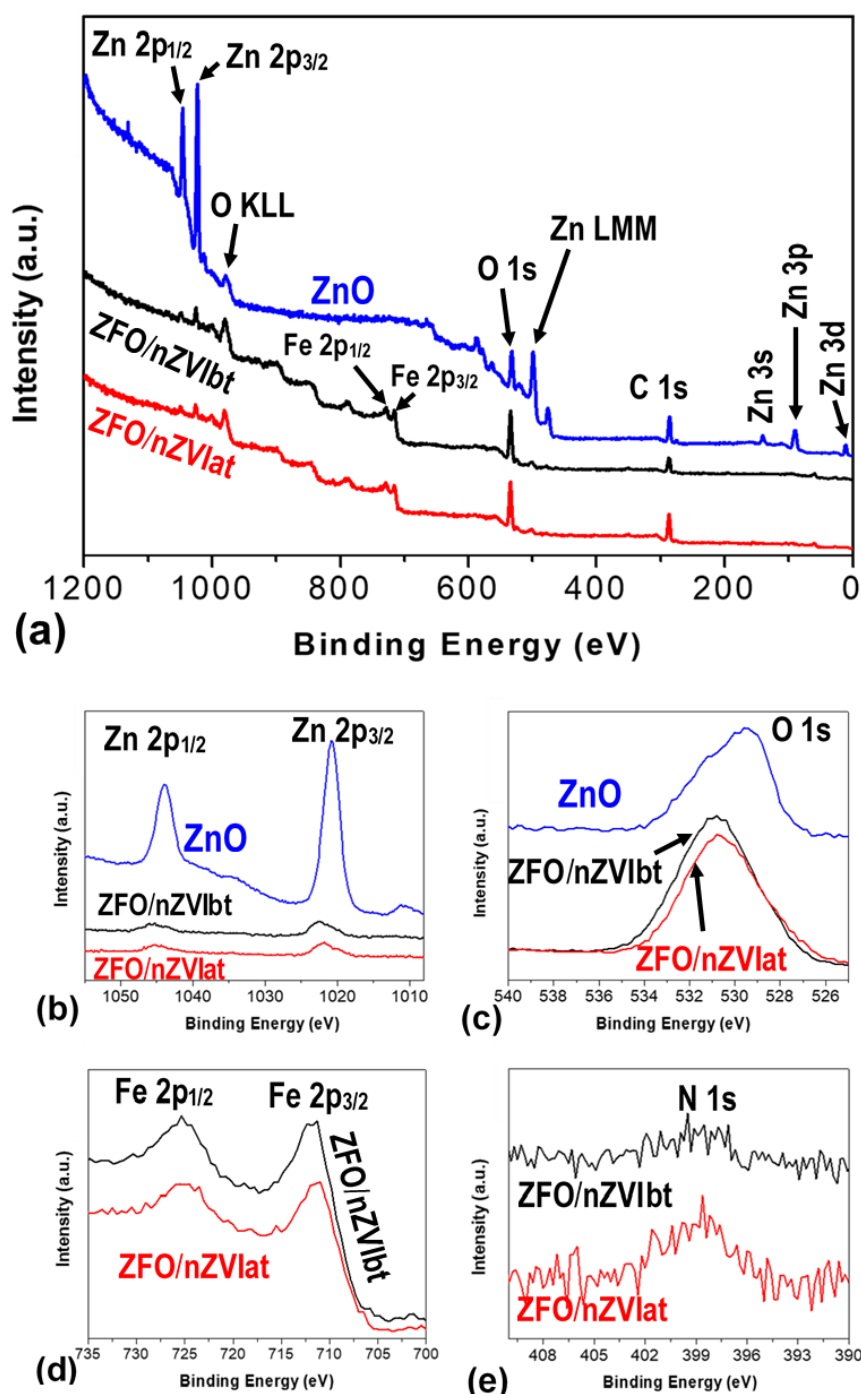


Figure 22. XPS survey spectra of ZnO nanoparticle and ZnFe₂O₄/nZVI nanocomposite **(a)** and high-resolution spectra of Zn 2p **(b)**, O 1s peak for ZnO and ZnFe₂O₄/nZVI **(c)**, Fe 2p **(d)** and N 1s **(e)** for ZnFe₂O₄/nZVI (“ZFO/nZVI bt” and “ZFO/nZVI at” denote ZnFe₂O₄/nZVI before and after treatment of contaminants, respectively).

Removal of NO₃⁻ by ZnO and ZnFe₂O₄/nZVI

The light fluxes that reaction solutions received in glass vials contained $38.5 \pm 0.3 \times 10^{-3}$

W/cm² of visible light ($\lambda = 400\text{-}700\text{ nm}$) and $1.6 \pm 0.1 \times 10^{-6}$ W/cm² of UV-A ($\lambda = 315\text{-}400\text{ nm}$) (**Table S7**). UV-B and UV-C were completely blocked by the UV filter film. Since UV light only accounted for $\sim 0.004\%$ of total light flux, and thus the light source used in our study can be considered as visible light only. The removal efficiencies of NO₃⁻ by ZnO and ZnFe₂O₄/nZVI under visible light were presented in **Figure 23a**. NO₃⁻ was barely removed by ZnO under light within 120 min ($k_{\text{obs}} = 4.0 \pm 0.6 \times 10^{-4}\text{ min}^{-1}$). On the other hand, an astonishing 100% removal was achieved by ZnFe₂O₄/nZVI nanocomposite within 120 min with the pseudo-first-order rate constant more than 100-folded ($k_{\text{obs}} = 4.5 \pm 0.6 \times 10^{-2}\text{ min}^{-1}$). Negligible difference was observed between the removal efficiency of NO₃⁻ by ZnO in dark and under visible light by 120 min (**Figure 23b**), which was expected because ZnO is known to be UV-active only.²⁰⁴ However, ZnFe₂O₄/nZVI only removed 31.5% of NO₃⁻ in dark by 120 min, demonstrating the significant role of visible light in enhancing the removal of NO₃⁻. The removal of As(V) by ZnO and ZnFe₂O₄/nZVI in dark reached 95.1% and 99.6% within 720 min, respectively (**Figure 23c**), and visible light displayed negligible impacts (**Figure 23d**). Therefore, adsorption might be the main mechanism for As(V) removal by both ZnO and ZnFe₂O₄/nZVI.

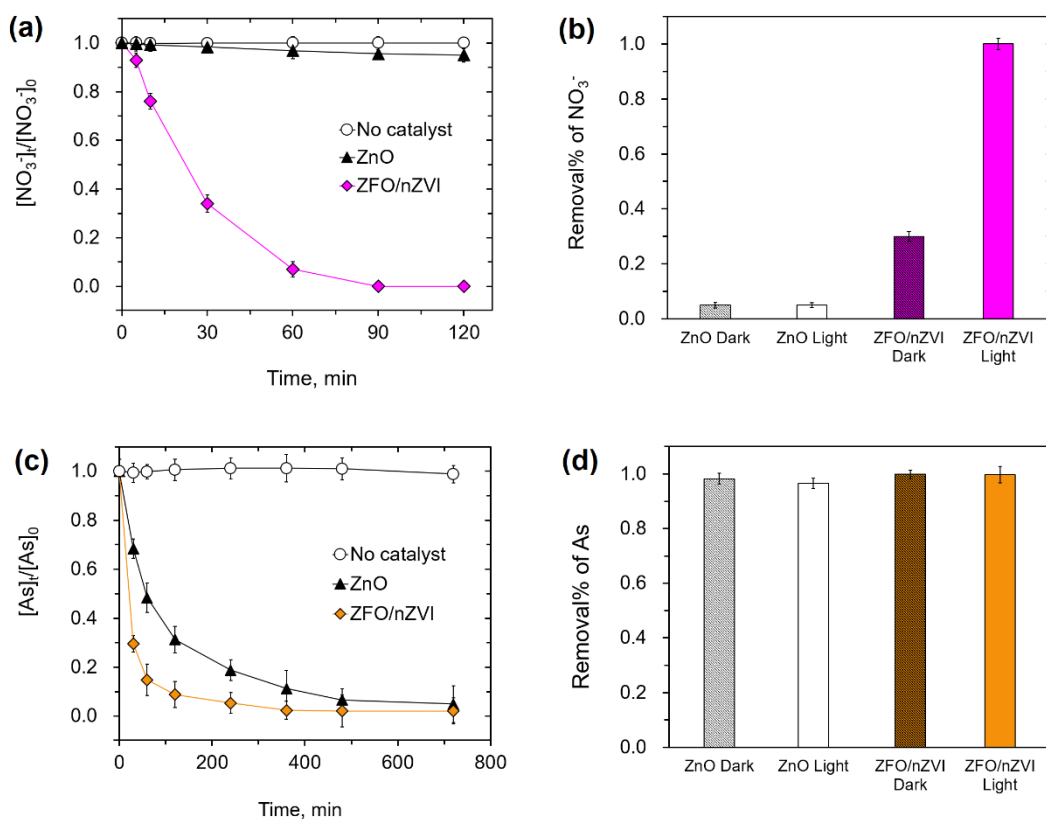


Figure 23. (a) The removal of NO₃⁻ over time by ZnO and ZnFe₂O₄/nZVI nanocomposite (labeled as ZFO/nZVI) under visible light and (b) the removal rate of NO₃⁻ at t = 120 min; (c) the removal of As(V) over time in dark and (d) the removal rate of As(V) at t = 720 min in dark and under visible light ([catalyst] = 0.2 g/L; [NO₃⁻]₀ = 50 mg/L; [As(V)]₀ = 100 μg/L; initial pH = 7.0).

Identifying the Main Reactive Species

To gain more insights into the removal mechanisms, the effects of four scavengers on the removal of NO₃⁻ and As(V) under visible light were shown in Figure 24. The quenching experiment for NO₃⁻ removal was not performed on ZnO due to its negligible removal rate. Trapping of h⁺ by FA dramatically boosted the NO₃⁻ removal by ZnFe₂O₄/nZVI from 37.2% to 100% (Figure 24a), suggesting that quenching of h⁺ by FA inhibited the rapid recombination of e⁻/h⁺ and enhanced NO₃⁻ removal. The introduction of AgNO₃ as an e⁻ scavenger significantly reduced the NO₃⁻ removal by ZnFe₂O₄/nZVI to only 7.1%, suggesting that reduction by photogenerated e⁻ was the main mechanism for NO₃⁻ removal by ZnFe₂O₄/nZVI

under visible light. Compared with the initial concentration of NO_3^- (0.8 mM), the extra NO_3^- (0.35 M) introduced by AgNO_3 was expected to have very minor impact on the removal efficiency. However, both IPA and pBQ showed negligible impact on the NO_3^- removal by $\text{ZnFe}_2\text{O}_4/\text{nZVI}$, indicating that neither $\text{O}_2^{\bullet-}$ nor $\bullet\text{OH}$ was involved in the NO_3^- reduction. In addition, generation of $\text{O}_2^{\bullet-}$ by e^- under anoxic condition is very unlikely. It can be concluded that ZnFe_2O_4 shell and skin layers can produce e^-/h^+ pairs under visible light, and e^- can effectively reduce NO_3^- with FA as the h^+ quencher. Furthermore, the nZVI core could also serve as an e^- source for NO_3^- reduction. On the other hand, none of the scavengers exhibited any impacts on the removal of As(V) by both ZnO and $\text{ZnFe}_2\text{O}_4/\text{nZVI}$, confirming that adsorption was the dominant mechanism (**Figure 24b**).

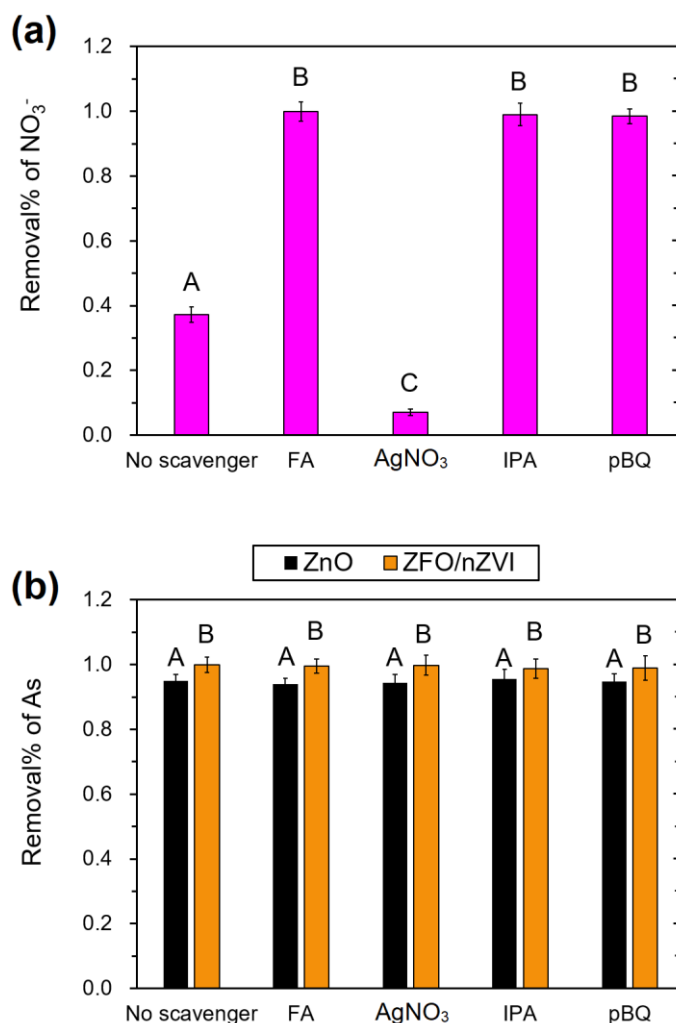


Figure 24. Effects of various scavengers on the removal rate of (a) NO₃⁻ by ZnFe₂O₄/nZVI by 120 min and (b) As(V) by ZnO and ZnFe₂O₄/nZVI (abbreviated as ZFO/nZVI) by 720 min. Different letters indicate significant differences ($p \leq 0.05$) in the removal rates in presence of scavengers for each catalyst according to one-way ANOVA followed by Tukey's test ([catalyst] = 0.2 g/L; [NO₃⁻]₀ = 50 mg/L; [As(V)]₀ = 100 μg/L; [scavenger] = 3.5 mM; initial pH = 7.0; FA was added in all groups except for "No scavenger").

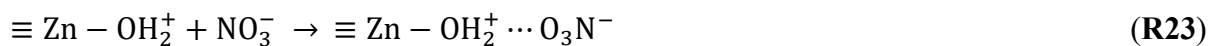
The Mechanisms of NO₃⁻ Removal by ZnFe₂O₄/nZVI

The highly efficient NO₃⁻ removal by the ZnFe₂O₄/nZVI nanocomposite can be attributed to the high adsorption capacity of the ZnFe₂O₄ skin layer, followed by reduction by e⁻, which can be either generated by ZnFe₂O₄ under light or directly provided by the nZVI cores. Based on the N₂ adsorption analysis, the Brunauer-Emmett-Teller (BET) surface area of the ZnFe₂O₄/nZVI nanocomposite reached an astonishing 290.1 m²/g (Figure S19), surpassing

ZnO nanoparticles and other ZnFe₂O₄-based nanocomposites reported previously.^{233–237}

Formation of heavily crumpled ZnFe₂O₄ thin skin layers significantly increased the specific surface area of the nanocomposite, which provided abundant adsorption sites for NO₃⁻ to attach.

The Van der Waals interaction could be an important intermolecular force that enabled NO₃⁻ adsorption. Despite of the slight negative charge that ZnFe₂O₄/nZVI carried at pH 7.0 (**Figure S18a**), the induced electrostatic repulsion was relatively weak. In addition, hydrogen bonding could be one of the main driving forces for NO₃⁻ adsorption that could be formed between NO₃⁻ and octahedral complex of Zn(H₂O)₆²⁺ on the surface of ZnFe₂O₄/nZVI (**R23**).²³⁸



An examination of the high-resolution spectra of Zn 2p, Fe 2p and O 1s peaks of the ZnFe₂O₄/nZVI after NO₃⁻ removal test under XPS indicated slight BE shifts, possibly due to the adsorption of nitrogen species. Indeed, high-resolution spectra of N 1s peak ZnFe₂O₄/nZVI at in **Figure 22e** indicated the presence of nitrogen in the synthesized ZnFe₂O₄/nZVI after NO₃⁻ removal, confirming the adsorption of NO₃⁻ on the ZnFe₂O₄/nZVI nanocomposite.

After concentrating on the surface, NO₃⁻ could be removed via photocatalytic reduction by e⁻ produced by ZnFe₂O₄. To confirm this, the photocatalytic properties of ZnFe₂O₄/nZVI in comparison to ZnO were examined. The light absorbance of ZnO and ZnFe₂O₄/nZVI were measured with an UV-Vis DRS (**Figure 25**). The ZnFe₂O₄/nZVI nanocomposite showed significantly higher absorbance than ZnO at the wavelength between 220-700 nm. In particular, the nanocomposite displayed an impressive light absorbance at the visible light range from 400-700 nm, suggesting a narrow bandgap for the nanocomposite. From the UV spectrum, the bandgap of ZnO and ZnFe₂O₄/nZVI were estimated. The absorption coefficient (α) is estimated

by the Kubelka-Munk function (**R24**), where R is the diffuse reflectance.²³⁹ The bandgaps (E_g) of the two photocatalysts were calculated using **R25**, where h is the Planck constant, ν is the photon's frequency, A is a constant, and the exponent n depends on the nature of the electron transition.²⁴⁰ The resulting Tauc plots are presented in **Figure 25b**. The E_g for ZnO and ZnFe₂O₄/nZVI are estimated to be 3.20 eV and 2.04 eV, respectively, which agreed well with the values reported in literatures for ZnO and ZnFe₂O₄.^{240,241}

$$\alpha = \frac{(1-R)^2}{2R} \quad (\text{R24})$$

$$(\alpha h\nu)^{\frac{1}{n}} = A(h\nu - E_g) \quad (\text{R25})$$

The PL spectra of ZnO and ZnFe₂O₄/nZVI are shown in **Figure 25c**. The peak at around 397 nm in both spectra is assigned to the near-band-edge emission of Zn-O bonds. The peak at around 420 nm in ZnFe₂O₄/nZVI is attributed to the “suppositional” Zn vacancies in the zinc ferrite lattice.^{209,242} The reduced PL intensity of the ZnFe₂O₄/nZVI nanocomposite compared to that of ZnO implies lower recombination of e⁻/h⁺ pairs and more effective charge separation. In summary, the ZnFe₂O₄/nZVI nanocomposite displayed superior photocatalytic properties compared to ZnO, which enabled the highly efficient reduction of NO₃⁻ by photogenerated e⁻.

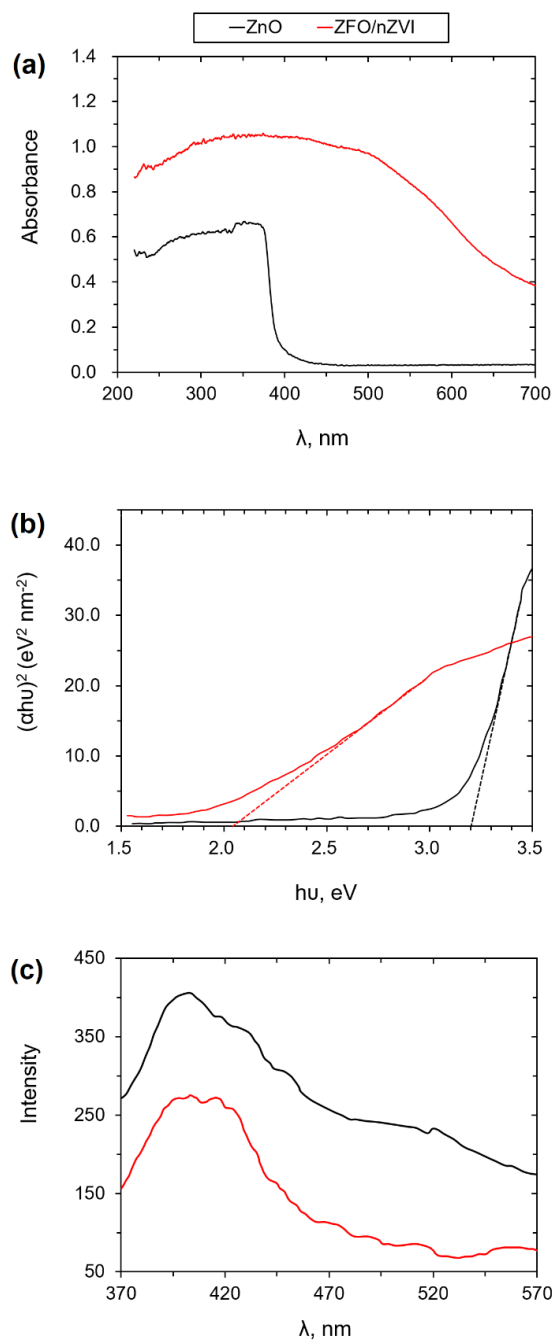
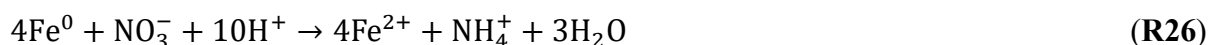


Figure 25. (a) The UV-Vis DRS spectra, (b) Tauc plots and (c) photoluminescence spectra of ZnO and ZnFe₂O₄/nZVI.

To determine the role of nZVI cores in the removal of NO₃⁻, we monitored the release of Fe ions from the nanocomposite because Fe²⁺ is a common byproduct of NO₃⁻ reduction by nZVI (R26). The total Fe ions released from the ZnFe₂O₄/nZVI nanocomposite in dark and under light is shown in Figure S20. Obviously, substantial leaching was observed throughout

the pH range both in the dark and under light. The lower concentration of Fe ions at higher pH can be attributed to the formation of insoluble Fe oxides and hydroxides. Since zinc ferrite generally displays high stability over a broad pH range and good recyclability,^{211,243} leaching of Fe from zinc ferrite was unlikely. Therefore, the leaching of Fe in dark was probably the byproduct of NO₃⁻ reduction by the nZVI cores. Considering the significantly higher NO₃⁻ removal by ZnFe₂O₄/nZVI under light, the markedly higher release of Fe ions under light was likely due to the oxidation of nZVI cores by the positive holes generated by ZnFe₂O₄ under light.



Finally, the Fe ions released to the solution could adsorb on the surface ZnFe₂O₄ to potentially form a single-atom catalyst (SAC) similarly as previously reported.^{244,245} We speculate that Fe SACs can be stabilized by oxygen-containing semiconductors either through direct bonding to surface oxo ligands or occupation of surface cation vacancies.²⁴⁶ At nano or sub-nano scale, Fe SACs on the surface of ZnFe₂O₄ can induce quantum size effects, in which confined electrons create a discrete energy level distribution and reduce the E_g. The reduced PL intensity might be partially due to the formation of chemical bonds between attached Fe²⁺ and Fe³⁺ and ZnFe₂O₄, which could facilitate the charge transfer between them and inhibit charge recombination.²⁴⁷ However, the interactions between Fe SACs and ZnFe₂O₄ were not confirmed in this study, and additional investigation with more advanced characterizations is needed.

Adsorption kinetics and isotherms of As(V) by ZnO and ZnFe₂O₄/nZVI

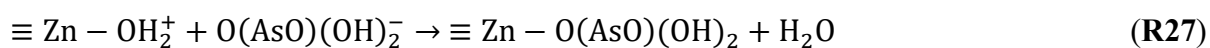
Results of arsenic adsorption kinetics on ZnO and ZnFe₂O₄/nZVI were shown in **Figure S21**, and the kinetic parameters were summarized in **Table S8**. Adsorption equilibrium was reached at 12 hours and 8 hours for ZnO and ZnFe₂O₄/nZVI, respectively (**Figure 23c**). In order to fit the pseudo-first-order kinetic model, the term $\ln\left(1 - \frac{q_t}{q_e}\right)$ was plotted versus time, and the slope represented k_{ads} (**Figure S21a**). Pseudo-second-order kinetic model has been successfully used to describe adsorption processes that are controlled by chemical reactions and has been widely used to predict arsenic adsorption on various adsorbents such as alumina, hematite, magnetite, and goethite.²⁴⁸⁻²⁵¹ The term $\frac{t}{q_t}$ was plotted versus time, and q_e and k_{ads} can be determined by the slope and intercept (**Figure S21b**). Compared with the pseudo-first-order model, the pseudo-second-order model fitted the data better, which agrees with the literature.^{248,252-254} The r^2 values were 0.99 and 1.00 for ZnO and ZnFe₂O₄/nZVI, respectively. Although ZnO and ZnFe₂O₄/nZVI had similar q_e (4.89 and 4.95 mg·g⁻¹, respectively), the second-order rate constant and initial adsorption rate of ZnFe₂O₄/nZVI were approximately 5 times higher than ZnO, indicating an overall much faster adsorption process for As on the nanocomposite.

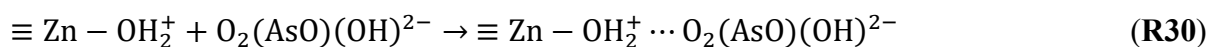
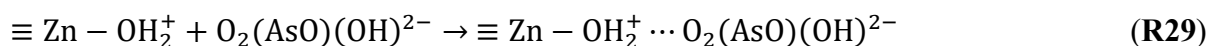
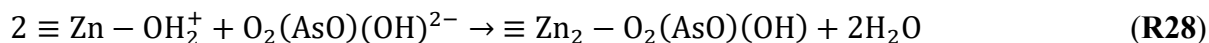
As adsorption isotherms on ZnO and ZnFe₂O₄/nZVI are shown in **Figure S22**, and the parameters obtained by fitting the experimental data are summarized in **Table S9**. The adsorption of As on both ZnO and ZnFe₂O₄/nZVI was better fitted with the Langmuir model ($R^2 > 0.99$), and the values of R_L for different initial As concentrations for ZnO and ZnFe₂O₄/nZVI all fell into the range of 0.005 - 0.446. In Langmuir isotherm, it is postulated that the surface of the adsorbent is homogeneous, and each adsorbed adsorbate molecule only occupies one adsorption site, assuming no interaction between adjacent adsorbate molecules.

Therefore, the fitting of experimental data suggested monolayer adsorption of As on both ZnO and ZnFe₂O₄/nZVI.²⁵⁵ Higher K_L value of ZnFe₂O₄/nZVI than ZnO suggested stronger interactions between As and the surface of ZnFe₂O₄/nZVI.

The Mechanisms of As(V) Removal by ZnFe₂O₄/nZVI

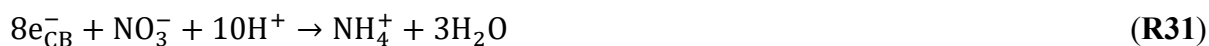
The unaffected As(V) removal in presence of different scavengers further supports our conclusion that adsorption was the dominant mechanism (**Figure 24b**). Electrostatic interaction and surface complexation were possible mechanisms for the As(V) removal by ZnFe₂O₄/nZVI. Since the second pK_a of As(V) is around 6.98, most As(V) existed as (AsO)(OH)₂O⁻ and (AsO)(OH)O₂²⁻ at neutral pH.²⁵⁶ Although ZnFe₂O₄/nZVI carries slightly negative charges at neutral pH, the total intermolecular force between ZnFe₂O₄/nZVI and As(V) could still be attractive until the electrostatic repulsion becomes greater than the Van der Waals force. Arsenate can also form inner-sphere surface complexations (**R27-28**) and hydrogen bonds (**R29-30**) with the octahedral complex of Zn(H₂O)₆²⁺ on the surface of ZnFe₂O₄.²⁵⁷⁻²⁵⁹ The ATR-FTIR spectra of the ZnFe₂O₄/nZVI nanocomposite before and after the experiment are presented in **Figure S23**. The broad peaks at around 3200 cm⁻¹ imply the presence of -OH groups in the adsorbed water molecules. After the experiment, two new peaks at 931 cm⁻¹ and 684 cm⁻¹ appeared, which can be ascribed to the symmetrical stretching of As-O bond in the deprotonated Zn-O₂-AsO₂(H₂O)₄ complex and the symmetrical stretching of As-OH bond in the protonated HAsO₄²⁻(H₂O)₄ complex.²⁶⁰ The two new peaks confirm the adsorption of arsenate on the surface of ZnFe₂O₄/nZVI via surface complexation. Furthermore, the stacked and wrapped skin layers provide more adsorption sites for As.





Effects of pH

Complete removal of NO_3^- was achieved by $\text{ZnFe}_2\text{O}_4/\text{nZVI}$ under visible light at pH 3.0-7.0, exhibiting an impressive stability in the removal efficiency throughout the acidic-to-neutral range (**Figure 26a**). At pH 9.0 and 11.0, the removal efficiency was decreased to 78.6% and 64.5%, respectively. The positive zeta potential of $\text{ZnFe}_2\text{O}_4/\text{nZVI}$ at pH 3.0 and 5.0 (**Figure S18a**) facilitates the adsorption of NO_3^- , while electrostatic repulsion prevented NO_3^- from approaching particle surface beyond pH_{ZPC} . Furthermore, NO_3^- reduction by nZVI and photo-induced electrons both consume protons, so an acidic condition favors NO_3^- removal (**R31**).



$\text{ZnFe}_2\text{O}_4/\text{nZVI}$ demonstrated over 95% of As(V) removal at pH 3.0-11.0, and the removal efficiency slightly decreased as pH increased (**Figure 26b**). This was likely due to the dominance of electrostatic interactions, which exerted a stronger inhibitory impact on the As(V) adsorption at higher pH. Significantly, the removal efficiency of As(V) by $\text{ZnFe}_2\text{O}_4/\text{nZVI}$ remained higher than ZnO across the pH range in this study.

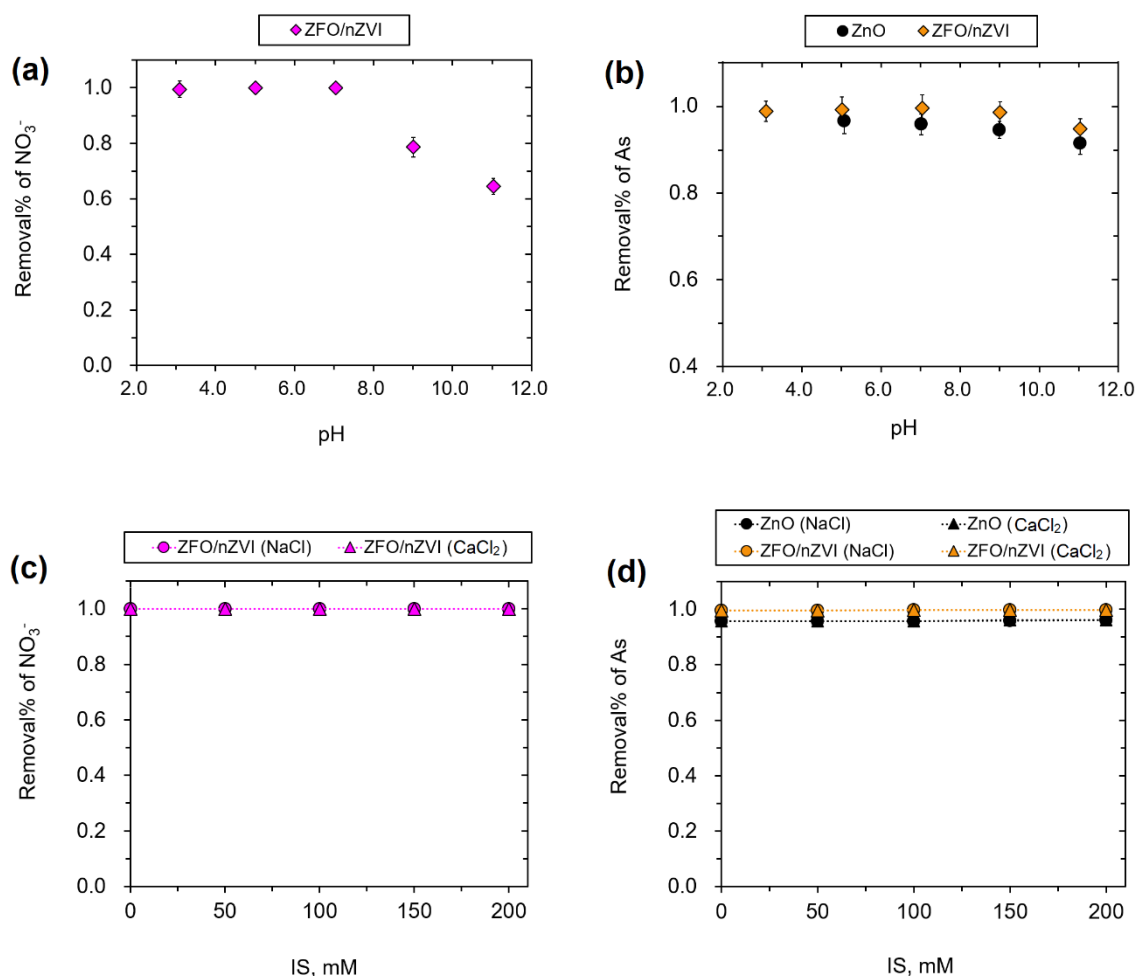


Figure 26. The effect of pH on the removal of (a) NO_3^- by $\text{ZnFe}_2\text{O}_4/\text{nZVI}$ and (b) As(V) by ZnO and $\text{ZnFe}_2\text{O}_4/\text{nZVI}$; the effect of IS on the removal of (c) NO_3^- by $\text{ZnFe}_2\text{O}_4/\text{nZVI}$ and (d) As(V) by ZnO and $\text{ZnFe}_2\text{O}_4/\text{nZVI}$ ([catalyst] = 0.2 g/L; $[\text{NO}_3^-]_0 = 50$ mg/L; $[\text{As(V)}]_0 = 100$ $\mu\text{g/L}$; initial pH = 3.0, 5.0, 7.0, 9.0, 11.0; IS = 0, 50, 100, 150, 200 mM, introduced by NaCl and CaCl_2 ; the removal rates for NO_3^- and As(V) were measured at 120 min and 720 min, respectively).

Effects of Ionic Strength (IS)

NO_3^- is known to form outer-sphere surface complexation with $-\text{OH}$ on metal oxide surfaces.²⁶¹ As IS increases, the Debye length, or the thickness of the diffuse layer decreases.²⁶² Reduction of Debye length lowers the energy barrier for NO_3^- to approach the metal oxide surfaces, which could facilitate adsorption. In addition, Lyklema (1978) reported that the critical coagulation concentration (CCC) of an ion is inversely related to the 6th order of its

charge ($1/Z^6$), similar to what Schulze-Hardy rule predicted.²⁶² In other word, in order to destabilize a suspension, the concentration required for a monovalent ion is 64 times that for a divalent ion. Since the concentration ratio between Na^+ and Ca^{2+} in our solution was much smaller (1: 1/3), the NO_3^- removal under the same IS should be higher in the presence of Ca^{2+} than Na^+ . However, the removal efficiency of NO_3^- by $\text{ZnFe}_2\text{O}_4/\text{nZVI}$ was already 100% under the initial IS (~ 0.5 mM), the impact of increasing IS was not observed (**Figure 26c**). The removal of As(V) was almost unaffected by IS for both ZnO and $\text{ZnFe}_2\text{O}_4/\text{nZVI}$, suggesting the formation of inner-sphere complexation between As(V) and the surface ligands of ZnO and $\text{ZnFe}_2\text{O}_4/\text{nZVI}$ (**Figure 26d**).²⁶³

Effects of Phosphate

Overall, the removal of NO_3^- and As(V) by $\text{ZnFe}_2\text{O}_4/\text{nZVI}$ were both impeded by the presence of phosphate. The removal rate of NO_3^- by $\text{ZnFe}_2\text{O}_4/\text{nZVI}$ was compromised by 12.7% and 53.2% in presence of 1.0 and 10.0 mg/L of phosphate, respectively (**Figure 27a**). Compared to ZnO, Although the removal rate of As(V) by $\text{ZnFe}_2\text{O}_4/\text{nZVI}$ was reduced by phosphate, the impact was remarkably less significant compared to ZnO. In presence of 1.0 and 10.0 mg/L of phosphate, ZnO only removed 59.1% and 12.7% of As(V), respectively, whereas 84.5% and 49.4% of As(V) was removed by $\text{ZnFe}_2\text{O}_4/\text{nZVI}$, respectively (**Figure 27b**). Competitive adsorption between phosphate and the two oxyanions was likely the dominant mechanism for the lower removal rate. Phosphate has been reported as one of the most inhibitive ligands for nitrate reduction.²⁶⁴ Phosphate is also known to compete with As(V) for adsorption on various adsorbents, including goethite,²⁶⁵ iron hydroxides,²⁶⁶ and clay

minerals²⁶⁷ due to their similar electrochemical properties and tetrahedral structure.^{268,269}

Phosphate could also react with Fe^{2+} and Fe^{3+} ions released from the nZVI core to form insoluble iron phosphate and cover the active sites on the surface of ZnFe_2O_4 and nZVI.²⁷⁰

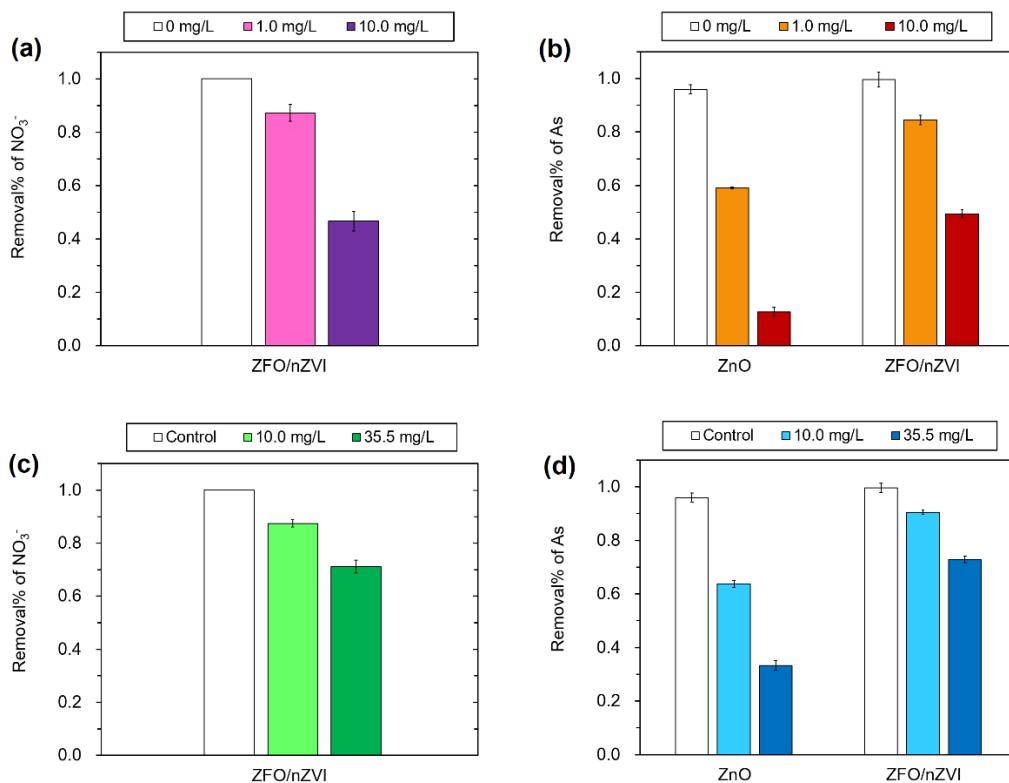
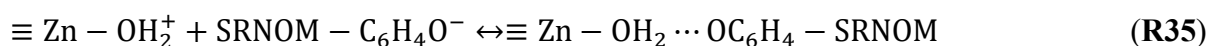
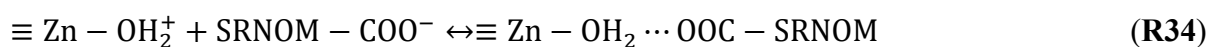
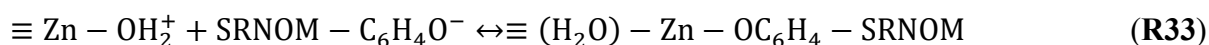
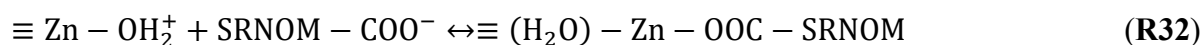


Figure 27. The effect of phosphate on the removal of (a) NO_3^- by $\text{ZnFe}_2\text{O}_4/\text{nZVI}$ and (b) As(V) by ZnO and $\text{ZnFe}_2\text{O}_4/\text{nZVI}$; the effect of NOM on the removal of (c) NO_3^- by $\text{ZnFe}_2\text{O}_4/\text{nZVI}$ and (d) As(V) by ZnO and $\text{ZnFe}_2\text{O}_4/\text{nZVI}$ ([catalyst] = 0.2 g/L; $[\text{NO}_3^-]_0 = 50$ mg/L; $[\text{As(V)}]_0 = 100$ $\mu\text{g/L}$; [phosphate] = 0, 1.0, and 10.0 mg/L; [NOM] = 0, 10.0, and 35.5 mg/L; the removal rates for NO_3^- and As(V) were measured at 120 min and 720 min, respectively).

Effect of NOM

The presence of 10.0 and 35.5 mg/L of NOM mildly hindered the removal of NO_3^- by $\text{ZnFe}_2\text{O}_4/\text{nZVI}$, only lowering the removal rate by 12.5% and 28.7%, respectively (Figure 27c). Similar trend was also observed for the removal of As(V). Significantly, 90.6% and 72.9% of As(V) was removed by $\text{ZnFe}_2\text{O}_4/\text{nZVI}$ with 10.0 and 35.5 mg/L of NOM, respectively (Figure 27d). NOMs consist of both unionized, relatively non-polar, and hydrophobic fractions and

strongly polar, ionized, and hydrophilic fractions. They typically carry negative charges in aqueous environment due to their acidic functional groups. Change in surface charge, steric repulsion, electron scavenging, and inner filter effect are suggested as major mechanisms for lower NO_3^- removal in the presence of NOMs. The amphiphilic property of NOMs allows them to adsorb to most surfaces and make the overall surface charge more negative.^{271,272} At pH 7.0, the phenolic group in NOM remained protonated, while carboxyl group was deprotonated. Adsorption of negatively charged NOM onto ZnO, nZVI, and $\text{ZnFe}_2\text{O}_4/\text{nZVI}$ induced stronger electrostatic repulsion between the particle surface and anions, reducing their adsorption. The bulky functional groups on NOM also cause steric repulsion. In addition, NOMs are known as scavengers of reactive oxygen species (ROS).²⁷³ The carboxyl groups in NOM can be readily reduced in the presence of available electrons.²⁷⁴ Hence, NOM could compete with nitrate for electrons. Another mechanism for lower nitrate removal by NOMs could stem from the inner filter effect (IFE), or light attenuation, due to the absorption of UV irradiation by NOMs which diminishes the available light for photocatalytic reaction.²⁷⁵ In addition to the four factors discussed above, competitive adsorption between NOM and As(V) might be another contributing factor. The carboxyl and phenolic groups in NOM could bind to Zn atoms through Zn-O bonds (**R32-33**) and hydrogen bonds (**R34-35**), similar to how As(V) binds to ZnO (**R27-30**).^{257,258}



The lower susceptibility of the ZnFe₂O₄/nZVI to the inhibitory effect of NOM could be explained by the possible screening effect of the ZnFe₂O₄ skin layer. The multi-layered structure of ZnFe₂O₄ skin layer could serve as a barrier to prevent bulky NOM from approaching the particle surface. Reduced NOM adsorption enabled the nanocomposite to achieve a higher removal of both oxyanions.

Conclusions

In conclusion, a novel visible-light active ZnFe₂O₄/nZVI nanocomposite with a unique core-shell-skin tertiary structure was synthesized via a liquid-phase reduction method. It exhibited high simultaneous removal efficiency for both NO₃⁻ and As(V) under visible light and remarkable stability at a broad pH range. Reduction by e⁻, which can be photo-generated by ZnFe₂O₄ or directly provided by nZVI, was the predominant mechanism for the removal of NO₃⁻, while adsorption was the main mechanism for the removal of As(V). The enhanced photocatalytic activity of the nanocomposite is attributed to its greater light absorption and enhanced charge separation. Compared with ZnO, the nanocomposite is less susceptible to the effects of various environmental factors. Nonetheless, its performance for NO₃⁻ and As(V) removal was markedly lowered by phosphate, and NOMs to a less extent. Future research needs to focus on developing selective capability of the nanocomposite materials to minimize the effect of phosphate and other water constituents. For water contaminated by both oxyanions but with limited phosphate, the ZnFe₂O₄/nZVI nanocomposite provides an effective alternative to current technologies.

To date, application of ferrite-based materials in water treatment is still rare. Besides

outstanding photocatalytic and magnetic properties, ferrites also display strong adsorption capacity to various other contaminants such as chromium,²⁷⁶ lead,²⁷⁷ phosphate,²⁷⁸ sulfur dioxide,²⁷⁹ and many organic compounds.²⁸⁰ Therefore, ferrite-based nanocomposite materials deserve more attention. Future studies should continue to explore the potential of this novel nanocomposite for the removal of contaminant mixtures in water and seek methods to further increase its photoactivity under broader light range and environmental conditions.

CHAPTER V

PHOTOCATALYTIC DEGRADATION OF PERFLUOROOCCTANOIC ACID BY TITANIUM-BASED METAL-ORGANIC FRAMEWORK MIL-125-NH₂

Introduction

Per- and polyfluoroalkyl substances (PFAS) are a large class of organo-fluorine compounds that are rapidly accumulating in soils, sediments, and water bodies owing to their widespread applications as surfactants and coatings in textiles, paper products, fire-fighting foams, cosmetics, and cookware.^{40,74,281} Perfluorooctanoic acid (PFOA), one of the most extensively detected PFAS, reached 6,570 parts per billion (ppb) in groundwater near U.S. military bases, which is almost five orders of magnitude higher than the EPA health advisory level for the sum of PFOA and perfluorooctanesulfonic acid (PFOS) in drinking water (0.070 ppb).⁵⁰ More than 12 PFAS have been detected at the ppb level in the blood serum of participants of the National Health and Nutrition Examination Survey (NHANES) since 1999. Among them, PFOA, PFOS, perfluorohexanesulfonic acid (PFHxS), and perfluorononanoic acid (PFNA) were detected in the blood serum of almost all participants.²⁸² *In vivo* studies suggested that exposure to PFAS may lead to higher cholesterol levels, disruption of hormones, reproductive problems, and increased risk of cancers.⁴⁶⁻⁴⁸ Significantly, high level of PFAS in the blood has been associated with low response to vaccines and poor resistance to infectious diseases, which may render the public more susceptible to the recent COVID pandemic.^{49,283,284}

Due to their amphiphilic nature and the abundance of exceedingly stable C-F bond with a bond dissociation energy (BDE) more than 500 kJ/mol,^{285,286} PFAS are highly resistant to conventional wastewater treatment, with their half-lives ranging from ~50 years in water to

more than 200 years in soil.^{74,287–290} The prevalence, persistence, and potential toxicity of PFAS have prompted extensive exploration of efficient treatment technologies in recent years.^{74,287,291,292} Currently, non-destructive technologies such as adsorption, filtration, and ion exchange are commonly used to remove PFAS from water, however, they tend to be less effective toward non-ionic and short-chain PFAS and require post-treatment for concentrated PFAS wastes.^{290,292,293} Among the destructive technologies, photocatalysis has emerged as a promising technology for PFAS degradation owing to its high removal efficiency and its utilization of sustainable energy.^{294–296} Homogeneous photocatalysis (e.g., UV/sulfite, UV/iodide, and UV/indole) has received intensive attention thanks to the formation of hydrated electron (e_{aq}^- , $E^0 = -2.9 \text{ V}_{\text{NHE}}$), the most reactive nucleophilic species that can effectively cleave C-F bonds.^{51–53,74,76,297} However, despite their high efficiency, these processes are often accompanied by undesirable toxic chemicals such as sulfite and iodide. In contrast, heterogeneous photocatalysis is capable of producing both reactive oxidizing species such as hole (h^+) and hydroxyl radical ($\bullet\text{OH}$), and reducing species such as e_{aq}^- , and has exhibited remarkable performance in degrading environmental pollutants in water.^{294,295,298}

Metal-organic frameworks (MOFs) are a group of crystalline, porous, coordination polymers constructed from metal clusters and organic ligands.²⁹⁹ Owing to their high structural and functional tunability, MOFs have been widely studied for gas separation,³⁰⁰ catalysis,³⁰¹ and biomedical applications.³⁰² In recent years, MOFs as photocatalysts in environmental applications have aroused intensive interest due to their ultra-high surface area and porosity, abundant active sites, and tunable photocatalytic properties.^{303–305} Surprisingly, PFAS-related studies with MOFs have been extremely scarce and mostly limited to adsorption.^{306–308} The

potential of photocatalytic MOFs in PFAS degradation has rarely been investigated. MIL-125-NH₂ is one of the most well-known photocatalytic MOFs, consisting of Ti₈O₈(OH)₄ clusters and 2-amino-terephthalic acid ligands.³⁰⁹ The introduction of the amino group substantially enhances the photocatalytic activity and reduces the bandgap of the original MIL-125 from 3.6 eV to about 2.6 eV,^{309,310} making MIL-125-NH₂ an ideal candidate for photocatalytic applications.^{311,312}

Despite the extensive research on PFAS degradation, knowledge gaps regarding the detailed reaction mechanisms of PFAS degradation remain. H/F exchange and chain-shortening are the two most frequently proposed reaction pathways between e_{aq}^- and PFAS.^{51,74,313} However, a clear understanding on the detailed reaction mechanisms in each pathway is still critically lacking. For example, the thermodynamic feasibility of each reaction step involved in chain-shortening and H/F exchange remains largely unknown. This knowledge is fundamental for developing technically sound and economically viable treatment technologies for PFAS.

In the present study, we demonstrated complete degradation and 66.7% overall defluorination of PFOA by MIL-125-NH₂ under irradiation using glucose as a non-hazardous, sacrificial reductant. DFT calculations were employed to determine the reaction thermodynamics of each step of the major degradation pathways of PFOA, which agreed well with the identified degradation metabolites. A unique degradation mechanism enabled by integrated e_{aq}^- and oxidizing reactive species was proposed. MIL-125-NH₂ also exhibited high recyclability and stability, showcasing the potential benefits of MOFs as photocatalysts for breaking the C-F bonds in PFAS to release fluoride ion.

Experimental Section

Chemicals and Materials

Perfluorooctanoic acid (95.0%), ammonium hydroxide (28.0-30.0%), and D-(+)-Glucose ($\geq 99.5\%$) was purchased from Sigma Aldrich (St. Louis, USA). Methanol (HPLC optima grade, $\geq 99.9\%$), ammonium acetate ($\geq 97.0\%$) were purchased from ThermoFisher Scientific (Hampton, USA). Commercial samples of MIL-125-NH₂ were provided by Framergy Inc. Milli-Q water prepared from a Myron L 750 II system was used as the solvent for all solutions in this study.

Photocatalytic degradation of PFOA by MIL-125-NH₂

A photochemical reactor system consisting of a medium pressure Hg-vapor immersion lamp (450 W, #7825-35), a double-walled quartz immersion well (#7874-38), and a 500 mL borosilicate glass reaction vessel (#7863-18) was purchased from Ace Glass (Vineland, USA) and used to perform the photocatalytic degradation experiments. The light fluxes in each wavelength regions emitted by the Hg-lamp was measured by a LS125 UV light meter (Linshang Technology, Shenzhen, China) and a Solar Light PMA2100 radiometer (Solar Light Company, Philadelphia, USA). A Thermo Haake C41P circulator equipped with a Haake Phoenix II control head (Hampton, USA) was connected with the photochemical reactor system to control the temperature at 20.00 ± 0.02 °C. A 75:25 mixture of water and ethylene glycol was used as the cooling fluid in the circulator. The initial concentration of PFOA was 100 $\mu\text{g/L}$, and the MOF loading was 2.5 g/L. The glucose concentration was varied at 0.01, 0.05, 0.2, and 0.5 M. The dispersion of MIL-125-NH₂ in ultrapure water was sonicated using an ultrasonic

processor (U.S. Solid, Cleveland, USA) for 10 minutes to achieve a uniform dispersion. The well-sonicated dispersion of MIL-125-NH₂ was transferred to the reaction vessel with constant stirring at 300 rpm using a glass-coated stir bar. Glucose was slowly added to the dispersion. The mixture was stirred for 10 minutes to ensure complete dissolution of glucose. The mixture was then spiked with PFOA stock solution to generate an initial PFOA concentration of 100 µg/L in the reaction mixture. The Hg-lamp was turned on to start the experiment (t = 0). In comparison, five groups of control experiments with initial PFOA concentration of 100 µg/L were also performed: (1) direct photolysis of PFOA, (2) 2.5 g/L of MIL-125-NH₂ in dark, (3) 2.5 g/L of MIL-125-NH₂ under light, (4) 0.5 M of glucose under light, and (5) 2.5 g/L of MIL-125-NH₂ and 0.5 M glucose in dark. In dark groups, the reactor was fully covered by aluminum foil to block any light. All experiments in this study were conducted under oxic condition. In each group of experiment, 2.0 mL of sample was extracted using a syringe needle at various time points (t=0, 1, 3, 6, 12, 24 hours) and then centrifuged in a micro-centrifuge at 12,000 rpm using a Sorvall Legend Micro 21R centrifuge (ThermoFisher Scientific) for 10 minutes. The supernatant in each sample was collected for subsequent analyses.

Solid-phase-extraction (SPE)

SPE was performed to extract PFOA and degradation metabolites from the collected supernatants using Waters Oasis WAX cartridges (1cc, 30 mg sorbent, 30 µm particle size) cartridges (Milford, USA) on a Supelco Visiprep SPE vacuum manifold purchased from MilliporeSigma (Burlington, USA). The cartridges were conditioned with 3.0 mL of 0.1% ammonium hydroxide in methanol and 3.0 mL of pure methanol, loaded with 1.0 mL of sample,

and then washed with 1.0 mL of 25 mM ammonium acetate. The sample was eluted with 1.0 mL of 0.1% ammonium hydroxide in methanol and then stored at 4°C before analysis.

Quantitative analysis of perfluorinated carboxylic acids (PFCAs)

The concentrations of five PFCAs (PFOA, PFHpA, PFHxA, PFPeA, and PFBA) in each sample were detected and quantified on a binary pump HPLC coupled to a triple quadrupole mass spectrometer (ThermoFisher Scientific, Waltham, USA) (LC-MS/MS). The injection volume of each sample was 10.0 μ L. Chromatographic separation was achieved using a Hypersil Gold 5 μ m 50 x 3 mm column (ThermoFisher Scientific) at 30 °C. Solvent A was water (0.1% formic acid). Solvent B was acetonitrile (0.1% formic acid). The flow rate was 0.5 mL·min⁻¹.

Untargeted analysis of degradation metabolites

To detect the plausible degradation metabolites of PFOA, untargeted liquid chromatography high resolution accurate mass spectrometry (LC-HRAM) analysis was performed on a Q Exactive Plus orbitrap mass spectrometer (ThermoFisher Scientific, Waltham, USA) coupled to a binary pump UltiMate 3000 HPLC. The acquired data was processed and analyzed using Compound Discoverer 3.3 (ThermoFisher Scientific) to screen and identify possible degradation metabolites.

Quenching experiments

To elucidate the roles of possible reactive species in the degradation of PFOA by MIL-

125-NH₂, glucose, AgNO₃, and SOD were used as the quenchers for h^+ , e_{aq}^- , and O₂^{•-}, respectively. Four groups of treatments were performed: (1) no quencher, (2) 0.5 M of glucose, (3) 0.5 M of glucose and 100 U·ml⁻¹ of SOD, and (4) 0.5 M of AgNO₃. In each treatment, 2.0 ml of sample was collected at t=1, 3, 6, 12, 24 hours to measure the PFOA concentrations.

Electron paramagnetic resonance (EPR)

EPR was used to probe possible reactive species in the reaction systems. The measurement was performed using a Bruker Elexsys E500 EPR equipped with both a standard resonator and a CoolEdge cryo system (Billerica, USA). The instrument settings are: 20.0 mW microwave power, 9.8 GHz microwave frequency, 100 kHz modulation frequency, 1.00 G modulation amplitude, 3515 G center field, 150 G sweep width, and 40.0 s sweep time. 50.0 mM of 5,5-dimethyl-1-pyrroline N-oxide (DMPO) was used as the spin trapping agent for •OH, and O₂^{•-}. The EPR measurement for •OH was conducted using 1:1 mixture of ultrapure water and acetonitrile as the solvent. To avoid the interference of •OH signal, the EPR measurement for O₂^{•-} was performed in pure methanol (MeOH). After 10 minutes of irradiation under the Hg-lamp, 5.0 ml of reaction solution was extracted and injected into a 2 mm quartz EPR tube using a syringe needle. The 2 mm quartz tube was then placed into a 4 mm quartz EPR tube, which was immediately loaded into EPR.

Recyclability and stability tests

To evaluate the recyclability of MIL-125-NH₂ in the degradation of PFOA, the experiment was conducted with 2.5 g/L of MOF, 0.5 M of glucose, and 100 µg/L of PFOA for 24 hours.

After each cycle, the residue of MOF was washed by ultrapure water (twice) and ethanol (twice), dried at 60°C for 12 hours, and then weighed. The recycled MOF was used to run a new cycle of experiment with the same initial glucose and PFOA concentration. A total of three cycles was conducted, following the same procedures to recycle the MOF. The concentration of PFOA at $t = 0, 3, 6, 12, 24$ hours in each cycle was measured.

To assess the stability of MIL-125-NH₂, a series of characterizations was performed on the MOF before and after three cycles of experiment. A JEOL JSM-7500F ultra-high-resolution FE-SEM was used to observe the morphological changes in the MOF particles. Thermogravimetric analysis (TGA) was conducted to determine the thermal stability of the MOF using a Mettler Toledo TGA/DSC1 equipped with a GC 200 Gas controller system. The changes in BET surface area and pore volume were determined by N₂ adsorption-desorption isotherm measurements at 77 K on a Micromeritics ASAP 2020 high-performance adsorption analyzer with subsequent analysis of the adsorption data performed using Micromeritics Microactive software. The micropore and mesopore size distributions of the MOF were analyzed using the density functional theory (DFT) and Barrett-Joyner-Halenda (BJH) models. To probe the crystal structure of the MOF, PXRD data was collected with a Bruker-AXS D8 short arm diffractometer equipped with a multiwire lynx eye detector using Cu (K α , $\lambda=1.542\text{\AA}$) and operated at a potential of 40 kV and a current of 40 mA.

Measurement of fluoride (F⁻) concentrations

The concentrations of fluoride (F⁻) in the collected samples were measured using a Dionex Integrion high performance ion chromatography (HPIC) system (Waltham, USA) equipped

with a conductivity detector, a Dionex IonPac AS19 column (4×250 mm), a Dionex IonPac AG19 (4×50 mm) guard column, and a Dionex ADRS 600 (4mm) suppressor. Considering the limit of quantification (LOQ) of the IC, the initial concentration of PFOA was increased to 1.0 mg/L in order to achieve a higher quantification accuracy. The initial concentration of glucose was controlled at 0.5 M. The F⁻ concentration in each sample was calculated using a standard calibration curve.

Results and Discussion

Photocatalytic degradation of PFOA

PFOA was efficiently degraded by MIL-125-NH₂ in 24 h (**Figure 28a**) under the irradiation of a Hg vapor lamp, whose light fluxes in different wavelength regions are presented in **Table S10**. Glucose as a benign *h*⁺ scavenger was crucial for the system. Without glucose, the removal of PFOA by MIL-125-NH₂ was inefficient (only ~13%) (**Figure S24**). The degradation of PFOA increased with the glucose concentration and complete degradation was achieved at 0.5 M glucose ($k_{obs} = 2.64 \pm 0.16 \times 10^{-3} \text{ min}^{-1}$). The corresponding degradation kinetics fitted well with the pseudo-first-order model ($r^2 > 0.99$) (**Figure S25, Table S11**). Complete degradation of PFOA was achieved within 24 h using 0.5 M glucose ($k_{obs} = 2.64 \pm 0.16 \times 10^{-3} \text{ min}^{-1}$). Even with a ten-fold increase of the initial PFOA concentration to 1.0 mg/L, 98.9% of PFOA was degraded within 24 h ($k_{obs} = 2.33 \pm 0.19 \times 10^{-3} \text{ min}^{-1}$) (**Figure 28b**). Based on the fluoride (F⁻) concentration in the supernatant, the calculated overall defluorination rate (overall deF%) using **Equation 36**:

$$\text{Overall deF\%} = \frac{[\text{F}^-]}{[\text{PFAS}]_0 \times N_{\text{C-F}}} \times 100\% \quad (\text{R36})$$

where $[\text{F}^-]$ is the measured F^- concentration in the supernatant, $[\text{PFAS}]_0$ is the initial PFAS concentration, and $N_{\text{C-F}}$ is the total number of C-F bonds in the parent PFAS molecule. The overall deF% in this system was comparable to the literature.^{51,314-316} It is important to note that the reactivity of e_{aq}^- is generally higher under alkaline condition (e.g., $\text{pH} \approx 10$) because quenching of e_{aq}^- by H^+ becomes noticeable under acidic condition to form less reactive hydrogen radical ($\bullet\text{H}$, $E^0 = -2.3 \text{ V}_{\text{NHE}}$).^{76,316-318} With the use of glucose in this study, the solution pH was maintained in the range of 4.6-5.8 throughout the experiment. Although the degradation efficiency of PFOA could be compromised by the scavenging effect of H^+ , this pH range is closer to that of real wastewater, and our results demonstrated the effectiveness of MIL-125-NH₂ at this pH range. In addition, MOFs constructed by hard acid metals and hard base ligands like MIL-125-NH₂ tend to be more stable under slightly acidic conditions.^{302,304}

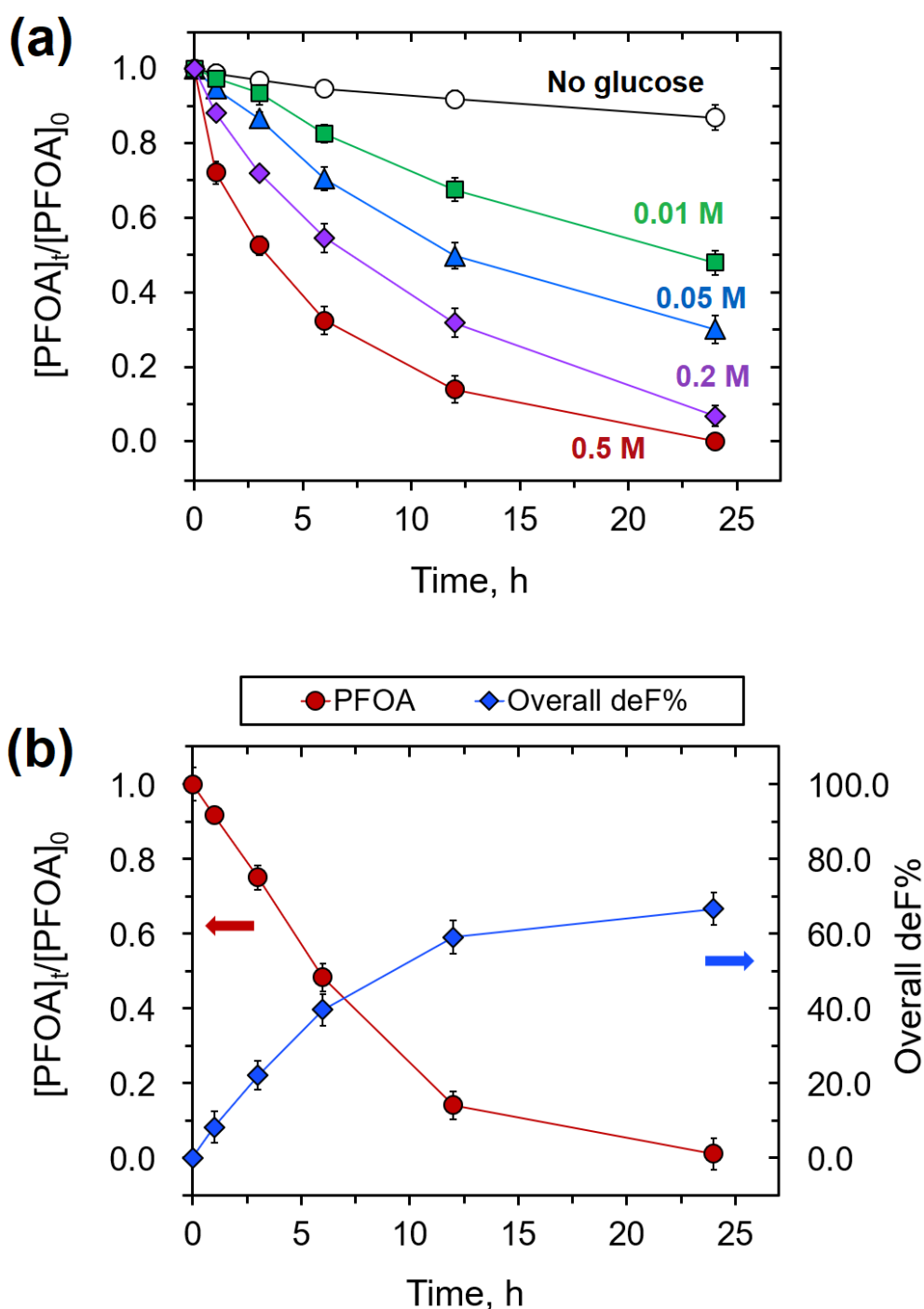


Figure 28. (a) Effect of glucose concentration on the removal efficiency of PFOA by MIL-125-NH₂ under light ($[PFOA]_0 = 100 \mu\text{g/L}$; MOF loading = 2.5 g/L; $[\text{glucose}]_0 = 0, 0.01, 0.05, 0.2, 0.5 \text{ M}$; $T = 20^\circ\text{C}$); (b) the decay of PFOA and corresponding overall deF% under light ($[PFOA]_0 = 1.0 \text{ mg/L}$; MOF loading = 2.5 g/L; $[\text{glucose}]_0 = 0.5 \text{ M}$; $T = 20^\circ\text{C}$).

Degradation metabolites and pathways of PFOA

The degradation metabolites of PFOA were screened using untargeted LC-MS/MS

analysis and are presented in **Figures S26-S28**. Two major types of metabolites were identified, including shorter-chain perfluorinated carboxylic acids (PFCAs) and fluorotelomer carboxylic acids (FTCAs, $C_nF_{2n+1}-(CH_2)_m-COO^-$), suggesting that chain shortening and H/F exchange are two primary pathways for PFOA degradation (**Figure 29**).^{51,74,319,320} Through chain shortening, a series of shorter-chain PFCAs including perfluoroheptanoic acid (PFHpA), perfluorohexanoic acid (PFHxA), perfluoropentanoic acid (PFPeA), perfluorobutanoic acid (PFBA), and perfluoropropanoic acid (PFPrA) were produced. To verify the proposed chain-shortening pathway, the change in concentration of PFHpA, PFHxA, PFPeA, and PFBA were monitored using targeted LC-MS analysis (**Figure 30**). The time profiles of PFHpA, PFHxA, and PFPeA showed a stepwise defluorination from long to short chain PFCAs, similar to previous literature reports.⁵¹ The formation of PFBA was not observed until after 6 hours, and a reduction in concentration was not observed within 24 h. This is likely due to the higher stability of PFBA and slower reaction kinetics with e_{aq}^- ,⁷⁴ which can be inferred from its lower removal efficiency by MIL-125-NH₂ under the same condition (**Figure S29**).⁷⁴ Although the concentration of PFPrA was not measured due to the lack of standards, the change of its peak area over time confirmed its formation (**Figure S30a**). Based on the metabolites, four steps of H/F exchange occurred on both PFOA and PFHpA, resulting in the formation of eight FTCAs with partial defluorination. The time profiles of the peak areas of these FTCA metabolites also displayed similar trends as the PFCAs (**Figure S30b-c**). Based on the time profiles of these shorter-chain PFCAs and FTCAs, the proposed degradation pathways of PFOA in the MOF system are illustrated in **Figure 29**.

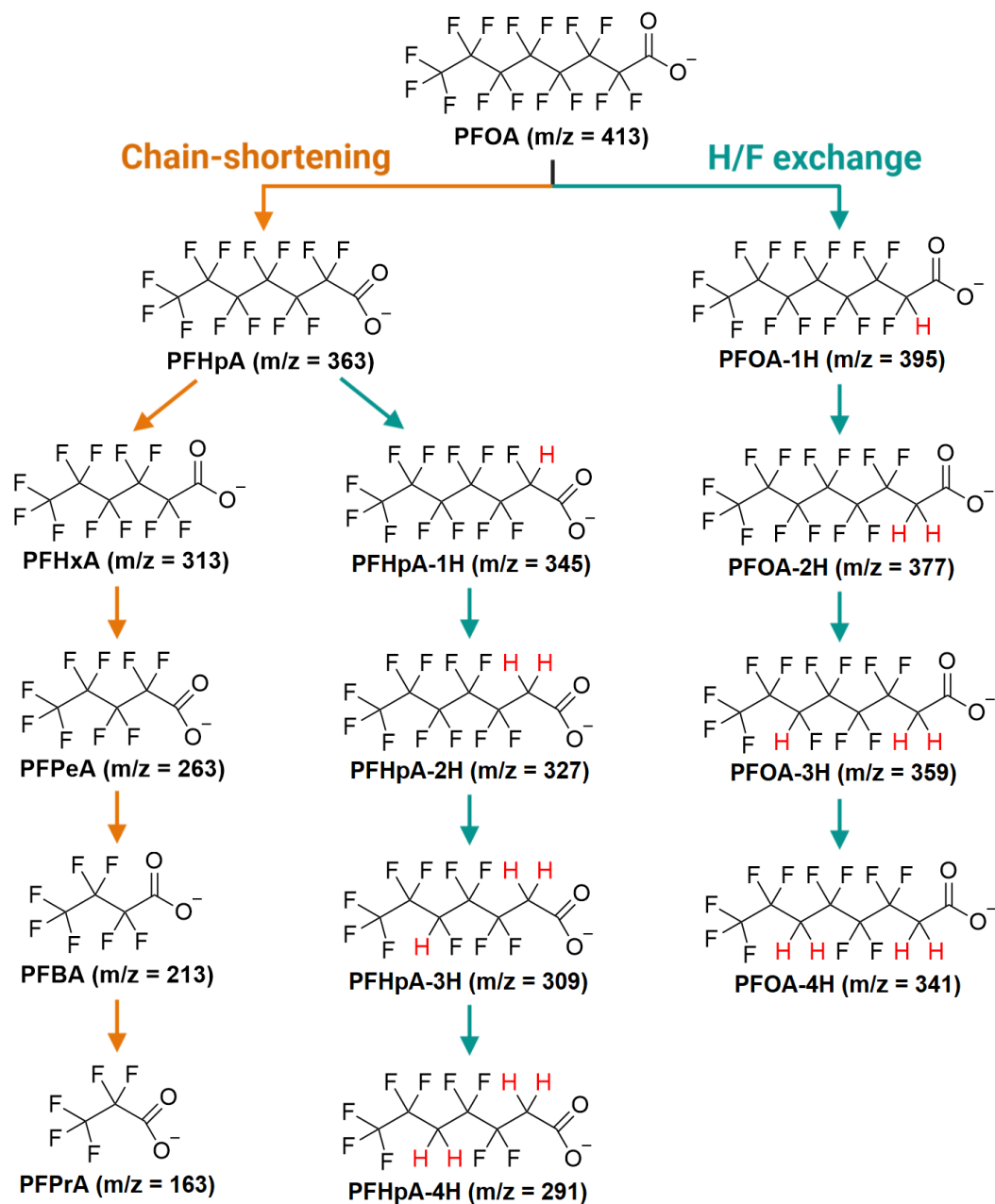


Figure 29. Plausible degradation metabolites and proposed degradation pathways of PFOA by MIL-125-NH₂/glucose under light

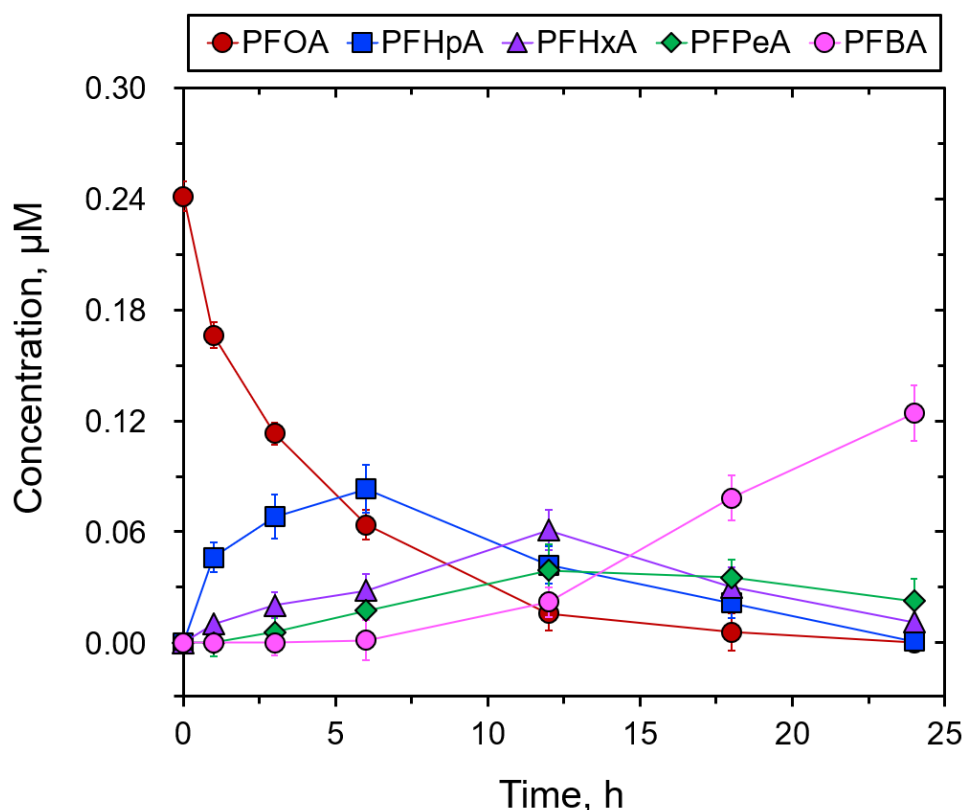
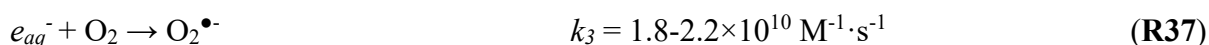


Figure 30. Changes in concentrations of PFOA, PFHpA, PFHxA, PFPeA, and PFBA over time ($[PFOA]_0 = 100 \mu\text{g/L}$; MOF loading = 2.5 g/L; $[\text{glucose}]_0 = 0.5 \text{ M}$; $T = 20^\circ\text{C}$).

Identifying the main reactive species

Identifying main reactive species. In order to identify main reactive species involved in the degradation of PFOA, AgNO_3 was used as a quencher for e_{aq}^- ,³²¹ and superoxide dismutase (SOD) was added to scavenge $\text{O}_2^{\bullet-}$,¹⁶⁰ a common product from e_{aq}^- and dissolved O_2 (**Equation 37**).^{322,323} Glucose in the system served as a quencher for h^+ .



The pseudo-first-order rate constants of PFOA degradation in presence of different quenchers were presented in **Table S12**. According to **Figure 31a**, e_{aq}^- was the dominant reactive species in the reductive degradation of PFOA while $\text{O}_2^{\bullet-}$ had a negligible role as evidenced by the minimal impact of $100 \text{ U} \cdot \text{ml}^{-1}$ SOD. Remarkably, even in the presence of 0.5

M AgNO₃, 42% of PFOA was degraded within 24 hours. The results suggested that even without e_{aq}^- , oxidizing species like h^+ and \bullet OH can also degrade PFOA, and \bullet OH could be produced by h^+ following **Equation 38**:



Electron paramagnetic resonance (EPR) technique was employed to provide direct evidence of the formation of reactive species with 5,5-dimethyl-1-pyrrolineN-oxide (DMPO) as the spin trapping agent. The formation of O₂^{•-} was verified by the signal of DMPO-O₂^{•-} adduct (**Figure 31b**), however, it did not contribute to the PFOA degradation according to the results of quenching study. The characteristic 1:2:2:1 peak of DMPO- \bullet OH adduct also confirmed the production of \bullet OH (**Figure 31c**). The EPR signals of DMPO-O₂^{•-} and DMPO- \bullet OH adducts can serve as indirect evidence for the presence of e_{aq}^- and h^+ . However, because the signals of DMPO- \bullet OH and DMPO-O₂^{•-} can overlap with each other, EPR was also conducted with the addition of both SOD and glucose. Interestingly, a weak signal of DMPO- \bullet OH was still observed (**Figure 31d**), confirming the formation of \bullet OH due to incomplete quenching of h^+ by glucose. Unlike non-porous photocatalysts, in which quenching of h^+ can occur efficiently on the particle surface, the structure of MOF is highly porous, and the reaction rate between glucose and h^+ on the MOF surface could be limited by the diffusion of glucose. Overall, the quenching study and EPR measurement suggested that our system contained multiple reactive species, with e_{aq}^- playing a major role and \bullet OH playing a supporting role in driving the PFOA degradation.

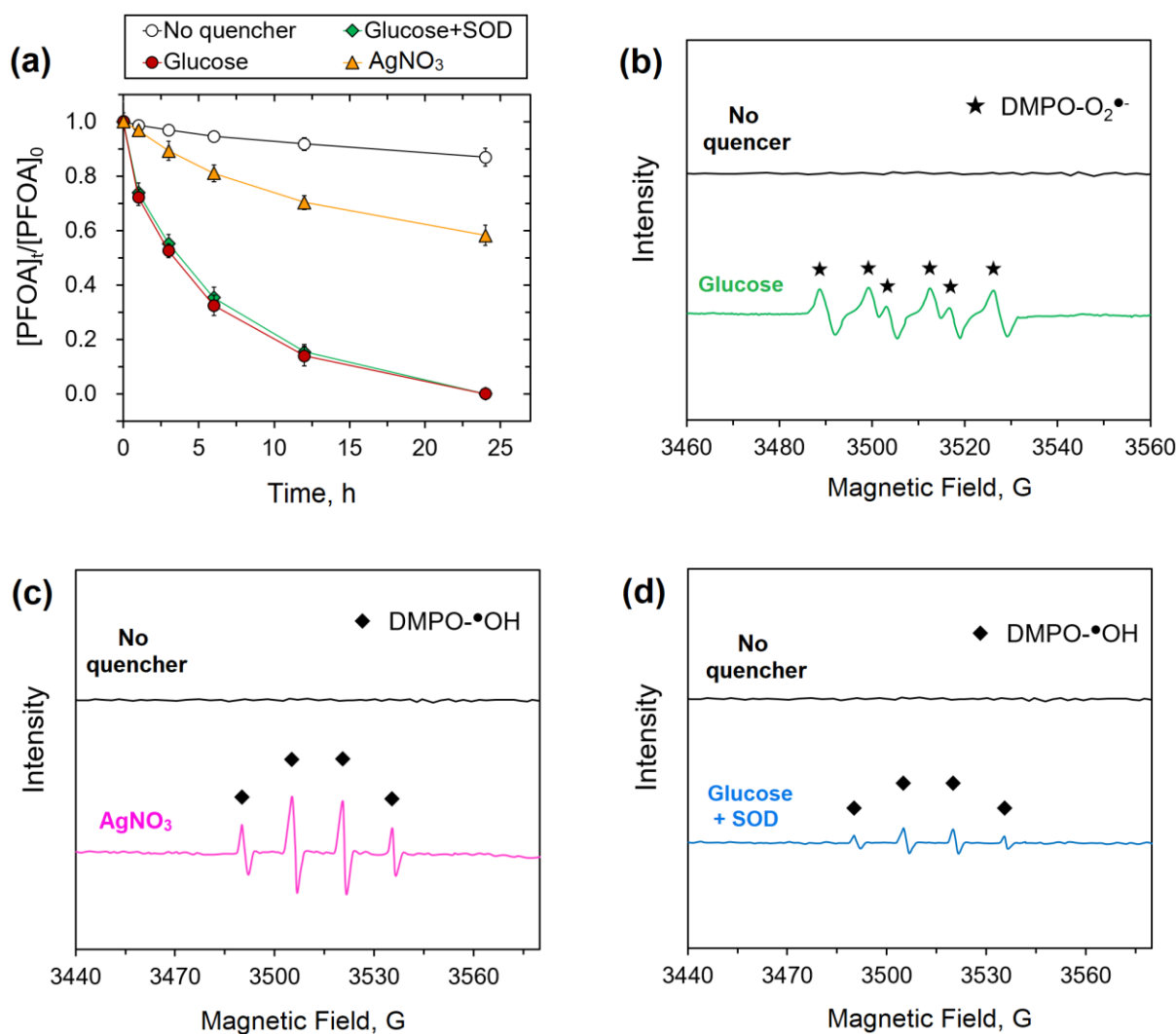


Figure 31. (a) Effects of quenchers on the removal of PFOA. The EPR spectra in presence of (b) AgNO₃, (c) glucose, and (d) glucose and SOD ($[PFOA]_0 = 100 \mu\text{g/L}$; MOF loading = 2.5 g/L; $[AgNO_3]_0 = [glucose]_0 = 0.5 \text{ M}$; $[SOD]_0 = 100 \text{ U}\cdot\text{ml}^{-1}$; $T = 20^\circ\text{C}$).

Recyclability and Stability

Many MOFs are known to suffer from poor recyclability and stability under aqueous conditions, which critically limit their feasibility in environmental applications.^{304,324} Therefore, the recyclability and stability of MIL-125-NH₂ in the current system were evaluated by monitoring its removal efficiency of PFOA and structural stability over three cycles. As shown in **Figure S30**, an astonishing 96.7% removal of PFOA was achieved by MIL-125-NH₂ after three cycles, with a very minor decrease in the pseudo-first-order rate constant (**Table S13**),

demonstrating its excellent recyclability. Furthermore, the stability of MIL-125-NH₂ was determined by powder X-ray diffraction (PXRD), thermogravimetric analysis (TGA), N₂ adsorption isotherm analysis, and scanning electron microscopy (SEM). The PXRD pattern of post-run MIL-125-NH₂ showed that the material retained a high degree of crystallinity, which matched well with the pre-run pattern and the simulated pattern from the single crystal data (**Figure 32a**). The similar TGA profiles of pre- and post-run MIL-125-NH₂ also suggested that the overall structure of MIL-125-NH₂ remained largely intact (**Figure S31**). The N₂ adsorption isotherm analysis showed a slight decrease in the total nitrogen uptake after three cycles from 373 to 310 cm³/g under standard temperature and pressure (STP), resulting in a reduction in the Brunauer-Emmett-Teller (BET) surface area from 1378 to 1098 m²/g (**Figure 32b**). The slight reduction in porosity was likely due to pore clogging by residual PFOA and its degradation products, or water. In addition, the DFT model and Barrett-Joyner-Halenda (BJH) model were employed to analyze the micro- and mesopore size distributions, respectively (**Figure 32c**). Both pre- and post-run MIL-125-NH₂ exhibited a high degree of microporosity, and the slight reduction in the differential pore volume at around 7 to 9 Å in the post-run sample was ascribed to pore clogging. On the other hand, the differential volume of mesopores at around 30 to 40 Å was markedly increased in the post-run sample (**Figure 32d**), agreeing well with the greater hysteresis in the N₂ adsorption isotherm at pressure above $P/P^\circ = 0.5$. The increase in mesoporosity could be attributed to the etching of MIL-125-NH₂ during extended exposure to water, which can also be inferred from the slightly rounded edges of MIL-125-NH₂ crystals shown in the SEM images (**Figure S32**). However, these etching factors were overall minor, with this data showing that the structural integrity of MIL-125-NH₂ was well-

maintained, indicating its high stability in the photodegradation experiments.

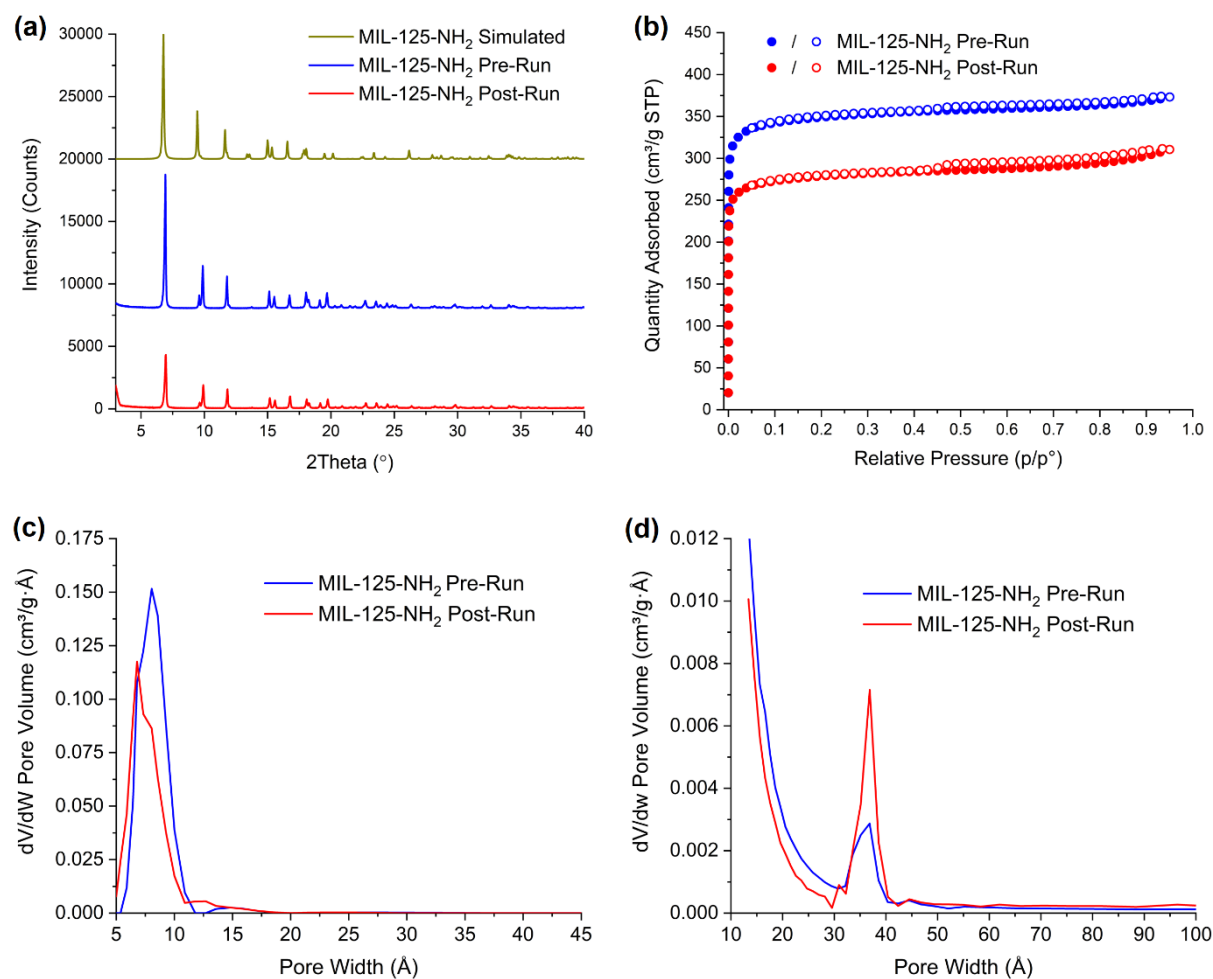


Figure 32. The (a) PXRD patterns, (b) N₂ adsorption isotherms, and (c) density functional theory (DFT) and (d) Barrett-Joyner-Halenda (BJH) pore size distribution curves of MIL-125-NH₂ before and after three cycles of photodegradation experiments.

Conclusions

This is the first mechanistic study on delineating the photocatalytic degradation of PFAS by MOFs. Complete PFOA degradation was achieved by MIL-125-NH₂ within 24 h with glucose as the sacrificial reductant, accompanied by a remarkable defluorination efficiency. Chain-shortening and H/F exchange are major pathways for PFOA degradation, both of which can be induced by e_{aq}^- . Significantly, a comprehensive mechanistic investigation supported by

DFT calculations unveiled the detailed reaction mechanisms in chain-shortening and H/F exchange, some of which were not discussed by previous literatures. Our results also highlighted the vital role of oxidizing reactive species like $\bullet\text{OH}$ in assisting the e_{aq}^- -initiated PFAS reduction, which could shed light on the design of a comprehensive system for more efficient defluorination. Furthermore, the performance and structural integrity of MIL-125- NH_2 remained stable after three cycles of experiments, displaying excellent recyclability and stability. These results exemplify the significant potentials of photocatalytic MOFs as a promising platform for efficient removal of PFAS in water.

CHAPTER VI

CONCLUSIONS AND RECOMMENDATIONS

In conclusion, this dissertation highlights several important potentials of AOPs and ARPs in the degradation of recalcitrant pollutants in water and contributes to closing existing knowledge gaps in these fields. In the studies of persulfates, direct activation of PDS by visible light and PMS by co-existing phosphate and carbonate to produce various reactive species were demonstrated, both of which have not been reported before. The results provide important insights for understanding the chemistry of persulfates and novel methods to activate them. In the study of heterogeneous photocatalysts, a ZFO/nZVI nanocomposite with a unique core-shell-skin tertiary structure is synthesized, which removed NO_3^- and As simultaneously. The work showed that a heterogeneous photocatalyst can be integrated with an adsorbent to achieve a synergistic effect in photocatalytic reduction and adsorption of toxic oxyanions, which sheds light on future technologies to tackle co-contamination of multiple pollutants. Furthermore, the first photocatalytic degradation of PFAS by MOF was demonstrated. The model MOF MIL-125-NH₂ not only displayed remarkable efficiency in the degradation and defluorination of PFAS but also showed high recyclability and stability. The results exemplified MOFs as promising photocatalysts for PFAS degradation and called for more studies to further optimize the system.

While significant progresses have been made in the above-mentioned studies, additional research is needed to further advance the knowledge. Specific recommendations for continued research include:

-
1. In the study of PDS activation, while it is exciting to confirm the activation of PDS by visible light, the quantum yield of PDS under visible light vs. UV light should be determined to further evaluate the effectiveness of visible light activation. Also, a comparative evaluation on the chemical and energy consumption between activation of PDS by visible light and heterogeneous catalysts is needed.
 2. In the study of PMS activation, although the enhance effects of phosphate and carbonate on pollutant degradation as well as formation of reactive species were observed, the underlying reaction mechanisms remain unclear. Theoretical calculations involving DFT may be utilized to probe the interactions between PMS and phosphate/carbonate and to determine the corresponding thermodynamics.
 3. In order to further exploit the applicability of the ZFO/nZVI nanocomposite, further modifications are necessary to overcome the hinderance effect of phosphate and NOM. Moreover, structural optimizations are needed to inhibit the charge recombination without relying on adding sacrificial reductants.
 4. In the study of PFAS degradation by MOF, despite of the excellent degradation efficiency of PFOA by e_{aq}^- , complete defluorination is not attainable for any technology that relies on either ARP or AOP. It is imperative to develop a more effective technology that utilizes multiple reactive species to achieve a complete degradation and defluorination of PFAS.

SUPPORTING INFORMATION

Supporting Figures

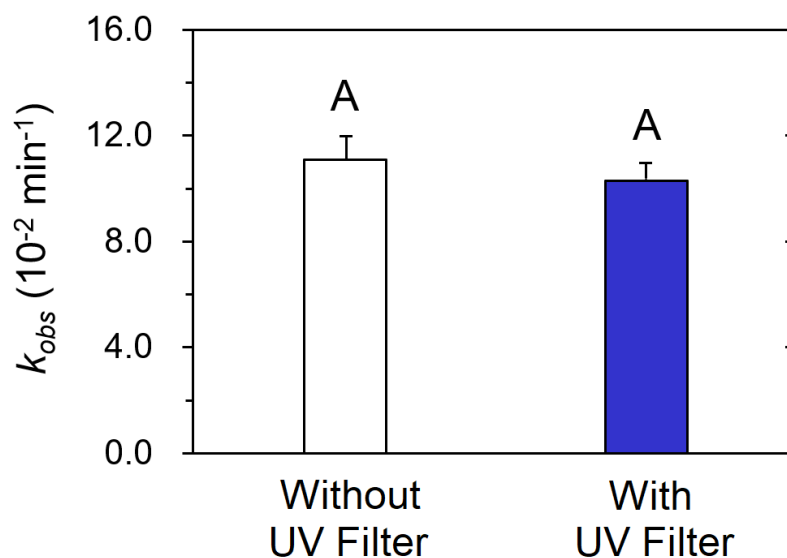


Figure S1. The pseudo-first-order rate constants of ATZ degradation by PDS Light with and without the UV filter ($[\text{ATZ}]_0 = 10.0 \mu\text{M}$, $[\text{PDS}]_0 = 5.0 \text{ mM}$, $[\text{Na}_2\text{HPO}_4] = 10.0 \text{ mM}$, $\text{pH}_0 = 7.0$, $T = 25 \text{ }^\circ\text{C}$; different letters indicate significant difference ($p \leq 0.05$) between the rate constants according to one-way ANOVA followed by Tukey's test).

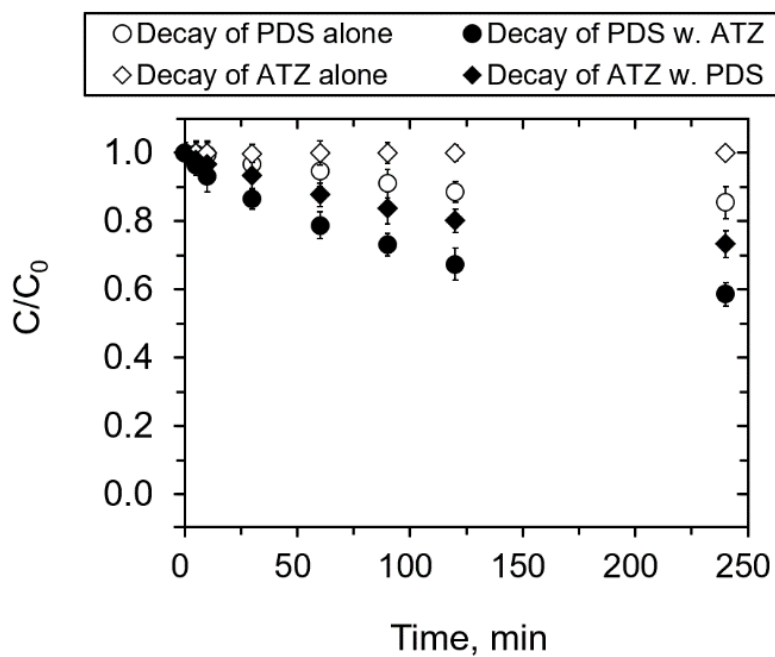


Figure S2. Decay of PDS and ATZ in the absence and presence of each other in dark ($[PDS]_0 = [ATZ]_0 = 5.0$ mM, $[Na_2HPO_4] = 10.0$ mM, $pH_0 = 7.0$, $T = 25$ °C).

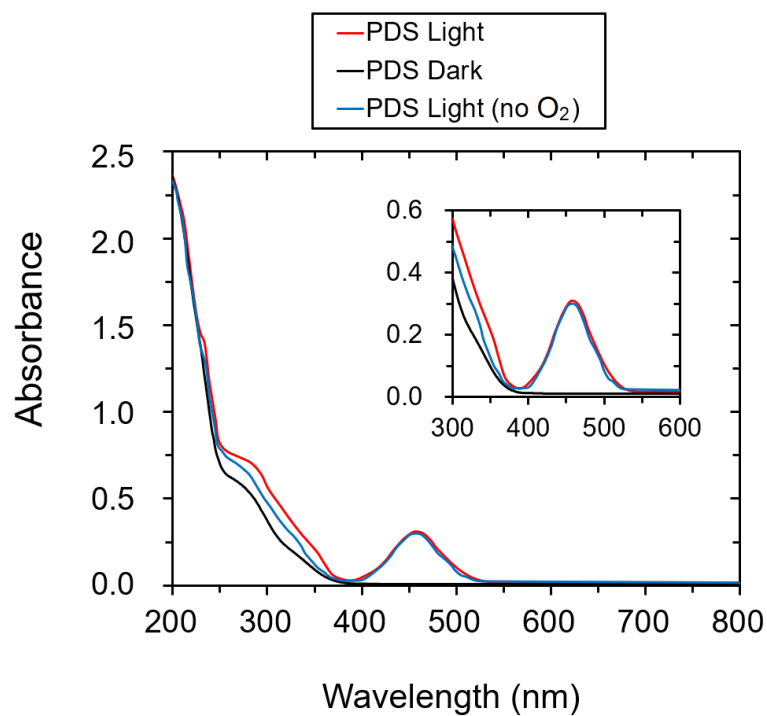


Figure S3. Detection of H₂O₂ based on the UV-Vis absorbance spectra of PDS Dark and PDS Light in the absence of ATZ; absorption at ~450 nm indicates the formation of peroxovanadate as a product of H₂O₂ and vanadate; a zoomed-in image is presented in the inset ([PDS]₀ = 5.0 mM, [NH₄VO₃]₀ = 10.0 mM, [Na₂HPO₄] = 10.0 mM).

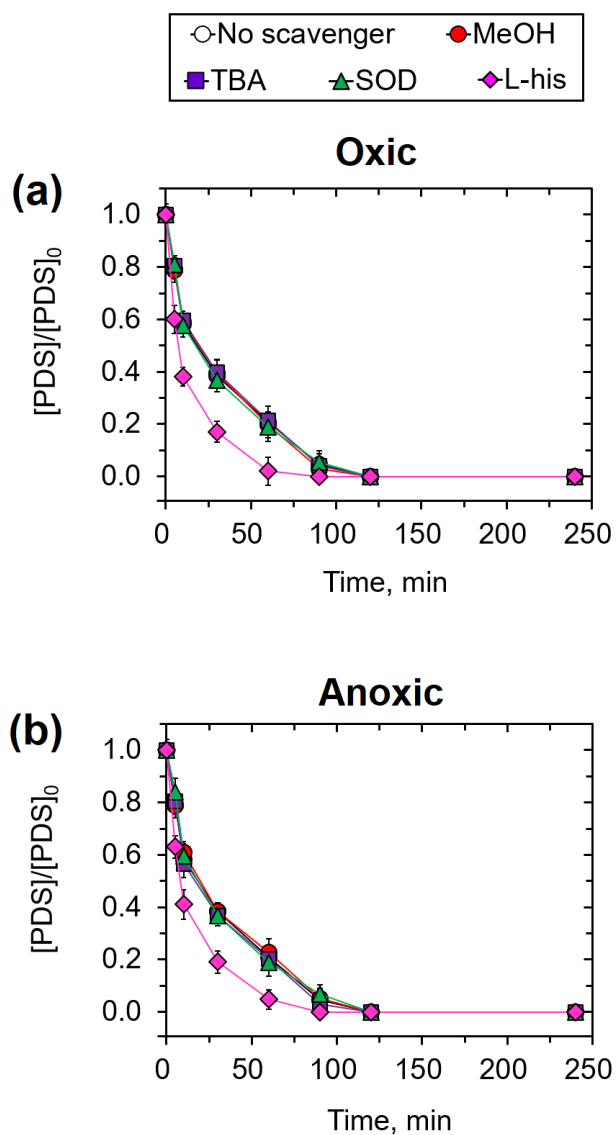


Figure S4. Decay of PDS with the presence of scavengers under (a) oxic and (b) anoxic condition under light; the control group in which no scavenger was present is shown in the figure but respective symbols are fully covered by other symbols ($[PDS]_0 = 5.0$ mM, $[Na_2HPO_4] = 10.0$ mM, $[MeOH]_0 = [TBA]_0 = [L-his]_0 = 0.5$ M, $[SOD]_0 = 50$ U·ml⁻¹, $pH_0 = 7.0$, $T = 25$ °C).

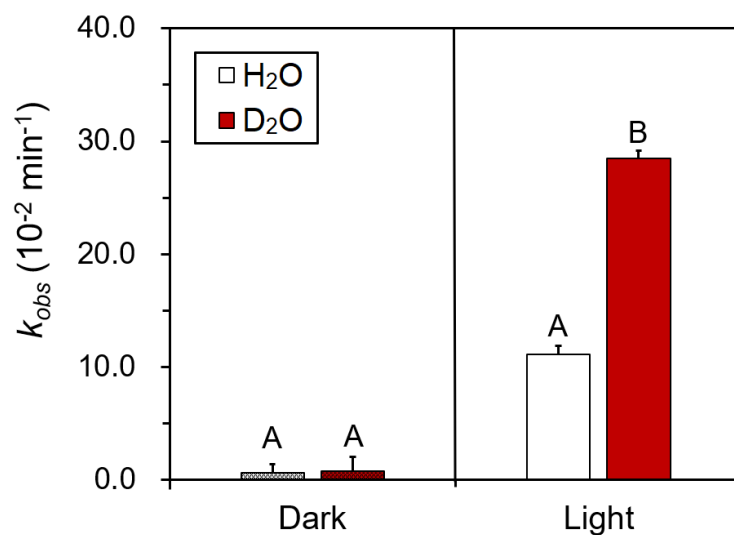


Figure S5. Pseudo-first-order rate constants of ATZ degradation by PDS in water and D₂O (different letters indicate significant differences between the rate constants according to one-way ANOVA followed by Tukey's test, ($p \leq 0.05$)).

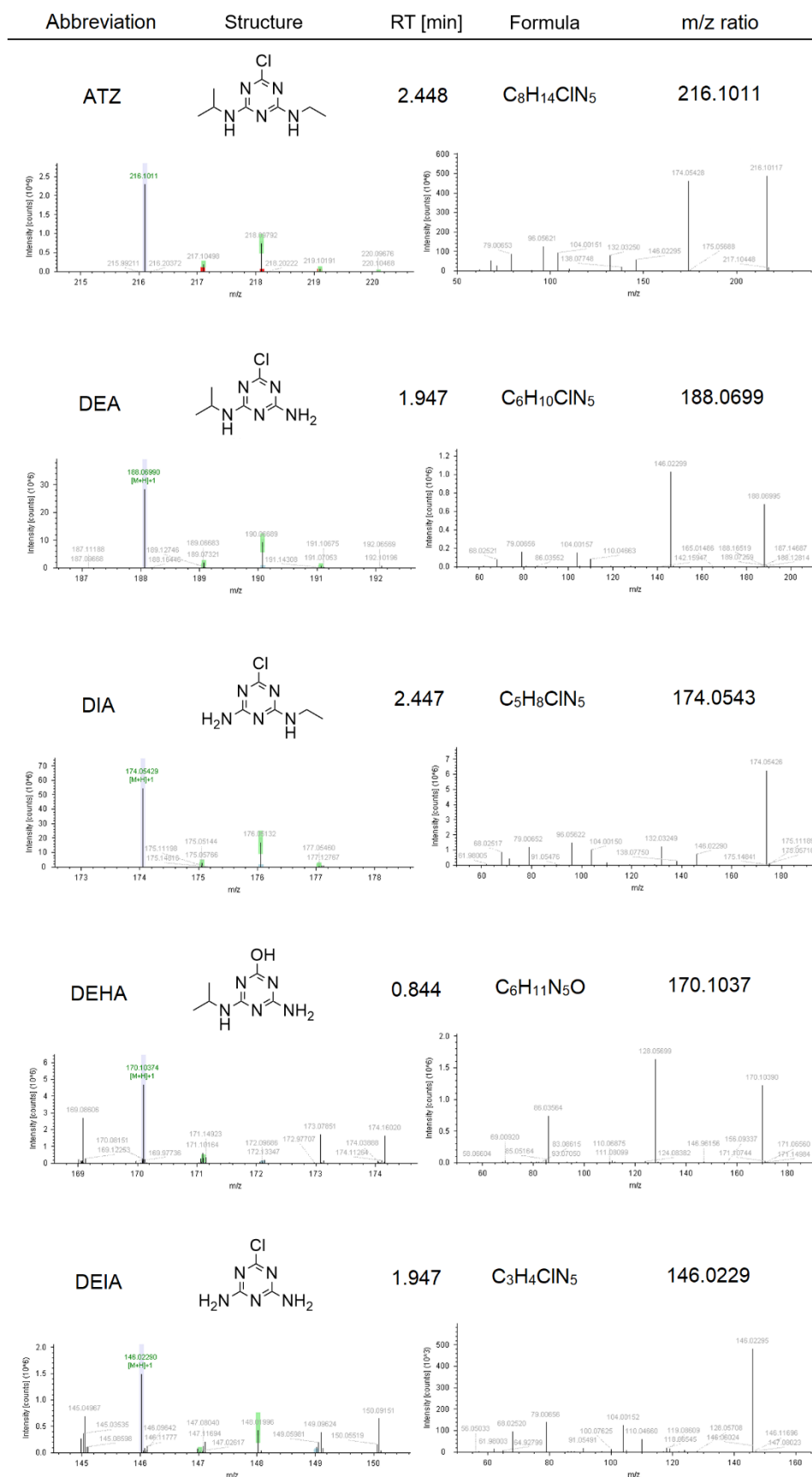


Figure S6. MS1 and MS2 spectra of identified degradation metabolites of ATZ in PDS Dark and PDS Light systems (the structures of identified metabolites are tentatively assigned).

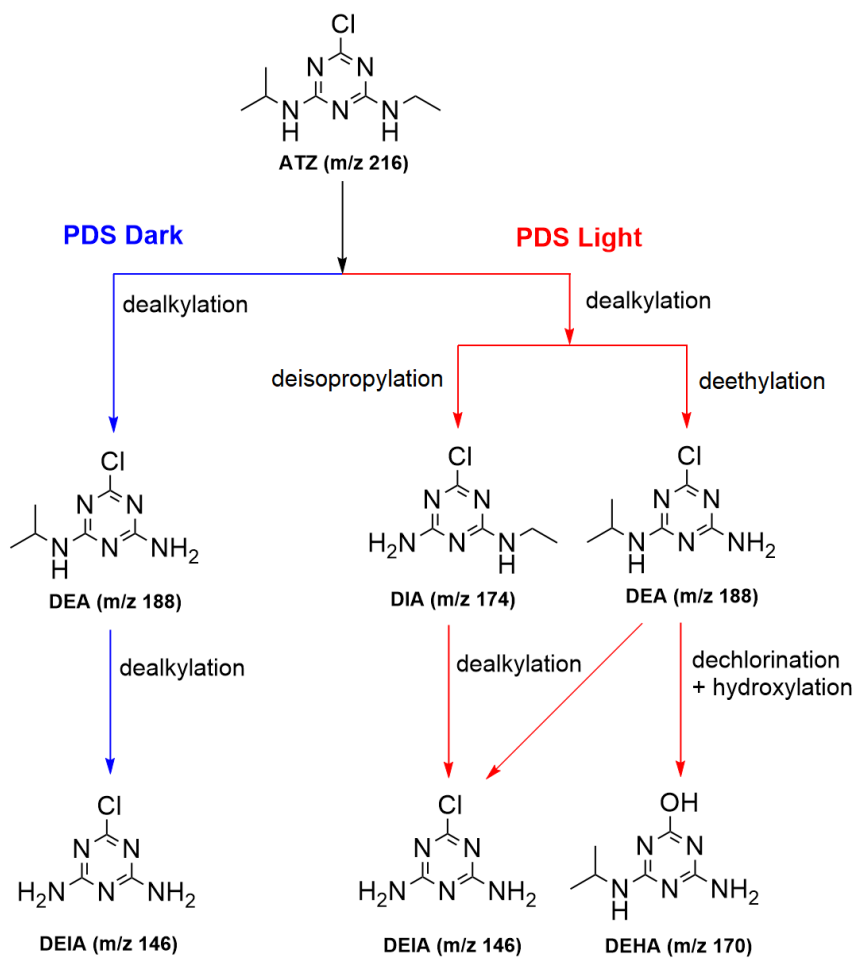


Figure S7. Proposed degradation pathways of ATZ by PDS Dark and PDS Light.

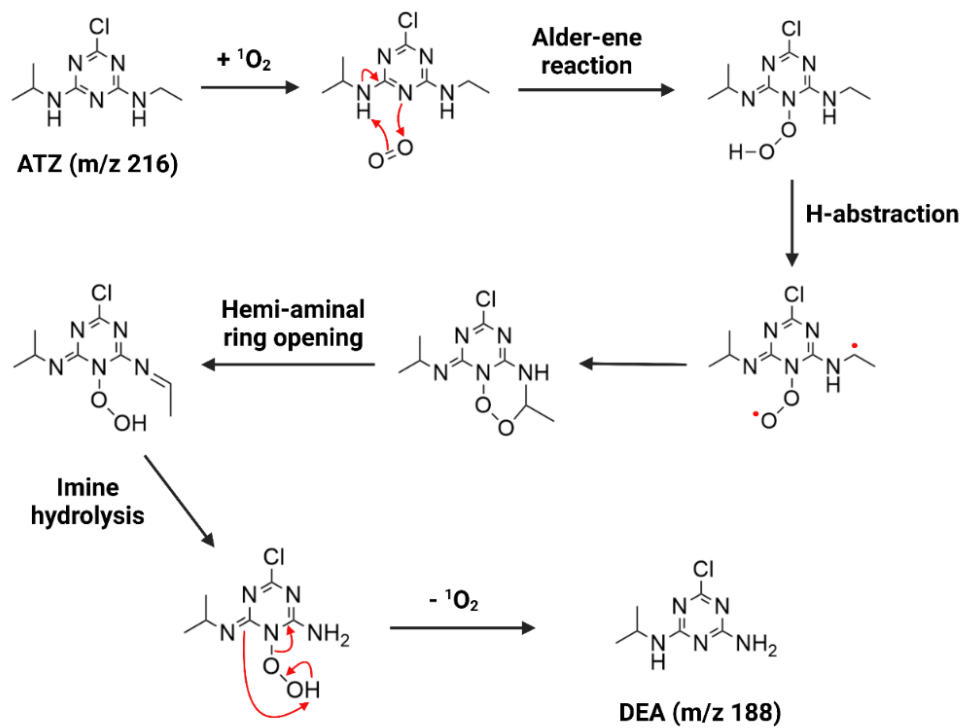


Figure S8. Possible degradation pathway of ATZ by $^1\text{O}_2$ in the PDS light system.

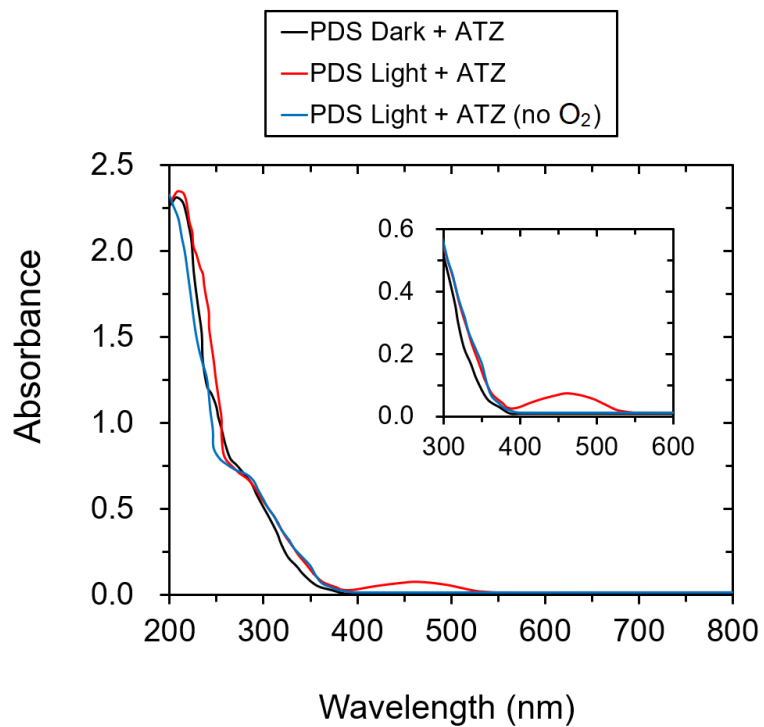


Figure S9. Detection of H₂O₂ based on the UV-Vis absorbance spectra of samples of PDS Dark and PDS Light in the presence of ATZ; absorption at ~450 nm indicates the formation of peroxovanadate as a product of H₂O₂ and vanadate; a zoomed-in image is presented in the inset ([PDS]₀ = 5.0 mM, [NH₄VO₃]₀ = 10.0 mM, [Na₂HPO₄] = 10.0 mM).

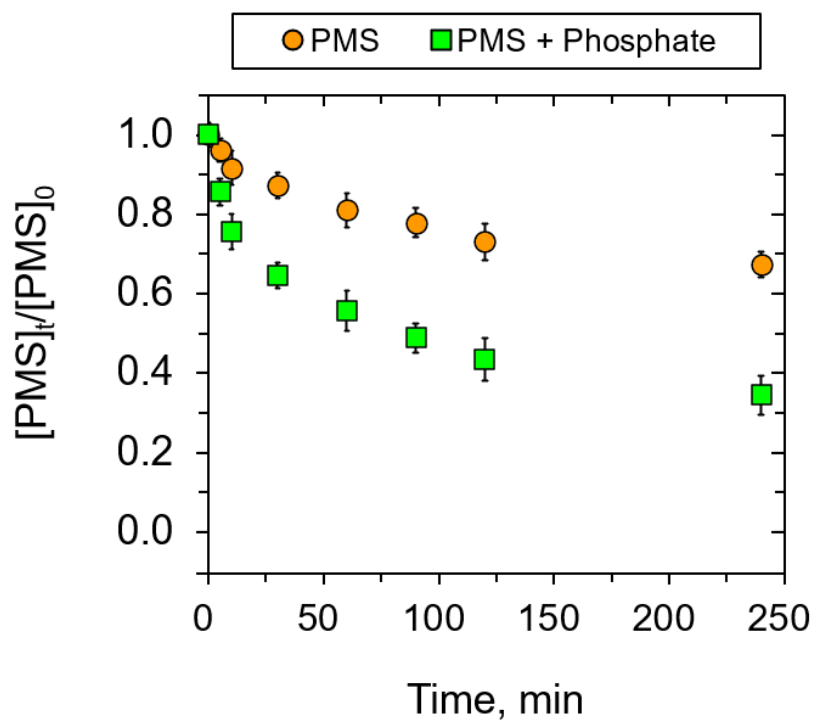


Figure S10. Decay of PMS with and without phosphate ($[ATZ]_0 = 10.0 \mu\text{M}$; $[PMS]_0 = 5.0 \text{ mM}$; $[\text{Na}_2\text{HPO}_4] = 0$ or 10.0 mM ; $\text{pH}_0 = 7.0$; $T = 25 \text{ }^\circ\text{C}$).

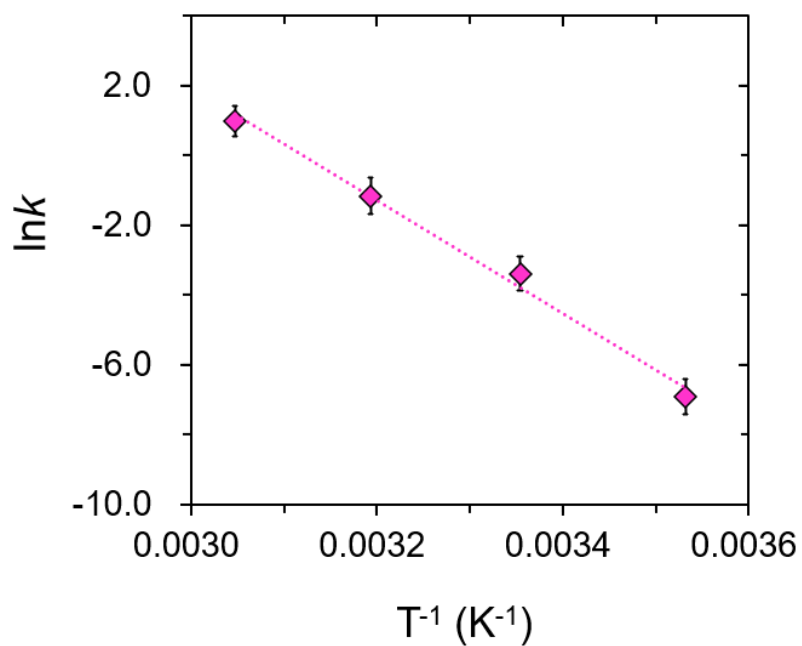


Figure S11. Relationship between rate constants of ATZ degradation and temperature ($[\text{ATZ}]_0 = 10.0 \mu\text{M}$; $[\text{PMS}]_0 = 5.0 \text{ mM}$; $[\text{Na}_2\text{HPO}_4] = 10.0 \text{ mM}$; $T = 10, 25, 40, 55 \text{ }^\circ\text{C}$).

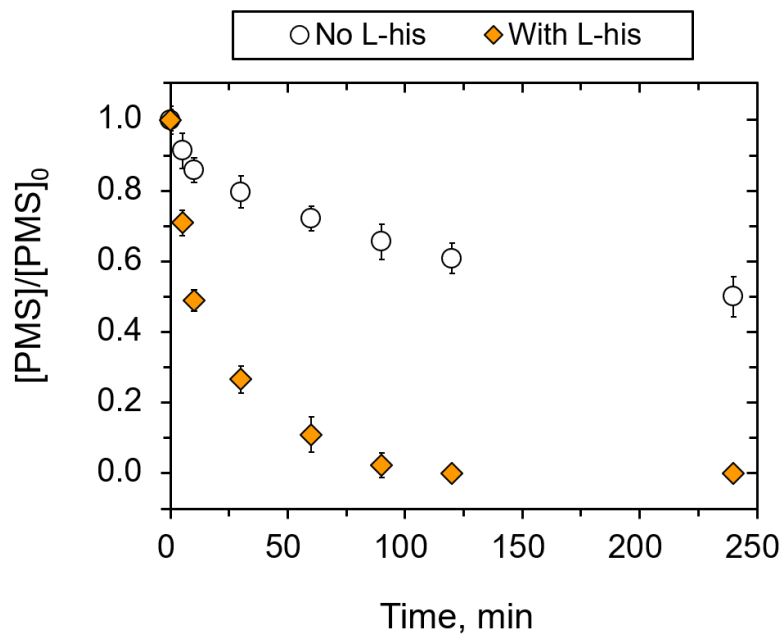


Figure S12. Decay of PMS in the presence and absence of L-his ($[PMS]_0 = 5.0$ mM; $[L\text{-his}]_0 = 0$ or 0.5 M; $[Na_2HPO_4] = 10.0$ mM; $pH_0 = 7.0$; $T = 25$ °C).

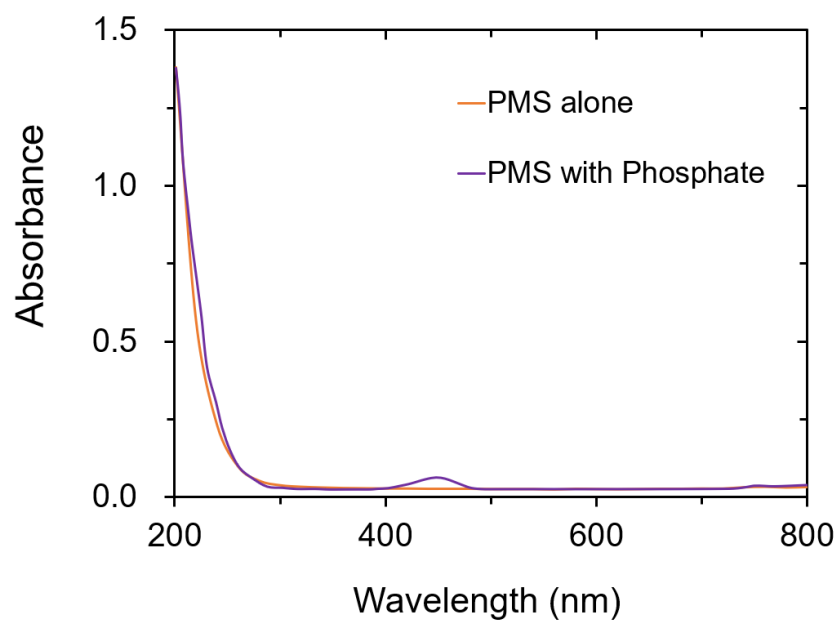


Figure S13. Detection of H_2O_2 based on the UV-Vis absorbance spectra of PMS with and without phosphate buffer; absorption at ~ 450 nm indicates the formation of peroxovanadate as a product of H_2O_2 and vanadate ($[\text{PMS}]_0 = 5.0$ mM; $[\text{NH}_4\text{VO}_3]_0 = 10.0$ mM; $[\text{Na}_2\text{HPO}_4] = 0$ or 10.0 mM; $T = 25$ °C).

Abbreviations	Structure	RT [min]	Formula	m/z ratio
ATZ	<chem>CC(C)Nc1nc(Cl)c2nc(C)nc12</chem>	2.492	C ₈ H ₁₄ ClN ₅	216.1011
CNIT	<chem>CC(C)Nc1nc(Cl)c2nc(C)nc12O</chem>	2.164	C ₈ H ₁₄ ClN ₅ O	232.0960
CDIT	<chem>CC(C)Nc1nc(Cl)c2nc(C)nc12C(=O)C</chem>	2.097	C ₈ H ₁₂ ClN ₅ O	230.1169
CDAT	<chem>NC1=NC(Cl)=NC(C)N1C(=O)C</chem>	2.007	C ₅ H ₆ ClN ₅ O	188.0696

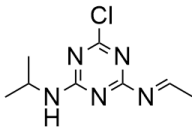
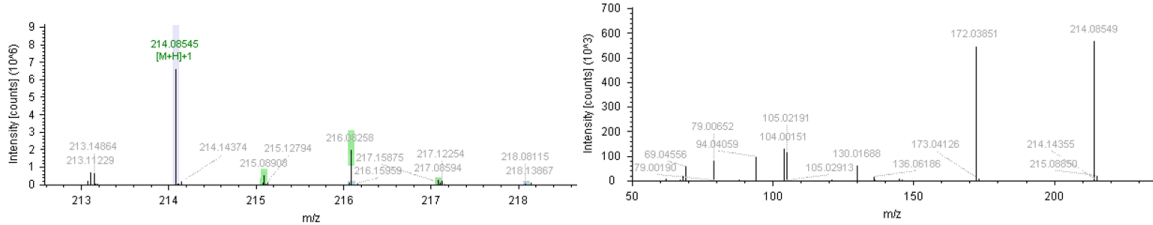
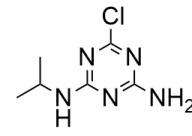
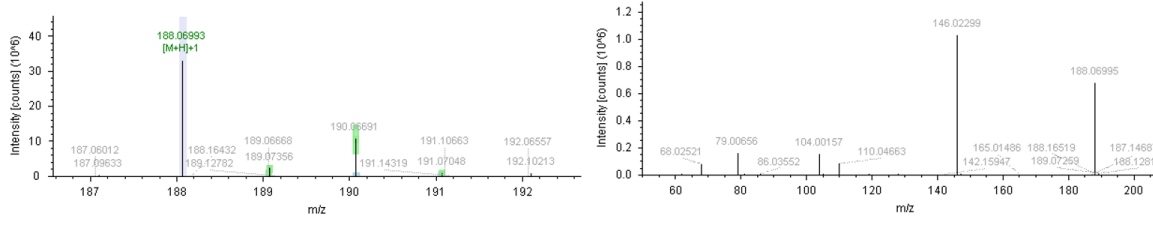
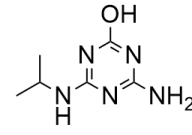
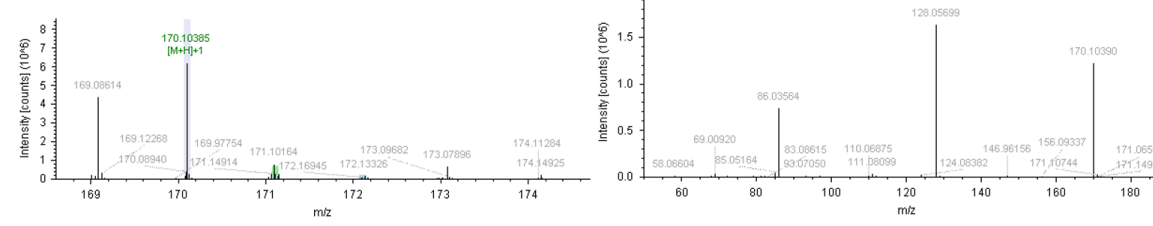
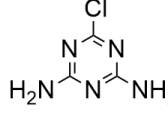
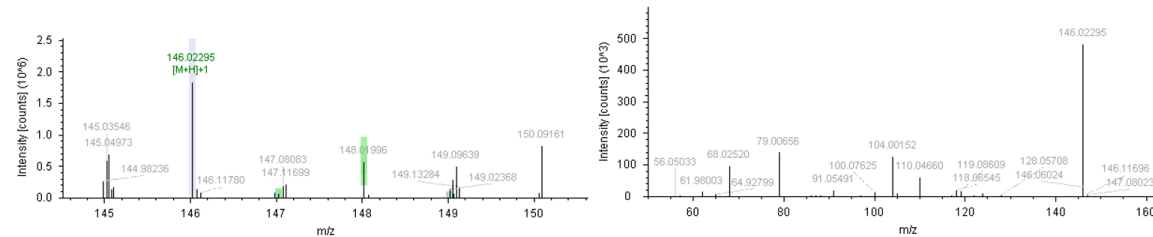
Abbreviations	Structure	RT [min]	Formula	m/z ratio
CVIT		2.064	C ₈ H ₁₂ ClN ₅	214.0854
				
DEA		1.947	C ₆ H ₁₀ ClN ₅	188.0699
				
DEHA		0.837	C ₆ H ₁₁ N ₅ O	170.1038
				
DEIA		1.944	C ₃ H ₄ ClN ₅	146.0229
				

Figure S14. MS1 and MS2 spectra of identified oxidation products of ATZ by PMS

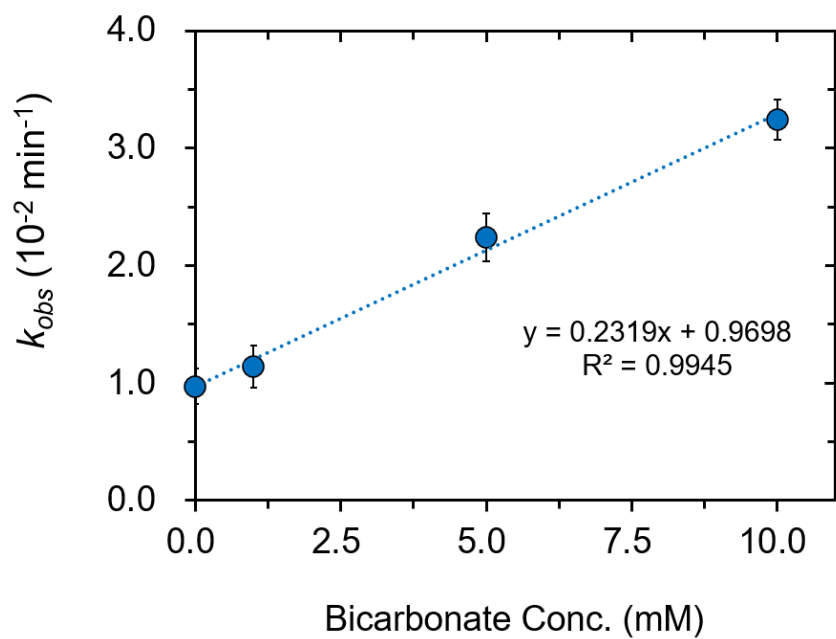


Figure S15. Linear relationship between the pseudo-first-order rate constant of ATZ degradation and HCO_3^- concentration ($[\text{ATZ}]_0 = 10.0 \mu\text{M}$; $[\text{PMS}]_0 = 5.0 \text{ mM}$; no phosphate buffer; $[\text{HCO}_3^-]_0 = 0, 1.0, 5.0, 10.0 \text{ mM}$; $\text{pH}_0 = 7.0$; $T = 25 \text{ }^\circ\text{C}$).

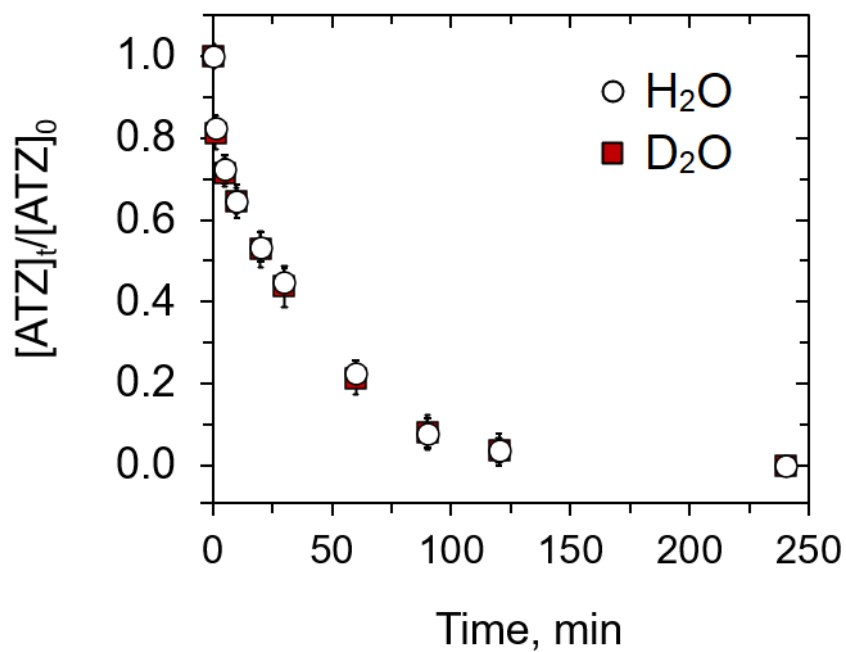


Figure S16. Degradation of ATZ by PMS in H₂O and D₂O in presence of 10 mM HCO₃⁻ ([ATZ]₀ = 10.0 μM; [PMS]₀ = 5.0 mM; [HCO₃⁻]₀ = 10.0 mM; pH₀ = 7.0; T = 25 °C).

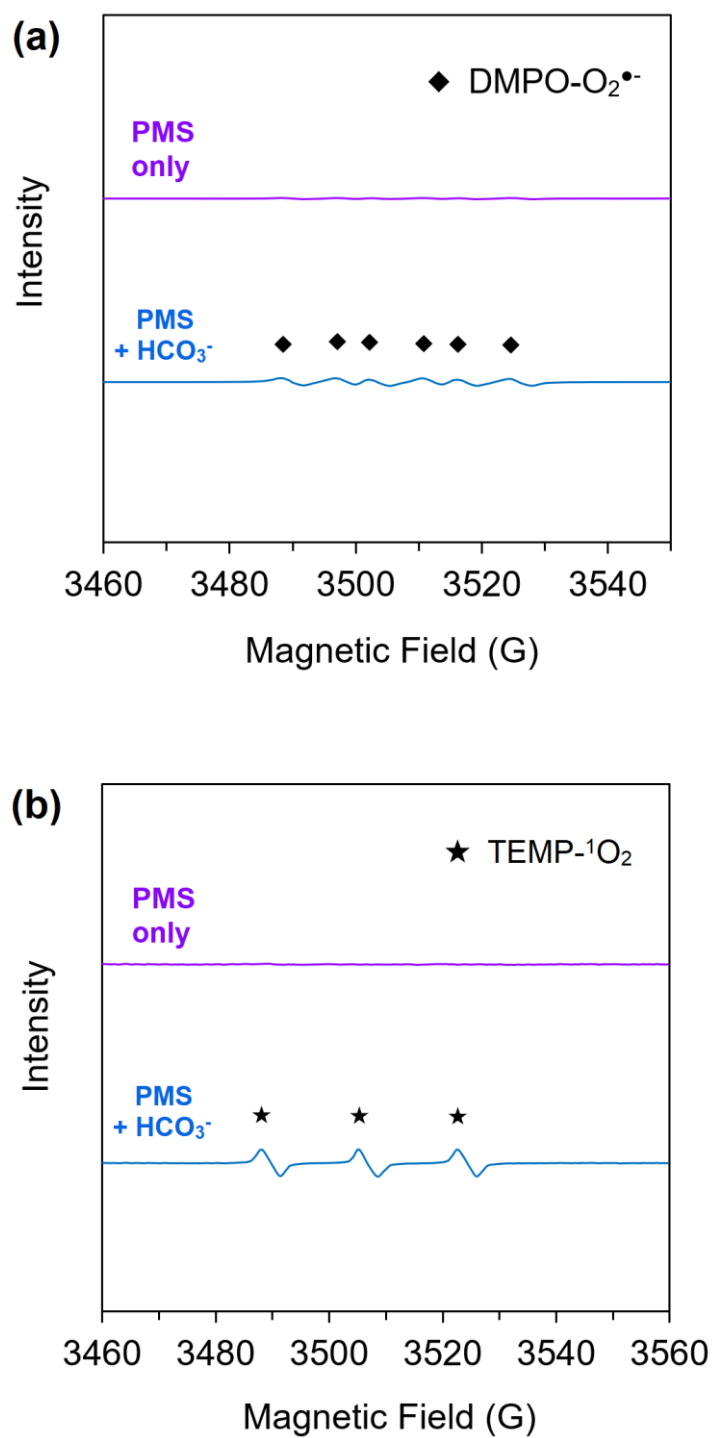


Figure S17. EPR spectra of (a) O₂^{•-} and (b) ¹O₂ for PMS with and without 10 mM HCO₃⁻ ([PMS]₀ = 5.0 mM; [DMPO] = [TEMP] = 50.0 mM; [HCO₃⁻]₀ = 0 or 10.0 mM; pH₀ = 7.0; T = 25 °C).

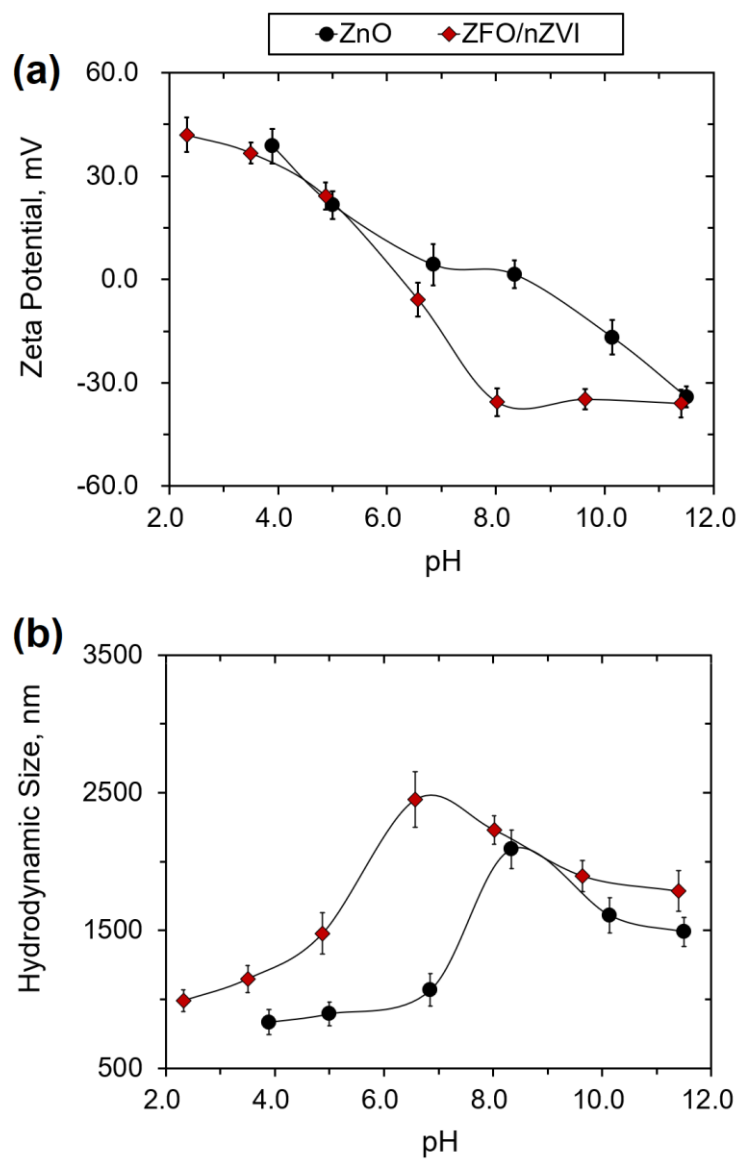


Figure S18. (a) Zeta potentials and (b) hydrodynamic sizes of ZnO and ZnFe₂O₄/nZVI at pH 2.0-11.5 ([catalyst] = 0.1 g/L).

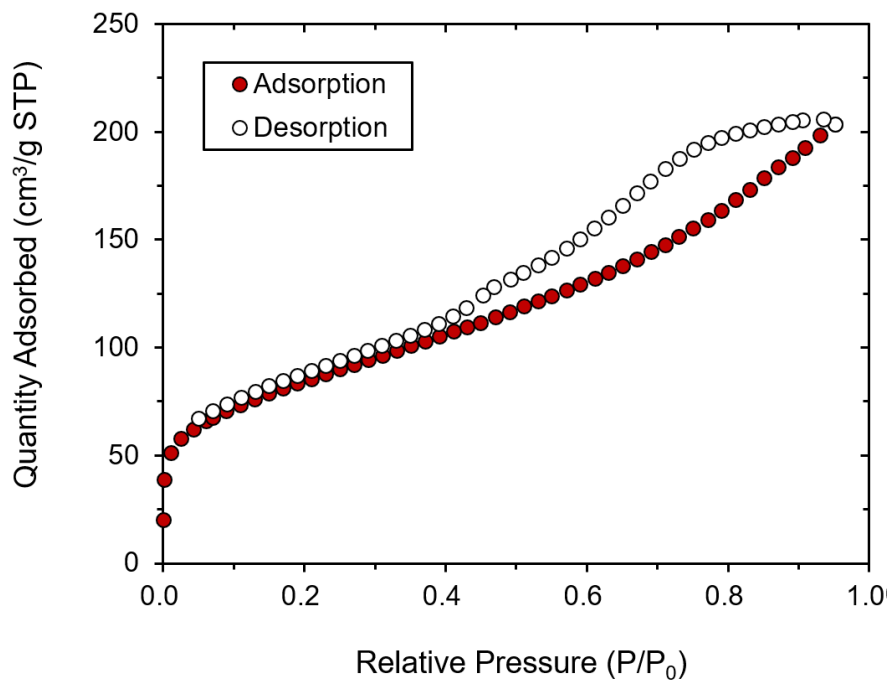


Figure S19. N₂ adsorption-desorption isotherm of ZnFe₂O₄/nZVI nanocomposite (T = 77 K)

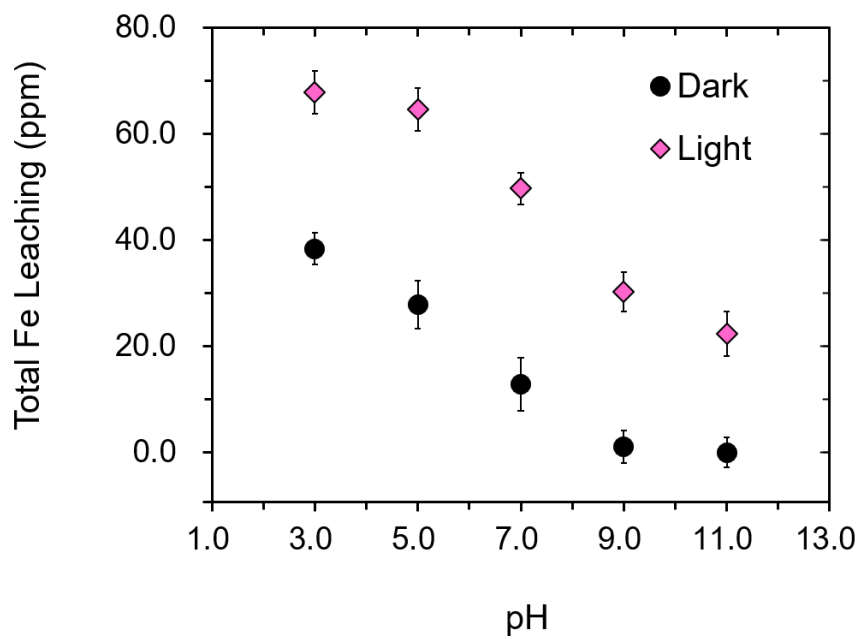


Figure S20. Total leaching of Fe from ZnFe₂O₄/nZVI in dark and under light at pH 3.0-11.0

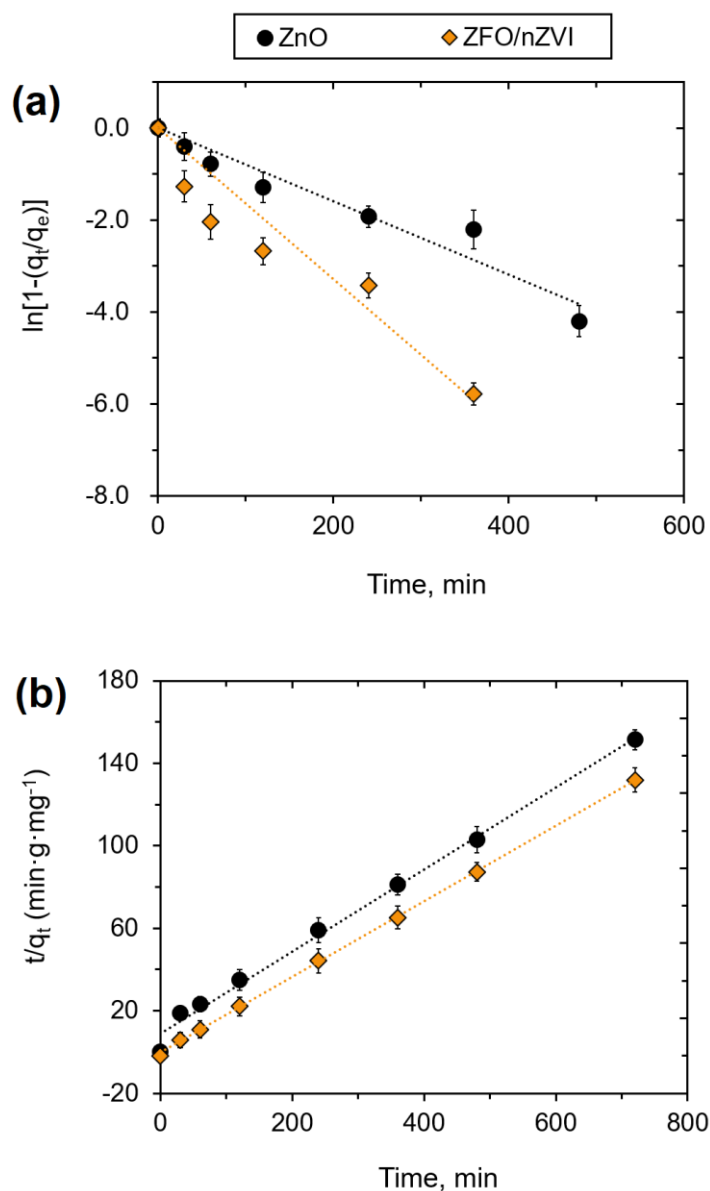


Figure S21. Linear fits of As adsorption with (b) pseudo-first-order and (c) pseudo-second-order kinetic models (ZnFe₂O₄/nZVI is abbreviated as ZFO/nZVI; [As]₀ = 100 μg/L; [adsorbent]₀ = 0.2 g/L; initial pH=7.0).

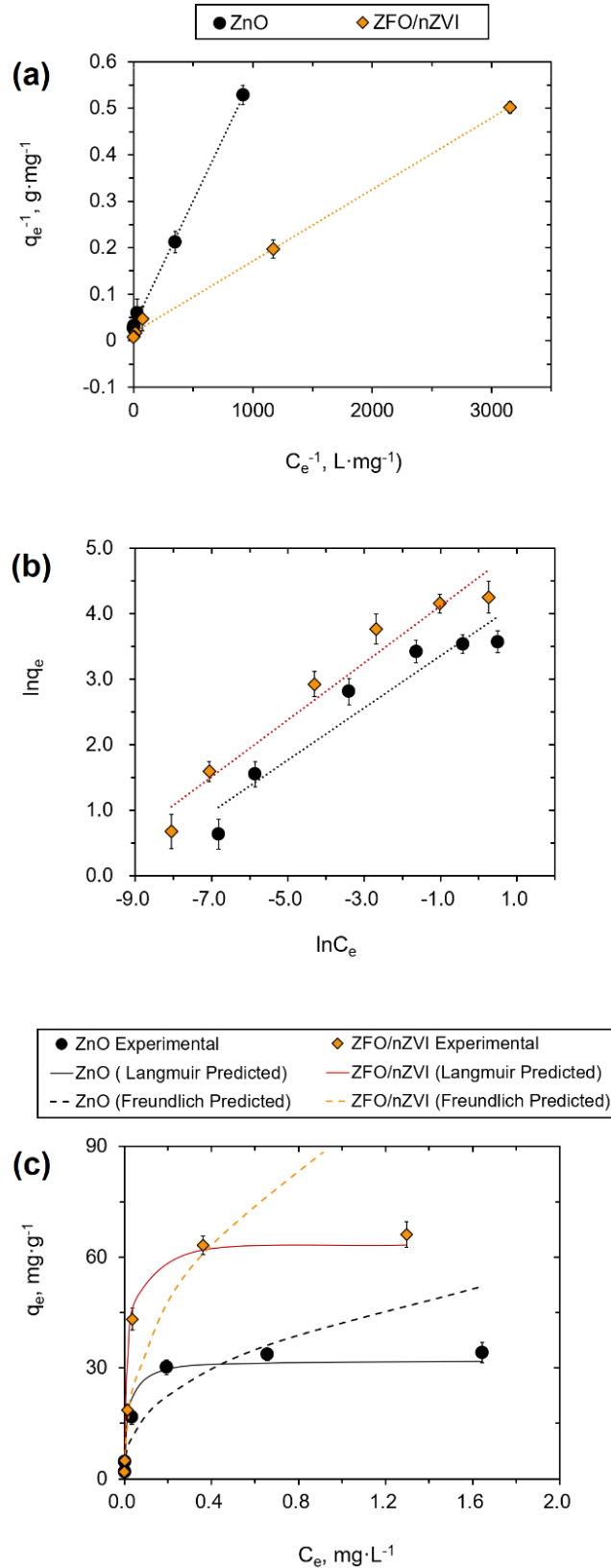


Figure S22. Linearized plots of As adsorption on ZnO and ZnFe₂O₄/nZVI with (a) Langmuir and (b) Freundlich model; (c) the experimental data of adsorption isotherm in comparison with q_e predicted by Langmuir and Freundlich model (ZnFe₂O₄/nZVI is abbreviated as ZFO/nZVI; [As]₀ = 100 µg/L; [adsorbent]₀ = 0.2 g/L; initial pH=7.0).

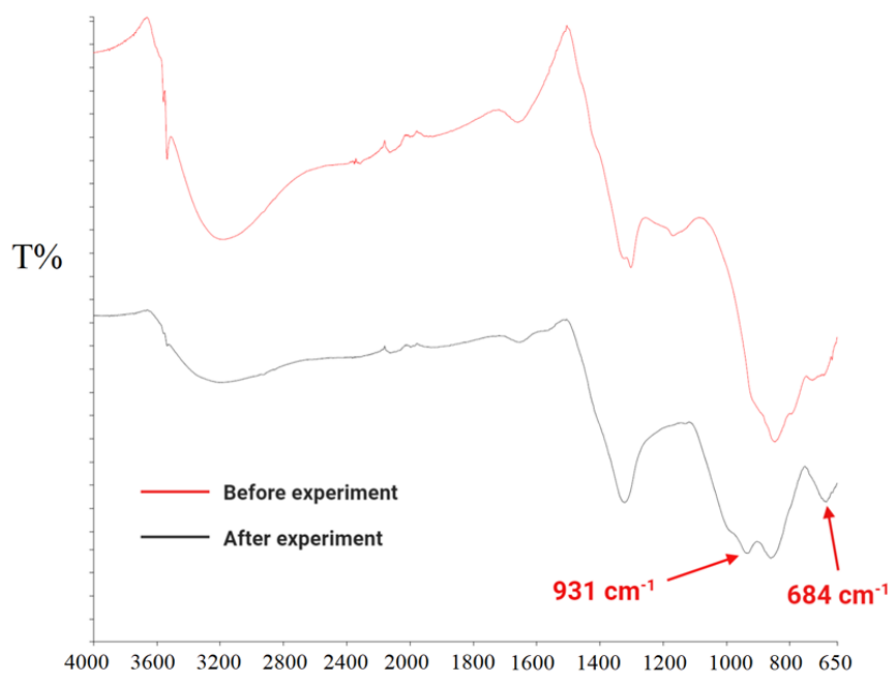


Figure S23. ATR-FITR spectra of the ZnFe₂O₄/nZVI nanocomposite before and after As adsorption.

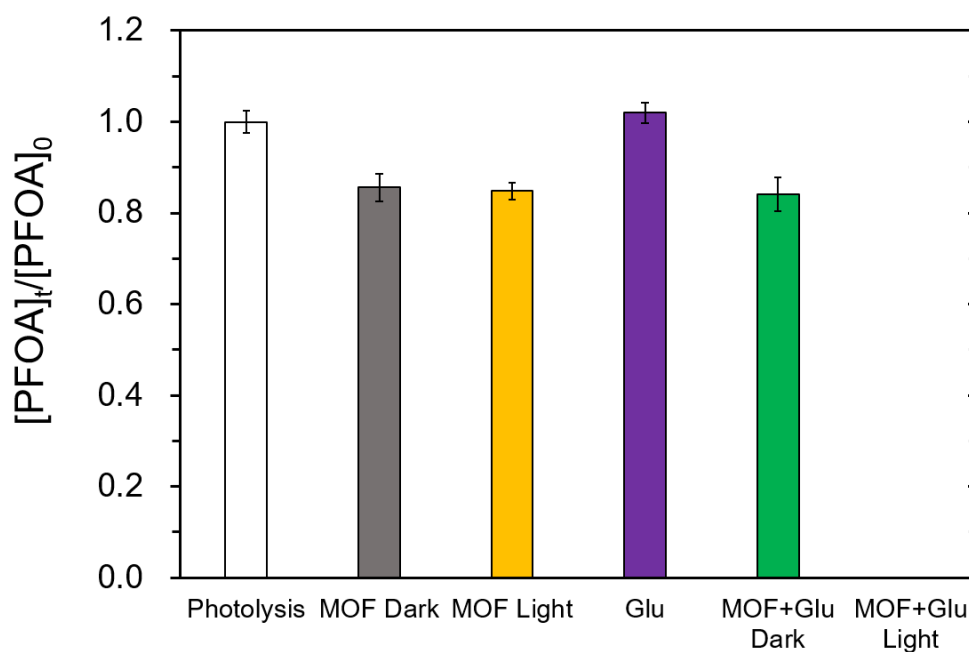


Figure S24. The decay of PFOA under different conditions ($[PFOA]_0 = 100 \mu\text{g/L}$; MOF loading = 0 or 2.5 g/L; $[\text{glucose}]_0 = 0$ or 0.5 M; reaction time = 24 hours; $T = 20^\circ\text{C}$).

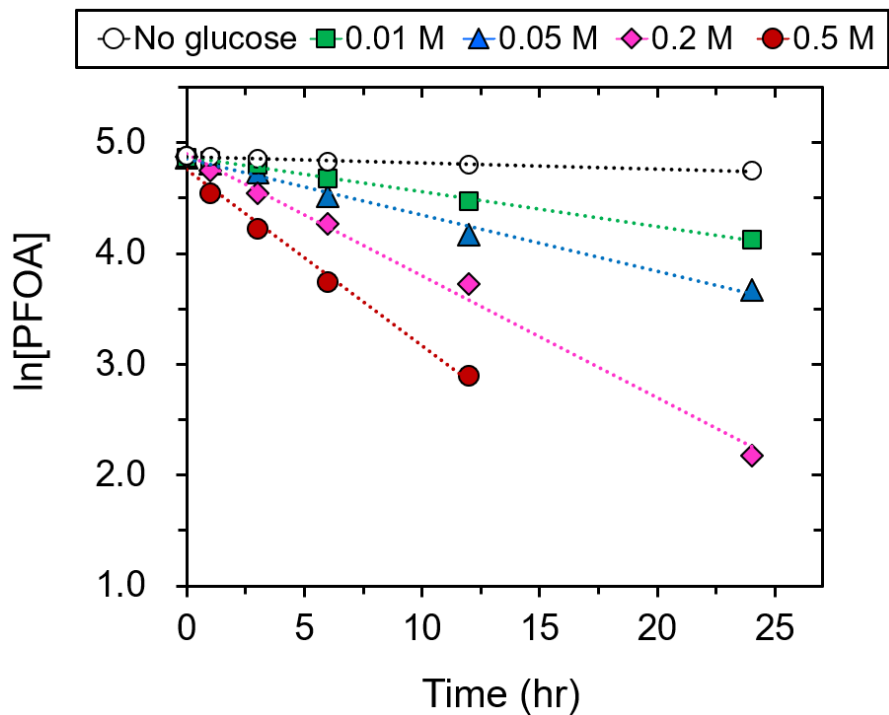


Figure S25. Fitted linear regression of PFOA decay by MIL-125-NH₂ in presence of different glucose concentrations ([PFOA]₀ = 100 μg/L; MOF loading = 2.5 g/L; [glucose]₀ = 0, 0.01, 0.05, 0.2, 0.5 M; T = 20°C).

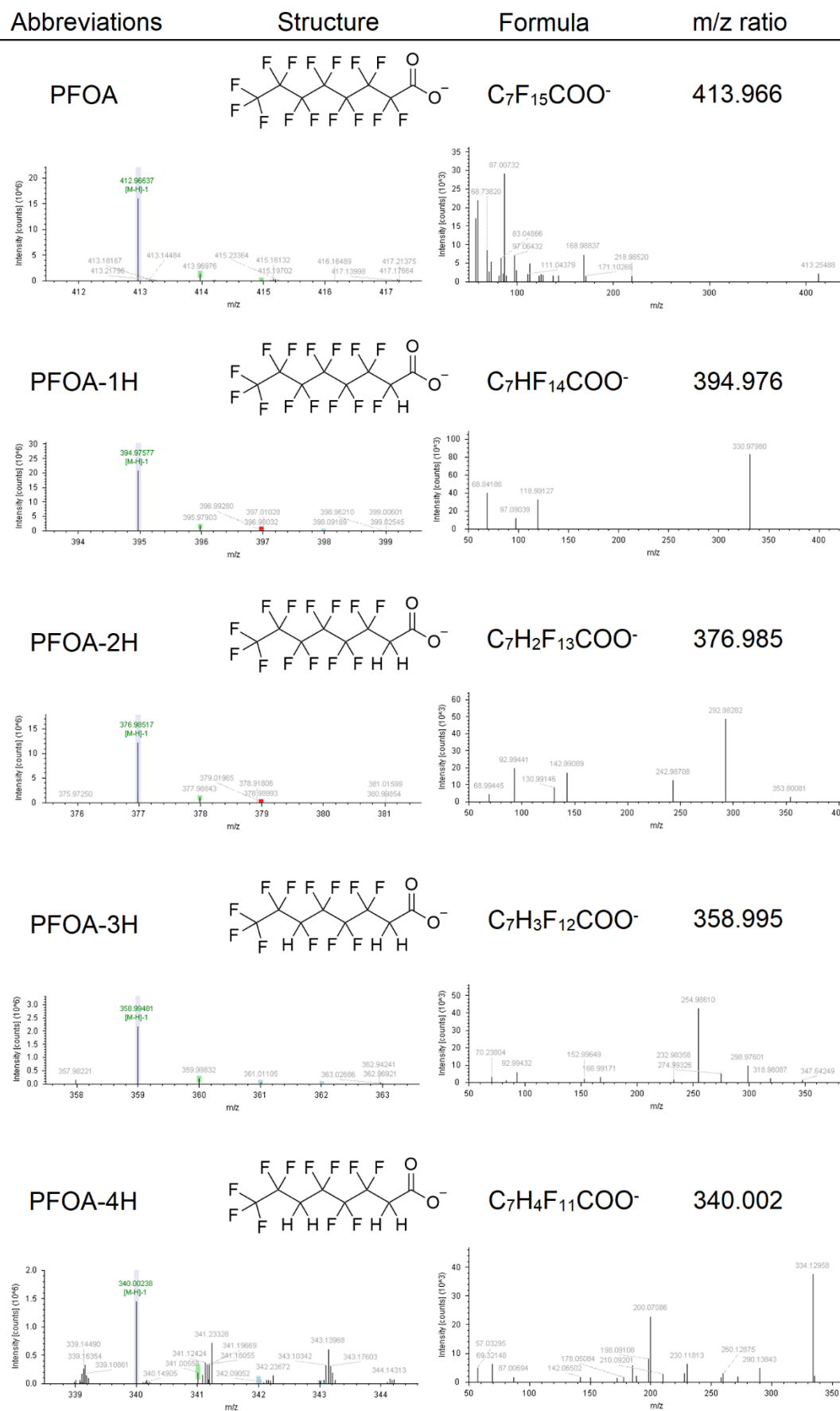


Figure S26. MS1 and MS2 spectra of possible degradation metabolites (part 1)

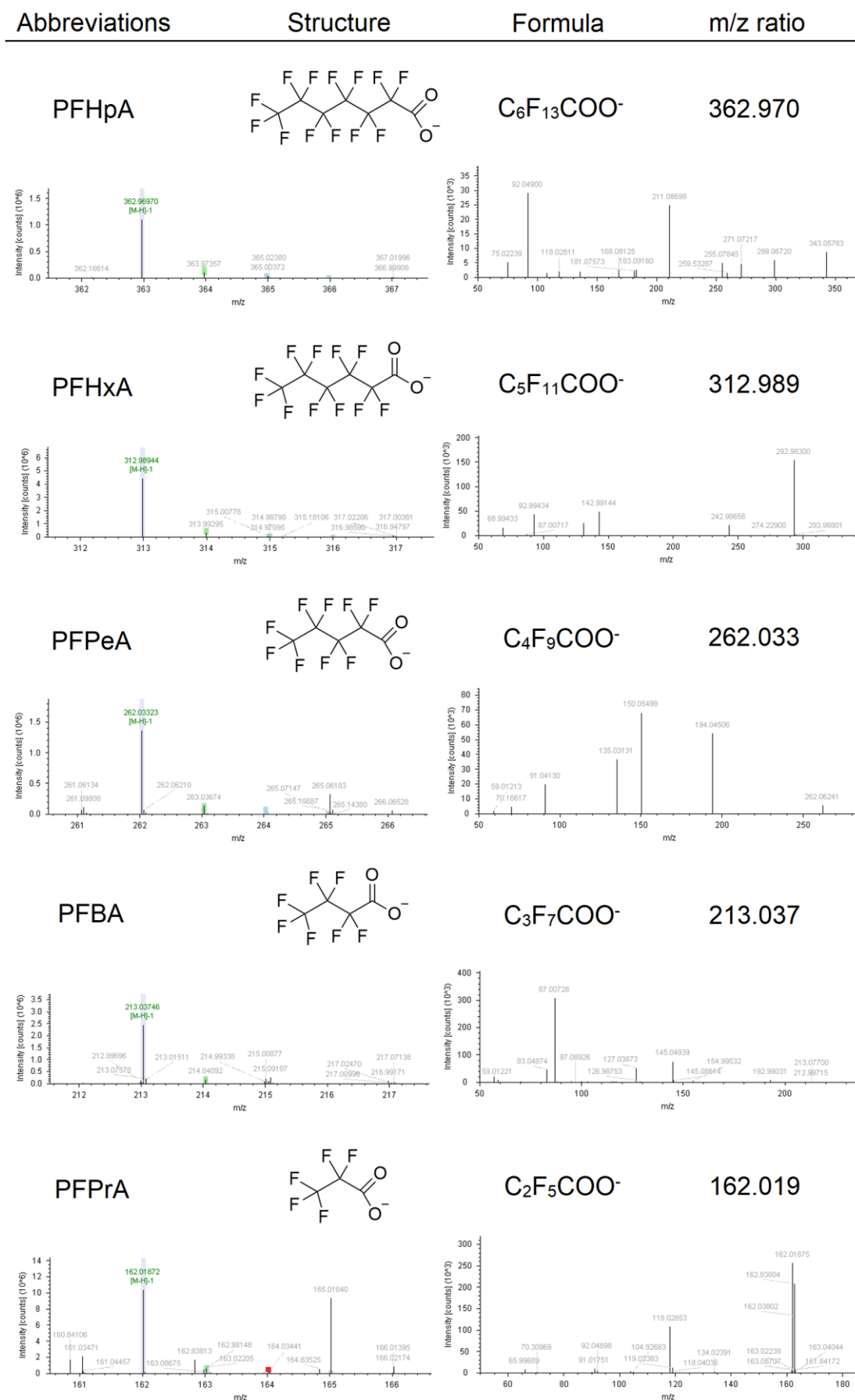


Figure S27. MS1 and MS2 spectra of possible degradation metabolites (part 2)

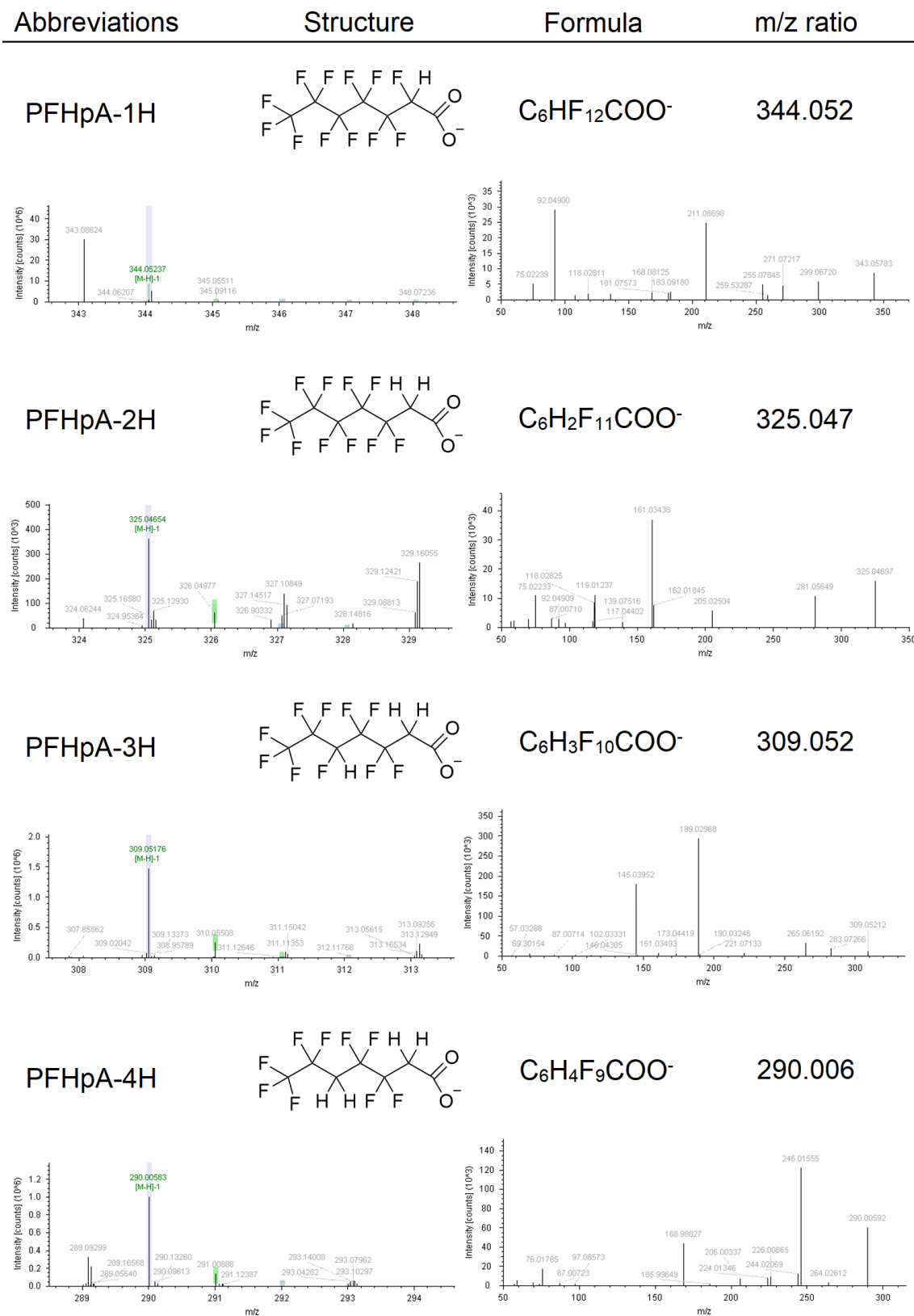


Figure S28. MS1 and MS2 spectra of possible degradation metabolites (part 3)

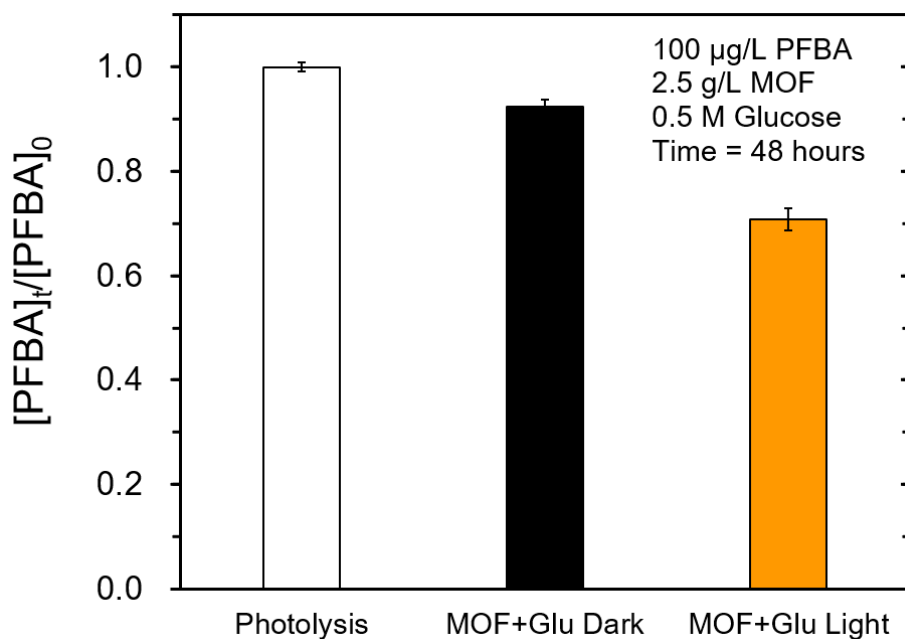


Figure S29. Removal efficiency of PFBA by direct photolysis and MIL-125-NH₂/glucose (in dark and under light irradiation) ([PFBA]₀ = 100 µg/L; MOF loading = 2.5 g/L; [glucose]₀ = 0.5 M; reaction time = 48 hours; T = 20°C).

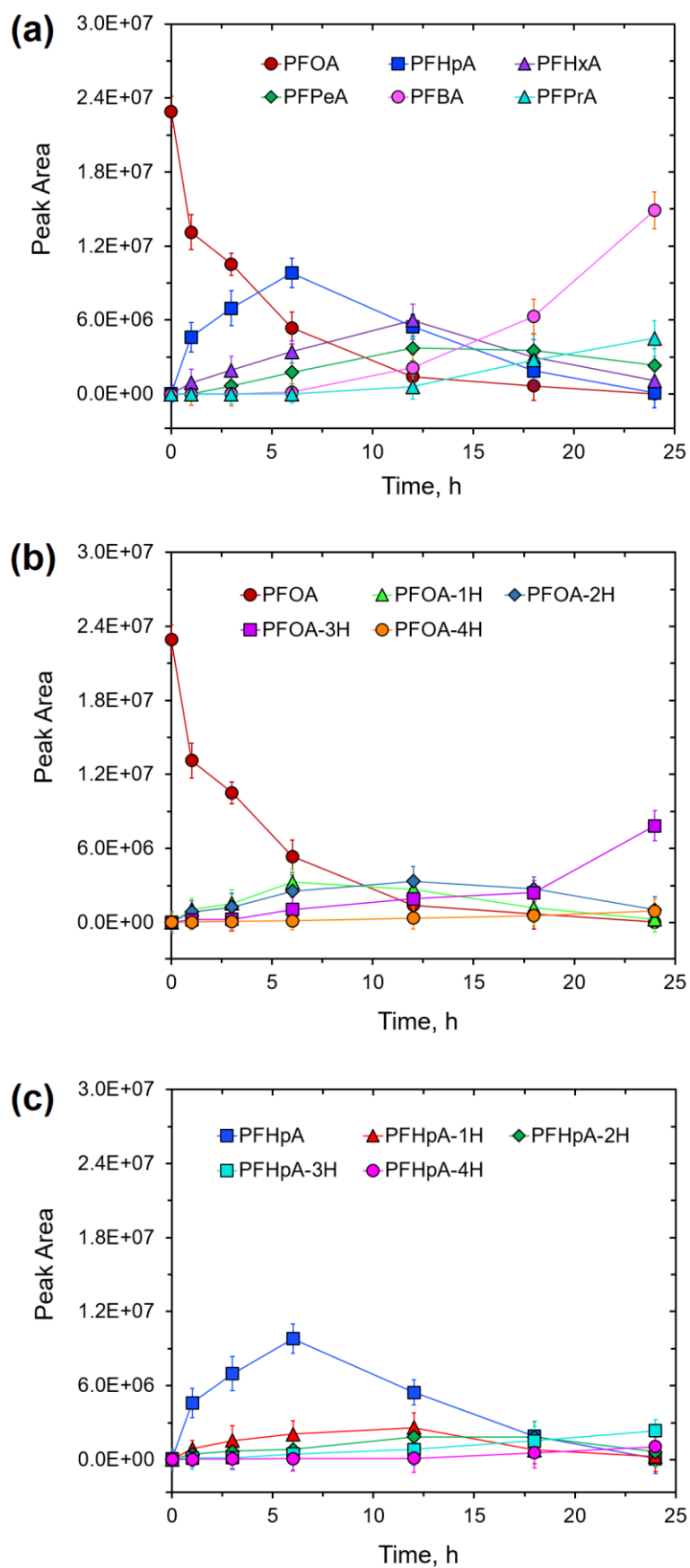


Figure S30. Changes in peak areas of (a) PFCAs, (b) FTCAs from PFOA, and (c) FTCAs from PFHpA over time

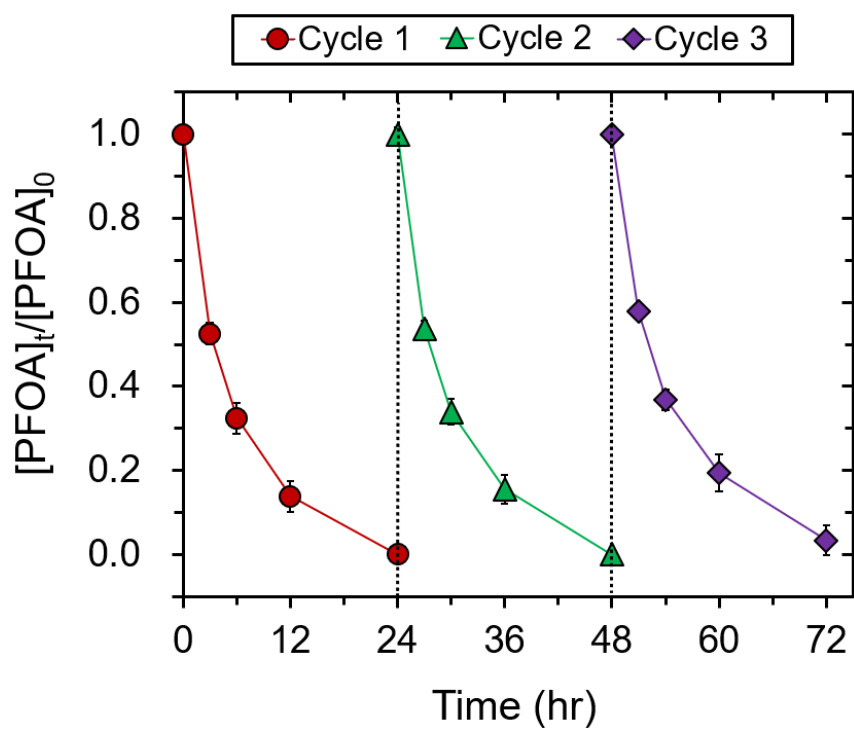


Figure S31. Decay of PFOA by MIL-125-NH₂ under light over three cycles ([PFOA]₀ = 100 μg/L; MOF loading = 2.5 g/L; [glucose]₀ = 0.5 M; T = 20°C).

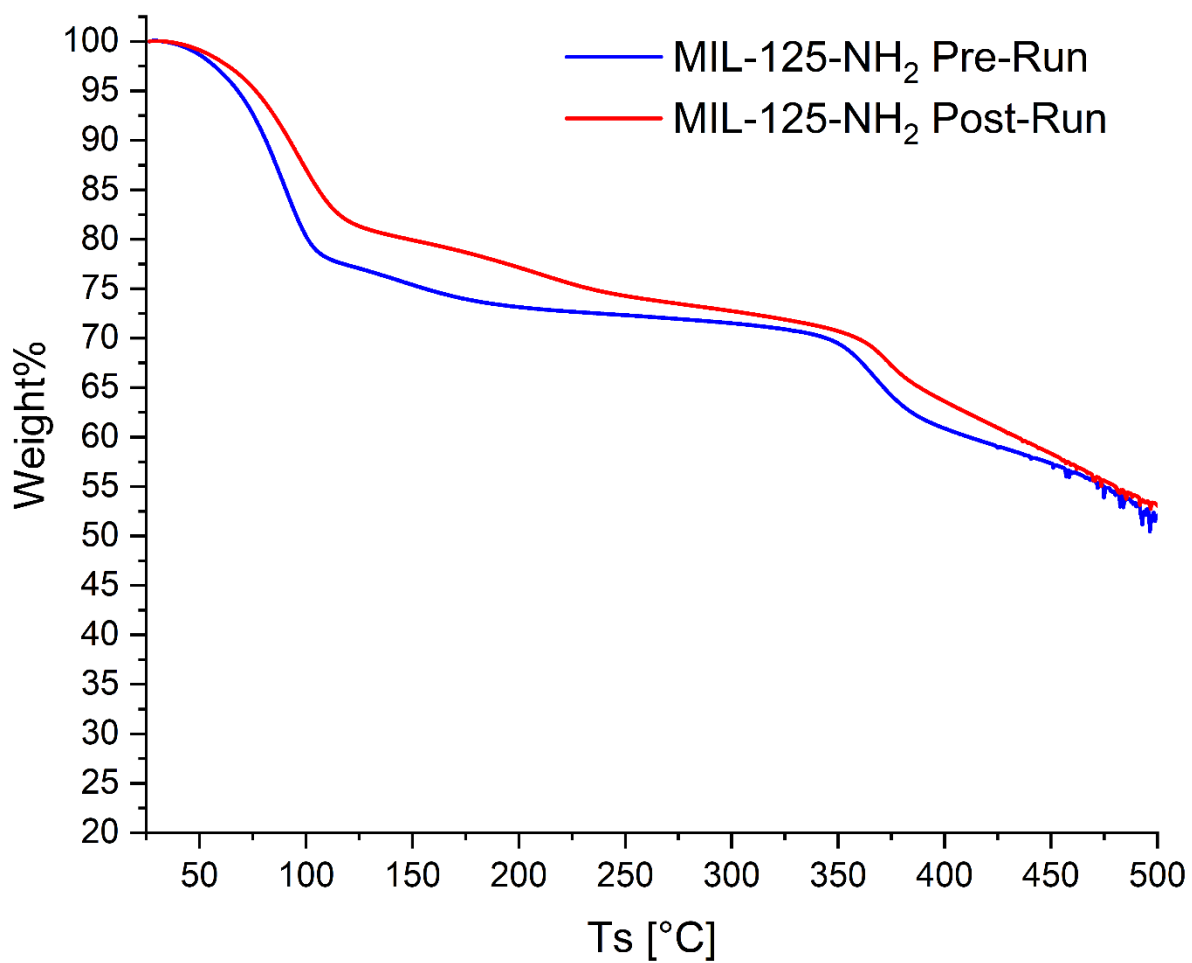


Figure S32. The TGA curves of MIL-125-NH₂ before and after three cycles of PFOA removal experiments under light.

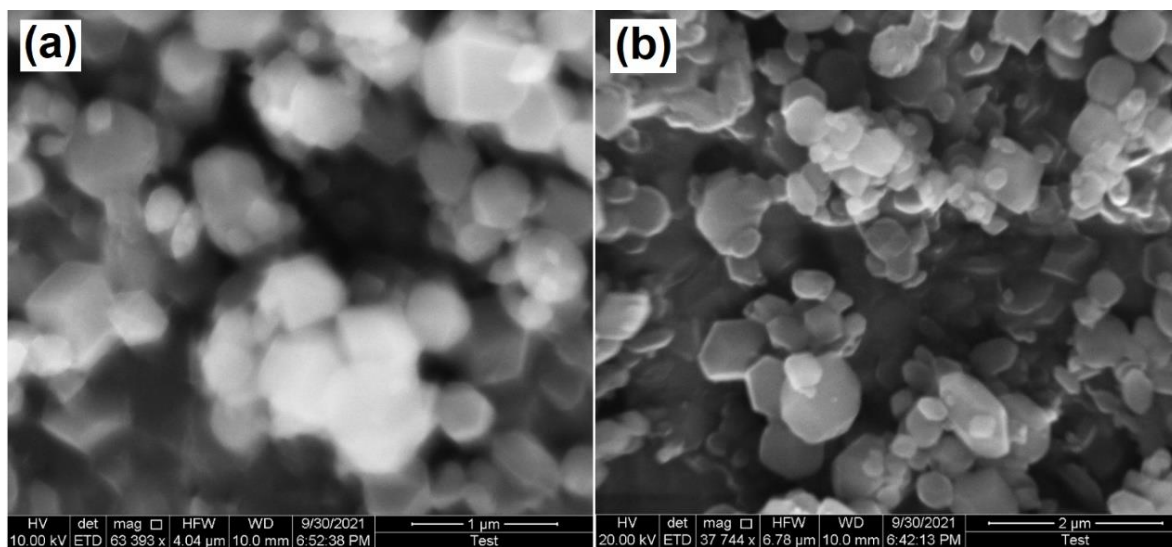


Figure S33. The SEM images of MIL-125-NH₂ (a) before and (b) after three cycles of PFOA removal experiments under light.

Supporting Tables

Table S1. Light fluxes received by the PDS reaction solutions with and without UV filter

	Wavelength (nm)	Flux (W/cm^2)	
		Without UV filter	With UV filter
Visible	400-700	$39.8 \pm 0.5 \times 10^{-3}$	$39.6 \pm 0.3 \times 10^{-3}$
UV-A	315-400	$8.1 \pm 0.2 \times 10^{-6}$	$2.0 \pm 0.2 \times 10^{-6}$
UV-B	280-315	$2.5 \pm 0.4 \times 10^{-6}$	0
UV-C	230-280	0	0

Table S2. Information about the identified degradation intermediates of ATZ by PDS in dark and under light

Full Names	Abbreviations	Molecular	m/z
2-chloro-4-amino-6-isopropylamino-1,3,5-triazine	DEA	$C_6H_{10}ClN_5$	188
2-chloro-4-ethylamino-6-amino-1,3,5-triazine	DIA	$C_5H_8ClN_5$	174
2-hydroxyl-4-Amino-6-(isopropylamino)-1,3,5-triazine	DEHA	$C_6H_{11}N_5O$	170
2-chloro-4,6-diamino-1,3,5-triazine	DEIA	$C_3H_4ClN_5$	146

Table S3. Pseudo-first-order rate constants of ATZ degradation by PMS at different temperatures

Temperature (°C)	k_{obs} (min⁻¹)	r²
10	$9.9 \pm 0.3 \times 10^{-4}$	0.93
25	$4.4 \pm 0.3 \times 10^{-2}$	0.98
40	$3.1 \pm 0.2 \times 10^{-1}$	0.95
55	2.7 ± 0.2	0.97

Table S4. Tentative oxidation products of ATZ in the PMS system

Full Names	Abbreviations	Molecular formula	m/z
1-((4-Chloro-6-(isopropylamino)-1,3,5-triazin-2-yl) amino) ethanol	CNIT	$C_8H_{14}ClN_5O$	232
N-(4-chloro-6-(isopropylamino)-1,3,5-triazin-2-yl) acetamide	CDIT	$C_8H_{12}ClN_5O$	230
6-chloro-N ² -isopropyl-N ⁴ - vinyl-1,3,5-triazine-2,4-diamine	CVIT	$C_8H_{12}ClN_5$	214
2-chloro-4-amino-6-isopropylamino-1,3,5-triazine	DEA	$C_6H_{10}ClN_5$	188
2-acetamido-4-amino-6-chloro-s-triazine	CDAT	$C_5H_6ClN_5O$	188
2-hydroxyl-4-Amino-6-(isopropylamino)-1,3,5-triazine	DEHA	$C_6H_{11}N_5O$	170
2-chloro-4,6-diamino-1,3,5-triazine	DEIA	$C_3H_4ClN_5$	146

Table S5. Pseudo-first-order rate constants of ATZ degradation by PMS in presence of HCO₃⁻

Anions	Concentration (mM)	<i>k</i>_{obs} (min⁻¹)	r²
No anions	0	9.7 ± 0.5×10 ⁻³	0.97
HCO ₃ ⁻	1.0	1.1 ± 0.2×10 ⁻²	0.99
	5.0	2.2 ± 0.2×10 ⁻²	1.00
	10.0	3.2 ± 0.3×10 ⁻²	0.99

Table S6. Pseudo-first-order rate constants of ATZ degradation by PMS in lake water and river water

Water sample	k_{obs} (min⁻¹)	r^2
Lake Bryan	$6.3 \pm 0.4 \times 10^{-3}$	0.99
Brazos River	$7.3 \pm 0.5 \times 10^{-3}$	0.97

Table S7. Light fluxes received by the ZnFe₂O₄/nZVI nanocomposite

	Wavelength (nm)	Flux (W/cm ²)
Visible	400-700	$38.5 \pm 0.3 \times 10^{-3}$
UV-A	315-400	$1.6 \pm 0.1 \times 10^{-6}$
UV-B	280-315	0
UV-C	230-280	0

Table S8. Kinetic parameters for As adsorption on ZnO and ZnFe₂O₄/nZVI

Adsorbent	Pseudo-first-order		Pseudo-second-order			
	k_{ads} (min ⁻¹)	r^2	q_e (mg·g ⁻¹)	k_{ads} (g·mg ⁻¹ ·min ⁻¹)	h (mg·g ⁻¹ ·min ⁻¹)	r^2
ZnO	0.008	0.97	4.89	0.005	0.1193	0.99
ZnFe ₂ O ₄ /nZVI	0.016	0.96	4.95	0.025	0.6217	1.00

Table S9. Isotherm parameters for As adsorption on ZnO and ZnFe₂O₄/nZVI

Adsorbent	Langmuir Model			Freundlich Model		
	q_{max} (mg·g ⁻¹)	K_L (L·mg ⁻¹)	R ²	n	K_F (mg·L ⁻¹ ·(L·mg ⁻¹) ⁿ)	R ²
ZnO	32.1543	62.20	0.998	0.398	42.82	0.911
ZnFe ₂ O ₄ /nZVI	58.8235	85.00	0.997	0.435	94.82	0.891

Table S10. Light fluxes emitted by the medium pressure Hg-lamp

	λ (nm)	Light flux (W/cm ²)
Visible	400-700	$1.3 \pm 0.2 \times 10^{-1}$
UV-A	315-400	$7.2 \pm 0.6 \times 10^{-2}$
UV-B	280-315	$1.3 \pm 0.1 \times 10^{-2}$
UV-C	230-280	$2.8 \pm 0.3 \times 10^{-4}$

Table S11. Pseudo-first-order rate constants of PFOA removal by MIL-125-NH₂ in presence of different glucose concentrations

	Rate Constant (10 ⁻³ min ⁻¹)	r ²
No glucose	0.101 ± 0.02	0.99
0.01 M	0.520 ± 0.03	1.00
0.05 M	0.847 ± 0.06	0.99
0.2 M	1.84 ± 0.10	0.99
0.5 M	2.64 ± 0.16	0.99

Table S12. Pseudo-first-order rate constants of PFOA removal by MIL-125-NH₂ in presence of different quenchers

	Rate Constant (10^{-3} min^{-1})	r^2
No quencher	0.101 ± 0.02	0.97
Glucose	2.64 ± 0.16	0.99
Glucose + SOD	2.51 ± 0.19	0.99
AgNO ₃	0.382 ± 0.04	0.96

Table S13. Pseudo-first-order rate constants of PFOA removal by MIL-125-NH₂ and recovery rate of dry mass over three cycles

	Rate Constant (10^{-3} min^{-1})	r^2	Dry mass recovery
Cycle 1	2.64 ± 0.16	0.99	90%
Cycle 2	2.54 ± 0.18	0.99	80%
Cycle 3	2.30 ± 0.15	1.00	64%

REFERENCES

- (1) Combi, T.; Pintado-Herrera, M. G.; Lara-Martin, P. A.; Misericocchi, S.; Langone, L.; Guerra, R. Distribution and Fate of Legacy and Emerging Contaminants along the Adriatic Sea: A Comparative Study. *Environ. Pollut.* **2016**, *218*, 1055–1064.
<https://doi.org/10.1016/J.ENVPOL.2016.08.057>.
- (2) Pintado-Herrera, M. G.; Wang, C.; Lu, J.; Chang, Y. P.; Chen, W.; Li, X.; Lara-Martín, P. A. Distribution, Mass Inventories, and Ecological Risk Assessment of Legacy and Emerging Contaminants in Sediments from the Pearl River Estuary in China. *J. Hazard. Mater.* **2017**, *323*, 128–138.
<https://doi.org/10.1016/J.JHAZMAT.2016.02.046>.
- (3) Ferrario, C.; Finizio, A.; Villa, S. Legacy and Emerging Contaminants in Meltwater of Three Alpine Glaciers. *Sci. Total Environ.* **2017**, *574*, 350–357.
<https://doi.org/10.1016/J.SCITOTENV.2016.09.067>.
- (4) Ateia, M.; Alalm, M. G.; Awfa, D.; Johnson, M. S.; Yoshimura, C. Modeling the Degradation and Disinfection of Water Pollutants by Photocatalysts and Composites: A Critical Review. *Sci. Total Environ.* **2020**, *698*, 134197.
<https://doi.org/10.1016/J.SCITOTENV.2019.134197>.
- (5) Sahu, S. K.; Ajmal, P. Y.; Pandit, G. G.; Puranik, V. D. Vertical Distribution of Polychlorinated Biphenyl Congeners in Sediment Core from Thane Creek Area of Mumbai, India. *J. Hazard. Mater.* **2009**, *164* (2–3).
<https://doi.org/10.1016/j.jhazmat.2008.08.113>.
- (6) McKnight, U. S.; Rasmussen, J. J.; Kronvang, B.; Binning, P. J.; Bjerg, P. L. Sources, Occurrence and Predicted Aquatic Impact of Legacy and Contemporary Pesticides in Streams. *Environ. Pollut.* **2015**, *200*. <https://doi.org/10.1016/j.envpol.2015.02.015>.
- (7) Bhatnagar, A.; Sillanpää, M. A Review of Emerging Adsorbents for Nitrate Removal from Water. *Chemical Engineering Journal*. 2011.
<https://doi.org/10.1016/j.cej.2011.01.103>.
- (8) Madhav, S.; Ahamad, A.; Singh, A. K.; Kushawaha, J.; Chauhan, J. S.; Sharma, S.;

-
- Singh, P. Water Pollutants: Sources and Impact on the Environment and Human Health; 2020. https://doi.org/10.1007/978-981-15-0671-0_4.
- (9) Lohmann, R.; Breivik, K.; Dachs, J.; Muir, D. Global Fate of POPs: Current and Future Research Directions. *Environmental Pollution*. 2007. <https://doi.org/10.1016/j.envpol.2007.06.051>.
- (10) Lee, H. J.; Kim, K. Y.; Hamm, S. Y.; Kim, M. S.; Kim, H. K.; Oh, J. E. Occurrence and Distribution of Pharmaceutical and Personal Care Products, Artificial Sweeteners, and Pesticides in Groundwater from an Agricultural Area in Korea. *Sci. Total Environ.* **2019**. <https://doi.org/10.1016/j.scitotenv.2018.12.258>.
- (11) Cucina, M.; Tacconi, C.; Ricci, A.; Pezzolla, D.; Sordi, S.; Zadra, C.; Gigliotti, G. Evaluation of Benefits and Risks Associated with the Agricultural Use of Organic Wastes of Pharmaceutical Origin. *Sci. Total Environ.* **2018**. <https://doi.org/10.1016/j.scitotenv.2017.09.154>.
- (12) Zhang, Q. Q.; Ying, G. G.; Pan, C. G.; Liu, Y. S.; Zhao, J. L. Comprehensive Evaluation of Antibiotics Emission and Fate in the River Basins of China: Source Analysis, Multimedia Modeling, and Linkage to Bacterial Resistance. *Environ. Sci. Technol.* **2015**. <https://doi.org/10.1021/acs.est.5b00729>.
- (13) Post, G. B.; Louis, J. B.; Lippincott, R. L.; Procopio, N. A. Occurrence of Perfluorinated Compounds in Raw Water from New Jersey Public Drinking Water Systems. *Environ. Sci. Technol.* **2013**. <https://doi.org/10.1021/es402884x>.
- (14) E. Galloway, J.; V. P. Moreno, A.; B. Lindstrom, A.; J. Strynar, M.; Newton, S.; A. May, A.; K. Weavers, L. Evidence of Air Dispersion: HFPO–DA and PFOA in Ohio and West Virginia Surface Water and Soil near a Fluoropolymer Production Facility. *Environ. Sci. & Technol.* **2020**, *54* (12), 7175–7184. <https://doi.org/10.1021/acs.est.9b07384>.
- (15) Hensen, B.; Olsson, O.; Kümmerer, K. A Strategy for an Initial Assessment of the Ecotoxicological Effects of Transformation Products of Pesticides in Aquatic Systems Following a Tiered Approach. *Environ. Int.* **2020**. <https://doi.org/10.1016/j.envint.2020.105533>.
- (16) Matsushita, T.; Morimoto, A.; Kuriyama, T.; Matsumoto, E.; Matsui, Y.; Shirasaki, N.;

-
- Kondo, T.; Takanashi, H.; Kameya, T. Removals of Pesticides and Pesticide Transformation Products during Drinking Water Treatment Processes and Their Impact on Mutagen Formation Potential after Chlorination. *Water Res.* **2018**.
<https://doi.org/10.1016/j.watres.2018.01.028>.
- (17) García-Galán, M. J.; Monllor-Alcaraz, L. S.; Postigo, C.; Uggetti, E.; López de Alda, M.; Díez-Montero, R.; García, J. Microalgae-Based Bioremediation of Water Contaminated by Pesticides in Peri-Urban Agricultural Areas. *Environ. Pollut.* **2020**.
<https://doi.org/10.1016/j.envpol.2020.114579>.
- (18) Tosi, S.; Costa, C.; Vesco, U.; Quaglia, G.; Guido, G. A 3-Year Survey of Italian Honey Bee-Collected Pollen Reveals Widespread Contamination by Agricultural Pesticides. *Sci. Total Environ.* **2018**. <https://doi.org/10.1016/j.scitotenv.2017.09.226>.
- (19) Fenner, K.; Canonica, S.; Wackett, L. P.; Elsner, M. Evaluating Pesticide Degradation in the Environment: Blind Spots and Emerging Opportunities. *Science*. 2013.
<https://doi.org/10.1126/science.1236281>.
- (20) Bexfield, L. M.; Belitz, K.; Lindsey, B. D.; Toccalino, P. L.; Nowell, L. H. Pesticides and Pesticide Degradates in Groundwater Used for Public Supply across the United States: Occurrence and Human-Health Context. *Environ. Sci. Technol.* **2021**.
<https://doi.org/10.1021/acs.est.0c05793>.
- (21) Moore, M. T.; Locke, M. A.; Cullum, R. F. Expanding Wetland Mitigation: Can Rice Fields Remediate Pesticides in Agricultural Runoff? *J. Environ. Qual.* **2018**.
<https://doi.org/10.2134/jeq2018.04.0154>.
- (22) Zhu, Y. C.; Yao, J.; Adamczyk, J.; Luttrell, R. Synergistic Toxicity and Physiological Impact of Imidacloprid Alone and Binary Mixtures with Seven Representative Pesticides on Honey Bee (*Apis Mellifera*). *PLoS One* **2017**.
<https://doi.org/10.1371/journal.pone.0176837>.
- (23) Cabirol, A.; Haase, A. The Neurophysiological Bases of the Impact of Neonicotinoid Pesticides on the Behaviour of Honeybees. *Insects*. 2019.
<https://doi.org/10.3390/insects10100344>.
- (24) Firake, D. M.; Thubru, D. P.; Behere, G. T. Eco-Toxicological Risk and Impact of Pesticides on Important Parasitoids of Cabbage Butterflies in Cruciferous Ecosystem.

-
- Chemosphere* **2017**. <https://doi.org/10.1016/j.chemosphere.2016.10.071>.
- (25) Djangalina, E.; Altynova, N.; Bakhtiyarova, S.; Kapysheva, U.; Zhaksymov, B.; Shadenova, E.; Baizhanov, M.; Sapargali, O.; Garshin, A.; Seisenbayeva, A.; Delannoy, M.; Jurjanz, S.; Khussainova, E.; Bekmanov, B.; Djansugurova, L. Comprehensive Assessment of Unutilized and Obsolete Pesticides Impact on Genetic Status and Health of Population of Almaty Region. *Ecotoxicol. Environ. Saf.* **2020**. <https://doi.org/10.1016/j.ecoenv.2020.110905>.
- (26) Kim, K. H.; Kabir, E.; Jahan, S. A. Exposure to Pesticides and the Associated Human Health Effects. *Science of the Total Environment*. 2017. <https://doi.org/10.1016/j.scitotenv.2016.09.009>.
- (27) Sabarwal, A.; Kumar, K.; Singh, R. P. Hazardous Effects of Chemical Pesticides on Human Health–Cancer and Other Associated Disorders. *Environmental Toxicology and Pharmacology*. 2018. <https://doi.org/10.1016/j.etap.2018.08.018>.
- (28) Nicolopoulou-Stamati, P.; Maipas, S.; Kotampasi, C.; Stamatis, P.; Hens, L. Chemical Pesticides and Human Health: The Urgent Need for a New Concept in Agriculture. *Front. Public Heal.* **2016**. <https://doi.org/10.3389/fpubh.2016.00148>.
- (29) Krzeminski, P.; Tomei, M. C.; Karaolia, P.; Langenhoff, A.; Almeida, C. M. R.; Felis, E.; Gritten, F.; Andersen, H. R.; Fernandes, T.; Manaia, C. M.; Rizzo, L.; Fatta-Kassinos, D. Performance of Secondary Wastewater Treatment Methods for the Removal of Contaminants of Emerging Concern Implicated in Crop Uptake and Antibiotic Resistance Spread: A Review. *Science of the Total Environment*. 2019. <https://doi.org/10.1016/j.scitotenv.2018.08.130>.
- (30) Kuppusamy, S.; Kakarla, D.; Venkateswarlu, K.; Megharaj, M.; Yoon, Y. E.; Lee, Y. B. Veterinary Antibiotics (VAs) Contamination as a Global Agro-Ecological Issue: A Critical View. *Agriculture, Ecosystems and Environment*. 2018. <https://doi.org/10.1016/j.agee.2018.01.026>.
- (31) Sarmah, A. K.; Meyer, M. T.; Boxall, A. B. A. A Global Perspective on the Use, Sales, Exposure Pathways, Occurrence, Fate and Effects of Veterinary Antibiotics (VAs) in the Environment. *Chemosphere*. 2006. <https://doi.org/10.1016/j.chemosphere.2006.03.026>.

-
- (32) Patel, M.; Kumar, R.; Kishor, K.; Mlsna, T.; Pittman, C. U.; Mohan, D. Pharmaceuticals of Emerging Concern in Aquatic Systems: Chemistry, Occurrence, Effects, and Removal Methods. *Chemical Reviews*. 2019. <https://doi.org/10.1021/acs.chemrev.8b00299>.
- (33) Bártíková, H.; Podlipná, R.; Skálová, L. Veterinary Drugs in the Environment and Their Toxicity to Plants. *Chemosphere*. 2016. <https://doi.org/10.1016/j.chemosphere.2015.10.137>.
- (34) Rojas, S.; Horcajada, P. Metal-Organic Frameworks for the Removal of Emerging Organic Contaminants in Water. *Chemical Reviews*. 2020. <https://doi.org/10.1021/acs.chemrev.9b00797>.
- (35) Bilal, M.; Mehmood, S.; Rasheed, T.; Iqbal, H. M. N. Antibiotics Traces in the Aquatic Environment: Persistence and Adverse Environmental Impact. *Current Opinion in Environmental Science and Health*. 2020. <https://doi.org/10.1016/j.coesh.2019.11.005>.
- (36) Schaidler, L. A.; Rodgers, K. M.; Rudel, R. A. Review of Organic Wastewater Compound Concentrations and Removal in Onsite Wastewater Treatment Systems. *Environmental Science and Technology*. 2017. <https://doi.org/10.1021/acs.est.6b04778>.
- (37) Li, R.; Wang, J. J.; Gaston, L. A.; Zhou, B.; Li, M.; Xiao, R.; Wang, Q.; Zhang, Z.; Huang, H.; Liang, W.; Huang, H.; Zhang, X. An Overview of Carbothermal Synthesis of Metal–Biochar Composites for the Removal of Oxyanion Contaminants from Aqueous Solution. *Carbon*. 2018. <https://doi.org/10.1016/j.carbon.2017.12.070>.
- (38) Hristovski, K. D.; Markovski, J. Engineering Metal (Hydr)Oxide Sorbents for Removal of Arsenate and Similar Weak-Acid Oxyanion Contaminants: A Critical Review with Emphasis on Factors Governing Sorption Processes. *Sci. Total Environ.* **2017**, 598. <https://doi.org/10.1016/j.scitotenv.2017.04.108>.
- (39) El-Moselhy, M. M.; Ates, A.; Çelebi, A. Synthesis and Characterization of Hybrid Iron Oxide Silicates for Selective Removal of Arsenic Oxyanions from Contaminated Water. *J. Colloid Interface Sci.* **2017**, 488. <https://doi.org/10.1016/j.jcis.2016.11.003>.
- (40) Xiao, F. Emerging Poly- and Perfluoroalkyl Substances in the Aquatic Environment: A

-
- Review of Current Literature. *Water Res.* **2017**, *124*, 482–495.
<https://doi.org/10.1016/J.WATRES.2017.07.024>.
- (41) Buck, R. C.; Franklin, J.; Berger, U.; Conder, J. M.; Cousins, I. T.; Voogt, P. De; Jensen, A. A.; Kannan, K.; Mabury, S. A.; van Leeuwen, S. P. J. Perfluoroalkyl and Polyfluoroalkyl Substances in the Environment: Terminology, Classification, and Origins. *Integr. Environ. Assess. Manag.* **2011**. <https://doi.org/10.1002/ieam.258>.
- (42) Nakayama, S. F.; Strynar, M. J.; Reiner, J. L.; Delinsky, A. D.; Lindstrom, A. B. Determination of Perfluorinated Compounds in the Upper Mississippi River Basin. *Environ. Sci. Technol.* **2010**, *44* (11). <https://doi.org/10.1021/es100382z>.
- (43) Barzen-Hanson, K. A.; Roberts, S. C.; Choyke, S.; Oetjen, K.; McAlees, A.; Riddell, N.; McCrindle, R.; Ferguson, P. L.; Higgins, C. P.; Field, J. A. Discovery of 40 Classes of Per- and Polyfluoroalkyl Substances in Historical Aqueous Film-Forming Foams (AFFFs) and AFFF-Impacted Groundwater. *Environ. Sci. Technol.* **2017**, *51* (4). <https://doi.org/10.1021/acs.est.6b05843>.
- (44) Lang, J. R.; Allred, B. M. K.; Field, J. A.; Levis, J. W.; Barlaz, M. A. National Estimate of Per- and Polyfluoroalkyl Substance (PFAS) Release to U.S. Municipal Landfill Leachate. *Environ. Sci. Technol.* **2017**, *51* (4).
<https://doi.org/10.1021/acs.est.6b05005>.
- (45) Higgins, C. P.; Field, J. A.; Criddle, C. S.; Luthy, R. G. Quantitative Determination of Perfluorochemicals in Sediments and Domestic Sludge. *Environ. Sci. Technol.* **2005**, *39* (11). <https://doi.org/10.1021/es048245p>.
- (46) Sunderland, E. M.; Hu, X. C.; Dassuncao, C.; Tokranov, A. K.; Wagner, C. C.; Allen, J. G. A Review of the Pathways of Human Exposure to Poly- and Perfluoroalkyl Substances (PFASs) and Present Understanding of Health Effects. *Journal of Exposure Science and Environmental Epidemiology*. 2019. <https://doi.org/10.1038/s41370-018-0094-1>.
- (47) Bell, E. M.; De Guise, S.; McCutcheon, J. R.; Lei, Y.; Levin, M.; Li, B.; Rusling, J. F.; Lawrence, D. A.; Cavallari, J. M.; O'Connell, C.; Javidi, B.; Wang, X.; Ryu, H. Exposure, Health Effects, Sensing, and Remediation of the Emerging PFAS Contaminants – Scientific Challenges and Potential Research Directions. *Science of*

-
- the Total Environment*. 2021. <https://doi.org/10.1016/j.scitotenv.2021.146399>.
- (48) Fenton, S. E.; Ducatman, A.; Boobis, A.; DeWitt, J. C.; Lau, C.; Ng, C.; Smith, J. S.; Roberts, S. M. Per- and Polyfluoroalkyl Substance Toxicity and Human Health Review: Current State of Knowledge and Strategies for Informing Future Research. *Environmental Toxicology and Chemistry*. 2021. <https://doi.org/10.1002/etc.4890>.
- (49) Grandjean, P.; Heilmann, C.; Weihe, P.; Nielsen, F.; Mogensen, U. B.; Timmermann, A.; Budtz-Jørgensen, E. Estimated Exposures to Perfluorinated Compounds in Infancy Predict Attenuated Vaccine Antibody Concentrations at Age 5-Years. *J. Immunotoxicol.* **2017**, *14* (1). <https://doi.org/10.1080/1547691X.2017.1360968>.
- (50) Schultz, M. M.; Barofsky, D. F.; Field, J. A. Quantitative Determination of Fluorotelomer Sulfonates in Groundwater by LC MS/MS. *Environ. Sci. Technol.* **2004**, *38* (6). <https://doi.org/10.1021/es035031j>.
- (51) Bentel, M. J.; Yu, Y.; Xu, L.; Li, Z.; Wong, B. M.; Men, Y.; Liu, J. Defluorination of Per- and Polyfluoroalkyl Substances (PFASs) with Hydrated Electrons: Structural Dependence and Implications to PFAS Remediation and Management. *Environ. Sci. Technol.* **2019**. <https://doi.org/10.1021/acs.est.8b06648>.
- (52) Tenorio, R.; Liu, J.; Xiao, X.; Maizel, A.; Higgins, C. P.; Schaefer, C. E.; Strathmann, T. J. Destruction of Per-and Polyfluoroalkyl Substances (PFASs) in Aqueous Film-Forming Foam (AFFF) with UV-Sulfite Photoreductive Treatment. *Environ. Sci. Technol.* **2020**, *54* (11). <https://doi.org/10.1021/acs.est.0c00961>.
- (53) Bao, Y.; Deng, S.; Jiang, X.; Qu, Y.; He, Y.; Liu, L.; Chai, Q.; Mumtaz, M.; Huang, J.; Cagnetta, G.; Yu, G. Degradation of PFOA Substitute: GenX (HFPO-DA Ammonium Salt): Oxidation with UV/Persulfate or Reduction with UV/Sulfite? *Environ. Sci. Technol.* **2018**, *52* (20). <https://doi.org/10.1021/acs.est.8b02172>.
- (54) Pi, Y.; Li, X.; Xia, Q.; Wu, J.; Li, Y.; Xiao, J.; Li, Z. Adsorptive and Photocatalytic Removal of Persistent Organic Pollutants (POPs) in Water by Metal-Organic Frameworks (MOFs). *Chemical Engineering Journal*. 2018. <https://doi.org/10.1016/j.cej.2017.12.092>.
- (55) Wang, Q.; Gao, Q.; Al-Enizi, A. M.; Nafady, A.; Ma, S. Recent Advances in MOF-Based Photocatalysis: Environmental Remediation under Visible Light. *Inorganic*

-
- Chemistry Frontiers*. 2020. <https://doi.org/10.1039/c9qi01120j>.
- (56) Zhang, X.; Wang, J.; Dong, X. X.; Lv, Y. K. Functionalized Metal-Organic Frameworks for Photocatalytic Degradation of Organic Pollutants in Environment. *Chemosphere*. 2020. <https://doi.org/10.1016/j.chemosphere.2019.125144>.
- (57) Dhangar, K.; Kumar, M. Tricks and Tracks in Removal of Emerging Contaminants from the Wastewater through Hybrid Treatment Systems: A Review. *Science of the Total Environment*. 2020. <https://doi.org/10.1016/j.scitotenv.2020.140320>.
- (58) Morsi, R.; Bilal, M.; Iqbal, H. M. N.; Ashraf, S. S. Laccases and Peroxidases: The Smart, Greener and Futuristic Biocatalytic Tools to Mitigate Recalcitrant Emerging Pollutants. *Science of the Total Environment*. 2020. <https://doi.org/10.1016/j.scitotenv.2020.136572>.
- (59) Salazar, H.; Martins, P. M.; Santos, B.; Fernandes, M. M.; Reizabal, A.; Sebastián, V.; Botelho, G.; Tavares, C. J.; Vilas-Vilela, J. L.; Lanceros-Mendez, S. Photocatalytic and Antimicrobial Multifunctional Nanocomposite Membranes for Emerging Pollutants Water Treatment Applications. *Chemosphere* **2020**. <https://doi.org/10.1016/j.chemosphere.2020.126299>.
- (60) Sun, H.; He, F.; Choi, W. Production of Reactive Oxygen Species by the Reaction of Periodate and Hydroxylamine for Rapid Removal of Organic Pollutants and Waterborne Bacteria. *Environ. Sci. Technol.* **2020**. <https://doi.org/10.1021/acs.est.0c00817>.
- (61) Jiang, N.; Shang, R.; Heijman, S. G. J.; Rietveld, L. C. High-Silica Zeolites for Adsorption of Organic Micro-Pollutants in Water Treatment: A Review. *Water Research*. 2018. <https://doi.org/10.1016/j.watres.2018.07.017>.
- (62) Pronk, W.; Ding, A.; Morgenroth, E.; Derlon, N.; Desmond, P.; Burkhardt, M.; Wu, B.; Fane, A. G. Gravity-Driven Membrane Filtration for Water and Wastewater Treatment: A Review. *Water Research*. 2019. <https://doi.org/10.1016/j.watres.2018.11.062>.
- (63) Ushani, U.; Lu, X.; Wang, J.; Zhang, Z.; Dai, J.; Tan, Y.; Wang, S.; Li, W.; Niu, C.; Cai, T.; Wang, N.; Zhen, G. Sulfate Radicals-Based Advanced Oxidation Technology in Various Environmental Remediation: A State-of-the-Art Review. *Chemical*

-
- Engineering Journal*. 2020. <https://doi.org/10.1016/j.cej.2020.126232>.
- (64) Trojanowicz, M.; Bojanowska-Czajka, A.; Bartosiewicz, I.; Kulisa, K. Advanced Oxidation/Reduction Processes Treatment for Aqueous Perfluorooctanoate (PFOA) and Perfluorooctanesulfonate (PFOS) – A Review of Recent Advances. *Chemical Engineering Journal*. 2018. <https://doi.org/10.1016/j.cej.2017.10.153>.
- (65) Qin, W.; Lin, Z.; Dong, H.; Yuan, X.; Qiang, Z.; Liu, S.; Xia, D. Kinetic and Mechanistic Insights into the Abatement of Clofibric Acid by Integrated UV/Ozone/Peroxydisulfate Process: A Modeling and Theoretical Study. *Water Res.* **2020**, *186*, 116336. <https://doi.org/10.1016/J.WATRES.2020.116336>.
- (66) Zhang, W.; Zhou, S.; Sun, J.; Meng, X.; Luo, J.; Zhou, D.; Crittenden, J. Impact of Chloride Ions on UV/H₂O₂ and UV/Persulfate Advanced Oxidation Processes. *Environ. Sci. Technol.* **2018**, *52* (13). <https://doi.org/10.1021/acs.est.8b01662>.
- (67) Lee, J.; Von Gunten, U.; Kim, J. H. Persulfate-Based Advanced Oxidation: Critical Assessment of Opportunities and Roadblocks. *Environmental Science and Technology*. 2020. <https://doi.org/10.1021/acs.est.9b07082>.
- (68) Guo, K.; Wu, Z.; Shang, C.; Yao, B.; Hou, S.; Yang, X.; Song, W.; Fang, J. Radical Chemistry and Structural Relationships of PPCP Degradation by UV/Chlorine Treatment in Simulated Drinking Water. *Environ. Sci. Technol.* **2017**. <https://doi.org/10.1021/acs.est.7b02059>.
- (69) Neta, P.; Huie, R. E.; Ross, A. B. Rate Constants for Reactions of Inorganic Radicals in Aqueous Solution. *J. Phys. Chem. Ref. Data* **1988**. <https://doi.org/10.1063/1.555808>.
- (70) Du, X.; Bai, X.; Xu, L.; Yang, L.; Jin, P. Visible-Light Activation of Persulfate by TiO₂/g-C₃N₄ Photocatalyst toward Efficient Degradation of Micropollutants. *Chem. Eng. J.* **2020**, *384*. <https://doi.org/10.1016/j.cej.2019.123245>.
- (71) Ji, Q.; Cheng, X.; Wu, Y.; Xiang, W.; He, H.; Xu, Z.; Xu, C.; Qi, C.; Li, S.; Zhang, L.; Yang, S. Visible Light Absorption by Perylene Diimide for Synergistic Persulfate Activation towards Efficient Photodegradation of Bisphenol A. *Appl. Catal. B Environ.* **2021**, *282*. <https://doi.org/10.1016/j.apcatb.2020.119579>.
- (72) Yang, L.; Bai, X.; Shi, J.; Du, X.; Xu, L.; Jin, P. Quasi-Full-Visible-Light Absorption

-
- by D35-TiO₂/g-C₃N₄ for Synergistic Persulfate Activation towards Efficient Photodegradation of Micropollutants. *Appl. Catal. B Environ.* **2019**, 256.
<https://doi.org/10.1016/j.apcatb.2019.117759>.
- (73) Yang, J.; Zhu, M.; Dionysiou, D. D. What Is the Role of Light in Persulfate-Based Advanced Oxidation for Water Treatment? *Water Research*. Elsevier Ltd February 2021, p 116627. <https://doi.org/10.1016/j.watres.2020.116627>.
- (74) Cui, J.; Gao, P.; Deng, Y. Destruction of Per- A Nd Polyfluoroalkyl Substances (PFAS) with Advanced Reduction Processes (ARPs): A Critical Review. *Environmental Science and Technology*. 2020.
<https://doi.org/10.1021/acs.est.9b05565>.
- (75) Vellanki, B. P.; Batchelor, B.; Abdel-Wahab, A. Advanced Reduction Processes: A New Class of Treatment Processes. *Environ. Eng. Sci.* **2013**, 30 (5).
<https://doi.org/10.1089/ees.2012.0273>.
- (76) Armstrong, D. A.; Huie, R. E.; Koppenol, W. H.; Lyman, S. V.; Merenyi, G.; Neta, P.; Ruscic, B.; Stanbury, D. M.; Steenken, S.; Wardman, P. Standard Electrode Potentials Involving Radicals in Aqueous Solution: Inorganic Radicals (IUPAC Technical Report). *Pure Appl. Chem.* **2015**. <https://doi.org/10.1515/pac-2014-0502>.
- (77) Hu, X.; Hu, X.; Peng, Q.; Zhou, L.; Tan, X.; Jiang, L.; Tang, C.; Wang, H.; Liu, S.; Wang, Y.; Ning, Z. Mechanisms Underlying the Photocatalytic Degradation Pathway of Ciprofloxacin with Heterogeneous TiO₂. *Chemical Engineering Journal*. 2020.
<https://doi.org/10.1016/j.cej.2019.122366>.
- (78) Bergamonti, L.; Bergonzi, C.; Graiff, C.; Lottici, P. P.; Bettini, R.; Elviri, L. 3D Printed Chitosan Scaffolds: A New TiO₂ Support for the Photocatalytic Degradation of Amoxicillin in Water. *Water Res.* **2019**.
<https://doi.org/10.1016/j.watres.2019.07.008>.
- (79) Cheng, Z.; Ling, L.; Wu, Z.; Fang, J.; Westerhoff, P.; Shang, C. A Novel Visible-Light-Driven Photocatalytic Chlorine Activation Process for Carbamazepine Degradation in Drinking Water. *Environ. Sci. Technol.* **2020**.
<https://doi.org/10.1021/acs.est.0c03170>.
- (80) Jin, C.; Li, W.; Chen, Y.; Li, R.; Huo, J.; He, Q.; Wang, Y. Efficient Photocatalytic

-
- Degradation and Adsorption of Tetracycline over Type-II Heterojunctions Consisting of ZnO Nanorods and K-Doped Exfoliated g-C₃N₄ Nanosheets. *Ind. Eng. Chem. Res.* **2020**. <https://doi.org/10.1021/acs.iecr.9b06911>.
- (81) Khaing, K. K.; Yin, D.; Ouyang, Y.; Xiao, S.; Liu, B.; Deng, L.; Li, L.; Guo, X.; Wang, J.; Liu, J.; Zhang, Y. Fabrication of 2D-2D Heterojunction Catalyst with Covalent Organic Framework (COF) and MoS₂ for Highly Efficient Photocatalytic Degradation of Organic Pollutants. *Inorg. Chem.* **2020**. <https://doi.org/10.1021/acs.inorgchem.0c00422>.
- (82) Rueda-Marquez, J. J.; Levchuk, I.; Fernández Ibañez, P.; Sillanpää, M. A Critical Review on Application of Photocatalysis for Toxicity Reduction of Real Wastewaters. *Journal of Cleaner Production.* 2020. <https://doi.org/10.1016/j.jclepro.2020.120694>.
- (83) Nakata, K.; Fujishima, A. TiO₂ Photocatalysis: Design and Applications. *Journal of Photochemistry and Photobiology C: Photochemistry Reviews.* 2012. <https://doi.org/10.1016/j.jphotochemrev.2012.06.001>.
- (84) Fujishima, A.; Zhang, X.; Tryk, D. A. TiO₂ Photocatalysis and Related Surface Phenomena. *Surface Science Reports.* 2008. <https://doi.org/10.1016/j.surfrep.2008.10.001>.
- (85) Wen, Y.; Zhang, P.; Sharma, V. K.; Ma, X.; Zhou, H.-C. Metal-Organic Frameworks for Environmental Applications. *Cell Reports Phys. Sci.* **2021**, 2 (2), 100348. <https://doi.org/10.1016/j.xcrp.2021.100348>.
- (86) Buxton, G. V.; Greenstock, C. L.; Phillips Helman, W.; Ross, A. B.; Helman, W. P. Rate Constants for Reactions of Peroxyl Radicals In. *Fluid Solut. J. Phys. Chem. Ref. Data* **1988**, 17, 413. <https://doi.org/10.1063/1.555805>.
- (87) Xueyue, M. +; Wang, P.; Xu, S.; Su, L.; Zhong, H.; Wang, H.; Li, Y.; Zhan, S. Single-Atom Catalysis Very Important Paper Almost 100 % Peroxymonosulfate Conversion to Singlet Oxygen on Single-Atom CoN₂ Sites. <https://doi.org/10.1002/anie.202014472>.
- (88) Wang, W.; Chen, M.; Wang, D.; Yan, M.; Liu, Z. Different Activation Methods in Sulfate Radical-Based Oxidation for Organic Pollutants Degradation: Catalytic Mechanism and Toxicity Assessment of Degradation Intermediates. *Sci. Total*

-
- Environ.* **2021**, 772, 145522. <https://doi.org/10.1016/j.scitotenv.2021.145522>.
- (89) Olmez-Hanci, T.; Arslan-Alaton, I. Comparison of Sulfate and Hydroxyl Radical Based Advanced Oxidation of Phenol. *Chem. Eng. J.* **2013**, 224 (1), 10–16. <https://doi.org/10.1016/j.cej.2012.11.007>.
- (90) Guan, Y. H.; Ma, J.; Li, X. C.; Fang, J. Y.; Chen, L. W. Influence of PH on the Formation of Sulfate and Hydroxyl Radicals in the UV/Peroxymonosulfate System. *Environ. Sci. Technol.* **2011**. <https://doi.org/10.1021/es2017363>.
- (91) Rate Constants of Sulfate Radical Anion Reactions with Organic Molecules: A Review L Aszl o Wojn Arovits, Erzs Ebet Tak Acs. **2018**. <https://doi.org/10.1016/j.chemosphere.2018.12.156>.
- (92) Ghanbari, F.; Moradi, M. Application of Peroxymonosulfate and Its Activation Methods for Degradation of Environmental Organic Pollutants: Review. *Chemical Engineering Journal*. Elsevier B.V. February 15, 2017, pp 41–62. <https://doi.org/10.1016/j.cej.2016.10.064>.
- (93) Ike, I. A.; Linden, K. G.; Orbell, J. D.; Duke, M. Critical Review of the Science and Sustainability of Persulphate Advanced Oxidation Processes. *Chemical Engineering Journal*. Elsevier B.V. April 15, 2018, pp 651–669. <https://doi.org/10.1016/j.cej.2018.01.034>.
- (94) Duan, X.; Sun, H.; Shao, Z.; Wang, S. Nonradical Reactions in Environmental Remediation Processes: Uncertainty and Challenges. *Applied Catalysis B: Environmental*. Elsevier B.V. May 1, 2018, pp 973–982. <https://doi.org/10.1016/j.apcatb.2017.11.051>.
- (95) Yang, L.; Xue, J.; He, L.; Wu, L.; Ma, Y.; Chen, H.; Li, H.; Peng, P.; Zhang, Z. Review on Ultrasound Assisted Persulfate Degradation of Organic Contaminants in Wastewater: Influences, Mechanisms and Prospective. *Chemical Engineering Journal*. Elsevier B.V. December 15, 2019, p 122146. <https://doi.org/10.1016/j.cej.2019.122146>.
- (96) Yang, J.; Zhu, M.; Dionysiou, D. D. What Is the Role of Light in Persulfate-Based Advanced Oxidation for Water Treatment? *Water Research*. Elsevier Ltd February 1, 2021, p 116627. <https://doi.org/10.1016/j.watres.2020.116627>.

-
- (97) Wang, W.; Wang, H.; Li, G.; An, T.; Zhao, H.; Wong, P. K. Catalyst-Free Activation of Persulfate by Visible Light for Water Disinfection: Efficiency and Mechanisms. *Water Res.* **2019**, *157*, 106–118. <https://doi.org/10.1016/j.watres.2019.03.071>.
- (98) Bu, Y.; Li, H.; Yu, W.; Pan, Y.; Li, L.; Wang, Y.; Pu, L.; Ding, J.; Gao, G.; Pan, B. Peroxydisulfate Activation and Singlet Oxygen Generation by Oxygen Vacancy for Degradation of Contaminants. *Environ. Sci. & Technol.* **2021**, *55* (3), 2110–2120. <https://doi.org/10.1021/acs.est.0c07274>.
- (99) Ren, W.; Nie, G.; Zhou, P.; Zhang, H.; Duan, X.; Wang, S. The Intrinsic Nature of Persulfate Activation and N-Doping in Carbocatalysis. *Environ. Sci. & Technol.* **2020**, *54* (10), 6438–6447. <https://doi.org/10.1021/acs.est.0c01161>.
- (100) Liu, G.; Li, C.; Stewart, B. A.; Liu, L.; Zhang, M.; Yang, M.; Lin, K. Enhanced Thermal Activation of Peroxymonosulfate by Activated Carbon for Efficient Removal of Perfluorooctanoic Acid. *Chem. Eng. J.* **2020**, *399*, 125722. <https://doi.org/10.1016/j.cej.2020.125722>.
- (101) Naim, S.; Ghauch, A. Ranitidine Abatement in Chemically Activated Persulfate Systems: Assessment of Industrial Iron Waste for Sustainable Applications. *Chem. Eng. J.* **2016**, *288*, 276–288. <https://doi.org/10.1016/J.CEJ.2015.11.101>.
- (102) Ayoub, G.; Ghauch, A. Assessment of Bimetallic and Trimetallic Iron-Based Systems for Persulfate Activation: Application to Sulfamethoxazole Degradation. *Chem. Eng. J.* **2014**, *256*, 280–292. <https://doi.org/10.1016/J.CEJ.2014.07.002>.
- (103) Waławek, S.; Lutze, H. V.; Grübel, K.; Padil, V. V. T.; Černík, M.; Dionysiou, D. D. Chemistry of Persulfates in Water and Wastewater Treatment: A Review. *Chemical Engineering Journal*. 2017. <https://doi.org/10.1016/j.cej.2017.07.132>.
- (104) W. Benson, S. Thermochemistry and Kinetics of Sulfur-Containing Molecules and Radicals. *Chem. Rev.* **2002**, *78* (1), 23–35. <https://doi.org/10.1021/cr60311a003>.
- (105) Kolthoff, I. M.; Miller, I. K. The Chemistry of Persulfate. I. The Kinetics and Mechanism of the Decomposition of the Persulfate Ion in Aqueous Medium. *J. Am. Chem. Soc.* **1951**, *73* (7). <https://doi.org/10.1021/ja01151a024>.
- (106) Yang, Q.; Ma, Y.; Chen, F.; Yao, F.; Sun, J.; Wang, S.; Yi, K.; Hou, L.; Li, X.; Wang, D. Recent Advances in Photo-Activated Sulfate Radical-Advanced Oxidation Process

-
- (SR-AOP) for Refractory Organic Pollutants Removal in Water. *Chemical Engineering Journal*. 2019. <https://doi.org/10.1016/j.cej.2019.122149>.
- (107) W. Benson, S. Thermochemistry and Kinetics of Sulfur-Containing Molecules and Radicals. *Chem. Rev.* **2002**, 78 (1), 23–35. <https://doi.org/10.1021/cr60311a003>.
- (108) El Asmar, R.; Baalbaki, A.; Abou Khalil, Z.; Naim, S.; Bejjani, A.; Ghauch, A. Iron-Based Metal Organic Framework MIL-88-A for the Degradation of Naproxen in Water through Persulfate Activation. *Chem. Eng. J.* **2021**, 405, 126701. <https://doi.org/10.1016/J.CEJ.2020.126701>.
- (109) Al Hakim, S.; Jaber, S.; Zein Eddine, N.; Baalbaki, A.; Ghauch, A. Degradation of Theophylline in a UV254/PS System: Matrix Effect and Application to a Factory Effluent. *Chem. Eng. J.* **2020**, 380, 122478. <https://doi.org/10.1016/J.CEJ.2019.122478>.
- (110) Wang, W.; Wang, H.; Li, G.; An, T.; Zhao, H.; Wong, P. K. Catalyst-Free Activation of Persulfate by Visible Light for Water Disinfection: Efficiency and Mechanisms. *Water Res.* **2019**, 157, 106–118. <https://doi.org/10.1016/j.watres.2019.03.071>.
- (111) Duan, X.; Sun, H.; Shao, Z.; Wang, S. Nonradical Reactions in Environmental Remediation Processes: Uncertainty and Challenges. *Applied Catalysis B: Environmental*. Elsevier B.V. May 2018, pp 973–982. <https://doi.org/10.1016/j.apcatb.2017.11.051>.
- (112) Miskoski, S.; García, N. A. INFLUENCE OF THE PEPTIDE BOND ON THE SINGLET MOLECULAR OXYGEN-MEDIATED (O₂[g]) PHOTOOXIDATION OF HISTIDINE and METHIONINE DIPEPTIDES. A KINETIC STUDY. *Photochem. Photobiol.* **1993**, 57 (3). <https://doi.org/10.1111/j.1751-1097.1993.tb02317.x>.
- (113) Motohashi, N.; Saito, Y. Competitive Measurement of Rate Constants for Hydroxyl Radical Reactions Using Radiolytic Hydroxylation of Benzoate. *Chem. Pharm. Bull.* **1993**, 41 (10). <https://doi.org/10.1248/cpb.41.1842>.
- (114) Redpath, J. L.; Willson, R. L. International Journal of Radiation Biology and Related Studies in Physics, Chemistry and Medicine Chain Reactions and Radiosensitization: Model Enzyme Studies. <https://doi.org/10.1080/09553007514550361>.
- (115) Haag, W. R.; Hoigné, J.; Gassman, E.; Braun, A. M. Singlet Oxygen in Surface Waters

-
- Part I: Furfuryl Alcohol as a Trapping Agent. *Chemosphere* **1984**, *13* (5–6).
[https://doi.org/10.1016/0045-6535\(84\)90199-1](https://doi.org/10.1016/0045-6535(84)90199-1).
- (116) Huie, R. E.; Clifton, C. L. Temperature Dependence of the Rate Constants for Reactions of the Sulfate Radical, SO₄⁻, with Anions. *J. Phys. Chem.* **1990**, *94* (23).
<https://doi.org/10.1021/j100386a015>.
- (117) Maruthamuthu, P.; Neta, P. Phosphate Radicals. Spectra, Acid-Base Equilibria, and Reactions with Inorganic Compounds. *J. Phys. Chem.* **1978**, *82* (6).
<https://doi.org/10.1021/j100495a019>.
- (118) Cheng, X.; Guo, H.; Zhang, Y.; Wu, X.; Liu, Y. Non-Photochemical Production of Singlet Oxygen via Activation of Persulfate by Carbon Nanotubes. *Water Res.* **2017**, *113*, 80–88. <https://doi.org/10.1016/j.watres.2017.02.016>.
- (119) Zhu, S.; Li, X.; Kang, J.; Duan, X.; Wang, S. Persulfate Activation on Crystallographic Manganese Oxides: Mechanism of Singlet Oxygen Evolution for Nonradical Selective Degradation of Aqueous Contaminants. *Environ. Sci. & Technol.* **2018**, *53* (1), 307–315. <https://doi.org/10.1021/acs.est.8b04669>.
- (120) Cheng, X.; Guo, H.; Li, W.; Yang, B.; Wang, J.; Zhang, Y.; Du, E. Metal-Free Carbocatalysis for Persulfate Activation toward Nonradical Oxidation: Enhanced Singlet Oxygen Generation Based on Active Sites and Electronic Property. *Chem. Eng. J.* **2020**, *396*, 125107. <https://doi.org/10.1016/J.CEJ.2020.125107>.
- (121) Zhu, S.; Jin, C.; Duan, X.; Wang, S.; Ho, S. H. Nonradical Oxidation in Persulfate Activation by Graphene-like Nanosheets (GNS): Differentiating the Contributions of Singlet Oxygen (1O₂) and Sorption-Dependent Electron Transfer. *Chem. Eng. J.* **2020**, *393*, 124725. <https://doi.org/10.1016/J.CEJ.2020.124725>.
- (122) Cheng, X.; Guo, H.; Zhang, Y.; Korshin, G. V.; Yang, B. Insights into the Mechanism of Nonradical Reactions of Persulfate Activated by Carbon Nanotubes: Activation Performance and Structure-Function Relationship. *Water Res.* **2019**, *157*, 406–414. <https://doi.org/10.1016/J.WATRES.2019.03.096>.
- (123) Zou, J.; Ma, J.; Zhang, X.; Xie, P. Rapid Spectrophotometric Determination of Peroxymonosulfate in Water with Cobalt-Mediated Oxidation Decolorization of Methyl Orange. *Chem. Eng. J.* **2014**, *253*, 34–39.

-
- <https://doi.org/10.1016/j.cej.2014.05.042>.
- (124) Liang, C.; Huang, C. F.; Mohanty, N.; Kurakalva, R. M. A Rapid Spectrophotometric Determination of Persulfate Anion in ISCO. *Chemosphere* **2008**, *73* (9), 1540–1543. <https://doi.org/10.1016/j.chemosphere.2008.08.043>.
- (125) Nogueira, R. F. P.; Oliveira, M. C.; Paterlini, W. C. Simple and Fast Spectrophotometric Determination of H₂O₂ in Photo-Fenton Reactions Using Metavanadate. *Talanta* **2005**, *66* (1). <https://doi.org/10.1016/j.talanta.2004.10.001>.
- (126) Mahadevaiah; Abdul Galil, M. S.; Yogendra Kumar, M. S.; Sathish, M. A.; Nagendrappa, G. Simple Spectrophotometric Method for the Determination of Sulfur Dioxide by Its Decolorizing Effect on the Peroxovanadate Complex. *J. Anal. Chem.* **2008**, *63* (3). <https://doi.org/10.1134/s1061934808030088>.
- (127) Wei, Z.; Villamena, F. A.; Weavers, L. K. Kinetics and Mechanism of Ultrasonic Activation of Persulfate: An in Situ EPR Spin Trapping Study. *Environ. Sci. Technol.* **2017**, *51* (6). <https://doi.org/10.1021/acs.est.6b05392>.
- (128) Villamena, F. A.; Merle, J. K.; Hadad, C. M.; Zweier, J. L. Superoxide Radical Anion Adduct of 5,5-Dimethyl-1-Pyrroline N-Oxide (DMPO). 2. The Thermodynamics of Decay and EPR Spectral Properties. *J. Phys. Chem. A* **2005**, *109* (27). <https://doi.org/10.1021/jp0524330>.
- (129) Zamora, P. L.; Villamena, F. A. Theoretical and Experimental Studies of the Spin Trapping of Inorganic Radicals by 5,5-Dimethyl-1-Pyrroline N-Oxide (DMPO). 3. Sulfur Dioxide, Sulfite, and Sulfate Radical Anions. *J. Phys. Chem. A* **2012**, *116* (26). <https://doi.org/10.1021/jp3039169>.
- (130) Cohen, S. G.; Parola, A.; Parsons, G. H. Photoreduction by Amines. *Chem. Rev.* **1973**, *73* (2). <https://doi.org/10.1021/cr60282a004>.
- (131) Yun, E.-T.; Hoon Lee, J.; Kim, J.; Park, H.-D.; Lee, J. Identifying the Nonradical Mechanism in the Peroxymonosulfate Activation Process: Singlet Oxygenation Versus Mediated Electron Transfer. *Environ. Sci. & Technol.* **2018**, *52* (12), 7032–7042. <https://doi.org/10.1021/acs.est.8b00959>.
- (132) Bielski, B. H. J.; Richter, H. W. A Study of the Superoxide Radical Chemistry by Stopped-Flow Radiolysis and Radiation Induced Oxygen Consumption. *J. Am. Chem.*

-
- Soc.* **1977**, *99* (9). <https://doi.org/10.1021/ja00451a028>.
- (133) Ogilby, P. R. Singlet Oxygen: There Is Indeed Something New under the Sun. *Chem. Soc. Rev.* **2010**, *39* (8). <https://doi.org/10.1039/b926014p>.
- (134) DeRosa, M. C.; Crutchley, R. J. Photosensitized Singlet Oxygen and Its Applications. *Coordination Chemistry Reviews.* 2002. [https://doi.org/10.1016/S0010-8545\(02\)00034-6](https://doi.org/10.1016/S0010-8545(02)00034-6).
- (135) Tsao, M.-S.; K. Wilmarth, W. The Aqueous Chemistry of Inorganic Free Radicals. I. The Mechanism of the Photolytic Decomposition of Aqueous Persulfate Ion and Evidence Regarding the Sulfate–Hydroxyl Radical Interconversion Equilibrium. *J. Phys. Chem.* **2002**, *63* (3), 346–353. <https://doi.org/10.1021/j150573a006>.
- (136) Herrmann, H.; Reese, A.; Zellner, R. Time-Resolved UV/VIS Diode Array Absorption Spectroscopy of SO_x⁻ (X=3, 4, 5) Radical Anions in Aqueous Solution. *J. Mol. Struct.* **1995**, *348*. [https://doi.org/10.1016/0022-2860\(95\)08619-7](https://doi.org/10.1016/0022-2860(95)08619-7).
- (137) Elliot, A. J. *Rate Constants And G-Values For The Simulation Of The Radiolysis Of Light Water Over The Range 0-300°C*; 1994.
- (138) Jiang, P.-Y.; Katsumura, Y.; Nagaishi, R.; Domae, M.; Lshikawa, K.; Lshigure, K.; Yoshida, Y. *Pulse Radiolysis Study of Concentrated Sulfuric Acid Solutions Formation Mechanism, Yield and Reactivity of Sulfate Radicals*; 1992; Vol. 88.
- (139) Koppenol, W. H. Reactions Involving Singlet Oxygen and the Superoxide Anion. *Nature* **1976**, *262* (5567). <https://doi.org/10.1038/262420a0>.
- (140) S. Furman, O.; L. Teel, A.; J. Watts, R. Mechanism of Base Activation of Persulfate. *Environ. Sci. & Technol.* **2010**, *44* (16), 6423–6428. <https://doi.org/10.1021/es1013714>.
- (141) Khan, A. U.; Kasha, M. Chemiluminescence Arising from Simultaneous Transitions in Pairs of Singlet Oxygen Molecules. *J. Am. Chem. Soc.* **1970**, *92* (11). <https://doi.org/10.1021/ja00714a010>.
- (142) Foote, C. S.; Shook, F. C.; Abakerli, R. A. Chemistry of Superoxide Ion. 4. Singlet Oxygen Is Not a Major Product of Dismutation. *J. Am. Chem. Soc.* **1980**, *102* (7). <https://doi.org/10.1021/ja00527a082>.
- (143) Arudi, R. L.; Bielski, B. H. J.; Allen, A. O. SEARCH FOR SINGLET OXYGEN

-
- LUMINESCENCE IN THE DISPROPORTIONATION OF HO₂/O₂. *Photochem. Photobiol.* **1984**, 39 (5). <https://doi.org/10.1111/j.1751-1097.1984.tb03912.x>.
- (144) Christensen, H.; Sehested, K. Reaction of Hydroxyl Radicals with Hydrogen at Elevated Temperatures. Determination of the Activation Energy. *J. Phys. Chem.* **1983**, 87 (1). <https://doi.org/10.1021/j100224a027>.
- (145) Rabani, J.; Matheson, M. S. The Pulse Radiolysis of Aqueous Solutions of Potassium Ferrocyanide. *J. Phys. Chem.* **1966**, 70 (3). <https://doi.org/10.1021/j100875a025>.
- (146) Koppenol, W. H.; Butler, J. Mechanism of Reactions Involving Singlet Oxygen and the Superoxide Anion. *FEBS Letters.* 1977. [https://doi.org/10.1016/0014-5793\(77\)80628-5](https://doi.org/10.1016/0014-5793(77)80628-5).
- (147) Merényi, G.; Lind, J. S. Role of a Peroxide Intermediate in the Chemiluminescence of Luminol. A Mechanistic Study. *J. Am. Chem. Soc.* **1980**, 102 (18). <https://doi.org/10.1021/ja00538a022>.
- (148) Christensen, H.; Sehested, K.; Corfitzen, H. Reactions of Hydroxyl Radicals with Hydrogen Peroxide at Ambient and Elevated Temperatures. *J. Phys. Chem.* **2002**, 86 (9), 1588–1590. <https://doi.org/10.1021/j100206a023>.
- (149) Koppenol, W. H.; Butler, J.; Van Leeuwen, J. *THE HABER-WEISS CYCLE*; Vol. 28.
- (150) Sehested, K.; Rasmussen, O. L.; Fricke, H. Rate Constants of OH with HO₂, O₂⁻, and H₂O₂⁺ from Hydrogen Peroxide Formation in Pulse-Irradiated Oxygenated Water. *J. Phys. Chem.* **1968**, 72 (2). <https://doi.org/10.1021/j100848a040>.
- (151) Elliot, A. J.; Buxton, G. V. Temperature Dependence of the Reactions OH + O₂⁻ and OH + HO₂ in Water up to 200 °C. *J. Chem. Soc. Faraday Trans.* **1992**, 88 (17). <https://doi.org/10.1039/FT9928802465>.
- (152) Christensen, H.; Sehested, K.; Corfitzen, H. Reactions of Hydroxyl Radicals with Hydrogen Peroxide at Ambient and Elevated Temperatures. *J. Phys. Chem.* **2002**, 86 (9), 1588–1590. <https://doi.org/10.1021/j100206a023>.
- (153) S. Furman, O.; L. Teel, A.; J. Watts, R. Mechanism of Base Activation of Persulfate. *Environ. Sci. & Technol.* **2010**, 44 (16), 6423–6428. <https://doi.org/10.1021/es1013714>.
- (154) V. Lutze, H.; Bircher, S.; Rapp, I.; Kerlin, N.; Bakkour, R.; Geisler, M.; von Sonntag,

-
- C.; C. Schmidt, T. Degradation of Chlorotriazine Pesticides by Sulfate Radicals and the Influence of Organic Matter. *Environ. Sci. & Technol.* **2015**, *49* (3), 1673–1680. <https://doi.org/10.1021/es503496u>.
- (155) Khan, J. A.; He, X.; Shah, N. S.; Khan, H. M.; Hapeshi, E.; Fatta-Kassinos, D.; Dionysiou, D. D. Kinetic and Mechanism Investigation on the Photochemical Degradation of Atrazine with Activated H_2O_2 , $S_2O_8^{2-}$ and HSO_5^- . <https://doi.org/10.1016/j.cej.2014.04.104>.
- (156) Manoj, P.; Prasanthkumar, K. P.; Manoj, V. M.; Aravind, U. K.; Manojkumar, T. K.; Aravindakumar, C. T. Oxidation of Substituted Triazines by Sulfate Radical Anion (SO_4^-) in Aqueous Medium: A Laser Flash Photolysis and Steady State Radiolysis Study. *J. Phys. Org. Chem.* **2007**, *20* (2). <https://doi.org/10.1002/poc.1134>.
- (157) Nosaka, Y.; Nosaka, A. Y. Generation and Detection of Reactive Oxygen Species in Photocatalysis. *Chemical Reviews*. 2017. <https://doi.org/10.1021/acs.chemrev.7b00161>.
- (158) Clifton, C. L.; Huie, R. E. Rate Constants for Hydrogen Abstraction Reactions of the Sulfate Radical, SO_4^- . Alcohols. *Int. J. Chem. Kinet.* **1989**, *21* (8). <https://doi.org/10.1002/kin.550210807>.
- (159) Buxton, G. V.; Greenstock, C. L.; Helman, W. P.; Ross, A. B. Critical Review of Rate Constants for Reactions of Hydrated Electrons, Hydrogen Atoms and Hydroxyl Radicals ($\cdot OH/\cdot O^-$ in Aqueous Solution. *J. Phys. Chem. Ref. Data* **1988**. <https://doi.org/10.1063/1.555805>.
- (160) Bors, W.; Czapski, G.; Saran, M. An Expanded Function for Superoxide Dismutase. *Free Radic. Res.* **1991**, *12* (1). <https://doi.org/10.3109/10715769109145811>.
- (161) R. Buettner, G. Superoxide Dismutase in Redox Biology: The Roles of Superoxide and Hydrogen Peroxide. *Anticancer. Agents Med. Chem.* **2012**, *11* (4). <https://doi.org/10.2174/187152011795677544>.
- (162) Fang, G.; Gao, J.; D. Dionysiou, D.; Liu, C.; Zhou, D. Activation of Persulfate by Quinones: Free Radical Reactions and Implication for the Degradation of PCBs. *Environ. Sci. & Technol.* **2013**, *47* (9), 4605–4611. <https://doi.org/10.1021/es400262n>.

-
- (163) Redpath, J. L.; Willson, R. L. International Journal of Radiation Biology and Related Studies in Physics, Chemistry and Medicine Chain Reactions and Radiosensitization: Model Enzyme Studies. <https://doi.org/10.1080/09553007514550361>.
- (164) Yang, Y.; Banerjee, G.; W. Brudvig, G.; Kim, J.-H.; J. Pignatello, J. Oxidation of Organic Compounds in Water by Unactivated Peroxymonosulfate. *Environ. Sci. & Technol.* **2018**, 52 (10), 5911–5919. <https://doi.org/10.1021/acs.est.8b00735>.
- (165) Yun, E.-T.; Hoon Lee, J.; Kim, J.; Park, H.-D.; Lee, J. Identifying the Nonradical Mechanism in the Peroxymonosulfate Activation Process: Singlet Oxygenation Versus Mediated Electron Transfer. *Environ. Sci. & Technol.* **2018**, 52 (12), 7032–7042. <https://doi.org/10.1021/acs.est.8b00959>.
- (166) Khan, A.; Zhang, K.; Sun, P.; Pan, H.; Cheng, Y.; Zhang, Y. High Performance of the A-Mn₂O₃ Nanocatalyst for Persulfate Activation: Degradation Process of Organic Contaminants via Singlet Oxygen. *J. Colloid Interface Sci.* **2021**, 584, 885–899. <https://doi.org/10.1016/j.jcis.2020.10.021>.
- (167) Davies, M. J.; Gilbert, B. C.; Stell, J. K.; Whitwood, A. C. Nucleophilic Substitution Reactions of Spin Adducts. Implications for the Correct Identification of Reaction Intermediates by EPR/Spin Trapping. *J. Chem. Soc. Perkin Trans. 2* **1992**, No. 3. <https://doi.org/10.1039/p29920000333>.
- (168) Timmins, G. S.; Liu, K. J.; Bechara, E. J. H.; Kotake, Y.; Swartz, H. M. Trapping of Free Radicals with Direct in Vivo EPR Detection: A Comparison of 5,5-Dimethyl-1-Pyrroline-N-Oxide and 5-Diethoxyphosphoryl-5-Methyl-1-Pyrroline-N-Oxide as Spin Traps for HO and SO₄^{•-}. *Free Radic. Biol. Med.* **1999**, 27 (3–4), 329–333. [https://doi.org/10.1016/S0891-5849\(99\)00049-0](https://doi.org/10.1016/S0891-5849(99)00049-0).
- (169) V. Lutze, H.; Bircher, S.; Rapp, I.; Kerlin, N.; Bakkour, R.; Geisler, M.; von Sonntag, C.; C. Schmidt, T. Degradation of Chlorotriazine Pesticides by Sulfate Radicals and the Influence of Organic Matter. *Environ. Sci. & Technol.* **2015**, 49 (3), 1673–1680. <https://doi.org/10.1021/es503496u>.
- (170) Khan, J. A.; He, X.; Shah, N. S.; Khan, H. M.; Hapeshi, E.; Fatta-Kassinos, D.; Dionysiou, D. D. Kinetic and Mechanism Investigation on the Photochemical Degradation of Atrazine with Activated H₂O₂, S₂O₈²⁻ and HSO₅⁻.

-
- <https://doi.org/10.1016/j.cej.2014.04.104>.
- (171) Song, W.; Li, J.; Fu, C.; Wang, Z.; Zhang, X.; Yang, J.; Hogland, W.; Gao, L. Kinetics and Pathway of Atrazine Degradation by a Novel Method: Persulfate Coupled with Dithionite. *Chem. Eng. J.* **2019**, *373*, 803–813.
<https://doi.org/10.1016/J.CEJ.2019.05.110>.
- (172) Wu, S.; He, H.; Li, X.; Yang, C.; Zeng, G.; Wu, B.; He, S.; Lu, L. Insights into Atrazine Degradation by Persulfate Activation Using Composite of Nanoscale Zero-Valent Iron and Graphene: Performances and Mechanisms. *Chem. Eng. J.* **2018**, *341*, 126–136. <https://doi.org/10.1016/J.CEJ.2018.01.136>.
- (173) Tauber, A.; von Sonntag, C.; Tauber, A.; von Sonntag, C. *Research Papers Products and Kinetics of the OH-Radical-Induced Dealkylation of Atrazine Produkte Und Kinetik Der OH-Radikalinduzierten Desalkylierung von Atrazin*; 2000; Vol. 28.
- (174) Aggelopoulos, C. A.; Tataraki, D.; Rassias, G. Degradation of Atrazine in Soil by Dielectric Barrier Discharge Plasma - Potential Singlet Oxygen Mediation. *Chem. Eng. J.* **2018**, *347*. <https://doi.org/10.1016/j.cej.2018.04.111>.
- (175) Ghauch, A.; Tuqan, A. M.; Kibbi, N. Ibuprofen Removal by Heated Persulfate in Aqueous Solution: A Kinetics Study. *Chem. Eng. J.* **2012**, *197*.
<https://doi.org/10.1016/j.cej.2012.05.051>.
- (176) Ghauch, A.; Ayoub, G.; Naim, S. Degradation of Sulfamethoxazole by Persulfate Assisted Micrometric Fe⁰ in Aqueous Solution. *Chem. Eng. J.* **2013**, *228*.
<https://doi.org/10.1016/j.cej.2013.05.045>.
- (177) Miao, J.; Geng, W.; Alvarez, P. J. J.; Long, M. 2D N-Doped Porous Carbon Derived from Polydopamine-Coated Graphitic Carbon Nitride for Efficient Nonradical Activation of Peroxymonosulfate. *Environ. Sci. Technol.* **2020**, *54* (13).
<https://doi.org/10.1021/acs.est.0c03207>.
- (178) Othman, I.; Hisham Zain, J.; Abu Haija, M.; Banat, F. Catalytic Activation of Peroxymonosulfate Using CeVO₄ for Phenol Degradation: An Insight into the Reaction Pathway. *Appl. Catal. B Environ.* **2020**, *266*, 118601.
<https://doi.org/10.1016/J.APCATB.2020.118601>.
- (179) Zhang, L. S.; Jiang, X. H.; Zhong, Z. A.; Tian, L.; Sun, Q.; Cui, Y. T.; Lu, X.; Zou, J.

-
- P.; Luo, S. L. Carbon Nitride Supported High-Loading Fe Single-Atom Catalyst for Activation of Peroxymonosulfate to Generate $^{1}O_2$ with 100 % Selectivity. *Angew. Chemie - Int. Ed.* **2021**, *60* (40). <https://doi.org/10.1002/anie.202109488>.
- (180) Chesney, A. R.; Booth, C. J.; Lietz, C. B.; Li, L.; Pedersen, J. A. Peroxymonosulfate Rapidly Inactivates the Disease-Associated Prion Protein. *Environ. Sci. Technol.* **2016**, *50* (13). <https://doi.org/10.1021/acs.est.5b06294>.
- (181) Lou, X.; Wu, L.; Guo, Y.; Chen, C.; Wang, Z.; Xiao, D.; Fang, C.; Liu, J.; Zhao, J.; Lu, S. Peroxymonosulfate Activation by Phosphate Anion for Organics Degradation in Water. *Chemosphere* **2014**, *117* (1), 582–585. <https://doi.org/10.1016/J.CHEMOSPHERE.2014.09.046>.
- (182) Wang, S.; Liu, Y.; Wang, J. Peroxymonosulfate Activation by Fe-Co-O-Codoped Graphite Carbon Nitride for Degradation of Sulfamethoxazole. *Environ. Sci. Technol.* **2020**, *54* (16). <https://doi.org/10.1021/acs.est.0c03256>.
- (183) Lei, Y.; Lu, J.; Zhu, M.; Xie, J.; Peng, S.; Zhu, C. Radical Chemistry of Diethyl Phthalate Oxidation via UV/Peroxymonosulfate Process: Roles of Primary and Secondary Radicals. *Chem. Eng. J.* **2020**, *379*, 122339. <https://doi.org/10.1016/J.CEJ.2019.122339>.
- (184) Sun, P.; Liu, H.; Feng, M.; Guo, L.; Zhai, Z.; Fang, Y.; Zhang, X.; Sharma, V. K. Nitrogen-Sulfur Co-Doped Industrial Graphene as an Efficient Peroxymonosulfate Activator: Singlet Oxygen-Dominated Catalytic Degradation of Organic Contaminants. *Appl. Catal. B Environ.* **2019**, *251*. <https://doi.org/10.1016/j.apcatb.2019.03.085>.
- (185) Zhou, Y.; Jiang, J.; Gao, Y.; Pang, S. Y.; Yang, Y.; Ma, J.; Gu, J.; Li, J.; Wang, Z.; Wang, L. H.; Yuan, L. P.; Yang, Y. Activation of Peroxymonosulfate by Phenols: Important Role of Quinone Intermediates and Involvement of Singlet Oxygen. *Water Res.* **2017**, *125*. <https://doi.org/10.1016/j.watres.2017.08.049>.
- (186) Nihemaiti, M.; Permala, R. R.; Croué, J. P. Reactivity of Unactivated Peroxymonosulfate with Nitrogenous Compounds. *Water Res.* **2020**, *169*. <https://doi.org/10.1016/j.watres.2019.115221>.
- (187) Wacławek, S.; Grübel, K.; Černík, M. Simple Spectrophotometric Determination of

-
- Monopersulfate. *Spectrochim. Acta Part A Mol. Biomol. Spectrosc.* **2015**, *149*, 928–933. <https://doi.org/10.1016/J.SAA.2015.05.029>.
- (188) Duan, P.; Liu, X.; Liu, B.; Akram, M.; Li, Y.; Pan, J.; Yue, Q.; Gao, B.; Xu, X. Effect of Phosphate on Peroxymonosulfate Activation: Accelerating Generation of Sulfate Radical and Underlying Mechanism. *Appl. Catal. B Environ.* **2021**, 298. <https://doi.org/10.1016/j.apcatb.2021.120532>.
- (189) Gong, C.; Chen, F.; Yang, Q.; Luo, K.; Yao, F.; Wang, S.; Wang, X.; Wu, J.; Li, X.; Wang, D.; Zeng, G. Heterogeneous Activation of Peroxymonosulfate by Fe-Co Layered Doubled Hydroxide for Efficient Catalytic Degradation of Rhoadmine B. *Chem. Eng. J.* **2017**, *321*, 222–232. <https://doi.org/10.1016/J.CEJ.2017.03.117>.
- (190) Hussain, H.; Green, I. R.; Ahmed, I. Journey Describing Applications of Oxone in Synthetic Chemistry. *Chemical Reviews*. 2013. <https://doi.org/10.1021/cr3004373>.
- (191) Feng, M.; Jinadatha, C.; McDonald, T. J.; Sharma, V. K. Accelerated Oxidation of Organic Contaminants by Ferrate(VI): The Overlooked Role of Reducing Additives. *Environ. Sci. Technol.* **2018**, *52* (19). <https://doi.org/10.1021/acs.est.8b03770>.
- (192) Asere, T. G.; Stevens, C. V.; Du Laing, G. Use of (Modified) Natural Adsorbents for Arsenic Remediation: A Review. *Science of the Total Environment*. 2019. <https://doi.org/10.1016/j.scitotenv.2019.04.237>.
- (193) Chaplin, B. P.; Reinhard, M.; Schneider, W. F.; Schüth, C.; Shapley, J. R.; Strathmann, T. J.; Werth, C. J. Critical Review of Pd-Based Catalytic Treatment of Priority Contaminants in Water. *Environmental Science and Technology*. 2012. <https://doi.org/10.1021/es204087q>.
- (194) Wang, J.; Kerl, C. F.; Hu, P.; Martin, M.; Mu, T.; Brüggewirth, L.; Wu, G.; Said-Pullicino, D.; Romani, M.; Wu, L.; Planer-Friedrich, B. Thiolated Arsenic Species Observed in Rice Paddy Pore Waters. *Nat. Geosci.* **2020**. <https://doi.org/10.1038/s41561-020-0533-1>.
- (195) Kretchik, J. T. Arsenic in Drinking Water. *Chemical Health and Safety*. 2002. [https://doi.org/10.1016/S1074-9098\(02\)00298-8](https://doi.org/10.1016/S1074-9098(02)00298-8).
- (196) Ward, M. H.; deKok, T. M.; Levallois, P.; Brender, J.; Gulis, G.; Nolan, B. T.; VanDerslice, J. Workgroup Report: Drinking-Water Nitrate and Health - Recent

-
- Findings and Research Needs. *Environ. Health Perspect.* **2005**.
<https://doi.org/10.1289/ehp.8043>.
- (197) DeSimone, L. A.; McMahon, P. B.; Rosen, M. R. *Water Quality in Principal Aquifers of the United States, 1991-2010*; 2014.
- (198) Nolan, B. T.; Ruddy, B. C.; Hitt, K. J.; Helsel, D. R. A National Look at Nitrate Contamination of Groundwater. *Water Conditioning and Purification*. 1998.
- (199) Hosono, T.; Nakano, T.; Shimizu, Y.; Onodera, S. ichi; Taniguchi, M. Hydrogeological Constraint on Nitrate and Arsenic Contamination in Asian Metropolitan Groundwater. *Hydrol. Process.* **2011**. <https://doi.org/10.1002/hyp.8015>.
- (200) Elton, J.; Hristovski, K.; Westerhoff, P. Titanium Dioxide-Based Hybrid Ion-Exchange Media for Simultaneous Removal of Arsenic and Nitrate. *ACS Symp. Ser.* **2013**.
<https://doi.org/10.1021/bk-2013-1123.ch013>.
- (201) Upadhyaya, G.; Jackson, J.; Clancy, T. M.; Hyun, S. P.; Brown, J.; Hayes, K. F.; Raskin, L. Simultaneous Removal of Nitrate and Arsenic from Drinking Water Sources Utilizing a Fixed-Bed Bioreactor System. *Water Res.* **2010**.
<https://doi.org/10.1016/j.watres.2010.07.037>.
- (202) Chong, M. N.; Jin, B.; Chow, C. W. K.; Saint, C. Recent Developments in Photocatalytic Water Treatment Technology: A Review. *Water Research*. 2010.
<https://doi.org/10.1016/j.watres.2010.02.039>.
- (203) Dong, S.; Feng, J.; Fan, M.; Pi, Y.; Hu, L.; Han, X.; Liu, M.; Sun, J.; Sun, J. Recent Developments in Heterogeneous Photocatalytic Water Treatment Using Visible Light-Responsive Photocatalysts: A Review. *RSC Advances*. 2015.
<https://doi.org/10.1039/c4ra13734e>.
- (204) Lee, K. M.; Lai, C. W.; Ngai, K. S.; Juan, J. C. Recent Developments of Zinc Oxide Based Photocatalyst in Water Treatment Technology: A Review. *Water Research*. 2016. <https://doi.org/10.1016/j.watres.2015.09.045>.
- (205) Chan, S. H. S.; Wu, T. Y.; Juan, J. C.; Teh, C. Y. Recent Developments of Metal Oxide Semiconductors as Photocatalysts in Advanced Oxidation Processes (AOPs) for Treatment of Dye Waste-Water. *Journal of Chemical Technology and Biotechnology*. 2011. <https://doi.org/10.1002/jctb.2636>.

-
- (206) Fu, Y.; Chen, H.; Sun, X.; Wang, X. Combination of Cobalt Ferrite and Graphene: High-Performance and Recyclable Visible-Light Photocatalysis. *Appl. Catal. B Environ.* **2012**. <https://doi.org/10.1016/j.apcatb.2011.10.009>.
- (207) Peeters, D.; Taffa, D. H.; Kerrigan, M. M.; Ney, A.; Jöns, N.; Rogalla, D.; Cwik, S.; Becker, H. W.; Grafen, M.; Ostendorf, A.; Winter, C. H.; Chakraborty, S.; Wark, M.; Devi, A. Photoactive Zinc Ferrites Fabricated via Conventional CVD Approach. *ACS Sustain. Chem. Eng.* **2017**. <https://doi.org/10.1021/acssuschemeng.6b02233>.
- (208) Casbeer, E.; Sharma, V. K.; Li, X. Z. Synthesis and Photocatalytic Activity of Ferrites under Visible Light: A Review. *Separation and Purification Technology*. **2012**. <https://doi.org/10.1016/j.seppur.2011.11.034>.
- (209) Hankare, P. P.; Patil, R. P.; Jadhav, A. V.; Garadkar, K. M.; Sasikala, R. Enhanced Photocatalytic Degradation of Methyl Red and Thymol Blue Using Titania-Alumina-Zinc Ferrite Nanocomposite. *Appl. Catal. B Environ.* **2011**. <https://doi.org/10.1016/j.apcatb.2011.07.033>.
- (210) Wu, C.; Xu, Y.; Xu, S.; Tu, J.; Tian, C.; Lin, Z. Enhanced Adsorption of Arsenate by Spinel Zinc Ferrite Nano Particles: Effect of Zinc Content and Site Occupation. *J. Environ. Sci. (China)* **2019**. <https://doi.org/10.1016/j.jes.2018.09.010>.
- (211) McDonald, K. J.; Choi, K. S. Synthesis and Photoelectrochemical Properties of Fe₂O₃/ZnFe₂O₄ Composite Photoanodes for Use in Solar Water Oxidation. *Chem. Mater.* **2011**. <https://doi.org/10.1021/cm202399g>.
- (212) Sousa, M. H.; Tourinho, F. A.; Depeyrot, J.; Da Silva, G. J.; Lara, M. C. F. L. New Electric Double-Layered Magnetic Fluids Based on Copper, Nickel, and Zinc Ferrite Nanostructures. *J. Phys. Chem. B* **2001**. <https://doi.org/10.1021/jp0039161>.
- (213) Gomes, J. A.; Azevedo, G. M.; Depeyrot, J.; Mestnik-Filho, J.; Paula, F. L. O.; Tourinho, F. A.; Perzynski, R. Structural, Chemical, and Magnetic Investigations of Core-Shell Zinc Ferrite Nanoparticles. *J. Phys. Chem. C* **2012**. <https://doi.org/10.1021/jp3055069>.
- (214) Park, C. M.; Kim, Y. M.; Kim, K. H.; Wang, D.; Su, C.; Yoon, Y. Potential Utility of Graphene-Based Nano Spinel Ferrites as Adsorbent and Photocatalyst for Removing Organic/Inorganic Contaminants from Aqueous Solutions: A Mini Review.

-
- Chemosphere*. 2019. <https://doi.org/10.1016/j.chemosphere.2019.01.063>.
- (215) Lv, H.; Ma, L.; Zeng, P.; Ke, D.; Peng, T. Synthesis of Floriated ZnFe₂O₄ with Porous Nanorod Structures and Its Photocatalytic Hydrogen Production under Visible Light. *J. Mater. Chem.* **2010**. <https://doi.org/10.1039/b919897k>.
- (216) Shihong, X.; Daolun, F.; Wenfeng, S. Preparations and Photocatalytic Properties of Visible-Light-Active Zinc Ferrite-Doped TiO₂ Photocatalyst. *J. Phys. Chem. C* **2009**. <https://doi.org/10.1021/jp806704y>.
- (217) Harish, K. N.; Bhojya Naik, H. S.; Prashanth Kumar, P. N.; Viswanath, R. Optical and Photocatalytic Properties of Solar Light Active Nd-Substituted Ni Ferrite Catalysts: For Environmental Protection. *ACS Sustain. Chem. Eng.* **2013**. <https://doi.org/10.1021/sc400060z>.
- (218) Wang, T.; Jiang, Z.; An, T.; Li, G.; Zhao, H.; Wong, P. K. Enhanced Visible-Light-Driven Photocatalytic Bacterial Inactivation by Ultrathin Carbon-Coated Magnetic Cobalt Ferrite Nanoparticles. *Environ. Sci. Technol.* **2018**. <https://doi.org/10.1021/acs.est.7b06537>.
- (219) Jun, B. M.; Elanchezhian, S. S.; Yoon, Y.; Wang, D.; Kim, S.; Muthu Prabhu, S.; Park, C. M. Accelerated Photocatalytic Degradation of Organic Pollutants over Carbonate-Rich Lanthanum-Substituted Zinc Spinel Ferrite Assembled Reduced Graphene Oxide by Ultraviolet (UV)-Activated Persulfate. *Chem. Eng. J.* **2020**. <https://doi.org/10.1016/j.cej.2020.124733>.
- (220) Miao, C.; Ji, S.; Xu, G.; Liu, G.; Zhang, L.; Ye, C. Micro-Nano-Structured Fe₂O₃/Ti/ZnFe₂O₄ Heterojunction Films for Water Oxidation. *ACS Appl. Mater. Interfaces* **2012**. <https://doi.org/10.1021/am3011466>.
- (221) Dom, R.; Kumar, G. S.; Hebalkar, N. Y.; Joshi, S. V.; Borse, P. H. Eco-Friendly Ferrite Nanocomposite Photoelectrode for Improved Solar Hydrogen Generation. *RSC Adv.* **2013**. <https://doi.org/10.1039/c3ra42051e>.
- (222) Liu, S. Q.; Zhu, X. L.; Zhou, Y.; Meng, Z. Da; Chen, Z. G.; Liu, C. B.; Chen, F.; Wu, Z. Y.; Qian, J. C. Smart Photocatalytic Removal of Ammonia through Molecular Recognition of Zinc Ferrite/Reduced Graphene Oxide Hybrid Catalyst under Visible-Light Irradiation. *Catal. Sci. Technol.* **2017**. <https://doi.org/10.1039/c7cy00797c>.

-
- (223) Hwang, Y. H.; Kim, D. G.; Shin, H. S. Mechanism Study of Nitrate Reduction by Nano Zero Valent Iron. *J. Hazard. Mater.* **2011**.
<https://doi.org/10.1016/j.jhazmat.2010.10.078>.
- (224) Mamindy-Pajany, Y.; Hurel, C.; Marmier, N.; Roméo, M. Arsenic (V) Adsorption from Aqueous Solution onto Goethite, Hematite, Magnetite and Zero-Valent Iron: Effects of PH, Concentration and Reversibility. *Desalination* **2011**.
<https://doi.org/10.1016/j.desal.2011.07.046>.
- (225) Sun, Y. P.; Li, X. qin; Cao, J.; Zhang, W. xian; Wang, H. P. Characterization of Zero-Valent Iron Nanoparticles. *Advances in Colloid and Interface Science.* 2006.
<https://doi.org/10.1016/j.cis.2006.03.001>.
- (226) Lubphoo, Y.; Chyan, J. M.; Grisdanurak, N.; Liao, C. H. Influence of Pd-Cu on Nanoscale Zero-Valent Iron Supported for Selective Reduction of Nitrate. *J. Taiwan Inst. Chem. Eng.* **2016**. <https://doi.org/10.1016/j.jtice.2015.08.005>.
- (227) Raven, K. P.; Jain, A.; Loeppert, R. H. Arsenite and Arsenate Adsorption on Ferrihydrite: Kinetics, Equilibrium, and Adsorption Envelopes. *Environ. Sci. Technol.* **1998**. <https://doi.org/10.1021/es970421p>.
- (228) Lin, T. F.; Wu, J. K. Adsorption of Arsenite and Arsenate within Activated Alumina Grains: Equilibrium and Kinetics. *Water Res.* **2001**. [https://doi.org/10.1016/S0043-1354\(00\)00467-X](https://doi.org/10.1016/S0043-1354(00)00467-X).
- (229) Duddridge, J. E.; Wainwright, M. Heavy Metals in River Sediments-Calculation of Metal Adsorption Maxima Using Langmuir and Freundlich Isotherms. *Environ. Pollution. Ser. B, Chem. Phys.* **1981**. [https://doi.org/10.1016/0143-148X\(81\)90061-6](https://doi.org/10.1016/0143-148X(81)90061-6).
- (230) Matsumoto, M. R. Modeling Cadmium Adsorption by Activated Carbon Using the Langmuir and Freundlich Isotherm Expressions. *Sep. Sci. Technol.* **1993**.
<https://doi.org/10.1080/01496399308016742>.
- (231) Al-Gaashani, R.; Radiman, S.; Daud, A. R.; Tabet, N.; Al-Douri, Y. XPS and Optical Studies of Different Morphologies of ZnO Nanostructures Prepared by Microwave Methods. *Ceram. Int.* **2013**. <https://doi.org/10.1016/j.ceramint.2012.08.075>.
- (232) Guo, X.; Zhu, H.; Si, M.; Jiang, C.; Xue, D.; Zhang, Z.; Li, Q. ZnFe₂O₄ Nanotubes: Microstructure and Magnetic Properties. *J. Phys. Chem. C* **2014**.

-
- <https://doi.org/10.1021/jp507991e>.
- (233) Kaluza, S.; Schröter, M. K.; Naumann d'Alnoncourt, R.; Reinecke, T.; Muhler, M. High Surface Area ZnO Nanoparticles via a Novel Continuous Precipitation Route. *Adv. Funct. Mater.* **2008**, *18* (22). <https://doi.org/10.1002/adfm.200800457>.
- (234) Wang, J.; Xia, Y.; Dong, Y.; Chen, R.; Xiang, L.; Komarneni, S. Defect-Rich ZnO Nanosheets of High Surface Area as an Efficient Visible-Light Photocatalyst. *Appl. Catal. B Environ.* **2016**, *192*, 8–16. <https://doi.org/10.1016/J.APCATB.2016.03.040>.
- (235) Zhang, R.; Huang, J.; Zhao, J.; Sun, Z.; Wang, Y. Sol-Gel Auto-Combustion Synthesis of Zinc Ferrite for Moderate Temperature Desulfurization. *Energy and Fuels* **2007**, *21* (5). <https://doi.org/10.1021/ef070064w>.
- (236) Fei, P.; Wang, Q.; Zhong, M.; Su, B. Preparation and Adsorption Properties of Enhanced Magnetic Zinc Ferrite-Reduced Graphene Oxide Nanocomposites via a Facile One-Pot Solvothermal Method. *J. Alloys Compd.* **2016**, *685*. <https://doi.org/10.1016/j.jallcom.2016.05.279>.
- (237) Cheng, P.; Li, W.; Zhou, T.; Jin, Y.; Gu, M. Physical and Photocatalytic Properties of Zinc Ferrite Doped Titania under Visible Light Irradiation. *J. Photochem. Photobiol. A Chem.* **2004**, *168* (1–2), 97–101. <https://doi.org/10.1016/J.JPHOTOCHEM.2004.05.018>.
- (238) Pavlov, M.; Siegbahn, P. E. M.; Sandström, M. Hydration of Beryllium, Magnesium, Calcium, and Zinc Ions Using Density Functional Theory. *J. Phys. Chem. A* **1998**. <https://doi.org/10.1021/jp972072r>.
- (239) Makuła, P.; Pacia, M.; Macyk, W. How To Correctly Determine the Band Gap Energy of Modified Semiconductor Photocatalysts Based on UV-Vis Spectra. *Journal of Physical Chemistry Letters*. 2018. <https://doi.org/10.1021/acs.jpcclett.8b02892>.
- (240) Fan, G.; Gu, Z.; Yang, L.; Li, F. Nanocrystalline Zinc Ferrite Photocatalysts Formed Using the Colloid Mill and Hydrothermal Technique. *Chem. Eng. J.* **2009**. <https://doi.org/10.1016/j.cej.2009.08.008>.
- (241) Georgekutty, R.; Seery, M. K.; Pillai, S. C. A Highly Efficient Ag-ZnO Photocatalyst: Synthesis, Properties, and Mechanism. *J. Phys. Chem. C* **2008**. <https://doi.org/10.1021/jp802729a>.

-
- (242) Li, J.; Huang, Z.; Wu, D.; Yin, G.; Liao, X.; Gu, J.; Han, D. Preparation and Protein Detection of Zn-Ferrite Film with Magnetic and Photoluminescence Properties. *J. Phys. Chem. C* **2010**. <https://doi.org/10.1021/jp907107s>.
- (243) Yang, H.; Bai, X.; Hao, P.; Tian, J.; Bo, Y.; Wang, X.; Liu, H. A Simple Gas Sensor Based on Zinc Ferrite Hollow Spheres: Highly Sensitivity, Excellent Selectivity and Long-Term Stability. *Sensors Actuators, B Chem.* **2019**. <https://doi.org/10.1016/j.snb.2018.10.056>.
- (244) Yang, L.; Cheng, D.; Xu, H.; Zeng, X.; Wan, X.; Shui, J.; Xiang, Z.; Cao, D. Unveiling the High-Activity Origin of Single-Atom Iron Catalysts for Oxygen Reduction Reaction. *Proc. Natl. Acad. Sci. U. S. A.* **2018**. <https://doi.org/10.1073/pnas.1800771115>.
- (245) Liu, Y.; Liu, J. C.; Li, T. H.; Duan, Z. H.; Zhang, T. Y.; Yan, M.; Li, W. L.; Xiao, H.; Wang, Y. G.; Chang, C. R.; Li, J. Unravelling the Enigma of Nonoxidative Conversion of Methane on Iron Single-Atom Catalysts. *Angew. Chemie - Int. Ed.* **2020**. <https://doi.org/10.1002/anie.202003908>.
- (246) Gao, C.; Low, J.; Long, R.; Kong, T.; Zhu, J.; Xiong, Y. Heterogeneous Single-Atom Photocatalysts: Fundamentals and Applications. *Chem. Rev.* **2020**. <https://doi.org/10.1021/acs.chemrev.9b00840>.
- (247) Yang, X. F.; Wang, A.; Qiao, B.; Li, J.; Liu, J.; Zhang, T. Single-Atom Catalysts: A New Frontier in Heterogeneous Catalysis. *Acc. Chem. Res.* **2013**. <https://doi.org/10.1021/ar300361m>.
- (248) Mertens, J.; Rose, J.; Kägi, R.; Chaurand, P.; Plötze, M.; Wehrli, B.; Furrer, G. Adsorption of Arsenic on Polyaluminum Granulate. *Environ. Sci. Technol.* **2012**. <https://doi.org/10.1021/es204508t>.
- (249) Kim, Y.; Kim, C.; Choi, I.; Rengaraj, S.; Yi, J. Arsenic Removal Using Mesoporous Alumina Prepared via a Templating Method. *Environ. Sci. Technol.* **2004**. <https://doi.org/10.1021/es0346431>.
- (250) Giménez, J.; Martínez, M.; de Pablo, J.; Rovira, M.; Duro, L. Arsenic Sorption onto Natural Hematite, Magnetite, and Goethite. *J. Hazard. Mater.* **2007**. <https://doi.org/10.1016/j.jhazmat.2006.07.020>.

-
- (251) Ho, Y. S.; McKay, G. Pseudo-Second Order Model for Sorption Processes. *Process Biochem.* **1999**. [https://doi.org/10.1016/S0032-9592\(98\)00112-5](https://doi.org/10.1016/S0032-9592(98)00112-5).
- (252) Gong, X. J.; Li, Y. S.; Dong, Y. Q.; Li, W. G. Arsenic Adsorption by Innovative Iron/Calcium in-Situ-Impregnated Mesoporous Activated Carbons from Low-Temperature Water and Effects of the Presence of Humic Acids. *Chemosphere* **2020**. <https://doi.org/10.1016/j.chemosphere.2020.126275>.
- (253) Wei, Y.; Wei, S.; Liu, C.; Chen, T.; Tang, Y.; Ma, J.; Yin, K.; Luo, S. Efficient Removal of Arsenic from Groundwater Using Iron Oxide Nanoneedle Array-Decorated Biochar Fibers with High Fe Utilization and Fast Adsorption Kinetics. *Water Res.* **2019**. <https://doi.org/10.1016/j.watres.2019.115107>.
- (254) Li, R.; Li, Q.; Gao, S.; Shang, J. K. Exceptional Arsenic Adsorption Performance of Hydrous Cerium Oxide Nanoparticles: Part A. Adsorption Capacity and Mechanism. *Chem. Eng. J.* **2012**. <https://doi.org/10.1016/j.cej.2012.01.061>.
- (255) Liu, C. H.; Chuang, Y. H.; Chen, T. Y.; Tian, Y.; Li, H.; Wang, M. K.; Zhang, W. Mechanism of Arsenic Adsorption on Magnetite Nanoparticles from Water: Thermodynamic and Spectroscopic Studies. *Environ. Sci. Technol.* **2015**. <https://doi.org/10.1021/acs.est.5b00381>.
- (256) Schwarzenbach, R. P.; Escher, B. I.; Fenner, K.; Hofstetter, T. B.; Johnson, C. A.; Von Gunten, U.; Wehrli, B. The Challenge of Micropollutants in Aquatic Systems. *Science*. 2006. <https://doi.org/10.1126/science.1127291>.
- (257) Liu, G. J.; Zhang, X. R.; Mcwilliams, L.; Talley, J. W.; Neal, C. R. Influence of Ionic Strength, Electrolyte Type, and NOM on As(V) Adsorption onto TiO₂. *J. Environ. Sci. Heal. - Part A Toxic/Hazardous Subst. Environ. Eng.* **2008**. <https://doi.org/10.1080/10934520701795749>.
- (258) Liu, G.; Zhang, X.; Talley, J. W.; Neal, C. R.; Wang, H. Effect of NOM on Arsenic Adsorption by TiO₂ in Simulated As(III)-Contaminated Raw Waters. *Water Res.* **2008**. <https://doi.org/10.1016/j.watres.2007.12.023>.
- (259) Dutta, P. K.; Ray, A. K.; Sharma, V. K.; Millero, F. J. Adsorption of Arsenate and Arsenite on Titanium Dioxide Suspensions. *J. Colloid Interface Sci.* **2004**. <https://doi.org/10.1016/j.jcis.2004.06.015>.

-
- (260) Myneni, S. C. B.; Traina, S. J.; Waychunas, G. A.; Logan, T. J. Experimental and Theoretical Vibrational Spectroscopic Evaluation of Arsenate Coordination in Aqueous Solutions, Solids, and at Mineral-Water Interfaces. *Geochim. Cosmochim. Acta* **1998**. [https://doi.org/10.1016/S0016-7037\(98\)00222-1](https://doi.org/10.1016/S0016-7037(98)00222-1).
- (261) Stumm, W. Chemistry of the Solid-Water Interface: Processes at the Mineral- Water and Particle-Water Interface in Natural Systems. *Chem. solid-water interface Process. Miner. water Part. interface Nat. Syst.* **1992**. [https://doi.org/10.1016/0016-7037\(93\)90027-t](https://doi.org/10.1016/0016-7037(93)90027-t).
- (262) Lyklema, J. Surface Chemistry of Colloids in Connection with Stability. In *The Scientific Basis of Flocculation*; 1978. https://doi.org/10.1007/978-94-009-9938-1_2.
- (263) Rahnemaie, R.; Hiemstra, T.; van Riemsdijk, W. H. Inner- and Outer-Sphere Complexation of Ions at the Goethite-Solution Interface. *J. Colloid Interface Sci.* **2006**. <https://doi.org/10.1016/j.jcis.2005.11.003>.
- (264) Su, C.; Puls, R. W. Nitrate Reduction by Zerovalent Iron: Effects of Formate, Oxalate, Citrate, Chloride, Sulfate, Borate, and Phosphate. *Environ. Sci. Technol.* **2004**. <https://doi.org/10.1021/es034650p>.
- (265) Kanematsu, M.; Young, T. M.; Fukushi, K.; Green, P. G.; Darby, J. L. Arsenic(III, V) Adsorption on a Goethite-Based Adsorbent in the Presence of Major Co-Existing Ions: Modeling Competitive Adsorption Consistent with Spectroscopic and Molecular Evidence. *Geochim. Cosmochim. Acta* **2013**. <https://doi.org/10.1016/j.gca.2012.09.055>.
- (266) Han, J.; Ro, H. M. Interpreting Competitive Adsorption of Arsenate and Phosphate on Nanosized Iron (Hydr)Oxides: Effects of PH and Surface Loading. *Environ. Sci. Pollut. Res.* **2018**. <https://doi.org/10.1007/s11356-018-2897-y>.
- (267) Goldberg, S. Competitive Adsorption of Arsenate and Arsenite on Oxides and Clay Minerals. *Soil Sci. Soc. Am. J.* **2002**. <https://doi.org/10.2136/sssaj2002.0413>.
- (268) Manning, B. A.; Goldberg, S. Modeling Competitive Adsorption of Arsenate with Phosphate and Molybdate on Oxide Minerals. *Soil Sci. Soc. Am. J.* **1996**. <https://doi.org/10.2136/sssaj1996.03615995006000010020x>.
- (269) Hongshao, Z.; Stanforth, R. Competitive Adsorption of Phosphate and Arsenate on

-
- Goethite. *Environ. Sci. Technol.* **2001**. <https://doi.org/10.1021/es010890y>.
- (270) He, Y.; Lin, H.; Dong, Y.; Li, B.; Wang, L.; Chu, S.; Luo, M.; Liu, J. Zeolite Supported Fe/Ni Bimetallic Nanoparticles for Simultaneous Removal of Nitrate and Phosphate: Synergistic Effect and Mechanism. *Chem. Eng. J.* **2018**. <https://doi.org/10.1016/j.cej.2018.04.088>.
- (271) Mohd Omar, F.; Abdul Aziz, H.; Stoll, S. Aggregation and Disaggregation of ZnO Nanoparticles: Influence of PH and Adsorption of Suwannee River Humic Acid. *Sci. Total Environ.* **2014**. <https://doi.org/10.1016/j.scitotenv.2013.08.044>.
- (272) Redman, A. D.; Macalady, D. L.; Ahmann, D. Natural Organic Matter Affects Arsenic Speciation and Sorption onto Hematite. *Environ. Sci. Technol.* **2002**. <https://doi.org/10.1021/es0112801>.
- (273) Long, M.; Brame, J.; Qin, F.; Bao, J.; Li, Q.; Alvarez, P. J. J. Phosphate Changes Effect of Humic Acids on TiO₂ Photocatalysis: From Inhibition to Mitigation of Electron-Hole Recombination. *Environ. Sci. Technol.* **2017**. <https://doi.org/10.1021/acs.est.6b04845>.
- (274) Benkeser, R. A.; Ehler, D. F. Selective Reduction of Aromatic Carboxyl Groups to Methyl in the Presence of Ester Functionality. a New Procedure for the Preparation of Ester-Containing Organosilanes. *J. Org. Chem.* **1973**. <https://doi.org/10.1021/jo00960a062>.
- (275) Chen, S.; Yu, Y. L.; Wang, J. H. Inner Filter Effect-Based Fluorescent Sensing Systems: A Review. *Analytica Chimica Acta.* **2018**. <https://doi.org/10.1016/j.aca.2017.10.026>.
- (276) Ahalya, K.; Suriyanarayanan, N.; Ranjithkumar, V. Effect of Cobalt Substitution on Structural and Magnetic Properties and Chromium Adsorption of Manganese Ferrite Nano Particles. *J. Magn. Magn. Mater.* **2014**. <https://doi.org/10.1016/j.jmmm.2014.07.030>.
- (277) Lingamdinne, L. P.; Koduru, J. R.; Chang, Y. Y.; Karri, R. R. Process Optimization and Adsorption Modeling of Pb(II) on Nickel Ferrite-Reduced Graphene Oxide Nano-Composite. *J. Mol. Liq.* **2018**. <https://doi.org/10.1016/j.molliq.2017.11.174>.
- (278) Gu, W.; Xie, Q.; Qi, C.; Zhao, L.; Wu, D. Phosphate Removal Using Zinc Ferrite

-
- Synthesized through a Facile Solvothermal Technique. *Powder Technol.* **2016**.
<https://doi.org/10.1016/j.powtec.2016.07.015>.
- (279) Glover, T. G.; Sabo, D.; Vaughan, L. A.; Rossin, J. A.; Zhang, Z. J. Adsorption of Sulfur Dioxide by CoFe₂O₄ Spinel Ferrite Nanoparticles and Corresponding Changes in Magnetism. *Langmuir* **2012**. <https://doi.org/10.1021/la3003417>.
- (280) Konicki, W.; Sibera, D.; Mijowska, E.; Lendzion-Bieluń, Z.; Narkiewicz, U. Equilibrium and Kinetic Studies on Acid Dye Acid Red 88 Adsorption by Magnetic ZnFe₂O₄ Spinel Ferrite Nanoparticles. *J. Colloid Interface Sci.* **2013**.
<https://doi.org/10.1016/j.jcis.2013.02.021>.
- (281) Rahman, M. F.; Peldszus, S.; Anderson, W. B. Behaviour and Fate of Perfluoroalkyl and Polyfluoroalkyl Substances (PFASs) in Drinking Water Treatment: A Review. *Water Research.* 2014. <https://doi.org/10.1016/j.watres.2013.10.045>.
- (282) Crinnion, W. J. The CDC Fourth National Report on Human Exposure to Environmental Chemicals: What It Tells Us about Our Toxic Burden and How It Assists Environmental Medicine Physicians. *Alternative Medicine Review.* 2010.
- (283) Looker, C.; Luster, M. I.; Calafat, A. M.; Johnson, V. J.; Burleson, G. R.; Burleson, F. G.; Fletcher, T. Influenza Vaccine Response in Adults Exposed to Perfluorooctanoate and Perfluorooctanesulfonate. *Toxicol. Sci.* **2014**, *138* (1).
<https://doi.org/10.1093/toxsci/kft269>.
- (284) NTP. National Toxicology Program (NTP) Monograph Immunotoxicity Associated with Exposure to Perfluorooctanoic Acid or Perfluorooctane Sulfonate. *Natl. Inst. Environ. Heal. Sci.* **2016**, No. September.
- (285) Giannetti, E. Thermal Stability and Bond Dissociation Energy of Fluorinated Polymers: A Critical Evaluation. *J. Fluor. Chem.* **2005**, *126* (4), 623–630.
<https://doi.org/10.1016/J.JFLUCHEM.2005.01.008>.
- (286) Moore, J. T.; Lu, C. C. Catalytic Hydrogenolysis of Aryl C-F Bonds Using a Bimetallic Rhodium-Indium Complex. *J. Am. Chem. Soc.* **2020**, *142* (27).
<https://doi.org/10.1021/jacs.0c04937>.
- (287) Singh, R. K.; Fernando, S.; Baygi, S. F.; Multari, N.; Thagard, S. M.; Holsen, T. M. Breakdown Products from Perfluorinated Alkyl Substances (PFAS) Degradation in a

-
- Plasma-Based Water Treatment Process. *Environ. Sci. Technol.* **2019**.
<https://doi.org/10.1021/acs.est.8b07031>.
- (288) Washington, J. W.; Jenkins, T. M.; Rankin, K.; Naile, J. E. Decades-Scale Degradation of Commercial, Side-Chain, Fluorotelomer-Based Polymers in Soils and Water. *Environ. Sci. Technol.* **2015**, *49* (2). <https://doi.org/10.1021/es504347u>.
- (289) Washington, J. W.; Jenkins, T. M. Abiotic Hydrolysis of Fluorotelomer-Based Polymers as a Source of Perfluorocarboxylates at the Global Scale. *Environ. Sci. Technol.* **2015**, *49* (24). <https://doi.org/10.1021/acs.est.5b03686>.
- (290) Radjenovic, J.; Duinslaeger, N.; Avval, S. S.; Chaplin, B. P. Facing the Challenge of Poly- And Perfluoroalkyl Substances in Water: Is Electrochemical Oxidation the Answer? *Environmental Science and Technology*. 2020.
<https://doi.org/10.1021/acs.est.0c06212>.
- (291) Ateia, M.; Alsaiee, A.; Karanfil, T.; Dichtel, W. Efficient PFAS Removal by Amine-Functionalized Sorbents: Critical Review of the Current Literature. *Environ. Sci. & Technol. Lett.* **2019**, *6* (12), 688–695.
<https://doi.org/10.1021/acs.estlett.9b00659>.
- (292) Gagliano, E.; Sgroi, M.; Falciglia, P. P.; Vagliasindi, F. G. A.; Roccaro, P. Removal of Poly- and Perfluoroalkyl Substances (PFAS) from Water by Adsorption: Role of PFAS Chain Length, Effect of Organic Matter and Challenges in Adsorbent Regeneration. *Water Res.* **2020**, *171*, 115381. <https://doi.org/10.1016/J.WATRES.2019.115381>.
- (293) Li, F.; Duan, J.; Tian, S.; Ji, H.; Zhu, Y.; Wei, Z.; Zhao, D. Short-Chain per- and Polyfluoroalkyl Substances in Aquatic Systems: Occurrence, Impacts and Treatment. *Chemical Engineering Journal*. 2020. <https://doi.org/10.1016/j.cej.2019.122506>.
- (294) Duan, L.; Wang, B.; Heck, K.; Guo, S.; Clark, C. A.; Arredondo, J.; Wang, M.; Senftle, T. P.; Westerhoff, P.; Wen, X.; Song, Y.; Wong, M. S. Efficient Photocatalytic PFOA Degradation over Boron Nitride. *Environ. Sci. Technol. Lett.* **2020**.
<https://doi.org/10.1021/acs.estlett.0c00434>.
- (295) Li, X.; Zhang, P.; Jin, L.; Shao, T.; Li, Z.; Cao, J. Efficient Photocatalytic Decomposition of Perfluorooctanoic Acid by Indium Oxide and Its Mechanism. *Environ. Sci. Technol.* **2012**, *46* (10). <https://doi.org/10.1021/es204279u>.

-
- (296) Zhao, B.; Zhang, P. Photocatalytic Decomposition of Perfluorooctanoic Acid with β -Ga₂O₃ Wide Bandgap Photocatalyst. *Catal. Commun.* **2009**, *10* (8).
<https://doi.org/10.1016/j.catcom.2009.01.017>.
- (297) Gao, J.; Liu, Z.; Bentel, M. J.; Yu, Y.; Men, Y.; Liu, J. Defluorination of Omega-Hydroperfluorocarboxylates (ω -HPFCAs): Distinct Reactivities from Perfluoro and Fluorotelomeric Carboxylates. *Environ. Sci. Technol.* **2021**, *55* (20).
<https://doi.org/10.1021/acs.est.1c04429>.
- (298) Sahu, S. P.; Qanbarzadeh, M.; Ateia, M.; Torkzadeh, H.; Maroli, A. S.; Cates, E. L. Rapid Degradation and Mineralization of Perfluorooctanoic Acid by a New Petitjeanite Bi₃O(OH)(PO₄)₂ Microparticle Ultraviolet Photocatalyst. *Environ. Sci. Technol. Lett.* **2018**, *5* (8). <https://doi.org/10.1021/acs.estlett.8b00395>.
- (299) Kirchon, A.; Feng, L.; Drake, H. F.; Joseph, E. A.; Zhou, H. C. From Fundamentals to Applications: A Toolbox for Robust and Multifunctional MOF Materials. *Chemical Society Reviews*. 2018. <https://doi.org/10.1039/c8cs00688a>.
- (300) Lin, R. B.; Xiang, S.; Xing, H.; Zhou, W.; Chen, B. Exploration of Porous Metal–Organic Frameworks for Gas Separation and Purification. *Coordination Chemistry Reviews*. 2019. <https://doi.org/10.1016/j.ccr.2017.09.027>.
- (301) Pascanu, V.; González Miera, G.; Inge, A. K.; Martín-Matute, B. Metal-Organic Frameworks as Catalysts for Organic Synthesis: A Critical Perspective. *Journal of the American Chemical Society*. 2019. <https://doi.org/10.1021/jacs.9b00733>.
- (302) Yuan, S.; Feng, L.; Wang, K.; Pang, J.; Bosch, M.; Lollar, C.; Sun, Y.; Qin, J.; Yang, X.; Zhang, P.; Wang, Q.; Zou, L.; Zhang, Y.; Zhang, L.; Fang, Y.; Li, J.; Zhou, H. C. Stable Metal–Organic Frameworks: Design, Synthesis, and Applications. *Advanced Materials*. 2018. <https://doi.org/10.1002/adma.201704303>.
- (303) Wang, B.; Lv, X. L.; Feng, D.; Xie, L. H.; Zhang, J.; Li, M.; Xie, Y.; Li, J. R.; Zhou, H. C. Highly Stable Zr(IV)-Based Metal-Organic Frameworks for the Detection and Removal of Antibiotics and Organic Explosives in Water. *J. Am. Chem. Soc.* **2016**.
<https://doi.org/10.1021/jacs.6b01663>.
- (304) Wen, Y.; Zhang, P.; Sharma, V. K.; Ma, X.; Zhou, H.-C. Metal-Organic Frameworks for Environmental Applications. *Cell Reports Phys. Sci.* **2021**, *2* (2), 100348.

-
- <https://doi.org/10.1016/j.xcrp.2021.100348>.
- (305) Wen, Y.; Feng, M.; Zhang, P.; Zhou, H.-C.; Sharma, V. K.; Ma, X. Metal Organic Frameworks (MOFs) as Photocatalysts for the Degradation of Agricultural Pollutants in Water. *ACS ES&T Eng.* **2021**, *1* (5). <https://doi.org/10.1021/acsestengg.1c00051>.
- (306) Suwannakot, P.; Lisi, F.; Ahmed, E.; Liang, K.; Babarao, R.; Gooding, J. J.; Donald, W. A. Metal-Organic Framework-Enhanced Solid-Phase Microextraction Mass Spectrometry for the Direct and Rapid Detection of Perfluorooctanoic Acid in Environmental Water Samples. *Anal. Chem.* **2020**, *92* (10). <https://doi.org/10.1021/acs.analchem.9b05524>.
- (307) Li, R.; Alomari, S.; Islamoglu, T.; Farha, O. K.; Fernando, S.; Thagard, S. M.; Holsen, T. M.; Wriedt, M. Systematic Study on the Removal of Per- and Polyfluoroalkyl Substances from Contaminated Groundwater Using Metal-Organic Frameworks. *Environ. Sci. Technol.* **2021**, *55* (22). <https://doi.org/10.1021/acs.est.1c03974>.
- (308) Li, R.; Alomari, S.; Stanton, R.; Wasson, M. C.; Islamoglu, T.; Farha, O. K.; Holsen, T. M.; Thagard, S. M.; Trivedi, D. J.; Wriedt, M. Efficient Removal of Per- And Polyfluoroalkyl Substances from Water with Zirconium-Based Metal-Organic Frameworks. *Chem. Mater.* **2021**, *33* (9). <https://doi.org/10.1021/acs.chemmater.1c00324>.
- (309) Vaesen, S.; Guillerm, V.; Yang, Q.; Wiersum, A. D.; Marszalek, B.; Gil, B.; Vimont, A.; Daturi, M.; Devic, T.; Llewellyn, P. L.; Serre, C.; Maurin, G.; De Weireld, G. A Robust Amino-Functionalized Titanium(IV) Based MOF for Improved Separation of Acid Gases. *Chem. Commun.* **2013**, *49* (86). <https://doi.org/10.1039/c3cc45828h>.
- (310) Hendon, C. H.; Tiana, D.; Fontecave, M.; Sanchez, C.; D'Arras, L.; Sassoye, C.; Rozes, L.; Mellot-Draznieks, C.; Walsh, A. Engineering the Optical Response of the Titanium-MIL-125 Metal-Organic Framework through Ligand Functionalization. *J. Am. Chem. Soc.* **2013**. <https://doi.org/10.1021/ja405350u>.
- (311) Kampouri, S.; Nguyen, T. N.; Spodaryk, M.; Palgrave, R. G.; Züttel, A.; Smit, B.; Stylianou, K. C. Concurrent Photocatalytic Hydrogen Generation and Dye Degradation Using MIL-125-NH₂ under Visible Light Irradiation. *Adv. Funct. Mater.* **2018**, *28* (52). <https://doi.org/10.1002/adfm.201806368>.

-
- (312) Chambers, M. B.; Wang, X.; Ellezam, L.; Ersen, O.; Fontecave, M.; Sanchez, C.; Rozes, L.; Mellot-Draznieks, C. Maximizing the Photocatalytic Activity of Metal-Organic Frameworks with Aminated-Functionalized Linkers: Substoichiometric Effects in MIL-125-NH₂. *J. Am. Chem. Soc.* **2017**, *139* (24).
<https://doi.org/10.1021/jacs.7b02186>.
- (313) Cheng, Z.; Chen, Q.; Liu, Z.; Liu, J.; Liu, Y.; Liu, S.; Gao, X.; Tan, Y.; Shen, Z. Interpretation of Reductive PFAS Defluorination with Quantum Chemical Parameters. *Environ. Sci. Technol. Lett.* **2021**, *8* (8). <https://doi.org/10.1021/acs.estlett.1c00403>.
- (314) Liu, Z.; Bentel, M. J.; Yu, Y.; Ren, C.; Gao, J.; Pulikkal, V. F.; Sun, M.; Men, Y.; Liu, J. Near-Quantitative Defluorination of Perfluorinated and Fluorotelomer Carboxylates and Sulfonates with Integrated Oxidation and Reduction. *Environ. Sci. Technol.* **2021**, *55* (10). <https://doi.org/10.1021/acs.est.1c00353>.
- (315) Long, M.; Donoso, J.; Bhati, M.; Elias, W. C.; Heck, K. N.; Luo, Y. H.; Lai, Y. J. S.; Gu, H.; Senftle, T. P.; Zhou, C.; Wong, M. S.; Rittmann, B. E. Adsorption and Reductive Defluorination of Perfluorooctanoic Acid over Palladium Nanoparticles. *Environ. Sci. Technol.* **2021**, *55* (21). <https://doi.org/10.1021/acs.est.1c03134>.
- (316) Chen, Z.; Teng, Y.; Mi, N.; Jin, X.; Yang, D.; Wang, C.; Wu, B.; Ren, H.; Zeng, G.; Gu, C. Highly Efficient Hydrated Electron Utilization and Reductive Destruction of Perfluoroalkyl Substances Induced by Intermolecular Interaction. *Environ. Sci. Technol.* **2021**, *55* (6). <https://doi.org/10.1021/acs.est.0c07927>.
- (317) Sun, Z.; Zhang, C.; Xing, L.; Zhou, Q.; Dong, W.; Hoffmann, M. R. UV/Nitriilotriacetic Acid Process as a Novel Strategy for Efficient Photoreductive Degradation of Perfluorooctanesulfonate. *Environ. Sci. Technol.* **2018**, *52* (5).
<https://doi.org/10.1021/acs.est.7b05912>.
- (318) Liu, G.; Feng, C.; Shao, P. Degradation of Perfluorooctanoic Acid with Hydrated Electron by a Heterogeneous Catalytic System. *Environ. Sci. & Technol.* **2021**, *0* (0). <https://doi.org/10.1021/acs.est.1c06793>.
- (319) Bentel, M. J.; Liu, Z.; Yu, Y.; Gao, J.; Men, Y.; Liu, J. Enhanced Degradation of Perfluorocarboxylic Acids (PFCAs) by UV/Sulfite Treatment: Reaction Mechanisms and System Efficiencies at PH 12. *Environ. Sci. Technol. Lett.* **2020**, *7* (5).

-
- <https://doi.org/10.1021/acs.estlett.0c00236>.
- (320) Bentel, M. J.; Yu, Y.; Xu, L.; Kwon, H.; Li, Z.; Wong, B. M.; Men, Y.; Liu, J. Degradation of Perfluoroalkyl Ether Carboxylic Acids with Hydrated Electrons: Structure-Reactivity Relationships and Environmental Implications. *Environ. Sci. Technol.* **2020**, *54* (4). <https://doi.org/10.1021/acs.est.9b05869>.
- (321) Kapoor, S.; Lawless, D.; Kennepohl, P.; Meisel, D.; Serpone, N. Reduction and Aggregation of Silver Ions in Aqueous Gelatin Solutions. *Langmuir* **1994**, *10* (9). <https://doi.org/10.1021/la00021a026>.
- (322) Elliot, A. J.; McCracken, D. R.; Buxton, G. V.; Wood, N. D. Estimation of Rate Constants for Near-Diffusion-Controlled Reactions in Water at High Temperatures. *J. Chem. Soc. Faraday Trans.* **1990**, *86* (9). <https://doi.org/10.1039/FT9908601539>.
- (323) Hentz, R. R.; Aziz, F.; Hansen, E. M. Pulse Radiolysis of Liquids at High Pressures. II. Diffusion-Controlled Reactions of the Hydrated Electron. *J. Chem. Phys.* **1972**, *56* (9). <https://doi.org/10.1063/1.1677893>.
- (324) Safy, M. E. A.; Amin, M.; Haikal, R. R.; Elshazly, B.; Wang, J.; Wang, Y.; Wöll, C.; Alkordi, M. H. Probing the Water Stability Limits and Degradation Pathways of Metal–Organic Frameworks. *Chem. - A Eur. J.* **2020**, *26* (31). <https://doi.org/10.1002/chem.202000207>.